学位論文

The study of warm molecular gas in the vicinity of active galactic nuclei with the near-infrared CO absorption band

(一酸化炭素近赤外線吸収バンドを用いた
活動銀河核近傍の高温分子ガスの研究)

平成 29 年 12 月博士（理学）申請

東京大学大学院理学系研究科
物理学専攻
馬場 俊介

The study of warm molecular gas in the vicinity of active galactic nuclei with the near-infrared CO absorption band

Shunsuke Baba

February 13, 2018

Abstract

An active galactic nucleus (AGN) is a galactic central region that exhibits intense activity being powered by mass accretion onto a supermassive black hole. Its energy output plays a significant role in the formation and evolution of the host galaxy. This central engine is considered to be surrounded by a dusty structure like a torus (AGN torus). The anisotropy of the torus is a key factor in understanding widely diverging appearances of AGNs. When an AGN is observed from the direction parallel to its torus axis, broad optical emission lines that originate from the vicinity of the nucleus are directly seen, and the AGN is recognized as type-1. When the AGN is viewed from the direction perpendicular to the axis, the broad lines are obscured by the extinction within the torus, only narrow optical emission lines originating from a region above the torus are observed, and the AGN is recognized as type-2. This viewing angle effect is the fundamental concept of the unification scheme of AGNs. Many modifications and extensions of this basic picture have been proposed to explain complicated characteristics of AGNs with different luminosities and multi-wavelength properties. In any case, at least it is certain that some anisotropic structure exists at the center of an AGN. For the establishment of a unified understanding of AGNs, it is essential to observe and investigate physical states and structures of AGN tori in a large sample including AGNs of different properties. However, the small parsec-scale sizes of AGN tori make it tough to perform spatially-resolved direct observations.

The strategy in this thesis is near-infrared spectroscopy of the CO fundamental rotational-vibrational absorption band centered at 4.67 μm. If a torus is viewed edge-on, using the bright near-infrared dust emission from the central region as the background continuum, we can expect to observe the foreground torus with an effectively high spatial resolution owing to the compactness of the continuum source. The aim of this thesis is to demonstrate the effectiveness of the CO absorption as a probe of a putative AGN torus and use it to investigate torus properties in galaxies of different luminosities and optical classifications. The Infrared Camera (IRC) onboard the AKARI satellite enables unique observations of the CO absorption even in less-luminous galaxies of infrared luminosities of 10^{11} $L_{\odot}$ or less. Its near-infrared grism spectroscopy covers wavelengths from 2.5 to 5.0 μm with a spectral resolution of about 100 and has a 1σ sensitivity of 0.5 mJy.

However, the IRC near-infrared spectrum is problematic at wavelengths longer than 4.9 μm being contaminated by the diffracted second-order light, which prevents the accurate flux cali-

bration in that range. To utilize the IRC observations for our study, we corrected for the effect of the contamination.

First, we fixed the artifact in the observations that had been conducted during the cryogenic phase of the satellite. The IRC wavelength calibration was revised by considering a higher-order effect caused by the wavelength dependence of the refractive index of the grism material. The new wavelength calibration revealed that the contamination occurs due to the nonlinearity arising from the refractive index, even if the order-sorting filter coated on the grism perfectly cuts off wavelengths shorter than 2.5 μm. The spectral responses from the first- and second-order light were simultaneously obtained by using standard objects of red and blue spectra, which leads contrastive strengths of the contamination. With the new responses, the first- and second-order light mixing in 4.9–5.0 μm were quantitatively decomposed for the first time.

We then proceeded to the post-cryogenic phase, during which the detector temperature had gradually increased. The revised wavelength calibration curve in the post-cryogenic phase was found to be consistent with that in the cryogenic phase and not to have any significant temperature dependence. The response from the first-order light was found to be smaller than that in the cryogenic phase by a factor of 0.7. The decline of the response during the period was evaluated to be 10%. The relative strength of the contaminating second-order light to the first-order spectrum was found to be smaller than that in the cryogenic phase by 25%, reflecting the degradation of the point-spread function around 2.5μm relevant to the contaminated range.

Next, using spectroscopic observations with the *AKARI* and *Spitzer* satellites, we analyzed band profiles of the CO absorption in nearby ten AGNs, which had been known to show the feature, by fitting a plane-parallel local thermal equilibrium gas model. The CO gas was found to be warm (200–500 K) and to have a large column density ($N_{\rm H} \gtrsim 10^{23}$ cm^{-2}). The heating of the gas is not explicable by either UV heating or shock heating because these processes cannot represent the observed large column densities. Instead, X-ray radiation from the nuclei is the most convincing candidate because it can produce large columns of warm gas of up to $N_{\rm H} \sim 10^{24}$ cm^{-2}. Based on the adoption of the CO abundance of CO/H $= 10^{-4}$, the hydrogen column density estimated from the CO band was smaller than that inferred from X-ray observations. These results can be explained that the region probed by the near-infrared CO absorption is in the vicinity of the nuclei and is located outside the X-ray emitting region. Furthermore, the almost unity covering factors required by the observed deep absorption profiles suggest that the probed region is close to the continuum source, which can be designated as the inner rim of the obscuring material around the AGNs.

Being motivated by the above result, we performed a systematic analysis of the CO band with a larger sample that includes less-luminous infrared galaxies. Nearby 47 infrared galaxies were selected from the *AKARI* post-cryogenic observations without any prior information on the presence or absence of the CO feature. Their band profiles were compared in different luminosity classes and optical classifications. Many of the sample galaxies showed warm large-column gas of $N_{\rm CO} \gtrsim 10^{19}$ cm^{-2} and $T_{\rm CO} \sim$ several $\times 10^2$ K, which can be considered to be heated by X-rays. High-luminosity galaxies ($> 10^{11}\ L_\odot$) showed deeper absorption profiles than less-luminous galaxies ($< 10^{11}\ L_\odot$). We found that the fraction of galaxies with $N_{\rm CO} > 10^{19}$ cm^{-2} had a peak

at a 14 μm monochromatic luminosity of 10^{10} $L_{\odot}$, being consistent with the obscured fraction measured in X-ray observations. Based on this result, the obscuring material observed in X-rays is being identified to be molecular gas. We also found that AGN-starburst composites had on average larger $N_{\rm CO}$ than Seyfert 2 galaxies. This result can be interpreted that the obscuration by an AGN torus is also effective in composites and that the torus is geometrically thicker in composites than in typical Seyfert galaxies. This picture is qualitatively consistent with the connection that supernovae in the circum-nuclear disk inflate the scale height of the torus.

Our studies indicate that warm molecular gas with a large column density exists in the vicinity of AGNs and that such gas has properties common to the obscuring material observed in X-rays. These results suggest that the anisotropic structure around an AGN consists of molecular gas, agreeing with the AGN unified model.

Contents

List of Tables

List of Figures

Chapter 1

Introduction

This chapter introduces basic information of the topics of this thesis. First, fundamental aspects of active galactic nuclei (AGNs) and the diversity among them are explained. Next, the unification scheme of AGNs and its key element, the AGN torus, are described. After mentioning various approaches to observe an AGN torus, we show our observation strategy. Finally, we state the aim of this thesis.

1.1 Active Galactic Nuclei (AGNs)

Almost every galaxy possesses a black hole whose mass is far larger than the stellar scale (10^6–10^{10} $M_\odot$) in its central region. It is remarkable that the mass of such a supermassive black hole (SMBH) tightly correlates with that of the spheroid part of the host galaxy (Magorrian et al. 1998; Marconi & Hunt 2003). This relation indicates that a galaxy forms and evolves being interacting with its SMBH. Some SMBHs exhibit intense activity by releasing the gravitational energy of accreting mass, and their luminosities are comparable to that of the host galaxies. Their radiative energy in the optical, ultra-violet (UV), and X-ray is absorbed and reproduced in the infrared (IR) by interstellar dust and leads high IR luminosities. These powerful central engines are called as active galactic nuclei (AGNs). Many studies propose that the energy output from an AGN plays as feedback into the evolution of the host galaxy in various ways as reviewed by Fabian (2012).

AGNs show a wide diversity in observational characteristics. The difference in optical properties has been studied since the oldest. AGNs are primary classified into those with and without broad (FWHM[1] $\sim 10^3$–10^4 km s^{-1}) emission lines in their optical spectra, and the two groups are called as type-1 and -2, respectively (Khachikian & Weedman 1974). Type-1 AGNs show both broad permitted lines and narrow (FWHM $\sim 10^2$–10^3 km s^{-1}) forbidden lines while type-2 AGNs show only narrow lines. More detailed classifications are described below.

Seyfert Galaxies Seyfert galaxies are AGNs with relatively low nuclear optical luminosity in the range of 10^{42}–10^{46} erg s^{-1}. Seyfert galaxies are divided into two groups, Seyfert 1s (Sy1s)

[1]Full width at the half maximum.

and Seyfert 2s (Sy2s), in the same way for type-1 and -2 AGNs. The number ratio of Sy2s to Sy1s in the local universe is 3–5 (Maia et al. 2003; Lu et al. 2010). There are more intermediate subgroups are defined between the two types, Seyfert 1.2, 1.5, 1.8, 1.9, based on the appearance of Balmer emission lines (Osterbrock 1977, 1981). Some Sy2s exhibit Sy1-like broad lines in the linearly-polarized spectrum (e.g., NGC 1068; Antonucci & Miller 1985). Such Sy2s are called hidden Seyfert 1 or prototypical Seyfert 2 while the others are recognized to have a "true" type-2 AGN.

Quasars Quasar is a class of AGNs that show the highest nuclear luminosities over 10^{46} erg s^{-1}. Because of the extremely high nuclear brightness, quasars appear stellar-like with their host galaxies barely seen. The optical spectrum of quasars resembles that of Seyferts, but the number ratio of type-1 to type-2 quasars in the local universe is ~ 1 (Reyes et al. 2008).

LINERs Low-ionization nuclear emission-line regions (LINERs) are characterized with the lowest luminosity less than 10^{42} erg s^{-1} and emission lines of low-ionization species (Heckman 1980). LINERs are distinguished from Seyferts and star formation dominated galaxies (H II galaxies) by diagnostics of flux ratios of optical lines (e.g., Baldwin et al. 1981; Kewley et al. 2001).

1.2 AGN Unification Scheme and AGN Torus

The fact that some type-2 AGNs show polarized broad emission lines indicates that the two types of AGNs are intrinsically the same or at least share common properties. This implication motivates the unification of different appearance of AGNs. The fundamental unification scheme called AGN unified model was proposed by Antonucci & Miller (1985) and Antonucci (1993). This model assumes the existence of an optically and geometrically thick torus-shaped molecular cloud (AGN torus) and explains the discrepancy of the two types as a viewing angle effect caused by the torus around the central engine. Figure 1.1 shows a schematic view of this model. The torus surrounds an central engine. Clouds that emit broad lines (broad line regions) are distributed in the funnel of the torus while those emit narrow lines (narrow line regions) are above the torus. Broad lines are directly observed if the torus is face-on against the line of sight. When the torus is edge-on, broad lines are not directly seen by the extinction within the torus but can be observed if they are scattered by hot electrons existing above the torus. The observed linear polarization supports this path of hidden broad lines (Antonucci & Miller 1985). The outer radius of the torus is estimated to be an order of 10 pc or less from IR spectral energy distribution (SED) analyses (Alonso-Herrero et al. 2011; Ramos Almeida et al. 2014; Ichikawa et al. 2015). The inner radius of the torus is depending on the nuclear luminosity and measured to be an order of 0.1 pc for 10^{44} erg s^{-1} from dust reverberation mappings (Kishimoto et al. 2007; Kawaguchi & Mori 2010, 2011). IR SED analyses and dust reverberation mappings are explained in Section 1.3.

Based on this concept, many modifications and extensions have been proposed (Netzer 2015).

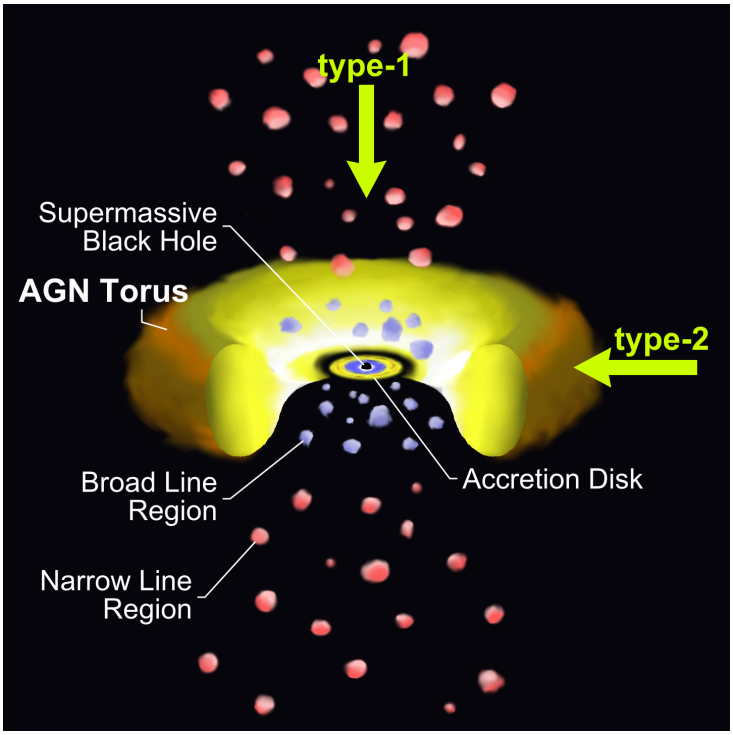

Figure 1.1: Conceptual picture of the AGN unified model.

Clumpy Torus Model Today it is widely accepted that the distribution of gas in the torus is clumpy rather than smooth. This idea, first proposed by Krolik & Begelman (1988), is called as clumpy torus model. The number fraction of type-1 to type-2 AGNs indicates that the aspect ratio of the torus is close to unity. Such a thick gas distribution requires a velocity dispersion along the torus axis comparable to the orbital velocity ($\sim 10^2$ km s^{-1}; Krolik & Begelman 1988). Such a large dispersion is not explainable as a thermal velocity because the dust cannot survive over the sublimation temperature (1500 K; Barvainis 1987). Hence the velocity dispersion is highly likely that between gas clumps within which the temperature does not exceed 1500 K. Besides, numerical simulations based on the assumption of the smooth distribution does not always represent the behavior of the mid-IR 10 micron silicate dust feature (Pier & Krolik 1992). Many simulation codes based on the clumpy distribution have been developed (e.g., Nenkova et al. 2008a,b; Schartmann et al. 2008; Hönig & Kishimoto 2010), and they successfully represent the silicate feature.

Receding Torus Model If we define the torus structure by the region where dust abundantly exists, the inner rim of the torus can be considered as the layer where dust grains sublimate. Because the incident flux that results in the sublimation temperature is constant, the inner radius is proportional to the square root of the nuclear luminosity. This model was first suggested by Lawrence (1991) and is called the receding torus model. This concept is supported by an observational fact that the ratio of the number of type-2 AGNs to the total number of all AGNs, which can be assumed as the solid angle fraction covered by a torus, decreases with increasing luminosity when the numbers are counted in optical and IR surveys (Simpson 2005; Toba et al.

2013, 2014). The obscured fraction (fraction of type-2 AGNs) observed in X-rays also decreases as a function of X-ray luminosities (Ueda et al. 2003; Lusso et al. 2013), but some authors argue that the fraction has a peak at a certain luminosity (Brightman & Nandra 2011a; Burlon et al. 2011). If the latter dependence in low luminosities is true, it suggests that in such low-luminosity AGNs some physical mechanisms other than the radiative energy input control the innermost structure of the tori.

Torus Geometry The geometry of AGN tori is not necessarily constant and is important to understand the diversity of AGNs. Prototypical type-2 AGNs (hidden type-1 AGNs) are suggested to have AGN tori of smaller opening angles and taller thicknesses (i.e., scale heights along the torus axis) than true type-2 AGNs do, based on an IR SED analysis (Ichikawa et al. 2015). In that case, the absence of broad polarized lines can be explained by the combination of a reduced volume of the scattering medium and a decreasing chance to escape from the scattering medium to outside the torus due to blocking by the tall wall of the torus. Additionally, the new class of AGNs that are almost entirely enshrouded by dust have been discovered (e.g., Ueda et al. 2007). These results indicate that the torus geometry has a wide variety.

Formation of the Torus It is a critical problem how to form and maintain the geometrically thick torus structure. One explanation is radiative pressure with the help of nuclear star-forming activity to enhance the accretion rate suggested by the three-dimensional hydrodynamic simulations by Wada (2012). His model, which calculates the X-ray heating and radiation pressure on the gas by a ray-tracing method, found that the radiative feedback drives a vertically circulating gas flow within the central tens parsecs and realize internal turbulent motion of large scale height. His model also implies that to maintain the geometrically thick structure for millions of years the mass accretion rate into the center needs to be enhanced by other mechanisms, such as supernova explosions (Wada & Norman 2002; Wada et al. 2009; Izumi et al. 2016) and stellar mass loss (Schartmann et al. 2010) in the surrounding environment. This is an example of a link between the torus formation and nuclear star formation.

1.3 Observations of the Torus

To understand the characteristics of AGNs, it is important to observe AGN tori and verify the AGN unified model. To overcome the too small size of the torus for observations, many approaches have been attempted. Some of them are introduced here.

Interferometric Observations Long baseline interferometry can realize the highest-class milliarcsecond angular resolution. García-Burillo et al. (2016) mapped the emission of the CO(6–5) emission line and the 432 μm continuum from the nearby Sy2 galaxy NGC 1068 (luminosity distance $D_{\rm L} = 14$ Mpc) with the Atacama Large Millimeter Array (ALMA) Cycle 2. Their observation achieved a resolution of ~ 4 pc and successfully resolved out a 7–10 pc sized putative torus. Imanishi et al. (2016) also observed NGC 1068 with ALMA but at HCN $J = 3$–2

and HCO^+ $J = 3$–2 lines and also imaged the putative torus. Tristram et al. (2014) observed the closest Sy2 galaxy Circinus galaxy with the MID-infrared Interferometric instrument at the Very Large Telescope Interferometer. They modeled the observed data assuming blackbody emitters with dust extinction and found two distinct components, a disk-like component of 1.1 pc width and an elongated polar component of 1.9 pc length, which possibly represent a small torus and a polar outflow. These radio and mid-IR interferometric observations succeeded in resolving the putative torus. However, the sample is limited to the closest sources. The angular resolution of these observations is still somewhat inadequate for a systematic study.

Infrared SED Analysis By fitting the IR SED with a prediction by a torus model, one can restrict the parameters of the model and estimate the torus geometry. In particular, the 10 μm silicate dust emission or absorption strongly constraints the model because it changes acutely with respect to the inclination of the torus and the amount of dust. Many studies in this approach have been conducted using clumpy torus models, and they revealed intrinsically different geometries between type-1 and -2 AGNs or between luminosity classes (e.g., Alonso-Herrero et al. 2011; Ramos Almeida et al. 2011, 2014; Ichikawa et al. 2015). However, this method cannot be straightforwardly adopted for galaxies that have a significant contribution from starburst activity because the AGN and starburst components in the SED are difficult to be decomposed.

X-Ray SED Analysis The X-ray spectrum of AGNs is characterized by a component of (absorbed) primal continuum emission, a hump of scattered light around 30 keV, the iron 6.4 keV line (Risaliti & Elvis 2004). The torus geometry and inclination are determined by decomposing these components. Some examples are Ueda et al. (2003); Brightman & Nandra (2011b); Burlon et al. (2011); Lusso et al. (2013). The results of X-ray spectral analyses are, however, severely model-dependent in heavily obscured AGNs because such objects do not provide sufficient counts during observations.

Reverberation Mapping Reverberation mapping is a technique to measure the inner radius of an AGN torus from the time lag from optical/UV flux variations to the following near-IR variations caused by the dust heated by the prior variation. Suganuma et al. (2006) measured and collected lag times between the flux variation of the optical continuum in the V band and that of the dust emission in the K band in nine Sy1 galaxies and found that the lag times are proportional to the square root of the optical luminosity as predicted by the receding torus. Though, the inner radii of the tori estimated by multiplying the lag times by the light speed are systematically smaller than the dust sublimation radii by a factor of 1/3 (Kishimoto et al. 2007). Kawaguchi & Mori (2010) explained this deviation by a dust sublimation layer that is concave and smoothly connected to the accretion disk in the equatorial plane due to anisotropic radiation of the accretion disk. As exampled above, the dust reverberation mapping can investigate the inner boundary of an AGN torus. However, it cannot obtain information on physical conditions of warm gas near the inner rim of the torus.

1.4 Spectroscopy of Near-IR Absorption

Our strategy to observe an AGN torus is spectroscopy of a near-IR absorption feature. Figure 1.2 schematically illustrates the concept of this approach. If the torus is viewed edge-on, using the bright near-IR radiation from the central region as the background continuum, we can observe foreground molecular gas clouds with an effectively high spatial resolution of parsec-scale owing to the compactness of the near-IR emitting region. We here describe the method in detail and review prior observations.

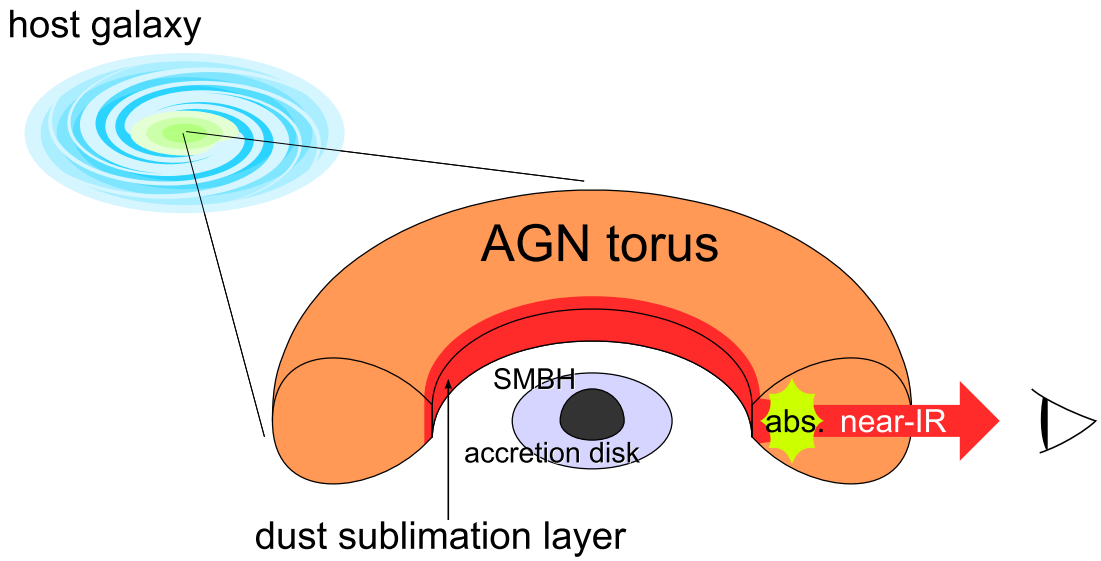

Figure 1.2: Schematic picture of the observation method of the near-IR absorption spectroscopy.

1.4.1 CO Fundamental Ro-Vibrational Transition

As an absorption feature to probe AGN tori, we propose that the fundamental rotational-vibrational transition of a CO molecule centered at 4.67 μm is the most effective because it provides us with much physical information. Figure 1.3 shows the energy diagram of this transition. Electric dipole transitions are restricted by selection rules as

$$\begin{cases} v = 1 \leftarrow 0, \\ \Delta J = \pm 1. \end{cases} \tag{1.1}$$

The two branches of $\Delta J = +1$ and -1 are named R- and P-branches, respectively. Due to the far different energy scales between the vibrational levels and rotational levels, this band contains multiple lines of a nearly constant interval associated with different rotation levels in a narrow wavelength range. Some calculated model spectra (Cami 2002) are shown in Figure 1.4. The CO band profile becomes deeper with increasing CO column density and becomes wider with increasing temperature. Increasing turbulent velocity changes each line broader. As these model spectra show, we can easily obtain information on the gas amount and gas excitation

state from one observation. In this respect, the near-IR CO absorption band is preferable to the (sub-)millimeter CO pure rotational emission lines, which are easily affected by contamination from the host galaxy and cannot be observed simultaneously.

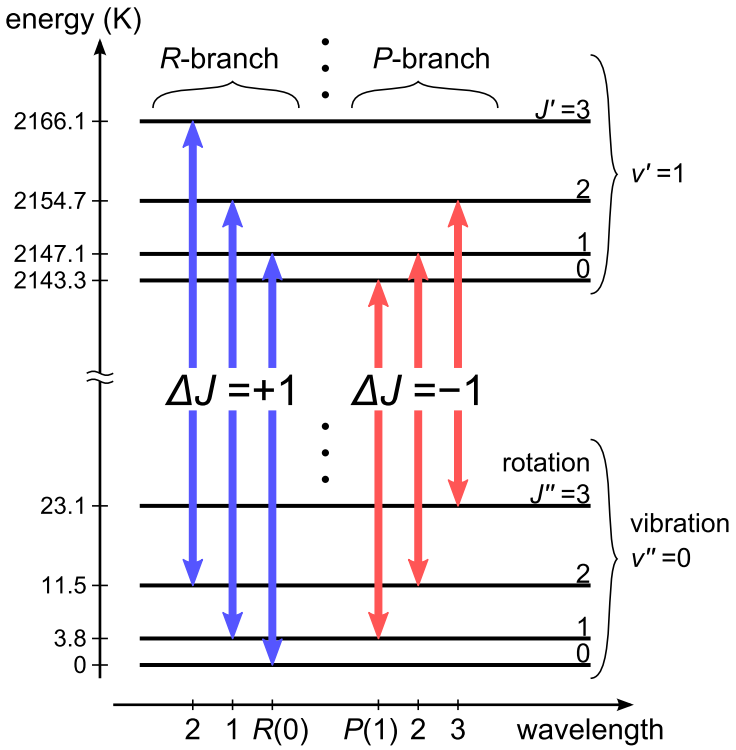

Figure 1.3: Energy diagram of the CO fundamental ro-vibrational transition.

1.4.2 Previous Studies

There are only a few previous studies that analyzed the CO absorption in AGNs. Geballe et al. (2006) and Shirahata et al. (2013, hereafter S13) observed the absorption band toward the heavily obscured ultra-luminous infrared galaxy (ULIRG[2]) IRAS 08572+3915 using the United Kingdom 3.8-m Infrared Telescope (UKIRT) and the 8.2-m Subaru telescope, respectively. Strong absorption lines were detected up to high rotational levels ($J \leq 17$), with the resulting population diagram showing the presence of large columns of warm molecular gas in the line of sight. Spoon et al. (2004, hereafter S04) observed another obscured ULIRG IRAS 00182−7112 using the *Spitzer Space Telescope* (Werner et al. 2004) and also detected strong CO absorption. Although their observation did not resolve the multiple lines owing to insufficient spectral resolution, they analyzed the entire absorption profile using a plane-parallel local thermal equilibrium (LTE) gas model (Cami 2002) and also found that the gas is warm and has a large column density. Spoon et al. (2005) reported that other three ULIRGs observed with *Spitzer* also show the CO absorption, but their spectra have not been analyzed in detail yet. Based on the high temperatures and large column densities, both S13 and S04 argued that the

[2]ULIRGs are defined as the galaxies that have IR (8–1000 μm) luminosities of $L_{\rm IR} > 10^{12}\ L_{\odot}$. Similarly, the galaxies of $10^{11} < L_{\rm IR} < 10^{12}\ L_{\odot}$ and $L_{\rm IR} < 10^{11}\ L_{\odot}$ are called LIRGs and IRGs, respectively.

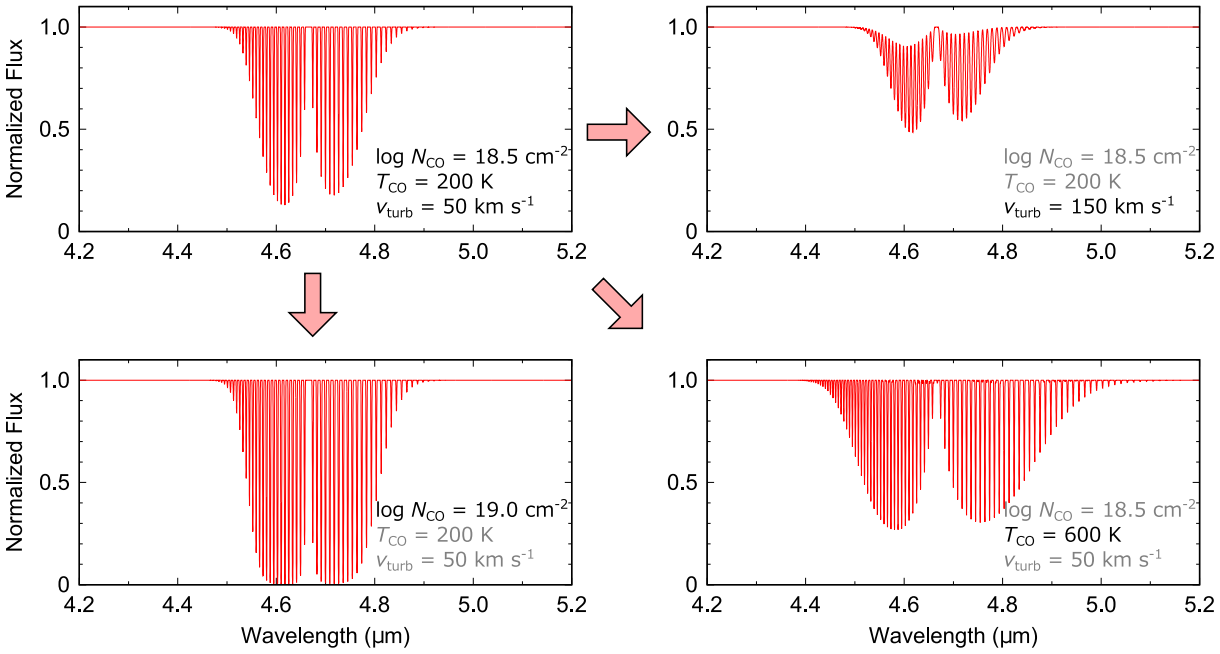

Figure 1.4: Model spectra of the CO fundamental ro-vibrational absorption lines. A single component gas that has homogeneous temperature and turbulent velocity is assumed. Each model is calculated at the CO column density, temperature, and turbulent velocity written at the right bottom corner. The three panels other than the upper left one show the results when only one parameter is changed from the upper left model.

observed gas should be in the vicinity of the dominant nuclear power source. S13 additionally proposed that the warm gas is heated by X-ray radiation from an AGN engine.

This CO absorption feature, however, does not always appear in all type-2 AGNs, in which the putative torus should be seen edge-on. Lutz et al. (2004) observed nearby 19 type-1 and 12 type-2 AGNs using the *Infrared Space Observatory* (*ISO*; Kessler et al. 1996), but none of them showed the CO feature. Lahuis et al. (2007) detected similar warm molecular gas toward obscured U/LIRGs through the mid-IR absorption bands of C_2H_2, HCN, and CO_2 but concluded that the gas is unlikely to be associated with the material surrounding AGNs because these molecules would be rapidly destroyed in an intense X-ray field. The two above studies controvert the hypothesis that CO absorption probes warm gas near the central region.

We assume that the reason for the small number of the analysis of the CO absorption in AGNs is due to severe constraints for observations. In a ground-based observation with Subaru like S13, the target must be brighter than $\sim$ 100 mJy at 5 μm for one-night observation, and must be in the redshift range of $z < 0.13$ so that the CO feature is captured in M-band. Because the wavelengths coverage of *Spitzer* starts from 5.2 μm to longer, observable AGNs are more distant than $z = 0.11$ and consequently limited to high-luminosity ones, roughly speaking, the ULIRG-class ones. If the ULIRG IRAS 00182−7112 ($z = 0.327$, $L_{IR} = 8 \times 10^{12}$ $L_\odot$) were a LIRG of $L_{IR} = 1 \times 10^{11}$ $L_\odot$, its flux density at the CO absorption would be ~ 0.3 mJy, which is below the 5σ sensitivity of *Spitzer* for 512-second integration (IRS Instrument Team and Science User Support Team 2011). The 1σ sensitivity of the ISOPHOT-S on board *ISO* for 256-second

integration is 26 mJy (Klaas et al. 1997).

The unique observation that overcomes those severe constraints is the near-IR spectroscopy with the *AKARI* satellite. This spectroscopy covers wavelengths from 2.5 to 5.0 μm with a spectral resolution of ~ 100 and has a 1σ sensitivity of 0.5 mJy (Section 2.1.2). In fact, several authors have detected the CO absorption in the *AKARI* spectra of AGNs (Imanishi et al. 2008, 2010; Ichikawa et al. 2014; Kim et al. 2015). The *AKARI* near-IR spectroscopy has a potential for a systematic analysis of the CO absorption with a large sample that includes galaxies in a wide luminosity range and galaxies of different optical classifications. However, the absorption profiles found in the *AKARI* spectra have never been analyzed in detail so far. The reason may be because the *AKARI* spectrum at wavelengths longer than 4.9 μm is problematic being contaminated by the diffracted second-order light, which prevents the accurate flux calibration in that range (Onaka et al. 2009). This artifact distorts the CO absorption profile from the correct shape.

1.5 The Aim of This Thesis

The aim of this thesis is to demonstrate the effectiveness of the CO absorption as a probe of the AGN torus and use it to investigate torus properties in galaxies of different luminosities and optical classifications. For this purpose, we by ourselves correct the *AKARI* observations for the effect of the contamination.

1.6 Outline of This Thesis

In the series of studies compiled in this theses, we solved the problem of the *AKARI* near-IR spectroscopy by ourselves and then analyzed the CO absorption in nearby AGNs to discuss the physical condition and geometrical structure of AGN tori. Chapter 2 explains the telescopes used in this thesis their roles in our analysis. Chapters 3 and 4 show the revision of the calibration of the *AKARI* spectroscopy. Chapters 5 and 6 present the results of the analysis of the CO band and discussion on them. Finally, in Chapter 7, we conclude the achievement of this thesis.

Chapter 2

Telescopes

In this study, we mainly used observed data obtained with three space telescopes: *AKARI*, *Spitzer*, and *WISE*. The current study requires continuous near-IR spectra in 4–6 μm of AGNs down to low luminosity classes for a systematic analysis of the CO ro-vibrational absorption band centered at $\lambda_{\rm rest} = 4.67$ μm. The *AKARI* satellite has a unique capability for such spectroscopy. However, since its spectral coverage is only up to 5 μm, it does not provide information on the continuum level at longer wavelengths of the CO band. For the reliable determination of continuum levels over the CO absorption, complementary spectra at wavelengths longer than 5 μm are needed. The *Spitzer Space Telescope* is useful for this requirement. Since the two telescopes have different aperture sizes, it is necessary to match the fluxes of the two spectra based on a consistent reference in determining continuum levels in order to cancel possible missed flux. The photometric measurement by *WISE* at four bands, which lie within the coverages of *AKARI* and *Spitzer*, can be used as the reference points for the scaling of the two spectra. This chapter briefly describes basic information of these telescopes.

2.1 *AKARI*

2.1.1 Mission Overview

AKARI is the Japanese first satellite dedicated to IR astronomy launched on 2006 February 21 (Murakami et al. 2007). The primal mission goal is to update the IR all-sky atlas produced by the previous *IRAS* satellite (Neugebauer et al. 1984) with a wider wavelength coverage and higher angular resolutions and sensitivities. *AKARI* carried out an all-sky survey in six bands centered at 9, 18, 65, 90, 100, and 160 μm using a 68.5-cm telescope and two focal-plane instruments: the Infrared Camera (IRC; Onaka et al. 2007) and the Far-Infrared Surveyor (FIS; Kawada et al. 2007). The IRC performed near- to mid-IR observations and was in charge of the two bands of the shortest wavelengths of the survey. The FIS conducted far-IR observations including the mapping at the other four bands. The angular resolutions of the survey are about 4″–7″ for the bands of the IRC (Onaka et al. 2007) and about 40″–60″ for those of the FIS (Kawada et al. 2007). These are more than five times superior to the *IRAS* ones.

The satellite's orbit was a Sun-synchronous polar orbit of a 700-km altitude. To enable mid- to far-IR observations, the satellite was cooled down both by liquid helium and by mechanical cryocoolers (Nakagawa et al. 2007). The liquid helium was 179 litters at the launch to be used up to 500 days on the orbit. Until the exhaustion of the cryogen, the temperature of the telescope and the instruments were kept to cryogenic temperatures.

2.1.2 Near-IR Spectroscopy

In addition to the all-sky survey, a lot of pointed observations were carried out. The IRC consists of three channels named NIR, MIR-S, MIR-L. The NIR and MIR-S/L channels are dedicated to the near- and mid-IR ranges, respectively, and each of them is capable of imaging and spectroscopic observations. It is remarkable that the grism spectroscopy in the NIR channel is a unique capability not available from other telescopes. It covers wavelengths from 2.5 to 5.0 μm, and its sensitivity is 0.5 mJy at 5 μm for 1σ per pointing. These continuous wavelength coverage and low detection limit are not available in ground-based observations being affected by the atmosphere and indispensable for the systematic study of the CO absorption. Although the Infrared Space Observatory (*ISO*; Kessler et al. 1996) also carried out near-IR spectroscopic observations in space, those observations were limited to bright sources of a few Jy. The grism mode has a spectral resolution of $R = \lambda/\Delta\lambda = 120$ at 3.6 μm(Ohyama et al. 2007), which is adequate to analyze absorption profiles of the CO ro-vibrational band in Chapters 5 and 6. Although the NIR channel is also capable of prism spectroscopy, its spectral resolution is relatively low ($R = 19$ at 3.5 μm; Ohyama et al. 2007), and there are less number of observations of AGNs performed in the prism mode.

The *AKARI* near-IR grism spectroscopy is the best opportunity for our purpose. However, a problem was known for the grism mode that its spectrum has blue-leak (i.e., the diffracted first-order spectrum is contaminated by the second-order light at longer wavelengths). This contamination prevented the accurate flux calibration at wavelengths longer than 4.9 μm and had not been fixed. Because the CO absorption band in nearby AGNs appears at the problematic range due to redshift, it is essential to correct for the contamination. Thus we at first established a method to correct for the effect of the contamination (Chapters 3 and 4).

2.1.3 Observational Phases

The period of the *AKARI* mission is divided into some phases based on cooling conditions. The definitions are summarized in Table 2.1. The first two months from the launch was a phase for performance verification on the orbit (PV phase). After that began a 6-month period primarily dedicated for the survey observation (Phase 1), and then followed the remaining cryogenic phase (Phase 2), during which extensive mapping observations and an increasing number of pointed observations up to the far-IR range were carried out. In this thesis, Phases 1 and 2 are collectively called as the cryogenic phase. After the liquid helium depleted on 2007 August 26, the temperature of the satellite began increasing. After a 9-month performance verification (PV2), the post-cryogenic science observations were started using only the IRC. Phase 3 is sometimes

called as the post-cryogenic phase in this thesis. Figure 2.1 shows the variation of the detector temperature of the NIR channel. The temperature had been kept to 10 K until the exhaustion of the cryogen, raised to 41 K before the beginning of Phase 3, and gradually increased to 47 K during that phase. This temperature change affects the performance of the grism mode spectroscopy and should be taken into consideration in the correction for the contaminating second-order light.

During Phase 3, although the operation temperature was not stable and the detector sensitivity was lower than that during Phases 1 and 2, many LIRGs and IRG were observed in the NIR grism mode. As mentioned in Chapter 1, such low-luminosity galaxies cannot be reliably observed by *Spitzer*/IRS. For a systematic study of the CO band, the *AKARI* post-cryogenic observations and the corrected calibration for those observations are necessary.

Table 2.1: Definition of sub-phases and corresponding temperature ranges

Phase	Date
PV	2006 Feb 21 – 2006 May 7
Phase 1	2006 May 8 – 2006 Nov 7
Phase 2	2006 Nov 8 – 2007 Aug 26
PV2	2007 Aug 26 – 2008 May 31
Phase 3	2008 Jun 1 – 2010 Feb 15

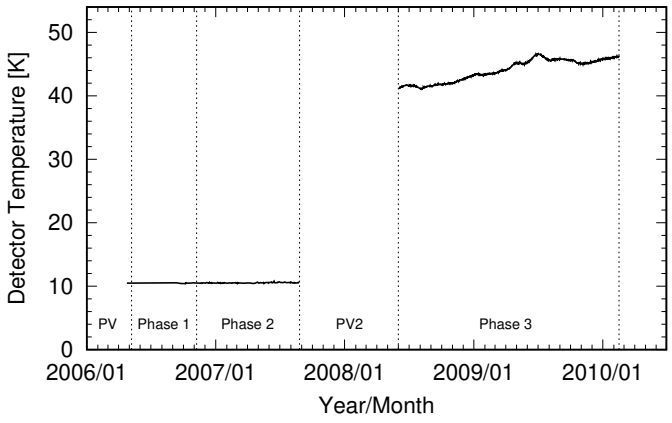

Figure 2.1: Temperature variation of the detector of the NIR channel during Phases 1, 2, and 3.

2.2 *Spitzer*

The *Spitzer Space Telescope* is the infrared space observatory launched by National Aeronautics and Space Administration (NASA) on 2003 August 25 (Werner et al. 2004). *Spitzer* performed a lot of pointed observations from a unique Earth-trailing solar orbit with an 85-cm telescope.

One of the focal plane instruments incorporated to *Spitzer* is the Infrared Spectrograph (IRS; Houck et al. 2004). The IRS consists of four separated modules of different wavelength coverages and spectral resolutions: Short-Low (SL), Short-High (SH), Long-Low (LL), and Long-High (LH). While the SH and LH modules cover a continuous wavelength range of 10–37 μm with a resolution of $\sim$600, the SL and LL modules cover a wider range of 5.2–38 μm with a varying resolution of 80–128. Although the spectrum that can be obtained with the latter two modules is inferior in resolution to that from the former two, its coverage near to the position of the CO band is useful for the following studies. Practically, its resolution is adequate for analyses of dust features such as PAH emissions or the 9.7 μm silicate dust absorption. The 1σ continuum sensitivity of the SL module at 6 μm for 512-second integration is about 0.05 mJy (IRS Instrument Team and Science User Support Team 2011).

The two low-resolution modules use separated slits, and each of them observes the first- and second-order spectra using subslits contained in the respective slit. The slit sizes are summarized in Table 2.2. Hence the IRS low-resolution full-coverage spectrum is made by stitching the four orders obtained with different slit widths. It should be paid attention to in the case of an extended source whether some flux is missed at borders of different parts. Moreover, when comparing the IRS spectrum with the *AKARI*/IRC spectrum, one should be careful of the difference that the former is slit spectroscopy whereas the latter is slitless spectroscopy.

Table 2.2: Definition of sub-phases and corresponding temperature ranges

Module	Order	Slit Size (arcsec^2)	λ (μm)	$R = \lambda/\Delta\lambda$
Short-Low	SL2	3.6×57	5.2–7.7	80–128
	SL1	3.7×57	7.4–14.5	64–128
Long-Low	LL2	10.5×168	14.0–21.3	80–128
	LL1	10.7×168	19.5–38.0	80–128

2.3 *WISE*

The *Wide-field Infrared Survey Explorer* (*WISE*) is the NASA's astronomical satellite launched on 2009 December 14 (Wright et al. 2010). *WISE* conducted all-sky mapping in near- to mid-IR four bands centered at 3.4, 4.6, 12, and 22 μm (named $W1$, $W2$, $W3$, and $W4$, respectively) with a 40-cm telescope in a Sun-synchronous low Earth orbit. The bands $W1$–4 have angular resolutions of $6\farcs1$, $6\farcs4$, $6\farcs5$, and $12\farcs0$, and their 5σ sensitivities for a point source are better than 0.08, 0.11, 1, and 6 mJy, respectively.

The satellite was cooled by solid hydrogen stored in two tanks. After the exhaustion of the secondary tank on 2010 August 5, the survey was continued in the three bands at shorter wavelengths until the primary tank depleted on 2010 September 29. After that, the operation in the $W1$ and $W2$ bands was extended to enhance data processing and explore near-earth objects, being funded by the NASA's Planetary Science Division (*NEOWISE*; Mainzer et al. 2011).

The data collected in the *WISE* and *NEOWISE* missions are cataloged in the AllWISE Data Release. The AllWISE Source Catalog in this release contains information of over 747 million objects detected in the coadded atlas image. This catalog is a unique database that provides homogeneous photometric measurement in bands within the *AKARI*/IRC and *Spitzer*/IRS spectral coverages and useful to compare the two spectra obtained in different aperture sizes. There is also the *WISE* All-Sky Source Catalog available, which is the first archive constructed from only exposures during the full cryogenic phase.

Chapter 3

Revised Wavelength and Spectral Response Calibrations for *AKARI* Near-Infrared Grism Spectroscopy: Cryogenic Phase

The content of this chapter is based on the study published in the paper: Baba, S., Nakagawa, T., Shirahata, M., Isobe, N., Usui, F., Ohyama, Y., Onaka, T., Yano, K., and Kochi, C. 2016, "Revised wavelength and spectral response calibrations for AKARI near-infrared grism spectroscopy: Cryogenic phase", Publications of the Astronomical Society of Japan, 68, 27.

The *AKARI* near-IR grism spectroscopy, which covers the wavelength range of 2.5–5.0 μm, is essential for the systematic study of the CO absorption, the main object of this thesis. However, this spectroscopic mode has a problem that the diffracted second-order light contaminates the first-order spectrum at wavelengths longer than 4.9 μm. To obtain the correct absorption spectra of the CO band, we corrected for the effect of the contamination. First, we performed a wavelength calibration under the consideration that the refractive index of the grism is a function of wavelengths. We found that the previous wavelength calibration had differed by up to 0.01 μm and that the contamination occurs even if the order-sorting filter perfectly cuts off wavelengths shorter than 2.5 μm because incident positions of the first- and second-order light do not linearly relate exactly due to the wavelength dependence of the refractive index. Secondly, we evaluated spectral responses of the system from the first- and second-order light simultaneously using two types of standard objects of different colors. The obtained response from the second-order light suggests leakage of the order-sorting filter. The relations between the output of the detector and the intensities of the first- and second-order light are formalized into a matrix equation. The contaminating second-order light can be subtracted by solving the matrix equation. These new calibrations extend the longer end of the reliable spectral coverage from 4.9 μm to 5.0 μm and enable the study of the CO absorption in nearby AGNs.

3.1 Introduction

As explained in Section 2.1, the grism spectroscopy in the wavelength range of 2.5–5.0 μm with the *AKARI* IRC NIR channel is a unique capability to observe the CO absorption band in various IR galaxies and to carry out a systematic analysis of the feature. To acquire the CO band profile, we need the spectrum in the wavelength range of 4.5–5.0 μm. This part is, unfortunately, in the longer end of the *AKARI* coverage and requires careful treatment. In particular, as mentioned before, that longest part is considered to be contaminated by the second-order light at wavelengths longer than 4.9 μm although an order-sorting filter is coated on the grism to prevent spectral overlapping (Onaka et al. 2009, Section 6.9.7). Despite this difficulty, the systematic study of the CO absorption, the object of this thesis, is impossible without this *AKARI* spectroscopy.

The latest official IDL-based data reduction package "IRC Spectroscopy Toolkit Version 20150331[1]" developed by the IRC team can extract a spectral image for each source after the basic processes (dark subtraction, linearity correction, flat fielding, and frame stacking) and can perform wavelength and flux calibrations for the image. However, those calibrations do not take into account the effect of the contamination. The pixel position of a spectral image along the dispersion direction is converted into wavelength upon a linear relation, within which the wavelength dependence of the refractive index of the grism material is ignored. The raw output of the detector is converted into flux density being divided by a spectral response function (the output per unit flux density at each wavelength) derived based on observations of some A- and K-type standard stars (Ohyama et al. 2007; Shimonishi et al. 2013)[2], which are severely contaminated by the second-order light. Figure 3.1(a) is an example of the CO absorption spectrum calibrated by the present toolkit. The spectrum shows a steep drop above 4.9 μm. Figure 3.1(b) is another example of the data reduction for a ULIRG based on the toolkit and also indicates the unnatural decrease. This artifact caused by the contamination prevents the analysis of the CO band profile.

If the wavelength calibration curve is really linear and the order-sorting filter ideally cuts off wavelengths shorter than 2.5 μm, the second-order light does not overlap with the first-order spectrum. The cause of the contamination may be due to the nonlinearity of the wavelength calibration curve and/or the leak of the filter. To remove the contamination component in the calibration, it is necessary, at first, to verify the nonlinearity and confirm the position where the second-order light incidents by taking into account the wavelength dependence of the refractive index of the grism material. It is also needed to derive the spectral responses against the first- and second-order lights separately. The two unknown values can be simultaneously determined by observing both a standard star and another object that has a predictable spectrum. As such an object, one with a red color, which causes little contamination of the second-order light contrastively to the standard star, is appropriate.

In this chapter, we explain the revision of the *AKARI* calibration performed to correct for the effect of the second-order light contamination. This chapter is dedicated to the cryogenic

[1]Distributed at the *AKARI* website (`http://www.ir.isas.jaxa.jp/AKARI/Observation/support/IRC/`).
[2]See also the change log of the IRC Spectroscopy Toolkit Version 20130813.

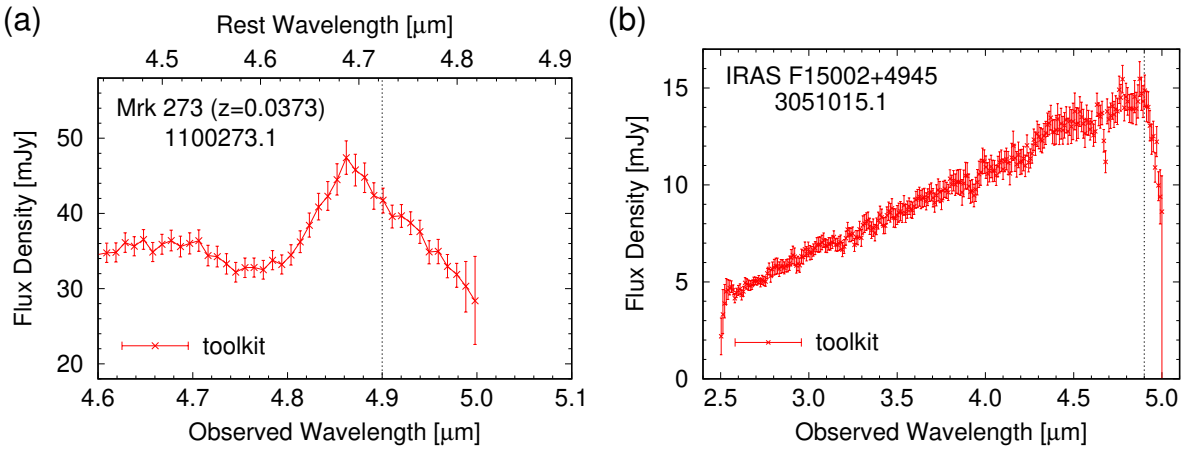

Figure 3.1: Examples of spectra calibrated by the toolkit. Each of them shows the artificial steep decrease at $\lambda_{\rm obs} = 4.9$ μm caused by the second-order light contamination. (a) CO absorption in the Seyfert 2 galaxy Mrk 273 ($z = 0.0373$). The observation ID is 1100273.1. (b) Featureless red spectrum of the ULIRG IRAS F15002+4945. The observation ID is 3051015.1.

phase of the satellite, during which the sensitivity of the detector is higher than in the post-cryogenic phase. A similar revision for the latter phase appears in Chapter 4. In section 3.2, the design of the NIR channel and that of the grism are described. In section 3.3, the revision of the wavelength calibration and the derivation of the spectral responses from the first- and second-order light are explained. The benefit of the new calibration is discussed in section 3.4. Finally, we summarize the result of our calibration in section 3.5.

3.2 Design of the IRC NIR Channel and the Grism

A grism is a prism combined with a transmission diffraction grating designed so that a ray of specific wavelength passes straight through. With the help of the diffraction grating, the grism has higher spectral resolving power than a prism, but at the same time, it produces higher order interference. In simple grating spectroscopy, the observing wavelength range is limited within an octave. An order-sorting filter is generally used to prevent overlap between light of different orders. The situation is more complex in the case of grism spectroscopy. The optical path difference within a grism depends on the refractive index of its material. Owing to the wavelength dependence of the refractive index, the second-order light can contaminate the first-order spectrum even if the order-sorting filter works perfectly. We therefore review the design of the IRC NIR channel and the grism considering this effect.

According to the ASTRO-F interim report volume 2 (SES data center 2002), the light that enters the NIR channel is first collimated by three lenses, diffracted by the grism mounted on the filter wheel, and focused by the plano-convex camera lens on the detector array. Figure 3.2 shows a schematic of the NIR channel and key parameters. Onaka et al. (2007) give a more detailed layout including the fore-optics. The spacing between the grism and the plano-convex lens is 27.7 mm. This lens is 6.5-mm thick and made of silicon. Since the refractive index of

silicon is 3.4 in the wavelength range of the grism mode (Frey et al. 2006), the second principal plane of the plano-convex lens is located 6.5/3.4=1.9 mm in front of its rear surface. The designed interval between the lens and the focal plane is 60 mm. Note that the actual in-flight interval between them may not be equal to this value because the focal position is optimized for low-temperature operation by slightly rearranging the optical elements. The report does not provide the in-flight value. Thus, we assumed the design value of 60 mm for the interval as a first approximation.

IR light of wavelength λ interferes constructively with the grism if the emitting angle θ satisfies

$$m\lambda = d\left[n\sin\alpha - \sin(\alpha-\theta)\right], \tag{3.1}$$

where m is an integer that denotes the order number, α is the blaze angle, d is the groove spacing, and n is the refractive index of the material of the grism. The grism is made of germanium (Ge). The design value of the blaze angle is $\alpha = 2.^{\circ}86$ and the groove spacing is $d = 21$ μm (Ohyama et al. 2007). The interval from the second principal plane of the lens to the detector is $L = 61.9$ mm (Figure 3.2); thus, IR rays of the emitting angle θ converges at a point separated by $L\tan\theta$ from the direct light point on the detector. Dividing the separation by the pixel pitch of the detector $p = 30$ μm, the pixel offset from the direct light position ΔY (in units of pixel number) is represented as

$$\Delta Y = (L/p)\tan\theta. \tag{3.2}$$

Consequently, the relation between wavelength λ and pixel offset ΔY is modeled by Equations (3.1) and (3.2). When θ is small, Equations (3.1) and (3.2) are simplified to

$$\Delta Y = \frac{L}{p}\left[\frac{m\lambda}{d} - (n-1)\alpha\right]. \tag{3.3}$$

If the refractive index n has no wavelength dependence, the pixel position linearly relates with the wavelength; hence, the first-order 5.0 μm and the second-order 2.5 μm correspond to the same position. The current toolkit uses a linear wavelength calibration based on this assumption, and it is expressed as

$$\lambda_{\rm tool}[\mu{\rm m}] = 0.00967625 \times \Delta Y[{\rm pix}] + 3.12121. \tag{3.4}$$

The front surface of the grism has multi-layer coating that cuts off the radiation with wavelengths shorter than 2.5 μm to avoid the contamination of the second-order light as an order-sorting filter. However, the refractive index of Ge changes by up to 1% as a function of wavelength between 2.5 and 5.0 μm (Frey et al. 2006). Moreover, the cut-off coating is not perfect and, in practice, there is leakage. Contamination by second-order light can occur even at wavelengths shorter than 5.0 μm.

The field-of-view of the NIR channel consists of four sections, each of which has a respective observational purpose. These sections are composed of two slits and two square-shaped apertures, which are shown in Figure 3.3. The wider slit is named Ns and the narrower one is named Nh. The width of the Ns and Nh slits are $5''$ and $3''$, respectively. These slits are designed for

observing extended sources. In the larger aperture (Nc), multi-object slit-less spectroscopy and imaging observations can be performed. The smaller aperture (Np) is equipped to observe a point source while avoiding overlaps with other sources. This aperture has size of $1' \times 1'$ (Onaka et al. 2007; Ohyama et al. 2007).

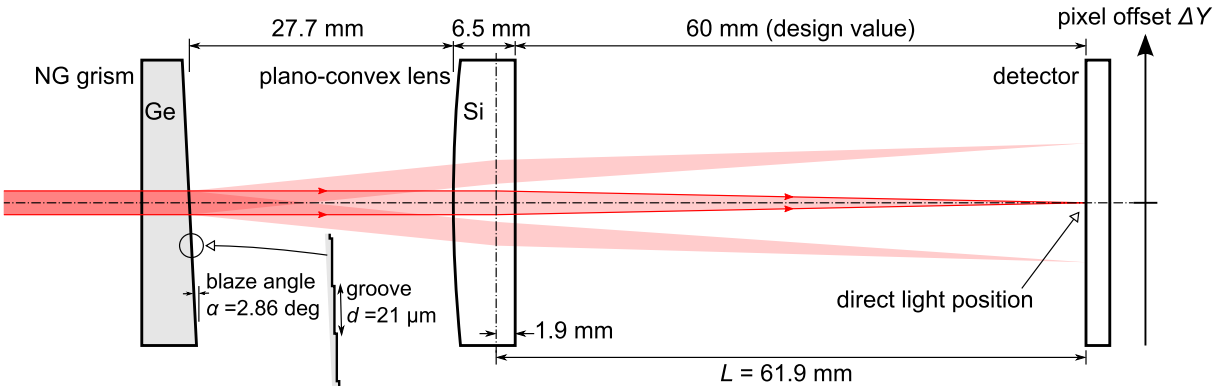

Figure 3.2: Schematic of the NIR channel. See the text for explanation.

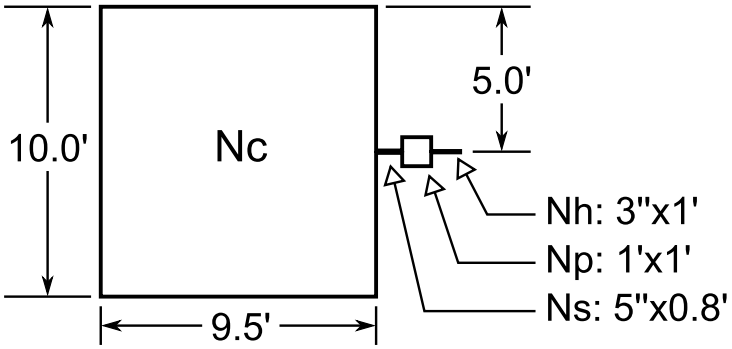

Figure 3.3: Field of view of the NIR channel.

The design of the grism mode does not precisely consider the wavelength dependence of the refractive index of the grism. The wavelength dependence can cause the contamination of the second-order light and must be considered in the flux calibration. The refractive index also depends on the temperature as well as the wavelength. In this chapter, we focus on observations before the exhaustion of liquid helium (Phases 1 and 2), when the temperature of the NIR channel was stable. Similar calibrations for the post-helium phase (Phase 3) appears in Chapter 4.

3.3 New Calibration Method for the IRC Grism Spectroscopy

3.3.1 Wavelength Calibration

In this section, based on observations of objects that show several emission lines, we revise the relation between the pixel offset and the wavelength for the grism mode using the equations described in the previous section and considering the refractive index as a function of the wave-

length. In addition to the relation for the first-order light, we also calculate the relation for the second-order light to identify the spectral range where the contamination occurs.

The wavelength-dependent refractive index $n(\lambda)$ of Ge was measured at cryogenic temperatures by Frey et al. (2006), and they gave it as a function of wavelength and temperature in the range of 1.9–5.5 μm and 20–300 K. The NIR channel was cooled down to $\sim$6 K during Phases 1 and 2 (Nakagawa et al. 2007). Extrapolation of the function provided by Frey et al. (2006) to lower temperatures suggests that the temperature dependence of the refractive index between 6 and 20 K is negligibly small ($\sim 0.01\%$). In our analysis, we used $n(\lambda)$ at 20 K as the operating refractive index of the grism.

The previous calibration expressed in Equation (3.4) was made based on observations of the recombination lines of the bright planetary nebula NGC6543 (Ohyama et al. 2007). To examine the effect of the wavelength dependence of the refractive index, we revisited the two observations of NGC6543 (Observation IDs 5020047.1 and 5020048.1). Both observations were carried out on 2006 April 29 using the Ns slit. We followed Yano et al. (in preparation) for the data reduction and the error estimate. One of the reduced spectra is shown in Figure 3.4. We fitted a Gaussian on a linear continuum to each recombination line excepting H I Pfβ and H I Pfε. H I Pfβ was fitted together with its immediate neighbor [K III] by two Gaussians on a linear continuum. Similarly, H I Pfε was fitted with He II 7–6. The fitted central wavelengths $\lambda_{\rm tool}$ are tabulated in Table 3.1 with theoretical values $\lambda_{\rm true}$ taken from the *ISO* line list[3]. The difference between $\lambda_{\rm tool}$ and $\lambda_{\rm true}$ relative to $\lambda_{\rm true}$ corresponds to velocity of 450 km s^{-1} on average. The velocity of NGC6543 relative to the local standard of rest is $V_{\rm LSR} = -51$ km s^{-1} (Schneider et al. 1983). The Doppler shift arising from $V_{\rm LSR}$ is smaller than the difference between $\lambda_{\rm tool}$ and $\lambda_{\rm true}$ by an order of magnitude. For the two observations, the orbital velocity of the satellite projected to the line-of-sight is 0.7 km s^{-1}. The Doppler shift caused by the satellite's motion is also smaller than the difference $\lambda_{\rm tool} - \lambda_{\rm true}$, by a few orders of magnitude. We thus ignored any Doppler effects.

Table 3.1: Fitted recombination lines

line	$\lambda_{\rm true}$ (μm)[a]	$\lambda_{\rm tool}$ (μm)[b]	
		5020047.1	5020048.1
H I Brβ	2.62587	2.62629 ± 0.00087	2.62559 ± 0.00044
H I Pfε	3.03920	3.04600 ± 0.00059	3.04581 ± 0.00049
H I Pfδ	3.29699	3.30523 ± 0.00054	3.30501 ± 0.00065
H I Pfγ	3.74056	3.74909 ± 0.00066	3.74914 ± 0.00049
H I Brα	4.05226	4.05811 ± 0.00035	4.05823 ± 0.00045
H I Pfβ	4.65378	4.65898 ± 0.00067	4.65886 ± 0.00086

[a] The theoretical wavelength of each line taken from the *ISO* line list.
[b] The wavelength of each line in the spectra processed by the toolkit (Figure 3.4).

[3] `http://www.mpe.mpg.de/ir/ISO/linelists/Hydrogenic.html`

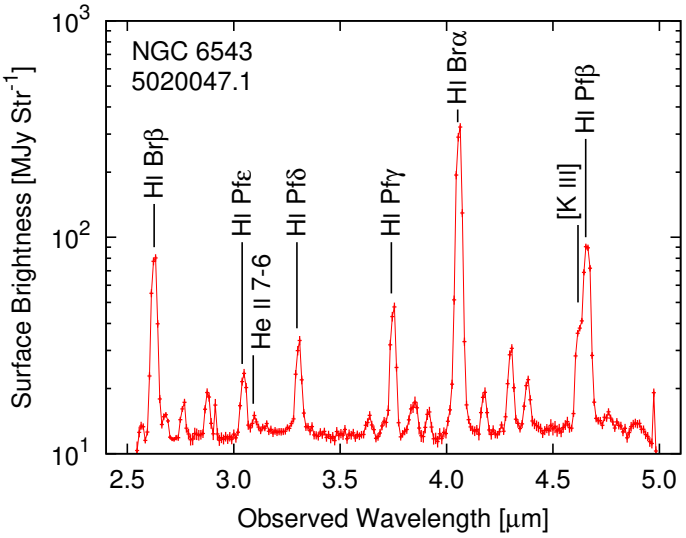

Figure 3.4: 2.5–5.0 μm spectra of NGC 6543 observed in the grism mode (observation ID: 5020047.1).

The differences between $\lambda_{\rm tool}$ and $\lambda_{\rm true}$ can be explained by the wavelength dependence of $n(\lambda)$. From Equations (3.1), (3.2), and (3.4), and $n(\lambda)$, the relation between the difference of $\lambda_{\rm tool} - \lambda_{\rm true}$ and $\lambda_{\rm true}$ can be estimated. Here, λ in Equation (3.1) is assumed as $\lambda_{\rm true}$. The estimates are denoted by the dotted line in Figure 3.5 and fail to reproduce the measured differences. The failure may be attributed to the possibility that the assumed $L = 61.9$ mm differs from the in-flight value. Thus, we took L and the blaze angle α as variables and fitted the curve to the differences. The obtained best fit is denoted by the solid line in Figure 3.5. The fitted parameters are $L = 63.92 \pm 0.03$ mm and $\alpha = 2\overset{\circ}{.}8690 \pm 0\overset{\circ}{.}0003$. The change in L is sufficiently small to be interpreted as the result of the adjustment of the focal length described in the previous section, and that in α is within the fabrication error. We adopted the best-fitting parameters in the following calibrations.

Using the best fit, the relation between ΔY and λ was calculated for both the first- and the second-order light. The obtained relations are shown in Figure 3.6(a). We denote the wavelength of the first-order light as $\lambda^{(1)}$ and that of the second-order light as $\lambda^{(2)}$. First-order light $\lambda^{(1)} = 5.00$ μm goes to $\Delta Y = 194.3$ pix, whereas second-order light $\lambda^{(2)} = 2.50$ μm goes to $\Delta Y = 189.7$ pix. The difference of 4.6 pixels stems from the wavelength dependence of the refractive index of Ge. The refractive index n is 3.940 at 5.00 μm and 3.983 at 2.50 μm (Figure 3.6(d)). According to Equation (3.4), Δn yields the difference of the pixel offset $(L/p)\Delta n\alpha$. Pixel offset $\Delta Y = 189.7$ pix corresponds to $\lambda^{(1)} = 4.95$ μm. Hence, even if the order-sorting filter of the grism perfectly cuts the radiation of $\lambda^{(2)} < 2.50$ μm, the second-order light contaminates the first-order spectra at $\lambda^{(1)} = 4.95$–5.00 μm. The derived pixel offset for the first-order light differs from that of the present wavelength calibration by up to 0.8 pixels at 3.5 μm (Figure 3.6(b)). This is a direct consequence of the fact that the observed wavelength difference $\lambda_{\rm tool} - \lambda_{\rm true}$ reaches the maximum 0.008 μm at $\lambda_{\rm true} = 3.5$ μm (see Figure 3.5). This difference is smaller than the shift of the positions for the first- and second-order light at about $\Delta Y \sim 190$ pix discussed above.

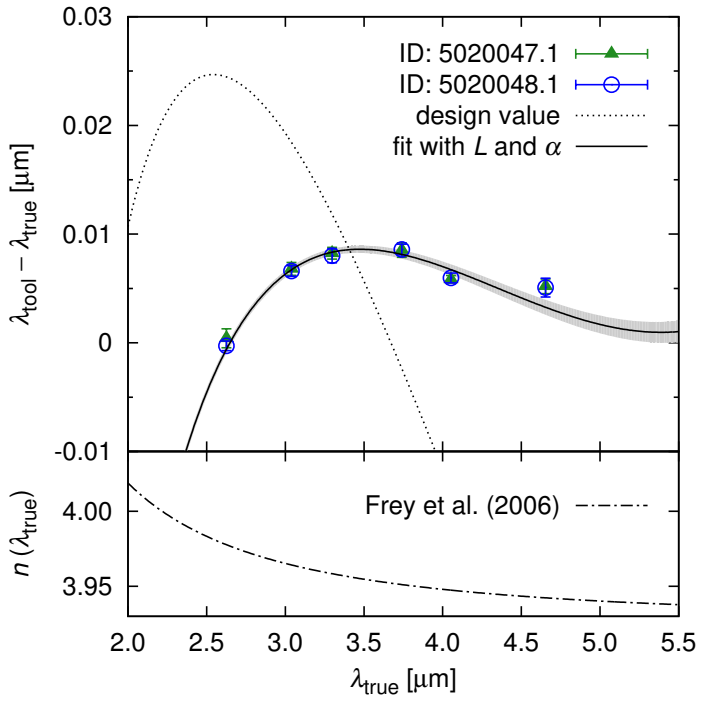

Figure 3.5: Top: The points indicate the differences between the tabulated wavelengths in Table 3.1. The dotted line represents the relation predicted from Equations (3.1), (3.2), and (3.4), and the refractive index shown in the bottom panel. The measured values are plotted as triangles and open circles. The solid line is the curve obtained by fitting the dotted line to the points with variable parameters L and α. The gray-shaded area denotes the one-sigma uncertainty of the best fit. Bottom: refractive index of Ge at 20 K (Frey et al. 2006).

This is because Ohyama et al. (2007) determined the dispersion and the wavelength origin in Equation (3.4) so that the equation represented the positions of the emission lines, but they did not consider whether it predicted the incident positions of the second-order light or not. The 1σ uncertainty of the revised wavelength calibration estimated from using L and α is ± 0.1 pixels or less (Figure 3.6(c)).

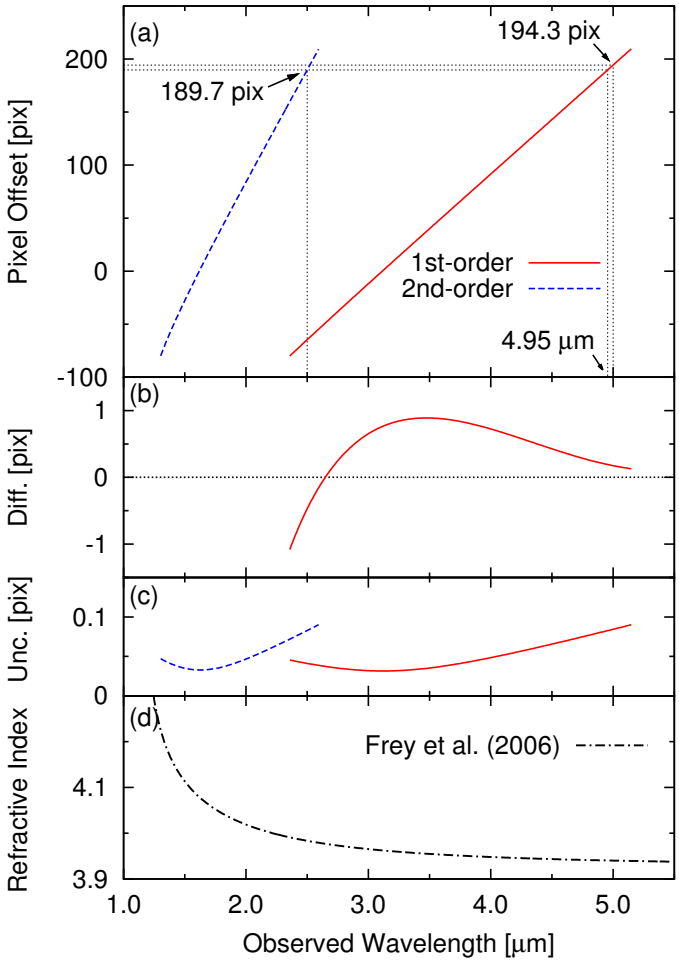

Figure 3.6: (a) The relation between the pixel offset and the wavelength for the first- and second-order light calculated with the wavelength-dependent refractive index of Ge. (b) Difference between the new and old wavelength calibration for the first-order light. The pixel offset of the present wavelength calibration (Equation 3.4) is subtracted from that shown in the top panel. (c) One-sigma uncertainty of the pixel offset. (d) Refractive index of Ge at 20 K (Frey et al. 2006), which is the same as the bottom panel of Figure 3.5 but is also shown in shorter wavelengths.

Taking the refractive index as a function of the wavelength, we succeeded in explaining the observed difference of the previous wavelength calibration. For the first time, to the best of our knowledge, it is also shown that, owing to the wavelength dependence of the refractive index, the contamination by the second-order light occurs even in the case of the perfect order-sorting filter.

3.3.2 Spectral Response Calibration

We obtained the relation between pixel offset and wavelength in the previous section. Next, we discuss the conversion of the output of the detector into the flux density, or flux calibration. We consider the response of the system not only for the first-order light but also for the second-order one, to quantify and subtract the second-order contamination.

Raw spectroscopic images are provided in analog-todigital units (ADU). A series of basic data reduction procedures (dark subtraction, linearity correction, flat fielding, stacking, etc.) and spectral image extraction can be performed with the toolkit (Ohyama et al. 2007).

If there is no contamination from the second-order light, the output at each pixel N in ADU is proportional to the flux density $F_\nu(\lambda)$. Hence, $N = R(\lambda)F_\nu(\lambda)$, where $R(\lambda)$ is the total spectral response of the system at wavelength λ. Even if contamination by the second-order light occurs, similar relations hold for the individual components of the first- and the second-order light, respectively. Therefore, the output at the ith pixel N_i can be written as

$$N_i = R^{(1)}(\lambda_i^{(1)})F_\nu(\lambda_i^{(1)}) + R^{(2)}(\lambda_i^{(2)})F_\nu(\lambda_i^{(2)}). \tag{3.5}$$

Here, $\lambda_i^{(1)}$ and $\lambda_i^{(2)}$ are the wavelengths of the first- and the second-order light in the ith pixel. $R^{(1)}(\lambda)$ and $R^{(2)}(\lambda)$ are the response functions from the first- and the second-order light. Note that the two functions are not equal ($R^{(1)}(\lambda) \neq R^{(2)}(\lambda)$) because the grism does not disperse higher-order light with the same efficiency as the first-order.

The present response $R^{(1)}(\lambda)$ from the first-order light was derived from observations of A- and K-type standard stars (Ohyama et al. 2007). Since these types of stars show blue spectra (RayleighJeans side) in 2.5–5.0 μm, this calibration scheme may result in severe contamination by second-order light, which leads to overestimates of $R^{(1)}$.

Because Equation (3.5) contains two unknown responses $R^{(1)}$ and $R^{(2)}$, it cannot be solved with one standard star. Even if the equation is simultaneously applied to two different standard stars, the response from the second-order light $R^{(2)}$ will have large uncertainty because these standard stars have similar spectra and do not provide sufficiently independent information for calibration. To reliably obtain $R^{(1)}(\lambda)$ and $R^{(2)}(\lambda)$, we used standard objects that have blue and red spectra, where the latter suffer much less from the second-order light than the ordinary standard stars do.

As for the blue standard objects, we used ordinary K-type standard stars. Table 3.2 summarizes Two-Micron All-Sky Survey (2MASS: Skrutskie et al. 2006) IDs, spectral types, and observational information of the two standard stars. KF09T1 was also used in the original spectral response calibration of the grism mode (Ohyama et al. 2007). Using the toolkit, we extracted the raw spectra. Only the sky fluctuation of the spectral image was taken as the uncertainty of the output. The obtained raw spectra of the stars are shown in Figure 3.7. We used model spectra provided by M. Cohen and coworkers (Cohen et al. 1996, 1999, 2003a,b; Cohen 2003) in the same manner as previous calibrations of the IRC (Ohyama et al. 2007; Tanabé et al. 2008; Shimonishi et al. 2013). Both raw spectra show small bumps at around 200 pixels. We attributed these bumps to the contaminating second-order light.

Table 3.2: Basic properties and observation log of standard stars

Object	2MASS ID	Type	Obs. ID	Obs. Date	aperture
KF01T4	J18040314+6654459	K1.5 III	5124053.1	2007 Apr 7	Nc
KF09T1	J17592304+6602561	K0 III	5020032.1	2006 Apr 24	Nc

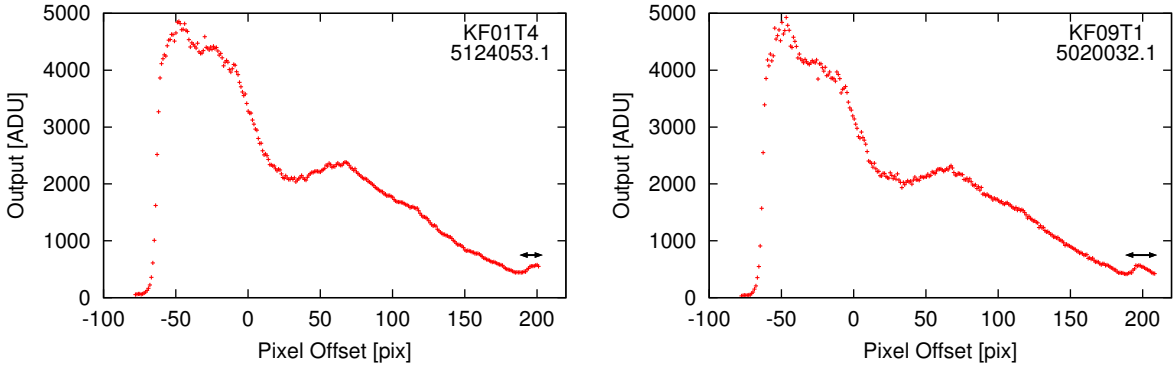

Figure 3.7: Raw spectra of standard stars observed in the grism mode. The arrows denote the ranges where the second-order light component causes anomalies. Left: KF01T4 (observation ID: 5124053.1). Right: KF09T1 (observation ID: 5020032.1).

We used two ultra-luminous IR galaxies (ULIRGs) Mrk 231 and IRAS 05189−2524 as the red standard objects. The dominant energy source of these ULIRGs is an AGN rather than starburst activity (Imanishi & Dudley 2000). Owing to the strong thermal radiation from the dust heated by the AGN, the spectra of the two ULIRGs do not show measurable emission or absorption features in the 3–4 μm range except for the 3.3-μm polycyclic aromatic hydrogen (PAH) emission (Imanishi & Dudley 2000; Imanishi et al. 2007b). Although IRAS 05189−2524 shows weak 3.4-μm absorption of carbonaceous dust with optical depth ∼0.04 (Imanishi & Dudley 2000), it is negligible in building the model spectrum. The 3.4-μm absorption would affect the continuum by less than 4%. Table 3.3 summarizes the redshift, optical classification, and observational information of the two ULIRGs. The raw spectra of the two ULIRGs were extracted in the same manner as the stars and are shown in Figure 3.8.

Table 3.3: Basic properties and observation log of ULIRGs

Object	redshift	Class[a]	Obs. ID	Obs. Date	aperture
Mrk 231	0.042	Seyfert 1	1100271.1	2007 May 30	Np
IRAS 05189−2524	0.043	Seyfert 2	1100129.1	2007 Mar 8	Np

[a] Veilleux et al. (1999).

To create the intrinsic model spectra of the ULIRGs, we compiled observations made with telescopes other than *AKARI*.

Archival data of the 2MASS, *Wide-field Infrared Survey Explorer* (*WISE*: Wright et al. 2010), and *Spitzer*/IRS were used. From the 2MASS All-Sky Extended Source Catalog, we took

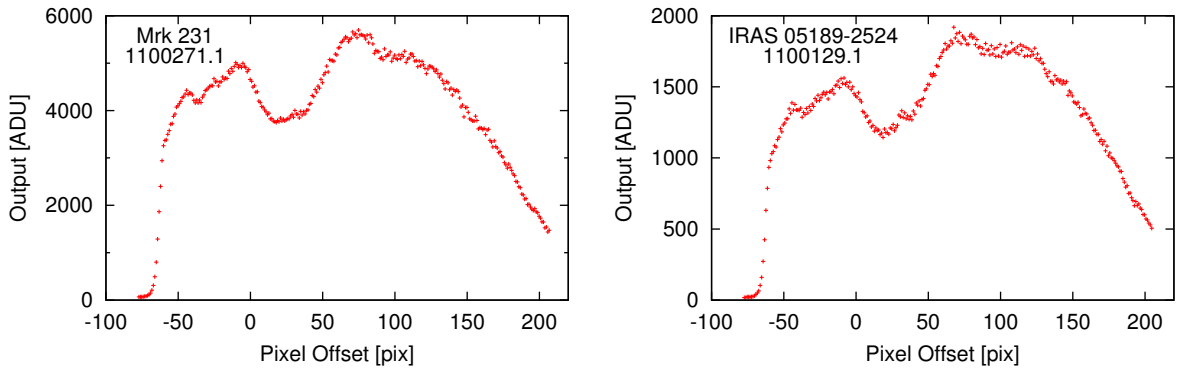

Figure 3.8: Raw spectra of ULIRGs observed in the grism mode. Left: Mrk 231 (observation ID: 110027.1). Right: IRAS 05189−2524 (observation ID: 1100129.1).

the J, H, and K_s total magnitudes extrapolated from the surface brightness profile (Skrutskie et al. 2006). The magnitudes were converted into flux densities using the mean wavelengths and corresponding flux densities for the zero magnitude provided by Rieke et al. (2008). Under the definition of the mean wavelength and zero magnitude, the color correction was normalized for the spectral energy distribution of F_λ = constant, or $F_\nu \propto \lambda^2$ (see Appendix E of Rieke et al. (2008)). Since the two ULIRGs show the same spectral shape in 1–2 μm, no color correction factor was applied.

The $W1$ and $W2$ profile-fit magnitudes were taken from the AllWISE Source Catalog. The fluxes for the zero magnitudes reported by Jarrett et al. (2011) and the color-correction factors provided by Wright et al. (2010) were used. The calibrated *Spitzer*/IRS spectroscopic data were also considered. These data are plotted in Figure 3.9. We fitted a cubic function to these data points for each ULIRG in the $\log F_\nu$-$\log \lambda$ plane to approximate their spectra. The fitted functions are shown in Figure 3.9.

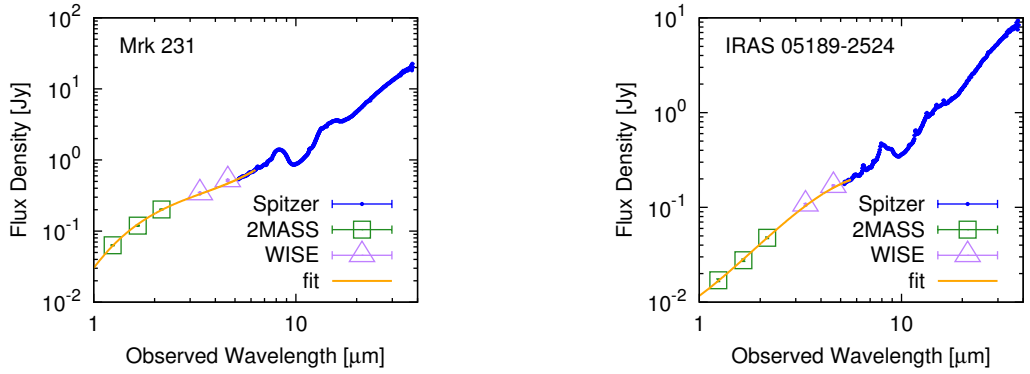

Figure 3.9: Flux densities of the ULIRGs observed with 2MASS, *WISE*, and *Spitzer*/IRS. Solid lines denote the fitted cubic functions, which were taken as the model spectra of the ULIRGs. The fitting ranges were intervals where the lines are drawn. Left: Mrk 231. Right: IRAS 05189−2524.

We calculated the spectral responses from two pairs of standard objects (KF01T4 and Mrk 231, and KF09T1 and IRAS 05189−2524). For the uncertainties of the responses, those in the

raw spectra, model spectra, and the wavelength calibration curve were propagated. The response from the first-order light has a measurement uncertainty of about 5%. The measurement uncertainty of the response from the second-order light is about 5% at 2.55 μm and increases at shorter wavelengths. At 2.3 μm, it becomes around 50%. Below 2.3 μm, the response from the second-order light is substantially zero. The responses have systematic uncertainty of at most 4% owing to the weak emission or absorption lines of the ULIRGs. Since we built the model spectra of the ULIRGs ignoring the PAH emission, we mask the data points affected by the PAH emission. The rest-frame full width at half-maximum of the PAH emission is 0.05 μm (Imanishi & Dudley 2000; Imanishi et al. 2007b); thus, we removed 15 data points ($\sim$0.15 μm) of the responses from the first-order light around $\lambda^{(1)} = (1 + z) \times 3.29$ μm, where z is the redshift of the ULIRGs and 3.29 μm is the peak wavelength of the PAH emission (Imanishi et al. 2008). The data points of the responses from the second-order light were also removed at wavelengths that correspond to the same masked pixel offsets. The two ULIRGs have similar redshifts, as listed in Table 3.3. Hence, the PAH-masked regions almost entirely overlap with each other. The results from the two pairs were averaged to reduce the uncertainty. Next, since the responses hardly change along a few pixels, we took the five-pixel-width moving average to reduce the pixel-to-pixel scatter in a manner similar to the spectral response calibration for the prism mode by Shimonishi et al. (2013). Finally, the responses shown in Figure 3.10 were obtained. The set of the responses ($R^{(1)}$ and $R^{(2)}$) covers the range of ΔY from -77.2 to 200.8 pixels. This range corresponds to that of $\lambda^{(1)} = 2.38$–5.06 μm and $\lambda^{(2)} = 1.31$–2.55 μm. The measurement uncertainty of the response from the first- and second-order light is minimized to about 2% and 2–26%, respectively.

The obtained spectral response from the first-order light $R^{(1)}$ agrees with the previous one within the uncertainties between 2.6 and 4.9 μm, where contamination by the second-order light is not expected. At wavelengths longer than 4.9 μm, $R^{(1)}$ of this work monotonically decreases, in contrast to that in the toolkit. The ratio of $R^{(1)}$ of this work to that of the toolkit is 0.63 at 5.0 μm and 0.96 at 2.6 μm. In addition to this, the response from the second-order light $R^{(2)}$, which is, to our knowledge, derived for the first time, increases at wavelengths longer than 2.5 μm. These results show that the previous response curve at wavelengths longer than 4.9 μm is contributed by the two components, first- and second-order light, and that we succeeded in separating them into the two responses $R^{(1)}$ and $R^{(2)}$. Moreover, the responses are significantly non-zero at wavelengths shorter than 2.5 μm. This means that the detector responds to the radiation of wavelengths shorter than 2.5 μm, beyond the nominal wavelength range of 2.5–5.0 μm. Therefore, this suggests that the order-sorting filter had some leakage below 2.5 μm.

Subtraction of the second-order-light component from the first-order spectra is formalized by extending the spectral response in the matrix that relates the output with the first-order spectrum. The first-order spectrum can be purely obtained from this equation. This is the main goal of our calibrations.

To evaluate the amount of the second-order light as a function of the wavelength, we need the intensity of the first-order light at the same wavelength. We assume that wavelength $\lambda_1^{(1)}$, which comes in at the first pixel as first-order light, enters between the $(k-1)$th and kth pixels

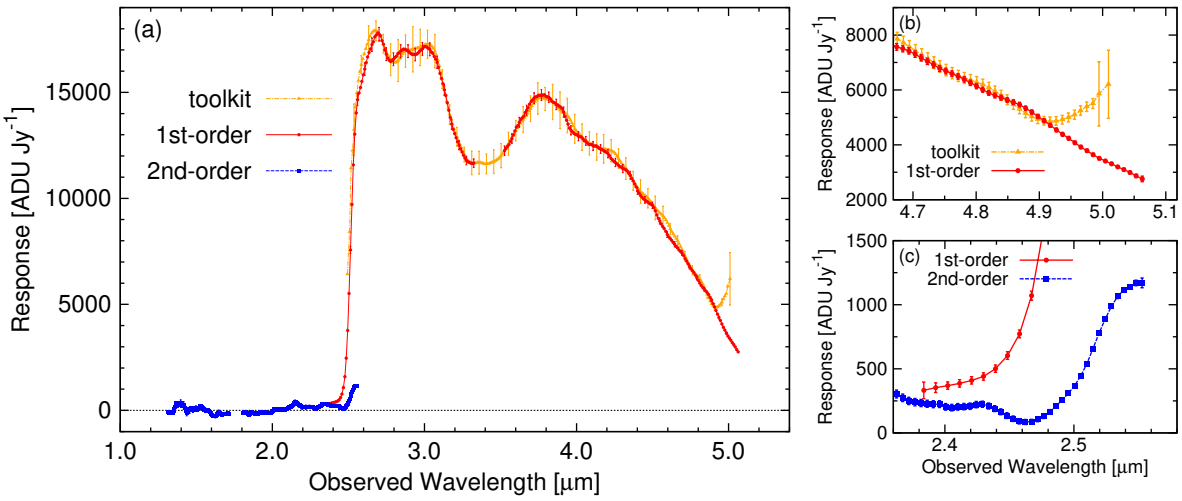

Figure 3.10: Spectral responses from the first- and second-order light and that of the present toolkit. (a) The entire plot. Gaps in the new response curves are masked ranges affected by the PAH emission. Error bars are drawn every five points. (b) and (c) Zoom-in plots around 5 μm and 2.5 μm, respectively. The scales of the abscissas of panels (b) and (c) are aligned so that the same pixel offsets line up vertically (e.g., $\lambda^{(2)} = 2.50$ μm and $\lambda^{(1)} = 4.95$ μm).

as second-order light. Based on this assumption, since the increment of $\lambda_i^{(2)}$ is about half of that of $\lambda_i^{(1)}$, the following magnitude relation holds:

$$\lambda_{k-1}^{(2)} < \lambda_1^{(1)} < \lambda_k^{(2)} < \lambda_{k+1}^{(2)} < \lambda_2^{(1)} < \cdots . \tag{3.6}$$

Hereafter, we define $R^{(1)}(\lambda_i^{(1)})$ as $R_i^{(1)}$, $R^{(2)}(\lambda_i^{(2)})$ as $R_i^{(2)}$, and $F_\nu(\lambda_i^{(1)})$ as $F_{\nu,i}$. Using these notations, the output at the kth pixel is

$$N_k = R_k^{(1)} F_{\nu,k} + R_k^{(2)} F_\nu(\lambda_k^{(2)}). \tag{3.7}$$

From the linear interpolation, the flux density of the second-order-light component at the kth pixel becomes

$$F_\nu(\lambda_k^{(2)}) = \frac{\lambda_2^{(1)} - \lambda_k^{(2)}}{\lambda_2^{(1)} - \lambda_1^{(1)}} F_{\nu,1} + \frac{\lambda_k^{(2)} - \lambda_1^{(1)}}{\lambda_2^{(1)} - \lambda_1^{(1)}} F_{\nu,2}. \tag{3.8}$$

Equations (3.7) and (3.8) can be combined into the following matrix.

$$\begin{pmatrix} N_1 \\ N_2 \\ \vdots \\ N_k \\ \vdots \end{pmatrix} = \begin{pmatrix} R_{1,1} & & & & \\ & R_{2,2} & & & \\ & & \ddots & & \\ R_{k,1} & R_{k,2} & & R_{k,k} & \\ \ddots & \ddots & & & \ddots \end{pmatrix} \begin{pmatrix} F_{\nu,1} \\ F_{\nu,2} \\ \vdots \\ F_{\nu,k} \\ \vdots \end{pmatrix} \tag{3.9}$$

$$R_{i,i} = R_i^{(1)} \tag{3.10}$$

$$R_{k,1} = \frac{\lambda_2^{(1)} - \lambda_k^{(2)}}{\lambda_2^{(1)} - \lambda_1^{(1)}} R_k^{(2)},\ R_{k,2} = \frac{\lambda_k^{(2)} - \lambda_1^{(1)}}{\lambda_2^{(1)} - \lambda_1^{(1)}} R_k^{(2)},\ \cdots \tag{3.11}$$

The response from the second-order light is included as the off-diagonal elements of this matrix. The inverse matrix of the response matrix can be analytically obtained (see Appendix A.1). Multiplying it with the column vector of the output, we can obtain the pure first-order spectrum $F_{\nu,i}$.

The spectral responses obtained in this section separate the components of the first- and second-order light and quantify the second-order-light contamination. The relations among the components of the first- and second-order light and the output can be formalized in one equation with the response matrix, whose diagonal and off-diagonal elements represent the responses from the first- and second-order light, respectively. The flux calibration that considers the contamination effect can be achieved by multiplying the inverse matrix of the response with the output.

3.4 Demonstrations of the Effectiveness of the New Flux Calibration

We here first demonstrate the matrix-formulated flux calibration for two objects that have different colors and compare the results with those from the toolkit. Next, we show how the correct CO absorption profile is recovered by our calibration method. In the following demonstrations, the response from the first-order light is interpolated into the PAH-masked range using a quadratic function of the wavelength.

Figure 3.11 compares the spectra of the ULIRG IRAS F15002+4945, which has appeared in Section 3.1 as an example of the toolkit calibration. This ULIRG has a red spectrum, and hence, the second-order light component is expected to be smaller than that of blue objects. The spectrum obtained by the new flux calibration shows a smooth distribution up to 5.0 μm, whereas that obtained by the toolkit decreases at 4.9 μm. This change reflects the revision of the first-order light response curve: the current one monotonically decreases at longest wavelengths in contrast to the previous one (see Figure 3.10(b)).

As another example, Figure 3.12 shows the result for an A0V star (HD 40624), which has a blue spectrum. In this case, the first-order spectrum at longer wavelengths is considered to be largely contaminated by the second-order light that comes from shorter wavelengths. This star was also observed in the prism mode just before the grism mode observation. Since the prism is not a grating element, any problems associated with the higher-order light cannot occur in the prism mode. The flux calibration results basically agree with the prism mode spectrum but disagree with it if the off-diagonal elements of the response matrix, which measure the contribution of the second-order light, are ignored. This suggests that our flux calibration successfully removes the second-order component.

The toolkit had not been able to correct the second-order light contamination of the first-

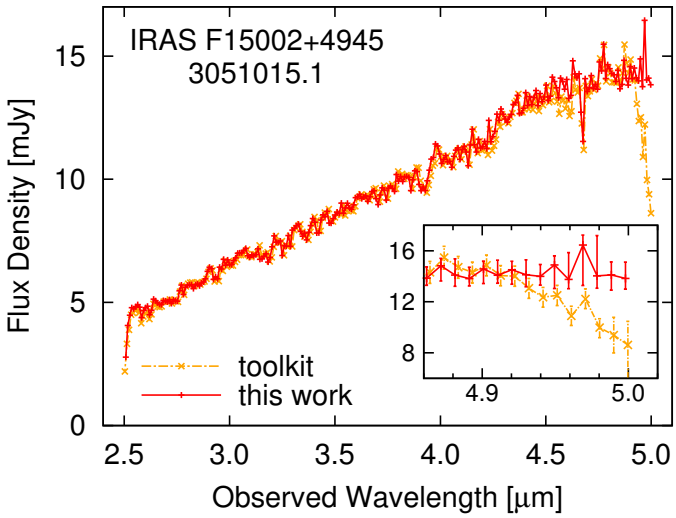

Figure 3.11: Demonstration of the matrix-formulated calibration for a ULIRG, IRAS F15002+4945 (observation ID: 3051015.1). The spectrum processed with the toolkit (Figure 3.1(b)) is also shown.

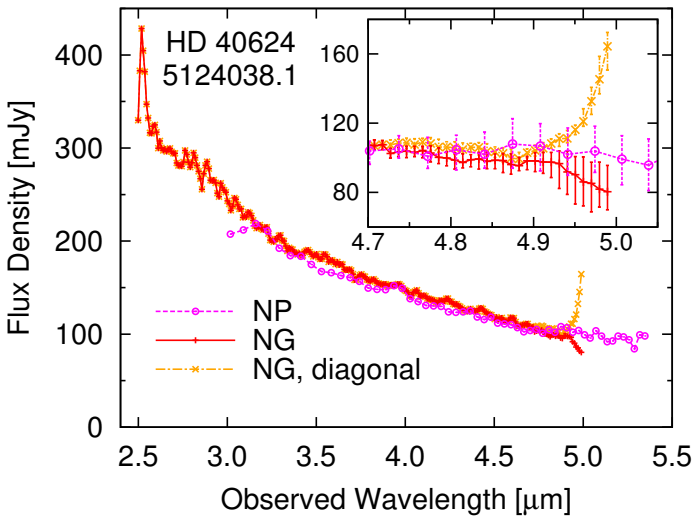

Figure 3.12: Demonstration of the matrix-formulated calibration for an A0V star, HD 40624 (observation ID: 5124038.1). The spectrum calculated with only the diagonal elements of the response matrix is also shown. The magenta points show the spectrum obtained in the prism mode observation of IRC. The prism mode spectrum in the 1.8–3.0 μm range was not obtained owing to the saturation of the detector.

order spectra in wavelengths longer than 4.9 μm. This effect had led the incorrect flux calibration, especially for red objects, and prevented obtaining accurate spectra in this wavelength range. The new flux calibration, which quantifies and subtracts the contamination, can resolve this problem for a wide range of objects, as shown by the above examples. Now we can accurately obtain the 4.9–5.0 μm spectra without the effect of the second-order light. Figure 3.13 compares the CO band spectra calibrated by the toolkit (presented in Figure 3.1(a)) and by our method. As this figure shows, the double-branched profile of the band is successfully recovered in the new result. Imanishi et al. (2008) reported that three ULIRGs observed in the grism mode during Phases 1 and 2 showed the CO absorption. However, these absorption spectra were significantly affected by the second-order contamination and had never been analyzed. Our new calibration, for the first time, enables the analysis of the CO absorption in nearby AGNs observed in the *AKARI* grism mode spectroscopy.

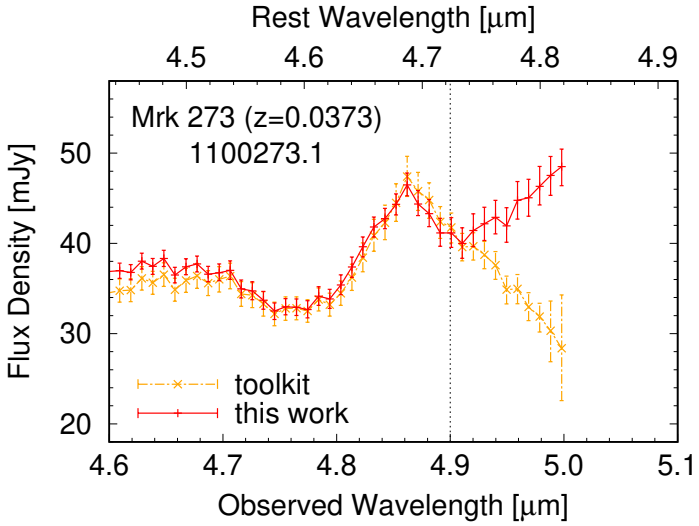

Figure 3.13: Demonstration of the matrix-formulated calibration for a CO absorption spectrum observed in the Seyfert 2 galaxy Mrk 273 (observation ID: 1100273.1). The spectrum processed with the toolkit (Figure 3.1(a)) is also shown.

Another science that may be allowed by the revised calibration is the analysis of the OCS ice absorption band at 4.9 μm (Boogert et al. 2015). The OCS ice can be used to study the evolution of circumstellar disks of young stellar objects. For instance, Aikawa et al. (2012) tentatively detected the OCS ice absorption toward a low-mass young stellar object IRCL1041-2 from the grism mode observation. The study of this feature in young stellar objects also requires the correction for the contamination.

3.5 Summary

In this chapter, we have described the revision of the wavelength and spectral response calibrations of the *AKARI* IRC grism mode spectroscopy. These new calibrations were performed to correct for the effect of the second-order light contamination in the first-order spectrum. First,

the refractive index of Ge, the material of the grism, was considered as a function of wavelength. The difference from the previous linear wavelength calibration was measured from the recombination lines of planetary nebulae, and we successfully represented it with the wavelength dependence of the refractive index. Next, the spectral responses from the first- and second-order light were simultaneously obtained using standard objects that show contrastive red and blue spectra. With these new responses, the first- and second-order light mixing in 4.9–5.0 μm were decomposed for the first time. Finally, the flux calibration with the set of the responses was formulated into a matrix form. This flux calibration was demonstrated to be able to remove the second-order-light component in both red and blue objects. The new calibrations enable us to obtain the correct 4.9–5.0 μm spectra in the grism mode and are essential for the study of the CO absorption in nearby AGNs, which appears Chapters 5 and 6. Note that the calibrations presented here are limited to the observations before the exhaustion of liquid helium (Phases 1 and 2). During the post-helium phase (Phase 3), the temperature of the detector exceeds 40 K, and hence, the operating conditions in Phase 3 largely differ from those in the earlier phases. Similar calibrations for Phase 3 is presented in Chapter 4.

Chapter 4

Revised Wavelength and Spectral Response Calibrations for *AKARI* Near-Infrared Grism Spectroscopy: Post-Cryogenic Phase

Following the re-calibration of the *AKARI* NIR grism spectroscopy in the cryogenic phase presented in Chapter 3, we revised the wavelength and spectral response calibration in the post-cryogenic phase in a similar manner. To assess the effect of the temperature increase during this period, we divided the period into three sub-phases and performed the calibrations separately. Similar to the cryogenic phase, we confirmed in every sub-phase the presence of the second-order light contamination due to the wavelength dependence of the refractive index of the grism material and succeeded in quantifying its effect on the spectral response function. Wavelength calibration curves in the three sub-phases coincide with each other and do not show any significant temperature dependence. Spectral response from the first-order light decreases as the temperature increases by $\sim 10\%$ from the beginning to the end of the post-cryogenic phase. We approximated the temperature dependence of the response as a linear relation and derived a correction factor as a function of temperature. The relative strength of the second-order light contamination to the first-order light decreased by 25% from the cryogenic phase due to the degradation of the point-spread function around 2.5 μm relevant to the contamination at 5 μm.

4.1 Introduction

During the post-cryogenic phase (Phase 3) of the *AKARI* satellite, a large number of near-IR spectroscopic observations of AGNs were performed. However, as well as cryogenic phase (Phases 1 and 2), those observations were suffered from the contamination from the second-order light. The latest published version of the official data reduction toolkit for Phase 3 (version 20150331) does not support the subtraction of the contamination. To utilize the observations during Phase

3 for the study of the CO absorption, we need to correct for the effect of the second-order light as we did in the cryogenic phase.

The major difference from the before is the operating temperature. Between the two periods, the temperature of the instrument jumped from $\sim$ 6 K to $>$ 40 K due to the exhaustion of liquid helium. Besides, during the latter period, the temperature was not stable and gradually increased with time. It has been known that the absolute sensitivity of the NIR grism mode had decreased to be roughly 70% of that in Phases 1 and 2 (Onaka et al. 2009, Section 6.9.4). Our detailed calibration that considers the higher order effects (the nonlinearity of the refractive index and the second-order light contamination) thus requires the evaluation of the effect of the temperature variation.

In this chapter, we explain the revision of the wavelength and spectral response calibrations in Phase 3. In section 4.2, we define three sub-phases that have different temperature ranges. Wavelength and spectral response calibrations are given in Sections 4.3 and 4.4, respectively, followed by the summary in Section 4.5.

4.2 Definition of Sub-Phases

The header of FTIS images obtained in the *AKARI* pointed observations contains the detector temperature at the data acquisition time. We measured the temperature at spectroscopic observations performed during Phase 3. The obtained temperature variation curve is shown in the top panel of Figure 4.1. The temperature began from 41 K and increased to 46.5 K during the first year making shoulders in June and December solstices due to small Earth avoidance angles shown in the bottom panel of Figure 4.1. The temperature then decreased and again turned to rise at the beginning of 2009 November when the average Earth avoidance angle was large.

We divided Phase 3 into three periods as tabulated in Table 4.1. These sub-phases correspond to the temperature ranges of $T < 42$ K, $42 < T < 44.5$ K, and $T > 44.5$ K. This definition was set so that we can secure a sufficient number of observations for the calibration in each sub-phase. We performed wavelength and spectral response calibrations separately for each sub-phase to assess their temperature dependence as explained in the following sections.

Table 4.1: Definition of sub-phases and corresponding temperature ranges

Sub-Phase	Date	Detector Temperature (K)
3-1	2008 Jun 1 – 2008 Oct 31	40.0–42.0
3-2	2008 Nov 1 – 2009 Apr 14	42.0–44.5
3-3	2009 Apr 15 – 2010 Feb 15	44.5–47.0

4.3 Wavelength Calibration

Similar to the procedure in Section 3.3.1, we measured the difference of the wavelength calibration of the toolkit (Equation (3.4)) from the Ns-slit observations of emission-line objects.

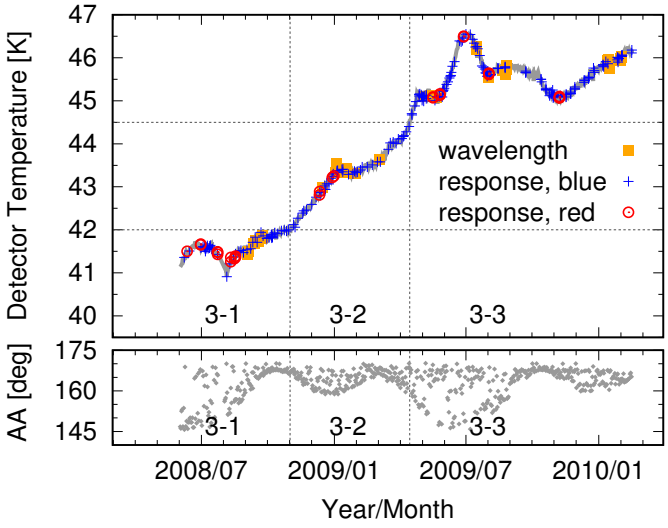

Figure 4.1: Top: variation of the detector temperature T in the NIR channel during Phase 3 is shown in a thick gray line. Orange filled squares indicate observations used in the wavelength calibration, and blue crosses and red open circles represent observations of the blue and red standard objects used in the spectral response calibration. Vertical dotted lines denote the borders between sub-phases 3-1, 3-2, and 3-3. These phases correspond to the temperature ranges of $T < 42$ K, $42 < T < 44.5$ K, and $T > 44.5$ K, as shown with horizontal dotted lines. Bottom: mean Earth avoidance angle of the satellite during each pointed observation. Not all of the pointed observations are plotted. The number of points is thinned out to about 1 per day.

Because the number of observations of planetary nebulae is small, we instead used Galactic H II regions as calibrators. Object names and observation IDs are listed in Table 4.2. For each observation, the detector temperatures recorded in the header of the FITS images were averaged, and its uncertainty was estimated from the deviation. The number of images for each spectroscopic observation was 8–10, including one reference frame. The obtained values are tabulated in Table 4.2.

A 2D spectral image was extracted from each observation by the latest toolkit in the standard manner. The image usually contained a lot of hot pixels, which are treated as the missing value in the present toolkit, as shown in Figure 4.2(a). We thus filled the lacking pixels with the median of their adjacent valid pixels. Figure 4.2(b) gives an example of this procedure. We extracted a 1D spectrum from the filled image and then fitted the H I Brα, Brβ, Pfβ, Pfγ, Pfε, Pf11, and Pf12 lines in the spectrum with a Gaussian on a liner baseline with the line width fixed to FWHM=0.031 μm. This is the same value adopted by Mori et al. (2014). We did not fit the Pfδ line because it is overlapped by the 3.3 μm PAH emission in the spectra of H II regions. The central wavelength $\lambda_{\rm tool}$ obtained from the line fitting is plotted in Figure 4.3 as the difference from the theoretical value $\lambda_{\rm true}$.

As we did for the cryogenic phase, we fitted the measured wavelength difference $\lambda_{\rm tool} - \lambda_{\rm true}$ with Equations (3.1), (3.2), and (3.4) taking α and L as free parameters. The refractive index $n(\lambda)$ was calculated with the equation of (Frey et al. 2006) at the average detector temperature of the observations used for the line fitting (Table 4.2). The resultant values of α and L are

Table 4.2: Galactic H II regions observed in the Ns slit

Phase	Object	Type[a]	Obs. ID	Date	Temp. (K)[b]
3-1	G330.868−0.365	GH II	5200110.1	2008 Sep 2	41.43 ± 0.03
	G331.386−0.359	unknown	5200114.1	2008 Sep 3	41.48 ± 0.03
	G333.122−0.446	GH II	5200122.1	2008 Sep 4	41.50 ± 0.02
	G345.528−0.051	unknown	5200134.1	2008 Sep 11	41.69 ± 0.02
	G347.611+0.204	GH II	5200138.1	2008 Sep 12	41.69 ± 0.04
	Sgr C	GH II	5200144.1	2008 Sep 18	41.74 ± 0.02
	G351.467−0.462	GH II	5200142.1	2008 Sep 14	41.76 ± 0.03
	AMWW35	GH II	5200160.1	2008 Sep 22	41.79 ± 0.05
	M8	GH II	5200162.1	2008 Sep 24	41.81 ± 0.02
	G8.137+0.228	GH II	5200164.1	2008 Sep 23	41.86 ± 0.02
3-2	RCW42	GH II	5200453.1	2008 Dec 15	42.98 ± 0.04
	G298.862−0.438	GH II	5200451.1	2009 Jan 30	43.31 ± 0.03
	G298.227−0.340	GH II	5200449.1	2009 Jan 28	43.32 ± 0.08
	G282.023−1.180	GH II	5200437.1	2009 Jan 2	43.34 ± 0.03
	G289.066−0.357	GH II	5200443.1	2009 Jan 13	43.34 ± 0.05
	NGC 3576	GH II	5200445.1	2009 Jan 17	43.37 ± 0.05
	NGC 3372	GH II	5200441.1	2009 Jan 10	43.38 ± 0.03
	NGC 3603	GH II	5200447.1	2009 Jan 17	43.42 ± 0.02
	RCW49	GH II	5200439.1	2009 Jan 4	43.55 ± 0.08
	G333.6−0.2s47	GH II	5200586.1	2009 Mar 4	43.64 ± 0.03
3-3	G81.679+0.537	UCH II	5200778.1	2009 May 21	45.07 ± 0.02
	W58A	GH II	5200768.1	2009 May 3	45.10 ± 0.03
	G75.783+0.343	UCH II	5200773.1	2009 May 11	45.10 ± 0.02
	G78.438+2.659	UCH II	5200777.1	2009 May 13	45.11 ± 0.02
	G289.066−0.357	GH II	5201356.2	2010 Jan 15	45.76 ± 0.11
			5201356.1	2010 Jan 14	45.87 ± 0.03
			5200881.1	2009 Jul 15	46.19 ± 0.06
			5200881.2	2009 Jul 15	46.26 ± 0.03
	G298.862−0.438	GH II	5200886.1	2009 Aug 1	45.55 ± 0.05
	G319.158−0.398	GH II	5200934.1	2009 Aug 25	45.62 ± 0.05
	G133.947+1.064	UCH II	5200959.1	2009 Aug 20	45.70 ± 0.09
	G319.392−0.009	GH II	5200936.2	2009 Aug 26	45.74 ± 0.02
			5200936.1	2009 Aug 26	45.81 ± 0.05
	G22566+5830	unknown	5201369.2	2010 Jan 14	45.88 ± 0.03
			5201369.1	2010 Jan 12	45.94 ± 0.07
	G22475+5939	unknown	5201368.1	2010 Jan 14	45.96 ± 0.02
	G12127−6244	unknown	5201366.1	2010 Jan 30	45.99 ± 0.05
			5201366.2	2010 Jan 30	45.99 ± 0.02
	G12272−6240	unknown	5201367.1	2010 Jan 31	45.94 ± 0.03
			5201367.2	2010 Feb 1	46.03 ± 0.01
			5201367.3	2010 Feb 1	46.00 ± 0.02

[a] Quoted from Mori et al. (2014); Conti & Crowther (2004); Crowther & Conti (2003). GH II: giant H II region. UCH II: ultracmoact H II region.
[b] Detector temperature. Also plotted in Figure 4.1

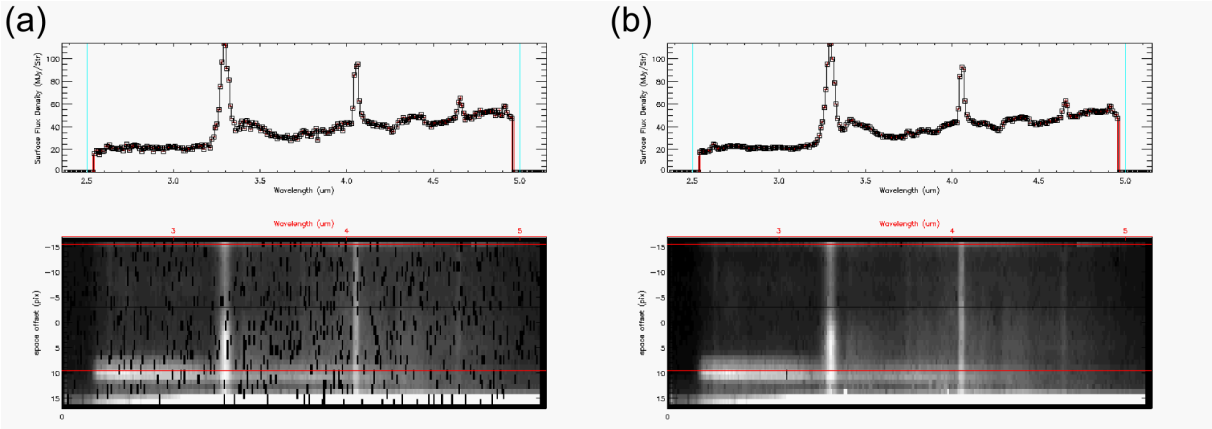

Figure 4.2: (a) 2D spectral image of the giant H II region G330.868−0.365 (observation ID: 5200110.1). Black cells represent hot pixels. The 1D spectrum in the top panel was obtained by integrating the 2D image along the spatial axis. (b) 2D spectral image and 1D spectrum of the same observation after the bad pixels were filled with the median of their adjacent valid pixels.

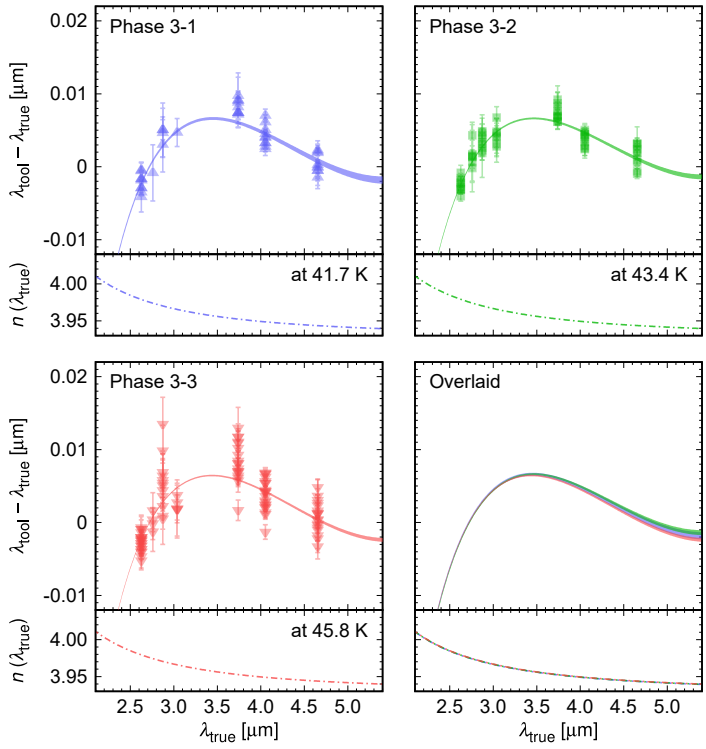

Figure 4.3: The measured difference of the previous wavelength calibration and the refractive index of Ge for the three sub-phases are shown in the quadrants other than the right bottom one. These plots are analogs of Figure 3.5 presented for the cryogenic phase. The top panel in each quadrant indicates the measured difference between the central wavelength obtained in the line fitting ($\lambda_{\rm tool}$) and the theoretical value ($\lambda_{\rm true}$). The overlaid transparent filled curve is the 1σ fitting error of the model described in Section 3.3.1. The bottom panel of each quadrant shows the refractive index of Ge at the average detector temperature of the observations listed in Table 4.2). In the right bottom quadrant, the fitting errors and the refractive indices in the three sub-phases are overlaid.

tabulated in Table 4.3 and the best-fitting model is shown in Figure 4.3 with $n(\lambda)$. The results of the three sub-phases coincide with each other within the 1σ fitting error. The temperature dependence of $n(\lambda)$ in 41–47 K and 1.2–5.5 μm is less than 0.4%. Therefore, we did not find any significant temperature dependence of the wavelength calibration. Then we fitted the model in the same manner to all the data points not dividing them into sub-phases. The obtained values for the two parameters are listed in Table 4.3.

Table 4.3: Average detector temperature and the fitted value of α and L

Phase	T (K)	α (deg)	L (mm)
3-1	41.7	2.86966 ± 0.00018	63.894 ± 0.013
3-2	43.4	2.86957 ± 0.00011	63.908 ± 0.009
3-3	45.8	2.86938 ± 0.00009	63.881 ± 0.007
all	44.3	2.86952 ± 0.00007	63.891 ± 0.005

Using the model fitted to the entire observations, we constructed the relation between the pixel offset from the direct light position ΔY and the first- and second-order wavelengths $\lambda^{(1)}$ and $\lambda^{(2)}$, which is presented in Figure 4.4(a). This figure indicates that the second-order light of $\lambda^{(2)} = 2.5$ μm incidents to the same position for the first-order light of $\lambda^{(1)} = 4.95$ μm. This clarifies the presence of the contamination. The difference from the result for the cryogenic phase is about 0.2 pixels. Thus there is little practical difference between the calibrations in the two phases.

4.4 Spectral Response Calibration

For each sub-phase, as in Phases 1 and 2, we simultaneously derived the spectral response function for the first- and second-order light using two types of standard objects: AGNs and infrared galaxies whose near-IR spectra can be modeled easily and standard stars that have a Cohen template. In this section, we explain the selection of the standard objects, the derivation of the spectral responses, and the evaluation of the temperature dependence.

4.4.1 Red Standard U/LIRGs

We searched infrared galaxies for which we can make a reliable model spectrum from earlier published results of the *AKARI* spectroscopy. Several authors have analyzed the Phase-3 near-IR grism mode observations of AGNs and infrared galaxies with earlier versions of the toolkit. We first explored the sample of Kim et al. (2015), who studied the spectra of 83 nearby and bright type-I AGNs and identified emission and absorption features. We selected the 41 AGNs for which Kim et al. (2015) had not identified any features. Secondly, we looked for the sample of Yamada et al. (2013). The authors investigated the spectra of 184 galaxies and measured the equivalent width of the 3.3 μm PAH emission, the luminosity of the Brα line, and the optical depth of the 3.1 μm H_2O ice absorption. Yamada et al. (2013) did not significantly detect any of

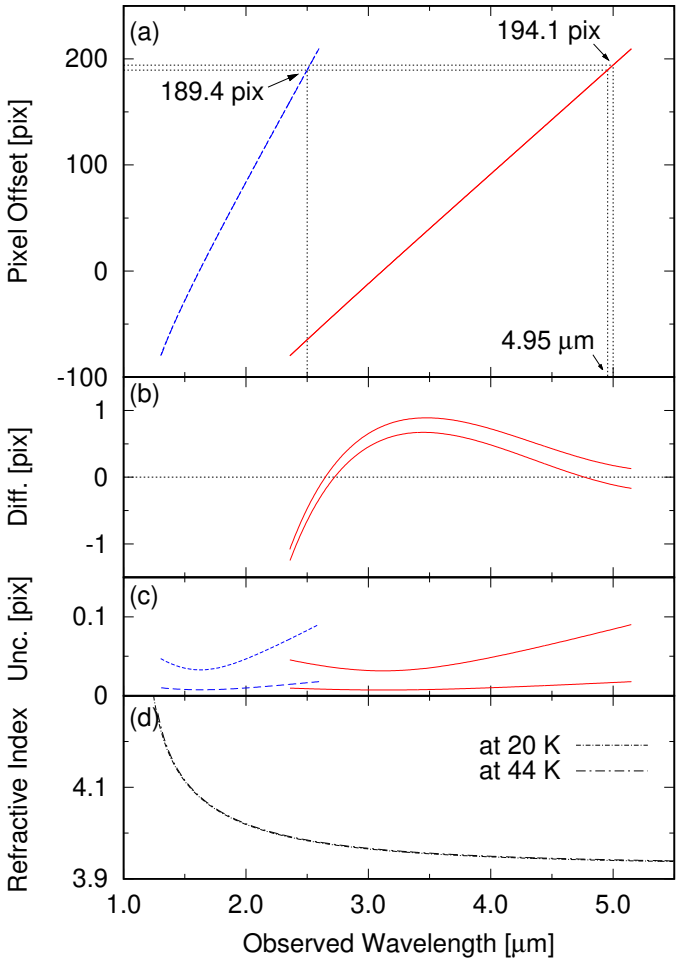

Figure 4.4: Revised wavelength calibration curve for Phase 3. This figure is an analog to Figure 3.6. For comparison, the result for the cryogenic phase is drawn in thin lines. (a) The relation between the pixel offset and the wavelength for the first- and second-order light. (b) Difference between the new and old wavelength calibration for the first-order light. The pixel offset of the present wavelength calibration is subtracted from that shown in the top panel. (c) One-sigma uncertainty of the pixel offset. (d) Refractive index of Ge.

the three features in 33 objects. Some of them were also analyzed by Imanishi et al. (2010). We discarded those for which Imanishi et al. (2010) had found significant PAH emission. Finally, 29 galaxies were selected from the sample of Yamada et al. (2013).

Our method to make a model spectrum of a red object, which is similar to that of Chapter 3, requires the *Spitzer*/IRS 5.2–32 μm spectrum and reliable 2MASS and *WISE* magnitudes. Among the 70 galaxies taken from the samples of Kim et al. (2015) and Yamada et al. (2013), 41 objects have the IRS spectra. To 2MASS, we set the criteria of `ph_qual`=AAA, `cc_flg`=000, $K_s < 13$ mag, and that the object has no neighbor brighter than 1% of itself at least one band within 15″. We also set the criterion of `ph_qual`=AAAA to *WISE*. Afterward, 23 galaxies satisfied these criteria.

The 2MASS and *WISE* magnitudes of each galaxy were converted into flux densities in Jy based on the zero magnitudes presented by Cohen et al. (2003b) and Jarrett et al. (2011), respectively. The color correction was performed upon the spectral slope inferred from the original band fluxes. The IRS spectrum was rescaled so that it matches the W3 and W4 fluxes because the IRS slit spectroscopy could miss the flux compared to the *AKARI* slitless observation. We then fitted the J, H, K, $W1$, and $W2$ band fluxes and the IRS data points at wavelengths shorter than 6.5 μm with a cubic function on the $\log F\nu$-$\log\lambda$ plane. The degree of freedom in this configuration was 44. We rejected bad fits having the reduced χ^2 value $\chi^2_\nu \equiv \chi^2/\mathrm{dof}$ apart from unity ($\chi^2_\nu < 0.63$ or $\chi^2_\nu > 1.46$), which correspond to being out of the 95% confidence range. Eventually, 13 U/LIRGs were accepted as red standard objects. The obtained model spectra of them are shown in Figure 4.5. The *AKARI* observations of them are listed in Table 4.4. Sub-phases 3-1, -2, and -3 contain 5, 3, and 8 objects, respectively, while having some overlap. Although IRAS 23060+0505 were observed twice during phase 3-2, we regarded the two observations as independent ones to let them be paired with different standard stars. We attached an ID to each object as shown in Table 4.4. The ID is to be paired with an observation set of a standard star.

The 2D spectral image was obtained from each observation with the latest toolkit. Bad pixels were filled up in the same way described in Section 4.3. From the corrected 2D image, a raw 1D spectrum expressed in the detector output N versus the pixel offset ΔY was extracted with the spatial width of five pixels ($\sim 7''$). We stacked multiple raw spectra of the same pair ID to reduce the uncertainty.

4.4.2 Blue Standard Stars

Several ordinary standard stars were originally observed for calibration purposes throughout Phase 3. Especially, the K0 III star KF09T1 (2MASS J17592304+6602561) was monitored frequently. These stars have Cohen templates (Cohen et al. 1996, 1999, 2003a,b; Cohen 2003). We used the templates as the model spectra for our calibration. The observations of the stars are tabulated in Table 4.5. We divided the observations of KF09T1 into subsets to match the number of the red standard U/LIRGs. The observation subsets were paired with those of the U/LIRGs via the pair IDs. Raw spectra were created per pair ID similarly to the U/LIRGs.

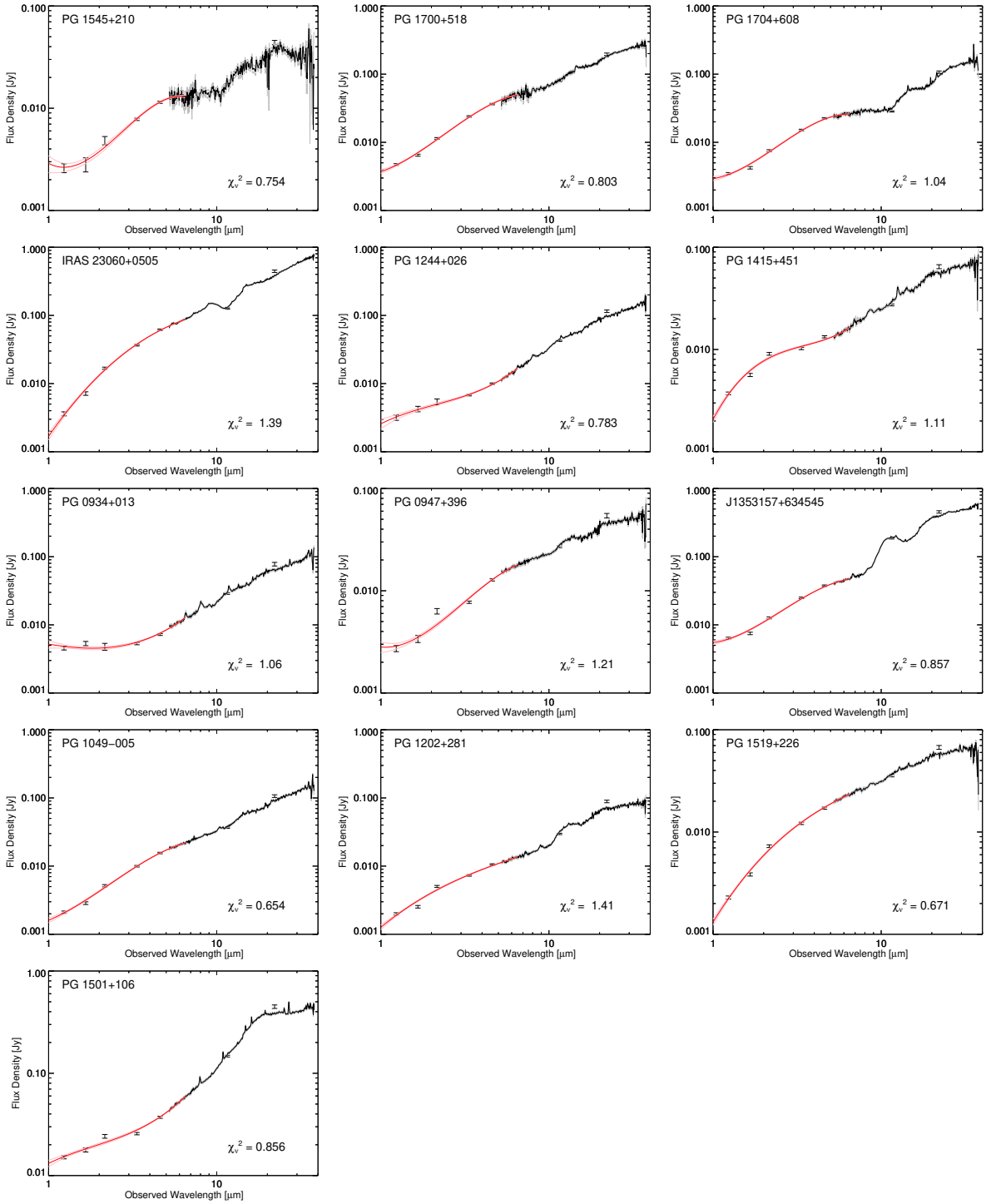

Figure 4.5: The spectrum of each U/LIRG used as a red standard object. Points with error bars represent the flux densities derived from the 2MASS and *WISE* magnitudes with the color correction considered. Black solid line and the accompanying gray lines denote the *Spitzer*/IRS spectrum and its uncertainty, respectively. The IRS spectrum is rescaled so that it fit to the *WISE* $W3$ and $W4$ bands. Red solid line and the accompanying light-red lines indicate the fitted cubic function and 1σ fitting error, respectively, which was used as the model spectrum in the calibration. The goodness of fit $\chi^2_\nu \equiv \chi^2/\mathrm{dof}$ is shown in the right bottom corner.

Table 4.4: Observations of U/LIRGs used as red standard objects

Phase	Pair ID[a]	Object	Obs. ID	Date	Temp. (K)[b]
3-1	1	PG 1545+210	1340496.1	2008 Aug 11	41.26 ± 0.03
			1340496.2	2008 Aug 11	41.36 ± 0.08
	2	PG 1700+518	1340465.1	2008 Aug 15	41.33 ± 0.01
			1340465.3	2008 Aug 17	41.36 ± 0.01
			1340465.2	2008 Aug 17	41.39 ± 0.01
	3	PG 1704+608	1340493.2	2008 Jul 23	41.43 ± 0.02
			1340493.3	2008 Jul 23	41.48 ± 0.01
			1340493.1	2008 Jul 23	41.49 ± 0.06
	4	IRAS 23060+0505	1120005.1	2008 Jun 11	41.50 ± 0.02
	5	PG 1244+026	1340529.1	2008 Jun 30	41.65 ± 0.05
			1340529.2	2008 Jun 30	41.67 ± 0.06
3-2	1	IRAS 23060+0505(1)	1120005.2	2008 Dec 11	42.81 ± 0.04
	2	IRAS 23060+0505(2)	1120005.3	2008 Dec 11	42.89 ± 0.04
	3	PG 1415+451	1340542.1	2008 Dec 29	43.22 ± 0.02
	4	PG 1244+026	1340529.3	2008 Dec 31	43.25 ± 0.03
3-3	1	PG 0934+013	1340513.2	2009 May 17	45.07 ± 0.02
			1340513.1	2009 May 17	45.09 ± 0.06
	2	PG 0947+396	1341144.1	2009 Nov 7	45.07 ± 0.02
			1341144.3	2009 Nov 7	45.07 ± 0.03
			1341144.2	2009 Nov 7	45.10 ± 0.03
	3	J1353157+634545	1920191.2	2009 May 26	45.13 ± 0.02
			1920191.1	2009 May 26	45.16 ± 0.04
	4	PG 1049−005	1340501.2	2009 Jun 4	45.35 ± 0.04
			1340501.1	2009 Jun 4	45.41 ± 0.04
			1340501.3	2009 Jun 4	45.41 ± 0.02
	5	PG 1202+281	1341158.1	2009 Dec 11	45.41 ± 0.02
	6	PG 1519+226	1340549.3	2009 Aug 3	45.61 ± 0.01
			1340549.1	2009 Aug 2	45.64 ± 0.02
			1340549.2	2009 Aug 3	45.64 ± 0.03
	7	PG 1501+106	1340548.1	2009 Aug 2	45.61 ± 0.02
			1340548.2	2009 Aug 2	45.63 ± 0.02
			1340548.3	2009 Aug 2	45.64 ± 0.03
	8	PG 1415+451	1340542.2	2009 Jun 28	46.49 ± 0.03
			1340542.3	2009 Jun 28	46.50 ± 0.02

[a] The ID attached to each pair of standard objects (corresponding to Table 4.5).
[b] Detector temperature. Also plotted in Figure 4.1

Table 4.5: Observations of stars used as blue standard objects

Phase	Pair ID[a]	Object	Type	Obs. ID	Date	Temp. (K)[b]
3-1	1	KF09T1(1)	K0 III	5200086.1	2008 Aug 5	40.91 ± 0.16
				5200086.2	2008 Aug 9	41.21 ± 0.02
				5200016.1	2008 Jun 7	41.36 ± 0.03
				5200086.3	2008 Aug 14	41.37 ± 0.02
				5200038.14	2008 Jul 23	41.43 ± 0.04
				5200086.4	2008 Aug 17	41.44 ± 0.03
				5200086.7	2008 Aug 28	41.47 ± 0.04
				5200038.4	2008 Jul 7	41.50 ± 0.04
				5200086.5	2008 Aug 22	41.50 ± 0.02
				5200016.2	2008 Jun 14	41.51 ± 0.03
				5200086.6	2008 Aug 25	41.52 ± 0.01
				5200288.1	2008 Sep 2	41.54 ± 0.07
				5200038.12	2008 Jul 15	41.55 ± 0.04
				5200038.5	2008 Jul 7	41.56 ± 0.01
				5200038.13	2008 Jul 16	41.56 ± 0.01
				5200288.2	2008 Sep 7	41.56 ± 0.02
				5200038.3	2008 Jul 6	41.57 ± 0.02
				5200038.8	2008 Jul 10	41.57 ± 0.04
				5200016.4	2008 Jun 30	41.58 ± 0.02
				5200038.9	2008 Jul 12	41.58 ± 0.02
	2	KF09T1(2)	K0 III	5200038.6	2008 Jul 8	41.59 ± 0.01
				5200038.2	2008 Jul 5	41.60 ± 0.02
				5200038.1	2008 Jul 3	41.61 ± 0.03
				5200038.10	2008 Jul 13	41.62 ± 0.02
				5200038.7	2008 Jul 9	41.63 ± 0.02
				5200038.11	2008 Jul 13	41.64 ± 0.01
				5200288.3	2008 Sep 10	41.71 ± 0.01
				5200288.5	2008 Sep 16	41.71 ± 0.04
				5200288.8	2008 Sep 29	41.80 ± 0.02
				5200327.1	2008 Oct 2	41.82 ± 0.01
				5200288.4	2008 Sep 13	41.83 ± 0.02
				5200288.7	2008 Sep 24	41.86 ± 0.03
				5200327.2	2008 Oct 5	41.88 ± 0.04
				5200327.4	2008 Oct 14	41.91 ± 0.02
				5200327.3	2008 Oct 10	41.93 ± 0.05
				5200288.6	2008 Sep 21	41.94 ± 0.10
				5200327.7	2008 Oct 26	41.97 ± 0.02
				5200327.5	2008 Oct 19	41.98 ± 0.02
				5200327.6	2008 Oct 23	41.99 ± 0.01
				5200327.8	2008 Oct 29	42.00 ± 0.02
	3	KF03T2	K1.5 III	5200313.1	2008 Oct 7	41.83 ± 0.02
				5200313.2	2008 Oct 7	41.83 ± 0.06
	4	KF03T1	K0 III	5200312.2	2008 Oct 6	41.81 ± 0.03
				5200312.1	2008 Oct 6	41.89 ± 0.03
	5	TYC 4212-455-1	A3 V	5200311.1	2008 Oct 6	41.85 ± 0.01
				5200311.2	2008 Oct 6	41.86 ± 0.04

Table 4.5: (*Continued*)

Phase	Pair ID[a]	Object	Type	Obs. ID	Date	Temp. (K)[b]
3-2	1	KF03T1	K0 III	5200403.1	2008 Nov 19	42.44 ± 0.01
	2	KF03T2	K1.5 III	5200457.1	2008 Dec 19	42.94 ± 0.08
				5200457.2	2008 Dec 21	43.07 ± 0.02
	3	KF01T4	K1.5 III	5200459.2	2009 Jan 4	43.33 ± 0.04
				5200459.1	2009 Jan 4	43.37 ± 0.02
	4	KF09T1	K0 III	5200402.1	2008 Nov 7	42.06 ± 0.06
				5200397.1	2008 Nov 5	42.12 ± 0.02
				5200397.2	2008 Nov 11	42.27 ± 0.02
				5200397.3	2008 Nov 18	42.39 ± 0.02
				5200397.4	2008 Nov 23	42.46 ± 0.07
				5200397.5	2008 Nov 30	42.59 ± 0.02
				5200533.1	2008 Dec 6	42.76 ± 0.02
				5200533.2	2008 Dec 12	42.80 ± 0.07
				5200533.3	2008 Dec 18	43.02 ± 0.02
				5200533.4	2008 Dec 24	43.07 ± 0.07
				5200458.1	2008 Dec 27	43.20 ± 0.04
				5200458.2	2008 Dec 29	43.24 ± 0.03
				5200533.8	2009 Jan 20	43.29 ± 0.02
				5200533.5	2008 Dec 30	43.30 ± 0.04
				5200533.9	2009 Jan 26	43.30 ± 0.02
				5200701.1	2009 Feb 1	43.34 ± 0.07
				5200533.6	2009 Jan 5	43.38 ± 0.06
				5200701.2	2009 Feb 5	43.39 ± 0.02
				5200533.7	2009 Jan 11	43.40 ± 0.03
				5200701.3	2009 Feb 8	43.46 ± 0.02
				5200701.4	2009 Feb 15	43.46 ± 0.02
				5200701.5	2009 Feb 22	43.51 ± 0.01
				5200701.6	2009 Mar 1	43.58 ± 0.02
				5200701.7	2009 Mar 5	43.58 ± 0.01
				5200701.8	2009 Mar 16	43.87 ± 0.02
				5200701.11	2009 Mar 27	44.01 ± 0.06
				5200701.9	2009 Mar 19	44.02 ± 0.16
				5200701.10	2009 Mar 23	44.04 ± 0.02
				5200701.12	2009 Mar 30	44.11 ± 0.02
				5200756.1	2009 Apr 4	44.12 ± 0.01
				5200797.1	2009 Apr 6	44.17 ± 0.03
				5200756.2	2009 Apr 7	44.19 ± 0.01
				5200756.3	2009 Apr 10	44.28 ± 0.03
				5200756.4	2009 Apr 14	44.40 ± 0.06
3-3	1	KF09T1(1)	K0 III	5200756.5	2009 Apr 18	44.67 ± 0.03
				5200797.2	2009 Apr 18	44.70 ± 0.03
				5200797.3	2009 Apr 22	44.88 ± 0.02
				5200756.6	2009 Apr 23	44.98 ± 0.01
				5200756.9	2009 May 4	44.99 ± 0.07
				5200797.7	2009 May 2	45.01 ± 0.05
				5200756.11	2009 May 19	45.01 ± 0.04

Table 4.5: (*Continued*)

Phase	Pair ID[a]	Object	Type	Obs. ID	Date	Temp. (K)[b]
				5200756.10	2009 May 7	45.05 ± 0.08
				5200797.14	2009 May 23	45.08 ± 0.02
				5200797.8	2009 May 2	45.09 ± 0.03
				5200797.9	2009 May 3	45.09 ± 0.04
				5200797.10	2009 May 4	45.09 ± 0.02
				5200797.15	2009 May 29	45.09 ± 0.09
				5201280.2	2009 Nov 8	45.09 ± 0.01
				5201283.2	2009 Nov 16	45.09 ± 0.02
				5200756.12	2009 May 22	45.10 ± 0.06
				5200756.13	2009 May 26	45.10 ± 0.03
				5201277.1	2009 Oct 30	45.10 ± 0.01
	2	KF09T1(2)	K0 III	5201280.1	2009 Nov 8	45.10 ± 0.01
				5200797.4	2009 Apr 28	45.11 ± 0.08
				5201277.2	2009 Oct 30	45.11 ± 0.02
				5200756.8	2009 May 1	45.12 ± 0.02
				5200797.6	2009 May 1	45.12 ± 0.02
				5200797.11	2009 May 4	45.12 ± 0.03
				5200797.12	2009 May 5	45.12 ± 0.06
				5201280.3	2009 Nov 8	45.12 ± 0.02
				5200797.13	2009 May 7	45.13 ± 0.01
				5201283.1	2009 Nov 16	45.14 ± 0.03
				5200756.7	2009 Apr 27	45.15 ± 0.03
				5201277.3	2009 Oct 31	45.15 ± 0.01
				5201283.3	2009 Nov 16	45.15 ± 0.02
				5200797.5	2009 Apr 29	45.16 ± 0.02
				5201286.2	2009 Nov 23	45.16 ± 0.02
				5201286.3	2009 Nov 23	45.17 ± 0.05
				5201286.1	2009 Nov 22	45.20 ± 0.03
				5200797.16	2009 May 30	45.22 ± 0.02
	3	KF01T4	K1.5 III	5201219.1	2009 Oct 25	45.12 ± 0.04
				5201219.3	2009 Oct 27	45.16 ± 0.03
				5201219.2	2009 Oct 27	45.20 ± 0.05
	4	KF09T1(3)	K0 III	5200756.14	2009 May 30	45.24 ± 0.01
				5200797.17	2009 May 31	45.25 ± 0.02
				5201274.3	2009 Oct 20	45.25 ± 0.02
				5201274.1	2009 Oct 20	45.26 ± 0.03
				5201289.1	2009 Nov 28	45.27 ± 0.02
				5201289.2	2009 Nov 28	45.28 ± 0.02
				5200920.1	2009 Jun 1	45.29 ± 0.03
				5201274.2	2009 Oct 20	45.29 ± 0.03
				5201289.3	2009 Nov 28	45.32 ± 0.02
				5200920.2	2009 Jun 4	45.38 ± 0.03
				5200920.3	2009 Jun 6	45.44 ± 0.02
				5201271.3	2009 Oct 14	45.44 ± 0.02
				5201271.1	2009 Oct 13	45.50 ± 0.03
				5201271.2	2009 Oct 13	45.50 ± 0.02
				5201496.1	2009 Dec 17	45.51 ± 0.02

Table 4.5: (*Continued*)

Phase	Pair ID[a]	Object	Type	Obs. ID	Date	Temp. (K)[b]
				5200920.4	2009 Jun 8	45.53 ± 0.02
				5201496.3	2009 Dec 18	45.54 ± 0.06
				5201496.2	2009 Dec 17	45.55 ± 0.03
	5	KF09T1(4)	K0 III	5200920.5	2009 Jun 10	45.57 ± 0.05
				5200920.28	2009 Jul 30	45.57 ± 0.04
				5200920.6	2009 Jun 10	45.59 ± 0.04
				5201170.3	2009 Aug 2	45.60 ± 0.02
				5201173.1	2009 Aug 4	45.60 ± 0.02
				5201173.2	2009 Aug 4	45.60 ± 0.03
				5201170.1	2009 Aug 2	45.61 ± 0.02
				5201170.2	2009 Aug 2	45.61 ± 0.02
				5201173.3	2009 Aug 4	45.61 ± 0.11
				5200920.26	2009 Jul 29	45.64 ± 0.02
				5200920.25	2009 Jul 28	45.65 ± 0.04
				5201182.3	2009 Sep 22	45.65 ± 0.06
				5200920.7	2009 Jun 11	45.66 ± 0.02
				5201182.1	2009 Sep 21	45.66 ± 0.02
				5201455.2	2009 Dec 25	45.66 ± 0.02
				5200920.27	2009 Jul 30	45.67 ± 0.02
				5200920.29	2009 Jul 31	45.69 ± 0.04
				5201182.2	2009 Sep 22	45.69 ± 0.02
	6	KF03T4	K1 III	5201220.2	2009 Oct 29	45.07 ± 0.05
				5201220.3	2009 Oct 30	45.11 ± 0.05
				5201220.1	2009 Oct 29	45.25 ± 0.11
				5201457.2	2009 Dec 11	45.43 ± 0.03
				5201457.3	2009 Dec 12	45.47 ± 0.03
				5201457.1	2009 Dec 11	45.48 ± 0.02
				5201458.1	2010 Jan 7	45.79 ± 0.09
				5201458.3	2010 Jan 13	45.86 ± 0.02
				5201458.2	2010 Jan 10	45.91 ± 0.02
				5201524.2	2010 Feb 1	46.03 ± 0.08
				5201524.1	2010 Feb 1	46.04 ± 0.02
				5201524.3	2010 Feb 2	46.06 ± 0.02
	7	KF09T1(5)	K0 III	5201455.3	2009 Dec 25	45.70 ± 0.02
				5200920.24	2009 Jul 27	45.74 ± 0.04
				5201176.2	2009 Aug 14	45.75 ± 0.04
				5201176.3	2009 Aug 14	45.75 ± 0.07
				5201176.1	2009 Aug 14	45.76 ± 0.02
				5201179.1	2009 Aug 24	45.76 ± 0.03
				5201455.1	2009 Dec 24	45.76 ± 0.05
				5200920.23	2009 Jul 25	45.78 ± 0.02
				5201179.2	2009 Aug 24	45.78 ± 0.02
				5201179.3	2009 Aug 24	45.79 ± 0.02
				5200920.8	2009 Jun 12	45.80 ± 0.05
				5200920.22	2009 Jul 23	45.81 ± 0.05
				5201499.1	2010 Jan 6	45.81 ± 0.02
				5201499.2	2010 Jan 6	45.83 ± 0.02

Table 4.5: (*Continued*)

Phase	Pair ID[a]	Object	Type	Obs. ID	Date	Temp. (K)[b]
				5201499.3	2010 Jan 6	45.84 ± 0.03
				5201502.3	2010 Jan 27	45.90 ± 0.07
				5200920.9	2009 Jun 15	45.91 ± 0.02
				5201502.1	2010 Jan 26	45.95 ± 0.02
	8	KF09T1(6)	K0 III	5201456.2	2010 Jan 28	45.98 ± 0.02
				5201502.2	2010 Jan 27	46.00 ± 0.01
				5201456.1	2010 Jan 26	46.01 ± 0.05
				5200920.21	2009 Jul 20	46.05 ± 0.03
				5201456.3	2010 Feb 1	46.06 ± 0.04
				5201636.1	2010 Feb 15	46.11 ± 0.05
				5201636.2	2010 Feb 15	46.18 ± 0.02
				5200920.20	2009 Jul 17	46.21 ± 0.04
				5200920.18	2009 Jul 14	46.25 ± 0.02
				5200920.19	2009 Jul 16	46.26 ± 0.04
				5200920.17	2009 Jul 12	46.34 ± 0.02
				5200920.11	2009 Jun 24	46.37 ± 0.04
				5200920.10	2009 Jun 22	46.39 ± 0.03
				5200920.12	2009 Jun 26	46.40 ± 0.08
				5200920.16	2009 Jul 10	46.43 ± 0.02
				5200920.13	2009 Jun 28	46.46 ± 0.02
				5200920.15	2009 Jul 7	46.54 ± 0.03
				5200920.14	2009 Jul 1	46.55 ± 0.04

[a] The ID attached to each pair of standard objects (corresponding to Table 4.4).
[b] Detector temperature. Also plotted in Figure 4.1

4.4.3 Temperature Dependence of Response Functions

From the results of the cryogenic phase and that of the Phase 3 wavelength calibration, it is certain that the second-order light contamination exists only at wavelengths longer than $\lambda^{(1)} > 4.9$ μm. For $\lambda^{(1)} > 4.9$ μm, we simultaneously calculated the spectral response functions against the first- and second-order light $R^{(1,2)}$ from each pair, by formulating Equation (3.5) for the two objects. For $\lambda^{(1)} < 4.9$ μm, we derived $R^{(1)}$ assuming $R^{(2)} = 0$ and using the star only because the standard stars had experienced other calibrations of such as 2MASS and *Spitzer*/IRS, and their templates had been better established than our model spectra of the U/LIRGs. We averaged the response curves obtained in each sub-phase after taking five-pixel smoothing and estimated its uncertainty from the standard deviation of the curves. The results of the three sub-phases are compared in Figure 4.6.

We cannot discuss the temperature dependence of the response curve for the second-order light from the right panel of Figure 4.6 because the results in the three phases have large uncertainty. On the contrary, the response curves for the first-order light certainly shows that the response has decreased with temperature during Phase 3. Moreover, the decrease appears not to have obvious wavelength dependence. To confirm this, we averaged the three response curves and derived the ratio of each response to the average. The obtained ratio is shown in

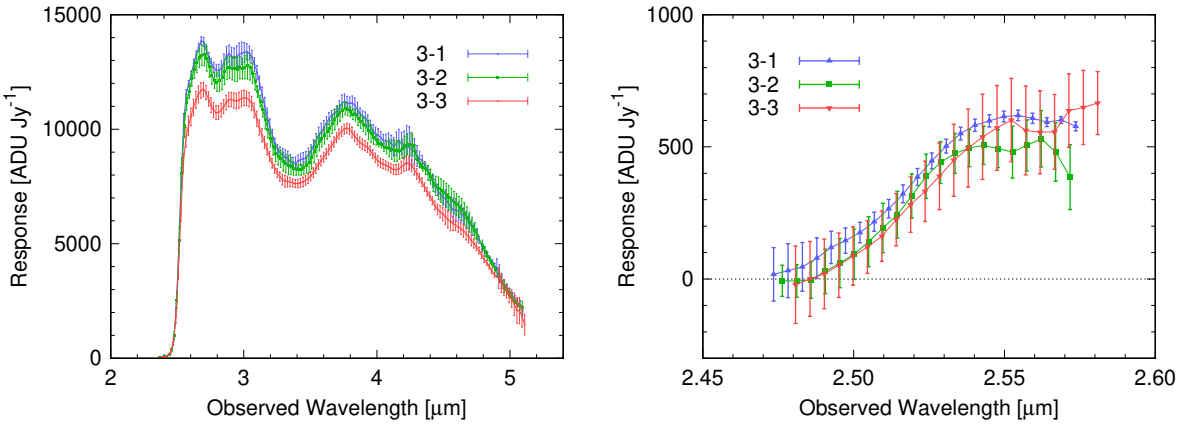

Figure 4.6: Spectral response curves in the three sub-pases. Left and right panels show the response from the first- and second-order light, respectively.

Figure 4.7. The averaged response curve appears in Figure 4.9 to be compared with the result of the cryogenic phase. Although there are large uncertainties in the response ratio around the ends of the observed range, in the bulk of the wavelength coverage, we cannot find any clear wavelength dependence. In each sub-phase, the level of the response ratio averaged in 2.5–4.7 μm, which is shown in a thick dot-dashed line in Figure 4.7, hits most of the points within the errors. We thus assume that the decrease of $R^{(1)}(\lambda)$ has no wavelength dependence.

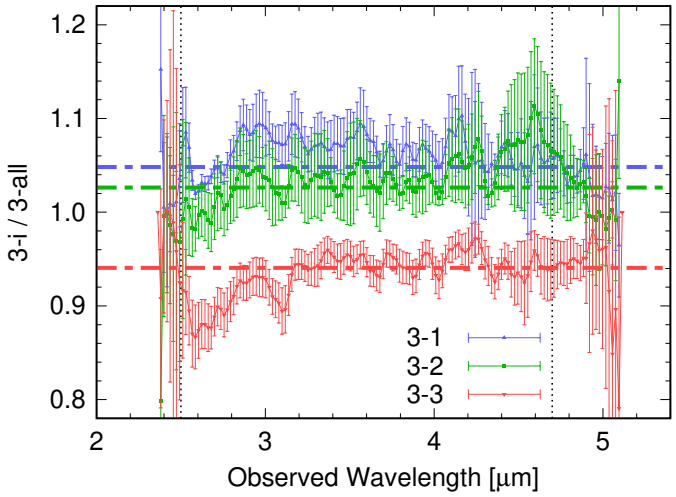

Figure 4.7: Ratio of the response in each sub-phase to the average of all sub-pases. Thick dot-dashed lines indicate the level of the response ratio averaged in the 2.5–4.7 μm range.

Figure 4.8 plots the level of the averaged response ratio against the average detector temperature of the observations used for the calibration. To derive a correction factor for the response decrease, we approximated it as a linear relation and fitted a function of the form of

$$f(T) = 1 + a(T - T_0), \tag{4.1}$$

to the three points in Figure 4.8. The obtained parameter values are,

$$\begin{cases} a = -0.0290 \text{ K}^{-1}, \\ T_0 = 43.55 \text{ K}. \end{cases} \tag{4.2}$$

The response decreasing rate a we found from the spectroscopic observations coincides the value derived from near-infrared photometric observation (Yamashita et al. in preparation). Thus the response decline can be attributed to the parts of the NIR channel shared in the spectroscopic and photometric modes. Because it is unlikely that the transmittance of the Si lenses had changed, the dominant cause of the decline should be the worsening of the detector sensitivity.

Users who want to reduce the data from a spectroscopic observation can adopt the averaged spectral response curve scaling it by the factor of $f(T)$. Although the temperature dependence of the spectral response for the second-order light is not trivial, we assume that it together scales with the same factor $f(T)$. This assumption would cause no practical problem because the variation of $f(T)$ during Phase 3 ($\sim 10\%$) is as small as the uncertainty of $R^{(2)}(\lambda)$ in each sub-phase. The analysis in Chapter 6 was conducted upon this assumption.

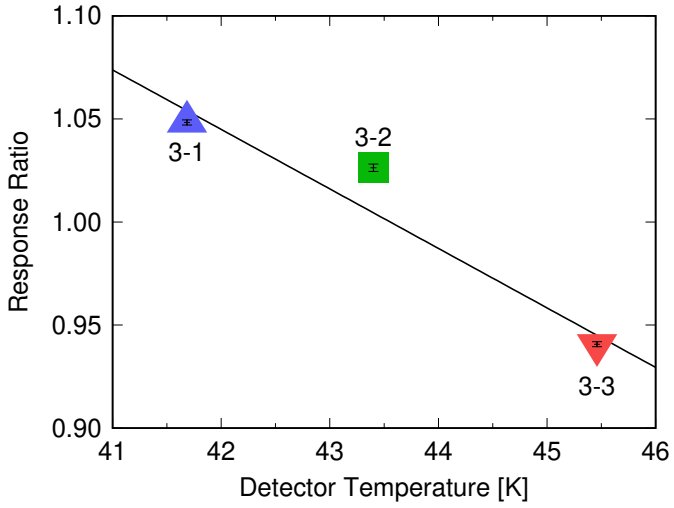

Figure 4.8: Plot of the averaged response ratio against the average detector temperature of the observations used for the calibration. Black solid line shows the linear function fitted to the three points and denotes the temperature correction factor expressed in Equations (4.1, 4.2).

4.4.4 Comparison with the cryogenic phase

The left panel of Figure 4.9 compares $R^{(1)}(\lambda)$ averaged among the three sub-phases and that obtained in the cryogenic phase. The relative shape of $R^{(1)}(\lambda)$ does not change from the cryogenic to post-cryogenic phase. This also justifies the assumption in the derivation of f(T). The absolute value of $R^{(1)}(\lambda)$ decreases by a factor of ~ 0.7, which represents the result of Onaka et al. (2009, Section 6.9.4).

The right panel of Figure 4.9 is the same comparison as the left panel but for $R^{(2)}(\lambda)$.

Contrast to $R^{(1)}$, $R^{(2)}$ decreases more than a factor of 0.7 from the cryogenic phase: it decreases by a factor of 0.52. This means that the relative strength of the second-order light contamination to the first-order light in the post-cryogenic phase is lower than that in the cryogenic phase by 25% if we observe the same object in both of the phases. This specific response decline around 2.5 μm is consistent to that found in the NP prism mode (Shimonishi et al. 2013). Figure 4.10 compares the prism-mode spectral response in the two phases and shows that the response at 2.5 μm had decreased more by 25% than those at the other wavelengths. This change has been explained as the lowering of the spectral resolution due to the degradation of the point-spread function in Phase 3 (Shimonishi et al. 2013; Onaka et al. 2009, Section 6.9.2). We here conclude that the change of the relative strength of the contamination in the grism mode was caused by the same reason: the degradation of the imaging performance at 2.5 μm.

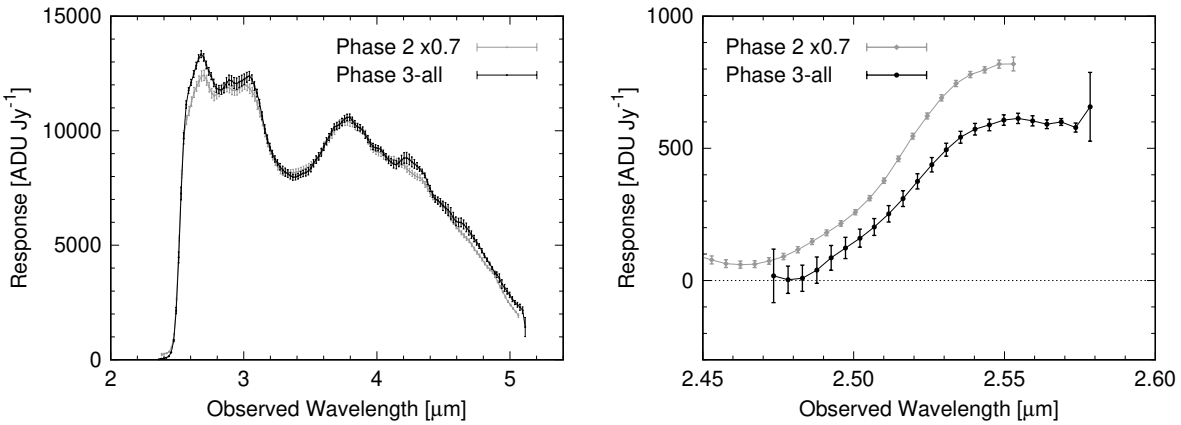

Figure 4.9: Comparison of the spectral responses in the cryogenic and post-cryogenic phases. The cryogenic response curves shown in Figure 3.10 are displayed being multiplied by a factor of 0.7.

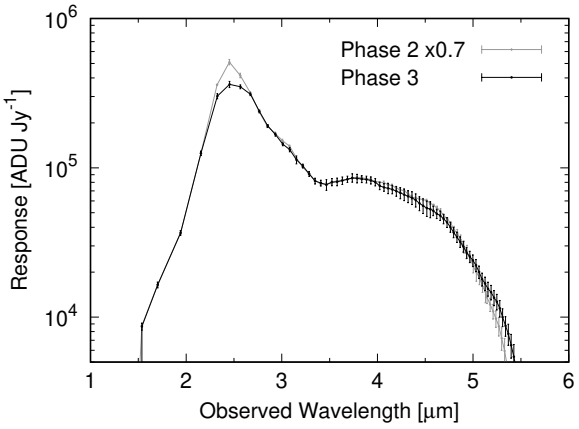

Figure 4.10: Comparison of the spectral response of the NP prism mode in the cryogenic and post-cryogenic phases presented by Shimonishi et al. (2013). The cryogenic curve is displayed being multiplied by a factor of 0.7

4.5 Summary

We carried out the correction for the second-order light contamination in the *AKARI* NIR grism spectroscopy scoping to the post-cryogenic phase (Phase 3). To assess the temperature dependence of the wavelength and spectral response calibrations, we defined three sub-phases, which correspond to different ranges of the detector temperature. Wavelength calibrations in the three sub-phases coincide with each other and do not show any temperature dependence. The final wavelength calibration curve obtained from the measurement of emission lines throughout Phase 3 confirms the presence of the second-order light contamination, similarly to Phase 1 and 2. It is shown that the spectral response from the first-order light had decreased by $\sim 10\%$ from the beginning to the end of the post-cryogenic phase. Based on the approximation that the decline of the response linearly relates to the temperature, a correction factor for the temperature dependence is obtained. The relative strength of the second-order light contamination to the first-order light is found to had lowered by 25% from the cryogenic phase. This change can be explained as the degradation of the point-spread function around 2.5 μm.

Chapter 5

The Near-Infrared CO Absorption Band as a Probe to the Innermost Part of an AGN Obscuring Material

The content of this chapter is based on the study published in the paper: Baba, S., Nakagawa, T., Isobe, N., and Shirahata, M. 2017, "The Near-Infrared CO Absorption Band as a Probe to the Innermost Part of an AGN Obscuring Material", The Astrophysical Journal, 852, 83.

As a preliminary investigation for systematic studies, we analyzed the 4.67 μm CO rovibrational absorption band profiles in selected ten luminous AGNs that had been known to show the feature in the *AKARI* and *Spitzer* spectra by fitting a plane-parallel local thermal equilibrium gas model. We found that CO gas is warm (200–500 K) and has a large column density ($N_{\rm H} \gtrsim 10^{23}$ cm^{-2}). The heating of the gas is not explicable by either UV heating or shock heating because these processes cannot represent the large column densities of the warm gas. Instead, X-ray photons from the nuclei, which can produce large columns of warm gas with up to $N_{\rm H} \sim 10^{24}$ cm^{-2}, are the most convincing power source. The hydrogen column density estimated from the CO band is smaller than that inferred from X-ray observations if the abundance of CO/H=10^{-4} is adopted. These results can be interpreted that the region probed by the near-infrared CO absorption is in the vicinity of the nuclei and is located outside the X-ray emitting region. Furthermore, the covering factors of nearly unity required by the observed deep absorption profiles suggest that the probed region is close to the continuum source, which can be designated as the inner rim of the obscuring material around the AGN.

5.1 Introduction

Active galactic nuclei (AGNs) show a wide diversity of observational characteristics in their spectra. AGN spectra differ primarily in terms of optical broad emission lines, the presence or absence of which are used to classify the AGNs as types 1 or 2, respectively. This dichotomy

has been attributed to a viewing angle effect caused by a putative AGN torus, an optically and geometrically thick torus-shaped dusty cloud that obscures direct emission from the nuclear region when the AGN is viewed edge-on (AGN unified model, Antonucci 1993). To understand the characteristics of AGNs, it is important to observe AGN tori and verify the AGN unified model. However, because of their small sizes on parsec scales, it is difficult to directly image AGN tori. Recent millimeter to sub-millimeter interferometric observations with the Atacama Large Millimeter Array of carbon monoxide (CO) pure rotational emission lines revealed the presence of gas concentrated near central nuclei (e.g., García-Burillo et al. 2016), but the highest spatial resolution that can be achieved with such observations is about several parsecs, even in the nearest AGNs. Thus, in distant galaxies millimeter and sub-millimeter emission lines are not suitable for resolving AGN tori from their hosts. An alternative observing method that can be applied to large numbers of AGNs is required.

The strategy we employ in this study is based on spectroscopy of the CO fundamental ro-vibrational absorption band centered at 4.67 μm ($v = 1 \leftarrow 0$, $\Delta J = \pm 1$). Using the bright near-IR radiation from the central region as the background continuum, this technique can observe foreground molecular gas clouds with an effectively high spatial resolution at the parsec scale because of to the compactness of the near-IR emitting region. Furthermore, because this band contains multiple lines with different rotation levels in a narrow wavelength range, it is possible to obtain information on the gas excitation state from one observation. In this respect, the near-IR CO absorption band is preferable to the (sub-)millimeter CO pure rotational emission lines, which are easily affected by contamination from the host galaxy and cannot be observed simultaneously.

As mentioned in Chapter 1, there are a few previous observations of the near-IR CO absorption. Geballe et al. (2006) and S13 observed the CO band toward the heavily obscured ULIRG IRAS 08572+3915 using UKIRT and Subaru, respectively, and detected strong absorption lines up to high rotational levels ($J \leq 17$). S04 observed another obscured ULIRG IRAS 00182−7112 with *Spitzer* and also detected strong CO absorption of high temperature. Based on the highly excited states, both authors argued that the observed gas should be in the vicinity of the dominant nuclear power source. S13 also proposed that the warm gas is heated by X-ray radiation from an AGN engine. The CO absorption, however, does not always appear in all type-2 AGNs. Lutz et al. (2004) observed nearby 12 type-2 AGNs with *ISO*, but none of them shows the CO feature. Lahuis et al. (2007) detected similar warm molecular gas toward obscured U/LIRGs through the mid-IR absorption bands of C_2H_2, HCN, and CO_2 but concluded that the gas is unlikely to be associated with the material surrounding AGNs because these molecules would be rapidly destroyed in an intense X-ray field. The two above studies controvert the hypothesis that CO absorption probes warm gas near the central region.

To assess the location of the region probed by CO ro-vibrational absorption, in this study we analyzed space telescope observations of the CO feature toward ten nearby AGNs and compared the results with the results from other X-ray and mid-IR observations. Such a systematic analysis of the CO absorption profile had not previously been performed, although detection of the feature has been reported in some objects (Imanishi et al. 2008, 2010; Spoon et al. 2005). Together with

a description of observations and data reduction, the selection of our targets is explained in Section 5.2. The method used to analyze the CO absorption profile is described in Section 5.3, followed by presentation of results in Section 5.4. We discuss these results and compare them with other observations in Section 5.5 and, finally, we give our conclusion in Section 5.6.

5.2 Targets, Observations, and Data Reduction

We used spectroscopic observations carried out with the *AKARI* satellite (Murakami et al. 2007) and the *Spitzer Space Telescope* (Werner et al. 2004) to collect targets that show CO absorption. *AKARI* and *Spitzer* have near- and mid-IR spectrometers, respectively, which cover complementary redshift ranges. Because we were not able to obtain information on the longward continuum level over the CO absorption from the *AKARI* observations themselves, *Spitzer* data were used to complement the spectrum in longer wavelengths. For these sources, we scaled the two spectra using *WISE* catalog magnitudes as reference points. In the following, we describe in detail the observations and data reduction techniques and present the spectra of the targets.

5.2.1 *AKARI*

We searched AGNs showing CO absorption from the archival data of the *AKARI* mission program AGNUL (PI: Takao Nakagawa). The program conducted many spectroscopic observations of nearby AGNs and ULIRGs using the Infrared Camera (IRC) in the NG grism mode. Almost all of the observations were performed through a $1' \times 1'$ aperture, and thus constituted slitless spectroscopy. The NG grism mode covers a wavelength range from 2.5 to 5.0 μm. Although its spectral resolution in general depends on the spatial extent of the target, if it is a point source, the resolution can be given as $R = 33.3\lambda$, where λ is the observed wavelength in μm (Onaka et al. 2007; Ohyama et al. 2007). The redshift range within which it is possible to observe the band center of the CO feature is $z < 0.07$. The AGNUL program also carried out observations in another dispersion mode (NP), but we excluded these from our sample because the spectral resolution of that mode was insufficient for the following analysis. The observation period of the program is divided into two parts: a cryogenic phase and a post-cryogenic phase. In this study, we scoped only cryogenic observations, which had been calibrated better than the post-cryogenic observations. A study using post-cryogenic data will be presented in Chapter 6.

Under the above conditions, 50 ULIRGs were observed, eight of which are within $z < 0.07$. We found that the six ULIRGs listed in the upper part of Table 5.1 show CO absorption. The other two ULIRGs are Mrk 231 and IRAS 05189−2524, which are classified as Sy1 and Sy2, respectively (Veilleux et al. 1995). Table 5.1 also presents the redshift, optical classification, and IR and X-ray AGN signatures of the six CO ULIRGs. Although some of these are not classified as Seyferts, either IR or X-ray diagnostics suggest that they are AGN hosts, and we therefore assumed that all six ULIRGs harbor an AGN and used them as targets for analysis. IRAS 23128−5919 is a merging system with a nuclear separation of $5''$ (Duc et al. 1997). The southern nucleus of the galaxy was detected in hard X-rays with *Chandra* and believed to be an

obscured AGN based on the observed X-ray hardness ratio (Iwasawa et al. 2011).

Table 5.1: Basic target data

Group	Object	z	$\log L_{\rm IR}$	Optical	AGN Sign		Ref.
			($L_\odot$)	Class	IR	X-ray	
(1)	(2)	(3)	(4)	(5)	(6)	(7)	(8)
AKARI	IRAS 06035−7102	0.0797	12.2	LI	✓	···	1; 6, 7; —
	IRAS 08572+3915	0.0583	12.1	LI	✓	✓	2, 3; 7, 8; 9
	UGC 5101	0.0392	12.0	LI	✓	✓	3; 7, 8; 9
	Mrk 273	0.0373	12.2	Sy2	✓	✓	2, 3; 6, 7; 9
	IRAS 19254−7245	0.0616	12.1	Sy2	✓	✓	1, 4; 7, 8; 10
	IRAS 23128−5919	0.0448	12.0	H II/Sy2/LI	—	✓	1; 6; 9
Spitzer	IRAS 00182−7112	0.3270	12.9	LI	✓	✓	5; 8; 11
	IRAS 00397−1312	0.2617	13.0	H II	✓	—	2; 8; 12
	IRAS 00406−3127	0.3424	12.8	Sy2	✓	···	4; 7; —
	IRAS 13352+6402	0.2366	12.5	?	✓	···	—; 7; —

NOTE—Column 1: target group. Column 2: object name. Column 3: redshift taken from the PSCz catalog (Saunders et al. 2000). Column 4: logarithm of the infrared (8–1000 μm) luminosity in units of the solar luminosity $L_\odot$ derived from Sanders & Mirabel (1996): $L_{\rm IR} = 2.1 \times 10^{39} \times D_{\rm L}^2 \times (13.48 f_{12} + 5.16 f_{25} + 2.58 f_{60} + f_{100})$ erg s^{-1}, where $D_{\rm L}$ is the distance in Mpc, and f_{12}, f_{25}, f_{60}, and f_{100} are *IRAS* fluxes in Jy. In calculating $D_{\rm L}$, $H_0 = 70$ km s^{-1} Mpc^{-1}, $\Omega_{\rm m} = 0.3$, and $\Omega_\Lambda = 0.7$ are adopted. The *IRAS* fluxes are taken from Sanders et al. (2003), Kim & Sanders (1998), or the *IRAS* Faint Source Catalog Version 2.0. For objects having upper limits in the *IRAS* fluxes, we evaluated the upper and lower limits of $L_{\rm IR}$ by assuming an actual flux equal to the upper limit and a zero value, respectively. Those upper and lower limits are quite close, with a difference less than 0.16 dex. Ultimately, the average of the two limits was adopted. Column 5: optical spectral classification. "LI", "Sy2", "H II", and "?" denote LINER, Seyfert 2, H II galaxy, and no optical classification, respectively. Columns 6 and 7: IR and X-ray AGN signatures, respectively. Check: present. Dash: absent. Dots: no data. The IR signature is based on the low equivalent widths of the 3.3 and/or 6.2 μm PAH emissions. The X-ray signature is based on a hard photon index and/or strong iron K lines. Column 8: references for columns 5, 6, and 7 with semicolons as delimiters. 1: Duc et al. (1997). 2: Veilleux et al. (1999). 3: Veilleux et al. (1995). 4: Allen et al. (1991). 5: Armus et al. (1989). 6: Imanishi et al. (2010). 7: Sargsyan et al. (2011). 8: Imanishi et al. (2008). 9: Iwasawa et al. (2011). 10: Braito et al. (2009). 11: Nandra & Iwasawa (2007). 12: Nardini & Risaliti (2011).

Table 5.2 summarizes observational information obtained from *AKARI*/IRC. To correct for the second-order light contamination, we reduced raw data in the manner described in Chapter 3. One-dimensional raw spectra were extracted using the official IRC Spectroscopy Toolkit Version 20150331 in the standard manner. To minimize uncertainty in the wavelength calibration, the wavelength origin was adjusted from the value reported by the toolkit by a few pixels based on the positions of features such as the 3.3 μm PAH emission band, H I Brα and Brβ emission lines, and 4.26 μm CO_2 absorption band. The wavelength dependence of the refractive index of the grism material was included in the wavelength calibration. Contamination from the second-order light was correctly removed in the flux calibration.

The flux uncertainty at i-th pixel, $\delta F_{\nu,i}$, was evaluated from the uncertainty in the signal in ADU (δN) and that in the spectral response at the wavelength of the pixel (δR_i) based on Equations (3.9) and (A.1). The former uncertainty δN was common to all points and was measured as the sky fluctuation in the part of the two-dimensional spectral image other than the spectrum of the source. This is the standard way incorporated in the toolkit. The latter uncertainty δR_i was that determined in Chapter 3. The flux uncertainty was then obtained through the error propagation that $\delta F_{\nu,i}/F_{\nu,i} = \sqrt{(\delta N/N_i)^2 + (\delta R_i/R_i)^2}$. When subtracting the second-order light, for example k-th pixel in Equation (3.9), we calculated the uncertainty in the final flux as

$$\delta F_{\nu,i} = \sqrt{(\delta D_{k,k})^2 N_k^2 + (\delta D_{k,1})^2 N_1^2 + (\delta D_{k,2})^2 N_2^2 + (D_{k,k}^2 + D_{k,1}^2 + D_{k,2}^2)(\delta N)^2},$$

where δD is the uncertainty in the matrix elements in Equations (A.1) calculated from δR. Although in the above equation δN appears three times, since N_k, N_1, and N_2 are independent, it is not triple counting.

Because the southern and northern parts of IRAS 23128−5919 were barely resolved in the two-dimensional spectral image, we selectively extracted flux from the southern part, which is known to be an AGN host as mentioned above. IRAS 06035−7102, IRAS 08572+3915, Mrk 273, and IRAS 19254−7245 also have double disks or nuclei, which we were not able to resolve because they either have small separations or are aligned in the dispersion direction of the two-dimensional spectral images.

Table 5.2: *AKARI*/IRC observation log

Object	Observation ID	Observation Date
IRAS 06035−7102	1100130.1	2007 Mar 11
IRAS 08572+3915	1100049.1	2006 Oct 26
UGC 5101	1100134.1	2007 Apr 22
Mrk 273	1100273.1	2007 Jun 8
IRAS 19254−7245	1100132.1	2007 Mar 30
IRAS 23128−5919	1100294.1	2007 May 10

5.2.2 *Spitzer*

Spoon et al. (2005) reported that four ULIRGs observed with the Infrared Spectrometer (IRS) onboard *Spitzer* (Houck et al. 2004) show CO absorption. The lower part of Table 5.1 presents basic information on these four ULIRGs. These ULIRGs are, except for IRAS 00406−3127, not optically classified as Seyferts but show IR AGN signatures. Thus, we investigated these ULIRGs in addition to the *AKARI* targets. The *Spitzer* targets are systematically more luminous than the *AKARI* targets. Table 5.3 summarizes the *Spitzer*/IRS observational information and tabulates the observations used to complement the spectra of the *AKARI* targets.

The spectra around the CO absorption were obtained in the IRS SL2 mode, which covers

wavelengths from 5.21 to 7.56 μm with a spectral resolution $R = 16.5\lambda$ at a slit width of 3.″6 (IRS Instrument Team and Science User Support Team 2011). This wavelength range corresponds to the redshift range $z = 0.12$–0.62. The spectral resolution is lower than that of the *AKARI*/IRC NG mode but sufficient for the following analysis. The calibrated *Spitzer*/IRS spectra including flux uncertainties were downloaded from the IRS Enhanced Products on the *Spitzer* Heritage Archive.

Table 5.3: *Spitzer*/IRS observation log

Object	AOR Key	Observation Date
IRAS 06035−7102 W	4969728	2004 Apr 14
IRAS 08572+3915 NW	4972032	2004 Apr 15
UGC 5101	4973056	2004 Mar 23
Mrk 273	4980224	2004 Apr 14
IRAS 19254−7245 S	12256512	2005 May 30
IRAS 23128−5919 S	4991744	2004 May 11
IRAS 00182−7112	7556352	2003 Nov 14
IRAS 00397−1312	4963584	2004 Jan 4
IRAS 00406−3127	12258816	2005 Jul 11
IRAS 13352+6402	12258560	2005 Mar 20

5.2.3 Scaling to the *WISE* Photometry

Because the *AKARI*/IRC spectra of the *AKARI* targets lacked the longward part of the CO absorption owing to redshift, we supplemented them with *Spitzer*/IRS ones to estimate the longward continuum levels. To reduce the effect of the different aperture sizes of *AKARI* and *Spitzer*, we scaled the fluxes of the two spectra so that they match with the *WISE* photometry (Wright et al. 2010). The procedure was as follows. Profile-fit magnitudes were taken from the AllWISE catalog and converted into fluxes in Jy based on the zero magnitudes presented by Jarrett et al. (2011), with color corrections taken into account. The color correction factor for the $W1$ band was calculated by integrating the product of the $W1$ spectral response function and the relative shape of the *AKARI* spectrum, and those factors for the $W3$ and $W4$ bands were similarly obtained using the relative shape of the *Spitzer* spectrum. The $W2$ band flux cannot put clear constraint because the band protrudes from the *AKARI* wavelength coverage. We thus evaluated only the lower limit for the factor, which resulted in the flux upper limit. The *AKARI* spectrum was scaled so that its flux density at the isophotal wavelength of the $W1$ band ($\lambda_{\rm obs} = 3.35$ μm) hits the color-corrected $W1$ flux, and confirmed not to pass over the $W2$ upper limit. The *Spitzer* spectrum was scaled so that its flux densities at the $W3$ and $W4$ isophotal wavelengths ($\lambda_{\rm obs} = 11.56$, 22.09 μm) fit the corrected fluxes of the two bands.

After the scaling, the two spectra agreed well so that we were able to draw baselines smoothly (Section 5.3.1). The obtained combined spectra are shown in Figure 5.1. The resultant scaling

shifts from the original fluxes were mainly within 20%, although the shift for the *Spitzer* spectrum of IRAS 23128−5919 was +64%. This large shift can be attributed to the compensation of the flux from the northern nucleus, which did not fall in the *Spitzer* slit but blends into the *AKARI* spectral extraction.

While the original flux uncertainties of the *AKARI* and *Spitzer* spectra were propagated into the combined spectra, the scale factor uncertainties were not, because only the continuum-normalized spectra were used in the analysis described below. However, the uncertainty in the ratio between the two scale factors, which affects the determination of the longward continuum level from the *Spitzer* spectrum, should be treated as a systematic error. The largest uncertainty in the ratio of the two scale factors was obtained in IRAS 23128−5919, in which the uncertainty was ±0.11 out of 1.54. We estimate the systematic error stemming from this uncertainty in Section 5.4.

Figure 5.2 shows the *Spitzer* spectra of the four *Spitzer* targets. In contrast to the *AKARI* spectra of the *AKARI* targets, these spectra entirely cover the CO absorption within themselves. We did not apply any scaling to these spectra because the absolute fluxes were not important, as only the continuum-normalized spectra were used in the analysis.

5.3 Analysis

5.3.1 Continuum-Normalized Spectra

We normalized each spectrum around the CO absorption with a continuum level estimated as a cubic spline curve interpolated between the pivots at 4.15, 4.35, 5.10, and 5.40 μm. These pivots were taken so that they avoid the Brα line at 4.05 μm, CO_2 absorption at 4.26 μm, and PAH emissions at 5.27 and 5.70 μm (Smith et al. 2007). In IRAS 13352+6402, we instead used a quadratic continuum that passes over the remaining three pivots, as its spectrum did not cover wavelengths shorter than 4.21 μm. Figure 5.3 shows the adopted continuum curves and the resulting normalized spectra. In this figure, double-branched features are observed, with the branches at the long and short wavelength sides representing the P- and R-branches, respectively. The depth of the absorption is deep, and the width of each branch is broad ($\sim$ 0.2 μm) compared to that observed toward Sgr A* ($\sim$ 0.05 μm, Lutz et al. 1996). These characteristics suggest that the CO gas has a large column density and a high temperature of up to $\sim$ 500 K.

5.3.2 Gas-Model Fitting

We used the plane-parallel LTE gas model developed by Cami (2002) to analyze the absorption profile. For simplicity, we assume that the CO gas comprises of a single component with uniform number density, temperature, and turbulent velocity (velocity width). We did not include any isotopomers other than $^{12}C^{16}O$. The model gives the flux normalized to the background intensity, including the contribution of both the absorption by the gas and the thermal emission from the gas itself. Because the observed absorption profiles suggested high gas temperatures, to accurately take the relative contribution of the gas in emission compared to the continuum into

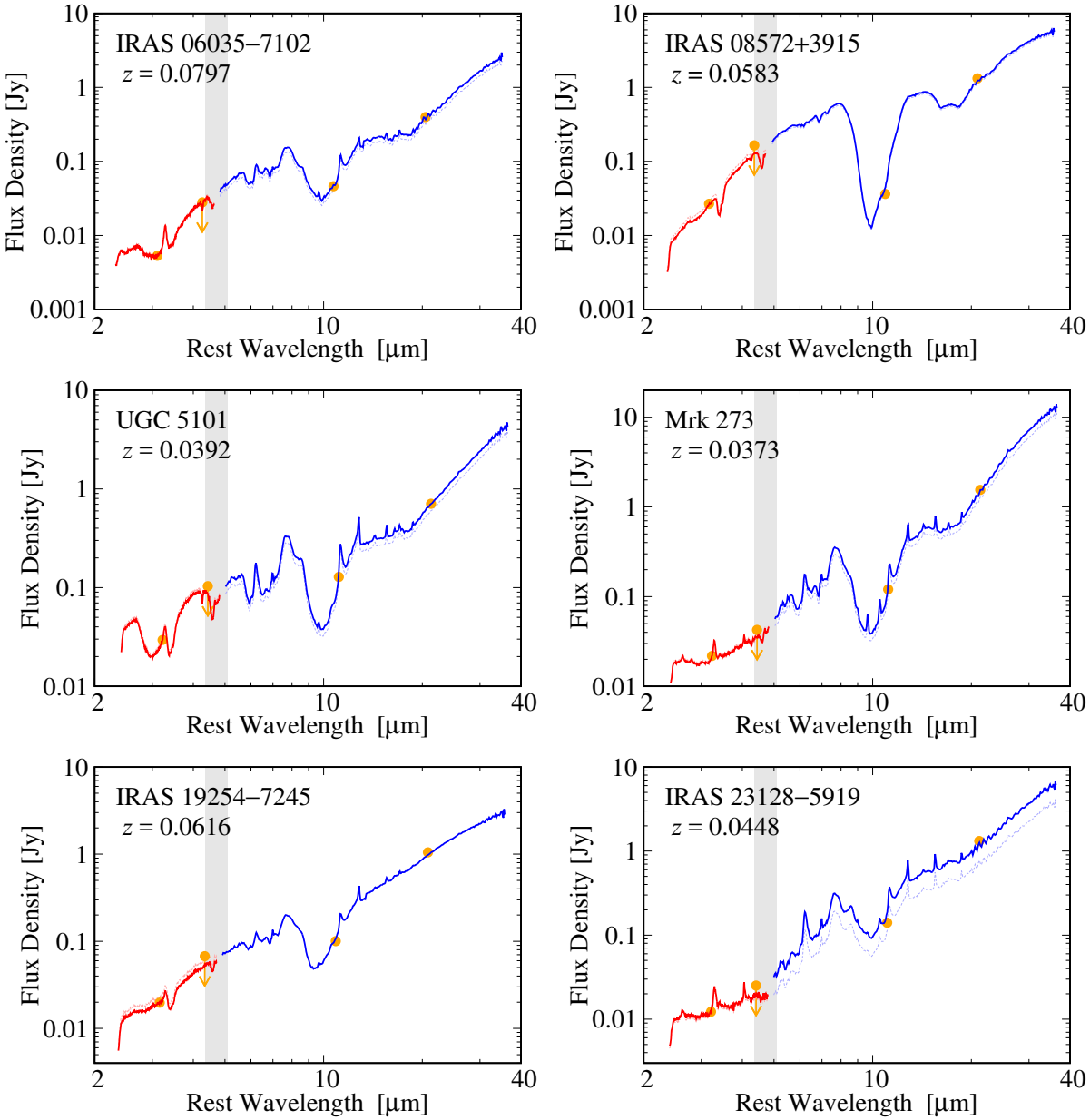

Figure 5.1: Combined spectrum of each *AKARI* target. Red and blue solid curves are the *AKARI*/IRC and *Spitzer*/IRS spectra scaled to match the *WISE* photometry, respectively (see text). Dashed lines in light colors, which are sometimes hidden behind the solid lines, are the original spectra before scaled. Orange filled circles represent the *WISE* photometric fluxes. The *AKARI* and *Spitzer* spectra are scaled so that they fit with the *WISE* points, but the $W2$ band (4.6 μm in the observed frame) flux shown with a downward arrow is used only as an upper limit. Gray shaded areas indicate the wavelength range in which the CO absorption appears.

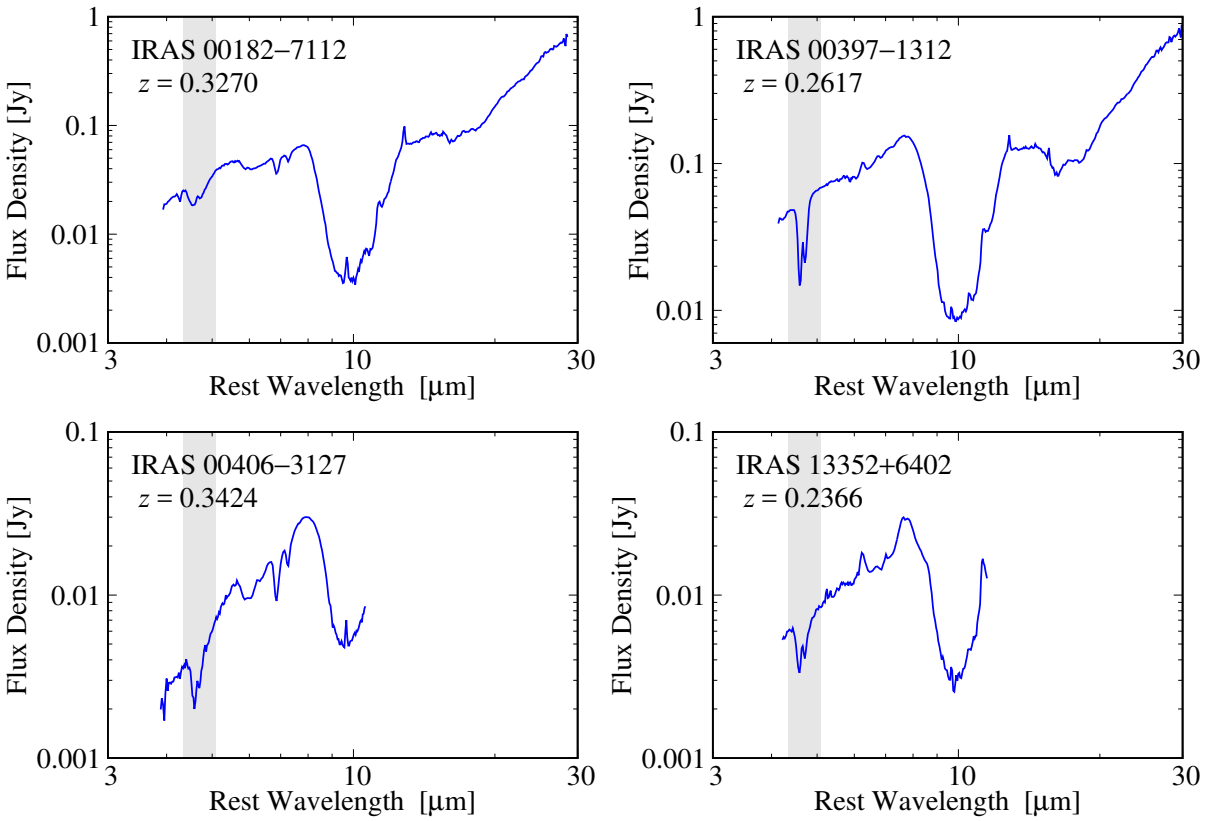

Figure 5.2: *Spitzer*/IRS spectrum of each *Spitzer* target (blue solid curves). Gray shaded areas indicate the wavelength range in which CO absorption appears.

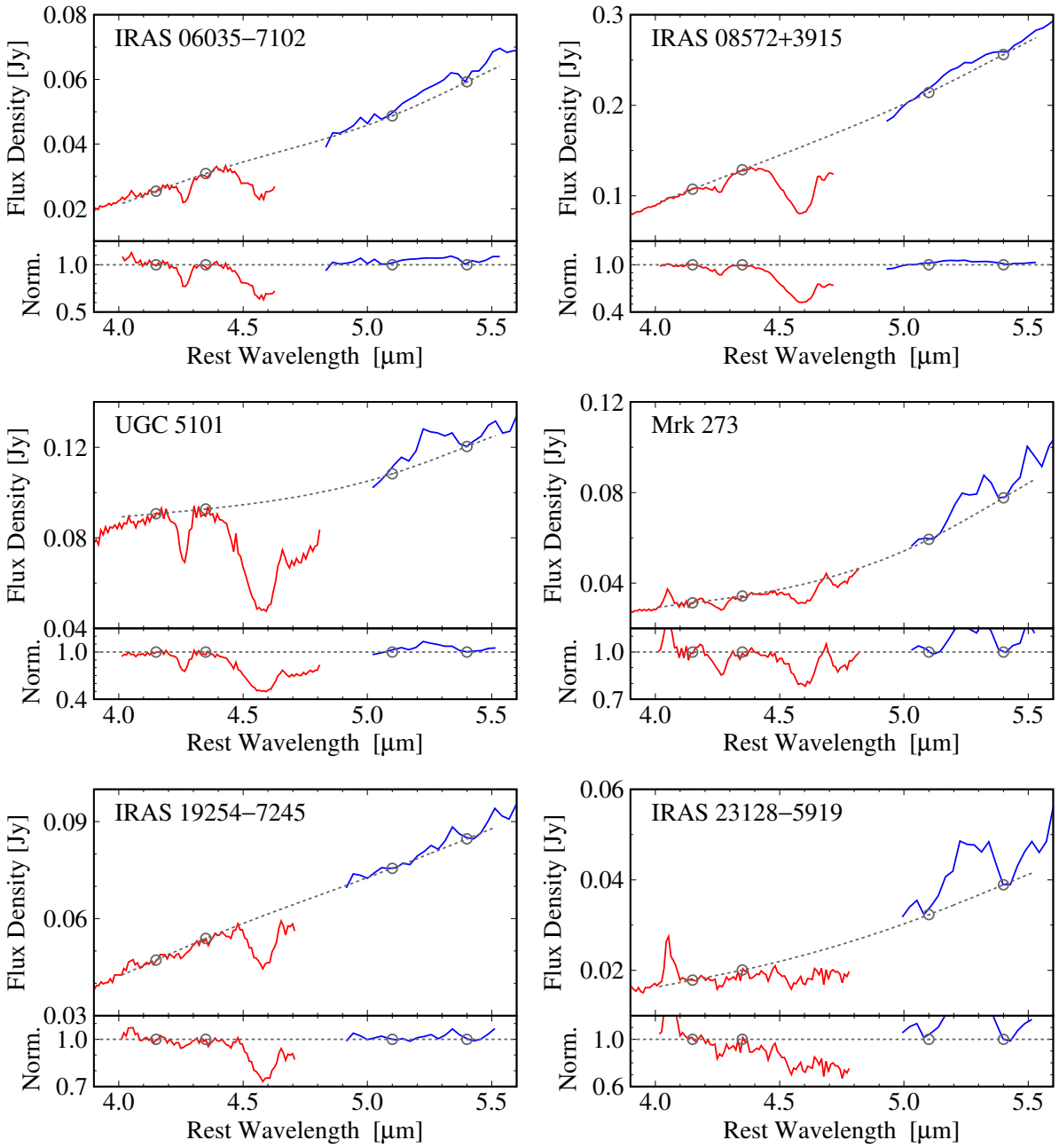

Figure 5.3: Continuum curves over the CO absorption (top) and continuum-normalized spectra (bottom). Red and blue curves are the *AKARI* and *Spitzer* spectra, respectively. Flux uncertainty is not shown here but is indicated in Figure 5.4. The continuum spectrum of each target (gray dotted line) is taken as a cubic spline curve that passes four pivots at 4.15, 4.35, 5.10, and 5.40 μm (gray open circles), except for IRAS 13352+6402, whose continuum is taken as a quadratic curve that passes the three pivots at longer wavelengths.

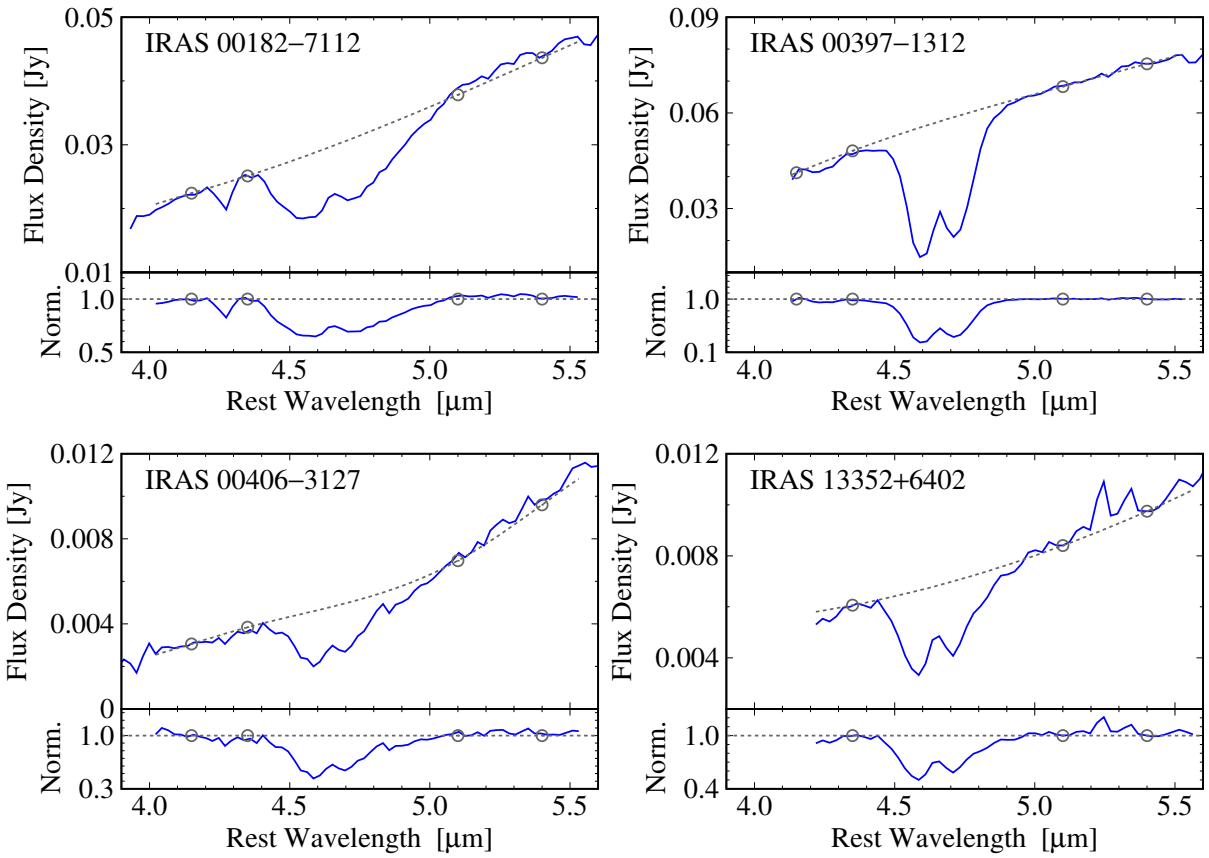

Figure 5.3: (*Continued*)

account, we needed to explicitly assume the temperature of the background radiation source. Assuming that the background continuum source is an optically thick hot dust sublimation layer, we set the continuum as a blackbody $I_{\nu,0} = B_\nu(T_{\rm BG})$ with a sublimation temperature $T_{\rm BG} = 1500$ K (Barvainis 1987). The intensity we observe, I_ν, is then the sum of the absorbed background, $I_{\nu,0}e^{-\tau_\nu}$, and the emission from the CO gas itself, $B_\nu(T_{\rm CO})(1 - e^{-\tau_\nu})$, where τ_ν is the optical depth of the CO gas, and $T_{\rm CO}$ is the gas temperature. Accordingly, the continuum-normalized intensity becomes

$$I_\nu/I_{\nu,0} = e^{-\tau_\nu} + \frac{B_\nu(T_{\rm CO})}{B_\nu(T_{\rm BG})}\left(1 - e^{-\tau_\nu}\right). \tag{5.1}$$

The optical depth for a transition $(v, J) = (0, J'') \rightarrow (1, J')$ at frequency ν_0 can be written as

$$\tau_\nu = N_{\rm CO}\frac{h\nu_0}{4\pi}g_{J''}B_{J''J'}\frac{e^{-E_{J''}/kT_{\rm CO}}}{Z(T_{\rm CO})}\left(1 - e^{-h\nu_0/kT_{\rm CO}}\right)\phi(\nu, \nu_0), \tag{5.2}$$

where $N_{\rm CO}$ is the total CO column density, $g_{J''} = (2J'' + 1)$ and $E_{J''}$ are the statistical weight and the energy level of the lower state, respectively, $B_{J''J'}$ is the Einstein coefficient of the transition, $Z(T_{\rm CO})$ is the partition function at $T_{\rm CO}$, and $\phi(\nu, \nu_0)$ is a line profile. We assumed a Gaussian profile for each transition with a common turbulent velocity $v_{\rm turb}$:

$$\phi(\nu, \nu_0) = \tfrac{1}{\sqrt{\pi}\Delta\nu_{\rm D}}e^{-(\nu-\nu_0)^2/\Delta\nu_{\rm D}^2}, \tag{5.3}$$

$$\Delta\nu_{\rm D} = \tfrac{v_{\rm turb}}{c}\nu_0. \tag{5.4}$$

From these equations, the intrinsic model spectrum can be parameterized by three variables: column density $N_{\rm CO}$, temperature $T_{\rm CO}$, and velocity width $v_{\rm turb}$.

We can fit the model (Equation (5.1)) to the data using $N_{\rm CO}$, $T_{\rm CO}$, and $v_{\rm turb}$ as free parameters. In the model calculation, we set the lower limit of the parameter range of $v_{\rm turb}$ to 10 km s^{-1} referring to the result of a similar gas model fitting for the CO band in IRAS 00182−7112 conducted by Spoon et al. (2004), who found $v_{\rm turb}$=50 km s^{-1}. Since the A coefficient of each transition is smaller than 35 s^{-1} (Goorvitch 1994), its natural width is more than 8 orders of magnitude narrower than the velocity width and thus negligible. In addition, we set the upper limit of $v_{\rm turb}$ to 300 km s^{-1}, where the FWHM of each line is comparable to the line spacing (~ 0.008 μm) between adjacent rotational levels. To represent instrumental spectral resolutions, intrinsic absorption spectra were convolved with a Gaussian of a dispersion of $0.03/(1 + z)$ μm for the *AKARI* targets and $0.06/(1 + z)$ μm for the *Spitzer* targets. The three parameters are somewhat degenerate with each other at such low resolutions since different rotational levels are not resolved, and the absorption spectrum is smoothed-out as a double-branched profile as observed in the previous subsection. Appendix B.1 explains how the parameters alter the absorption profile.

Because most of the targets show absorption dominated spectra, the contribution from emission lines within the CO band can be generally expected to be small. However, there is some concern. The Pfβ line at 4.65 μm may be superimposed over the CO absorption. The theo-

retical line ratio of Pfβ/Brα is 0.20 under the Case B condition, with $n_{\rm e} \sim 10^2$–10^7 cm^{-3} and $T_{\rm e} \sim$(3–30)$\times 10^3$ K (Storey & Hummer 1995). Considering the small equivalent width of the Brα line, we ignored the contribution from Pfβ in all the targets except for Mrk 273, in which the observed intensity near the CO band center exceeded unity. Yano et al. (in preparation) found that this galaxy shows an anomalous Brβ/Brα ratio in the *AKARI* spectrum. Accordingly, we attributed the high intensity to the effect of Pfβ and masked the data points within the $\pm 3\sigma$ wavelength range around that line assuming a line width at FWHM = 0.03 μm and excluded those points from the fitting process. There is no other H I line predicted to be stronger than the Pfβ line.

Another possible contamination is the molecular hydrogen pure-rotational line H_2 0–0 S(9) at 4.69 μm. We estimated its flux from those of H_2 0–0 $S(7)$ at 5.51 μm and $S(3)$ at 9.66 μm. We did not use the $S(6)$, $S(5)$, and $S(4)$ lines at 6.11, 6.91, and 8.03 μm, respectively, because they can be blended with PAH emissions. On the assumption that $J = 5$, 9, and 11 levels are in LTE, the $S(9)$ line peak is derived to be smaller than 4% of the continuum level at 4.69 μm in all the galaxies. We thus ignore the contribution of the $S(9)$ line.

There are some fine structure lines that possibly appear over the CO band: [Mg IV] 4.49 μm, [Ar VI] 4.53 μm, and [Na VII] 4.69 μm. These transitions start from high excitation stages of 80, 75, and 172 eV, respectively, and, in Seyfert galaxies, usually observed to be weaker than the [Mg V] 5.61 μm line, whose excitation potential is 109 eV (Lutz et al. 2000; Sturm et al. 2002). We did not significantly detect the [Mg V] line above the 3σ level in all the targets. Hence we ignored any contribution from the three lines.

5.4 Results

We derived the best-fit models using an iterative least-chi-square method and confirmed that they definitely provided the minimum χ^2 values through grid calculation. In the computation of the χ^2 values, uncertainties in the normalized flux of the data points were taken into account. In IRAS 00397−1312 and 13352+6402, because the observed data points appeared to be systematically displaced to shorter wavelengths from the best models we obtained at first, we manually shifted the points of the two galaxies by 0.009 and 0.010 μm, respectively, and then again fitted the model. These amounts are about the same as the wavelength calibration accuracy in the SL2 order of the IRS spectrum (0.008 μm RMS, IRS Instrument Team and Science User Support Team 2011). After this shifting, the reduced chi-squares for the two galaxies improved from 23.99 to 7.88 and from 7.14 to 3.39, respectively.

Figure 5.4 shows the best-fit CO gas model for each galaxy. The fitting process returned quite high reduced χ^2 values ($\chi^2_\nu \equiv \chi^2/{\rm dof}$). We consider that these poor fits originate from the difficulty in determining the continuum levels over the broad CO band. Some other possibilities concerning limitations of the current model are discussed in Section 5.5.1. We speculate that there is a systematic trend in which the observed flux in the red wing of the P-branch is higher than the model prediction; possible origins of this trend are also discussed in Section 5.5.1.

For mathematically correct treatment of the parameter errors of each galaxy, we posteriorly

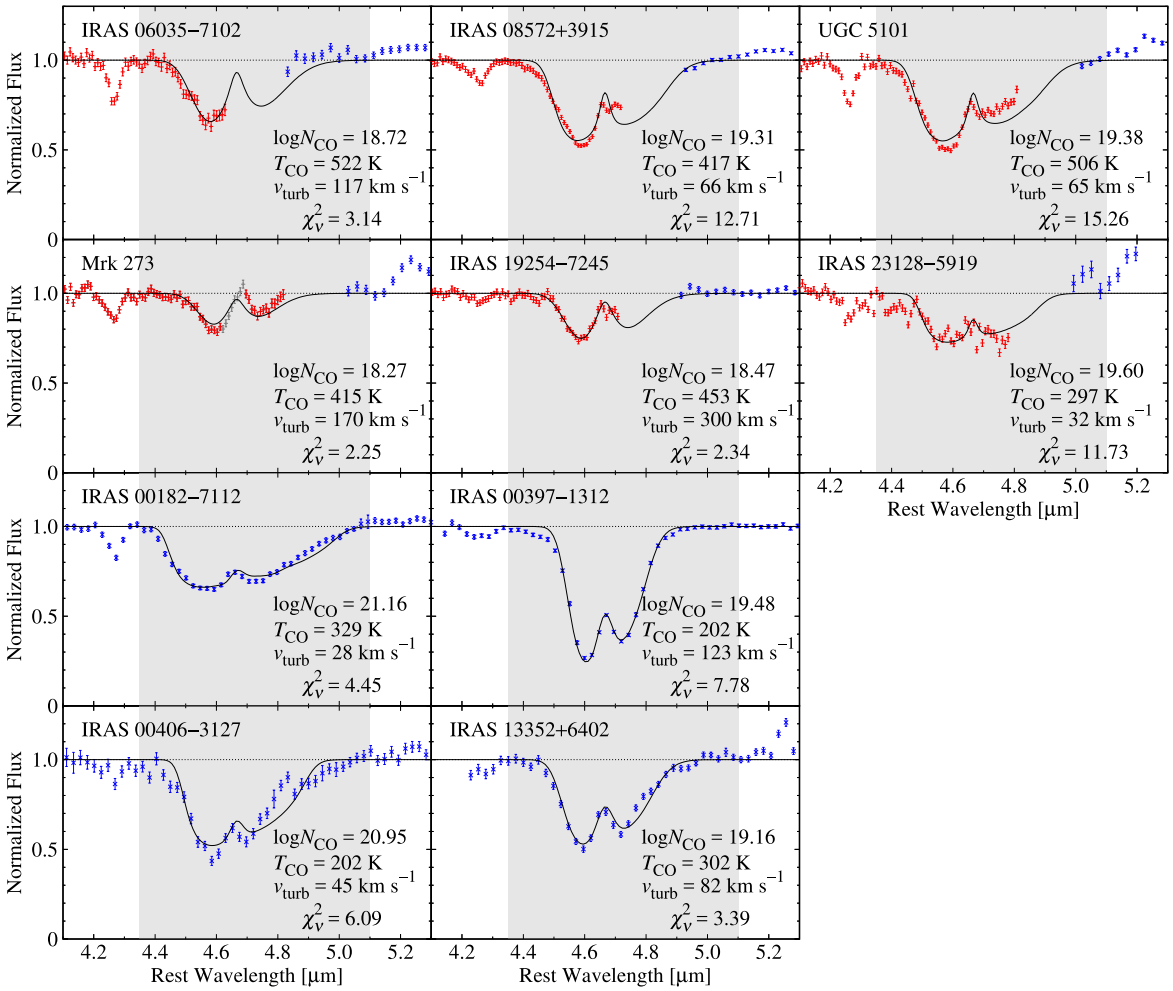

Figure 5.4: Results of the gas-model fitting obtained before the addition of $\sigma_{\rm sys}$. Black solid lines denote the best-fit CO absorption profiles. Red and blue points are data from the *AKARI*/IRC and *Spitzer*/IRS spectra, respectively. Gray shaded areas indicate the wavelength range used for the spectral fitting. Dark-gray points in the spectrum of Mrk 273 were excluded from the fitting to avoid the possible contribution from the Pfβ (4.65 μm) emission. The best-fit parameters and the goodness-of-fit $\chi^2_\nu \equiv \chi^2/{\rm dof}$ are noted at the right bottom corners.

added a common systematic error $\sigma_{\rm sys}$ to the statistical errors in the normalized flux σ_i shown in Figure 5.4 linearly ($\sigma_i \rightarrow \sigma_i + \sigma_{\rm sys}$) so that the resultant χ^2_ν reached close to unity. Table 5.4 tabulates $\sigma_{\rm sys}$ introduced and the best-fit parameters and their errors determined after the addition of $\sigma_{\rm sys}$. Figure 5.5 shows the new best-fit absorption profiles with their confidence ranges. A set of color maps of the $\Delta\chi^2$ value is shown in Appendix B.2. Hereafter, we use the numbers in Table 5.4 for discussion, otherwise noted. Among our targets, the CO absorptions in IRAS 00182−7112 and IRAS 08572+3915 were also analyzed by S04 and S13, respectively. Comparisons between their results and ours appear in Appendix B.3.

Table 5.4: Best-fit parameters and goodness of fit after the addition of $\sigma_{\rm sys}$

Object	$\sigma_{\rm sys}$	$\log N_{\rm CO}$ (in cm^{-2})	$T_{\rm CO}$ (K)	$v_{\rm turb}$ (km s^{-1})	χ^2/dof
IRAS 06035−7102	0.02	$18.73^{+0.17}_{-0.07}$	516^{+52}_{-71}	> 40	36.8/38
IRAS 08572+3915	0.03	$19.36^{+0.15}_{-0.12}$	420^{+36}_{-36}	62^{+7}_{-6}	43.8/43
UGC 5101	0.04	$19.48^{+0.22}_{-0.15}$	493^{+58}_{-59}	58^{+7}_{-7}	51.8/49
Mrk 273	0.01	$18.27^{+0.03}_{-0.03}$	414^{+44}_{-39}	> 44	43.9/42
IRAS 19254−7245	0.01	$18.46^{+0.05}_{-0.02}$	452^{+24}_{-27}	> 53	39.6/44
IRAS 23128−5919	0.05	> 18.85	302^{+92}_{-207}	33^{+8}_{-13}	42.2/48
IRAS 00182−7112	0.02	$21.19^{+0.74}_{-1.16}$	328^{+140}_{-51}	28^{+8}_{-3}	20.8/30
IRAS 00397−1312	0.02	$19.45^{+0.12}_{-0.10}$	204^{+13}_{-14}	124^{+14}_{-12}	21.7/28
IRAS 00406−3127	0.04	$20.92^{+1.23}_{-1.33}$	207^{+130}_{-58}	44^{+22}_{-5}	33.1/30
IRAS 13352+6402	0.02	$19.17^{+0.20}_{-0.13}$	302^{+31}_{-33}	80^{+19}_{-13}	21.0/28

NOTE—All errors represent the 68% confidence interval for one parameter of interest ($\Delta\chi^2 = 1$).

We found that the observed CO gas has a high temperature and large column density. The average $T_{\rm CO}$ is 360 K, which is far higher than the typical temperature of molecular gas in ordinary star-forming regions (10–10^2 K, Hollenbach & Tielens 1999). The logarithm of $N_{\rm CO}$ in units of cm^{-2} is on average 19.5,[1] which corresponds to a molecular hydrogen column density of $\log N_{\rm H_2} \sim 23.5$ if a CO abundance [CO]/[H$_2$] = 10^{-4} is adopted. This large column density can be converted to extinction at M-band (5 μm) of $A_M \sim 8$ if we assume $N_{\rm H} = 2N_{\rm H_2}$ and Galactic relations $N_{\rm H}/A_V = 1.9 \times 10^{21}$ cm^{-2} mag^{-1} (Bohlin et al. 1978) and $A_V/A_M \sim 40$ ($R_V = 3.1$, Draine 2003). Because we were able to observe CO gas absorption with this large column density, the extinction by dust must not be too high. This could suggest that the dust-to-gas ratio in AGN neighborhoods is lower than the Galactic value. Note that the estimate of A_M have a major uncertainty depending on the assumption of the abundance ratio. The ratio measured in Galactic objects differs in (0.8–3)$\times 10^{-4}$ (Dickman 1978; Frerking et al. 1982; Watson et al. 1985; Black et al. 1990; Lacy et al. 1994). There is no direct measurement of the CO abundance in ULIRGs, to our knowledge. The range of the abundance leads $3 < A_M < 10$.

For the results of the *AKARI* targets, we estimated the systematic error stemming from the

[1] Throughout this chapter, the logarithm of column density is presented in units of cm^{-2}.

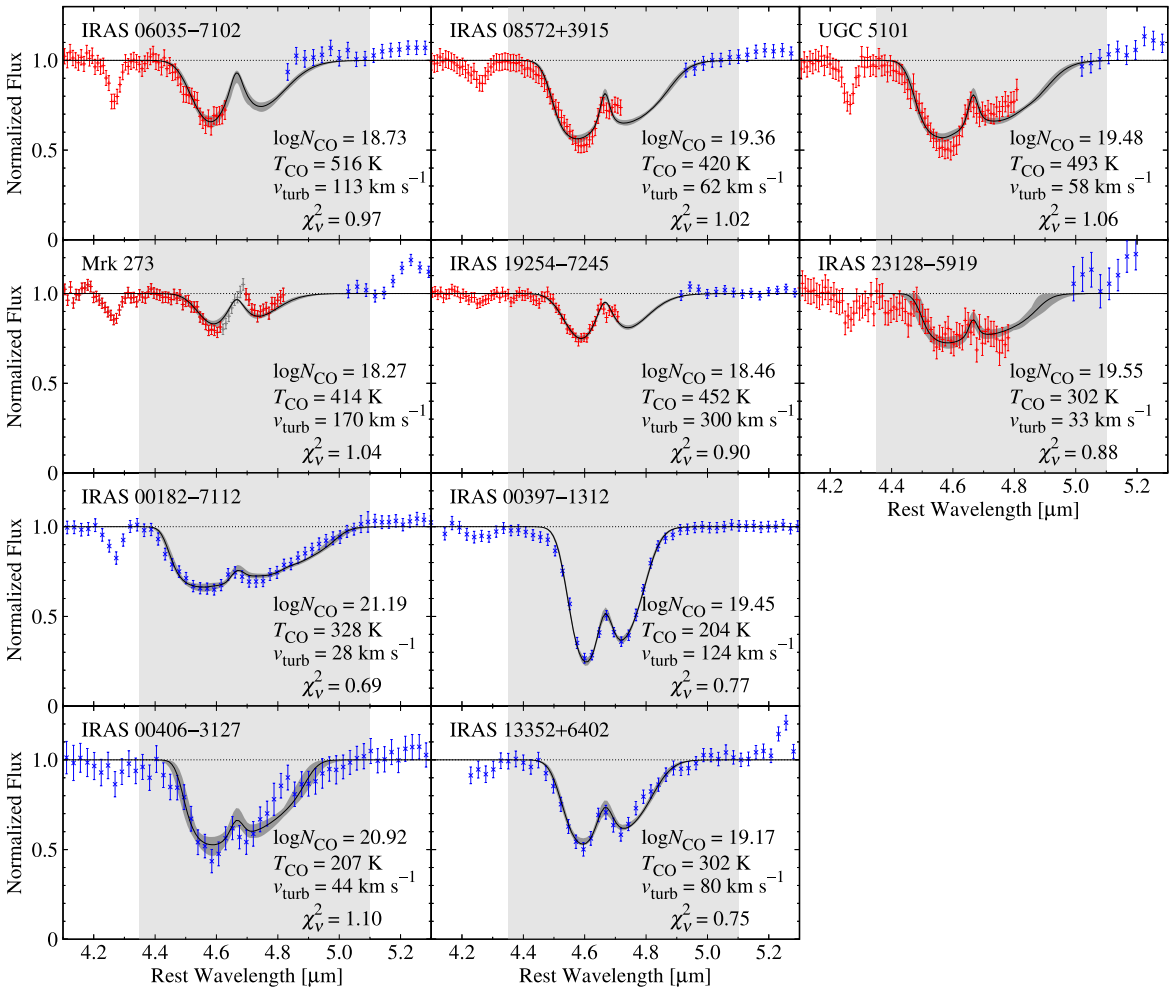

Figure 5.5: Results of gas-model fitting obtained after the addition of $\sigma_{\rm sys}$. The symbols are the same as in Figure 5.4, but here the gray-filled curves represent the 68% joint confidence range of the best-fit models.

scaling of the *AKARI* and *Spitzer* spectra. In IRAS 23128−5919, the ratio of the scaling factor for the *Spitzer* spectrum to that for *AKARI* was determined to be 1.54 ± 0.11; this uncertainty was the largest among all the *AKARI* targets (Section 5.2). Changing the amount of scaling by this uncertainty, the fitting result of this galaxy differs by $\Delta(\log N_{\rm CO}) \sim 0.2$, $\Delta T_{\rm CO} \sim 40$ K, $\Delta v_{\rm turb} \sim 2$ km s^{-1}. We therefore estimate that the systematic error is smaller than these values and conclude that this error does not affect the following discussion.

5.5 Discussion

5.5.1 Limitations of the Current Model

As the model simplifies the CO gas temperature to a uniform value, the results should be treated as first order approximations. Here, we note some effects that are not incorporated in the current approximation.

If there are two or more temperature components, the higher-temperature components will make the column density appear to be larger. Under the current spectral fitting, the band wings strictly constrain the solution. The higher-temperature components work to lower the flux in the band wings in an effect similar to that of increasing the column density (see also Appendix B.1). The high reduced χ^2 values we obtained in the fitting may therefore be the result of over simplification of multi-temperature components. Although this factor is of concern, given the quality of the *AKARI* and *Spitzer* spectra, it is difficult to fit a more complicated multi-temperature gas model.

If there is an optically-thin foreground dust screen in front of the CO gas, as shown Figure 5.6(a), its thermal radiation will fill up the absorption. The observed potential trend in the shallow red wing of the P-branch (Section 5.4) may be caused by this effect. Similarly, if the CO gas extends to a larger solid angle than the continuum source as shown in Figure 5.6(b), the band profile would be skewed, as the outer part of the CO gas contributes merely by emission without absorbing the background light. This effect can be quantified in terms of the area ratio, f, of the CO gas to the background source. We can introduce f into Equation (5.1) by multiplying it with the second term. The increase of the normalized flux density owing to f is larger at longer wavelengths because $B_\nu(T_{\rm CO})$ is redder than $B_\nu(T_{\rm BG})$ at 4.67 μm. This effect can also cause the systematic trend seen in the shallow red wing in the P-branch. However, if $T_{\rm CO} \sim 300$ K, f must be very large ($\sim 10^3$) because $B_\nu(T_{\rm CO})$ is at the Wien side at that wavelength. This effect would therefore appear not to fully explain the systematic trend.

We did not adopt any Doppler shifts into the modeled absorption. The implied systematic poor fit in the red wing in the P-branch can also be interpreted as blueshift from the systemic velocity. A shift of ~ 0.02 μm requires a velocity of ~ -1000 km s^{-1}. Such high-velocity molecular outflows have in fact been found in far-IR OH emission lines (e.g., Fischer et al. 2010; Spoon et al. 2013) and are comparable with column densities as large as $N_{\rm H} \sim 10^{23}$ cm^{-2} (González-Alfonso et al. 2017). Thus, the poor fit in the P-branch may be a signature of warm molecular outflows. However, such a conclusion from only the present broad blurred absorption profiles is not robust, and verification will require other observations at higher spectral

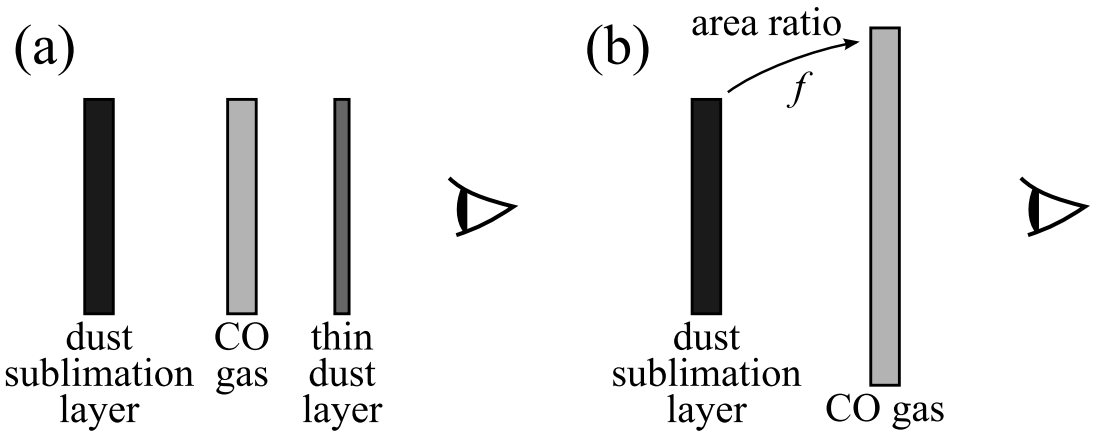

Figure 5.6: Two types of geometries beyond the model assumption. (a) Geometry in which another foreground thin dust layer is present. (b) Geometry in which the CO gas layer extends beyond the background dust sublimation layer with an area ratio f.

resolutions that can resolve different rotational levels.

Some other absorption bands possibly overlap the CO band. If present, ^{13}CO gas and CO ice features appear at wavelengths longer than the ^{12}CO gas band center. These would deepen the P-branch of the ^{12}CO profile, but this contribution is contrary to the observed pattern, suggesting that there is no signature of such features. On the other hand, the XCN ice feature, whose center is 4.62 μm and FWHM is 0.05 μm, possibly superimposes on the $R-$branch of the gas phase ^{12}CO band, as was observed in the starburst/AGN galaxy NGC 4945 (Spoon et al. 2003) and the starburst galaxy NGC 253 (Yamagishi et al. 2011). However, this ice band is narrower than the observed width of the CO R-branch and thus unlikely to mimic it. Although there are weak implications of such an additional narrow absorption at the peak of the branch in some targets such as UGC 5101 (Figure 5.5), we cannot rule out the possibility that the responsible absorber is not XCN ice but another, colder CO gas component.

As it is difficult to discuss the above effects in detail based on the present *AKARI* and *Spitzer* spectra, we do not further pursue them in this thesis.

5.5.2 Effect of the Assumption on the Dust Sublimation Temperature

In our model, we fixed $T_{\rm BG}$ to be 1500 K. Here we discuss the change in the results caused when a different temperature is adopted. Given that the maximum sublimation temperatures for silicate and graphite dust grains are 1400 and 1800 K, respectively (Netzer 2015), $T_{\rm BG}$ could change by a few times 10^2 K. Hence we performed the same model fitting at $T_{\rm BG}$=1400 and 1600 K. At $N_{\rm CO} < 10^{20}$ cm^{-2}, the resultant $\log N_{\rm CO}$, $T_{\rm CO}$, $v_{\rm turb}$ did not differ from the result at 1500 K by larger than 0.005, 1 K, 1 km s^{-1}, respectively. In the two galaxies of $N_{\rm CO} > 10^{20}$ cm^{-2}, IRAS 00182−7112 and IRAS 00406−3127, $\log N_{\rm CO}$ more largely changed by as large as 0.1, $T_{\rm CO}$ did by as large as 10 K, but those changes were smaller than 10% of the parameter errors obtained at 1500 K. Therefore, the uncertainty in the adopted value of $T_{\rm BG}$ does not critically affect the results.

5.5.3 Heating Mechanism

Our most important finding is that the observed CO gas has a high temperature and a large column density. The typical temperature $T_{\rm CO} \sim 400$ K is far higher than that of molecular gas in ordinary star-forming regions (10–10^2 K, Hollenbach & Tielens 1999). The typical column density $N_{\rm CO} \sim 10^{19}$ cm^{-2} corresponds to $N_{\rm H_2} \sim 10^{23}$ cm^{-2} if we assume an abundance ratio [CO]/[H_2] = 2×10^{-4} (Dickman 1978). Here, we consider what mechanism can heat the observed large columns of warm gas through a discussion of three candidates.

The first candidate heating source is ultraviolet (UV) photons emitted from the central accretion disk. An intense UV radiation field incident on a cloud forms a photon-dominated region (PDR) and determines its thermal and chemical structures. Several authors have modeled the PDR under various conditions (e.g., Tielens & Hollenbach 1985; Hollenbach & Tielens 1999). Meijerink & Spaans (2005) developed PDR models at four conditions specified by the combination of the gas number density ($n_{\rm H} = 10^3$ or $10^{5.5}$ cm^{-3}) and the incident far-UV flux ($G_0 = 10^3$ or 10^5). Here G_0 is a flux measure normalized at 1.6×10^{-3} erg cm^{-2} s^{-1} (Habing 1969). In all the cases except for the high-density and low-flux case ($n_{\rm H} = 10^{5.5}$ cm^{-3} and $G_0 = 10^3$), the maximum gas temperature exceeds 10^3 K, which is sufficiently higher than the observed values of $T_{\rm CO}$. However, in the models, the gas temperature afterward decreases steeply because of strong attenuation by dust and drops to 10^2 K before the column density $N_{\rm H}$ reaches 10^{22} cm^{-2}. Moreover, the CO abundance is suppressed in this PDR region due to photo-dissociation: the CO/C ratio is lower than unity at $N_{\rm H} < 10^{22}$ cm^{-2}. The achievable warm ($> 10^2$ K) CO column density is only $N_{\rm CO} \sim 10^{16}$ cm^{-2} and far smaller than the observed values ($\gtrsim 10^{18}$ cm^{-2}) by two orders of magnitude. This suggests that UV heating cannot represent the observed large columns of warm gas.

In the study of CO pure rotational emission lines, merely detecting high-J lines with a high excitation temperature does not rule out the possibility of PDRs as the origin of the emission (Mashian et al. 2015). Actually, Loenen et al. (2010) reproduced the spectral line energy distribution (SLED) of the starburst galaxy M82 up to $J = 12$ using only PDRs. However, the PDRs introduced in their analysis had column densities only on the order of $N_{\rm H} \sim 10^{21}$ cm^{-2}. In our observation of the fundamental CO ro-vibrational transition, the broad band width was equivalent to the detection of highly excited lines at $J \gtrsim 20$. More importantly, the obtained column density is too large ($N_{\rm H} \gtrsim 10^{22}$ cm^{-2}) to be reproduced by PDRs and requires other heating sources.

The next candidate is shock heating. Given that many of the observed galaxies are merging systems or in disturbed morphologies, it is reasonable to conjecture that their gas is powered by shocks arising from turbulent motion. A number of studies have discussed the physical and chemical processes in shock propagation in interstellar clouds (e.g., McKee et al. 1984; Hollenbach & McKee 1989; Neufeld & Dalgarno 1989). With a shock velocity of ~ 100 km s^{-1} and a pre-shock density of 10^4–10^6 cm^{-3}, the post-shock temperature structure begins with the initial value of $\gtrsim 10^4$ K, where the gas is heated by UV photons from the vicinity of the shock front. The temperature then gradually decreases until the UV radiation is sufficiently attenuated and molecular recombination becomes effective. After this point, OH molecules become the major

coolant and the gas temperature rapidly falls below $\sim 10^3$ K. This rapid drop is followed by an equilibrium between OH cooling and heating owing to H_2 formation on dust grains. CO rotational transitions also significantly contribute to cooling in this phase. Under this balance, the temperature remains at $\sim 10^2$ K until H_2 formation is completed.

Because the molecular-forming region downstream of a shock provides gas temperatures higher than 10^2 K, shock heating can explain observed T_{CO} values. On the other hand, the scale of the column density in the warm gas layer is $N_H \lesssim 10^{22}$ cm^{-2} and the CO relative abundance is nearly constant at $\sim 10^{-4}$ (Hollenbach & McKee 1989; Neufeld & Dalgarno 1989). Hence, shock heating can produce a warm CO gas with column densities of up to $N_{CO} \sim 10^{18}$ cm^{-2}. This upper bound is comparable to the smallest N_{CO} we observed. Thus, while there is still room for a partial contribution from shock heating, it cannot fully account for the heating mechanism of the CO gas.

The third heating source candidate is X-ray photons emitted from the nuclear region of the AGN. A strong X-ray radiation field incident on a cloud creates an X-ray-dominated region (XDR) that drives its internal thermal and chemical processes. Although this process is similar to PDR formation by UV photons, X-ray photons can penetrate more deeply into clouds because of their small cross sections. Meijerink & Spaans (2005) modeled XDRs with chemical reactions under four conditions involving combinations of two densities ($n_H = 10^3$ and $10^{5.5}$ cm^{-3}) and two incident X-ray fluxes ($F_X = 1.6$ and 160 erg cm^{-2} s^{-1}). In all cases except those with high density and low flux, the simulated temperatures are in the range 10^2–10^4 K and accord with observed T_{CO} values. Moreover, the temperatures remain higher than 10^2 K up to a column density of $N_H \sim 10^{24}$ cm^{-2}. This scale of heating is more than two orders of magnitude larger than those resulting from the previous two mechanisms. In all cases, N_{CO} reaches 10^{18} cm^{-2} before the temperature falls to 10^2 K (compare Figures 6 and 8 in Meijerink & Spaans 2005), demonstrating that such XDRs can account for the observed warm CO gas of a large column density. In addition, the dense and intense case ($n_H = 10^{5.5}$ cm^{-3} and $F_X = 160$ erg cm^{-2} s^{-1}) gives the largest N_{CO} at $T = 100$ K among all cases (10^{20} cm^{-2}), suggesting that the two sources of large $N_{CO} \sim 10^{21}$ cm^{-2}, IRAS 00182−7112 and IRAS 00406−3127, require more extreme XRDs.

We attempted to distinguish shock and X-ray heating on the basis of the CO SLED of the rotational transitions. Such lines are one of the major coolants in a shocked gas. This discussion is analogous to that argued by Meijerink et al. (2013) for NGC 6240 and Mrk 231, which are nearby merger/starburst and Sy1 galaxies, respectively. These two galaxies are similar in terms of their CO SLED shapes,with a flat distribution up to higher rotational levels, but differ in terms of their line-to-continuum ratios L_{CO}/L_{IR}, where L_{CO} is the total luminosity of the ^{12}CO lines including CO $J = 1$–0 through $J = 13$–12. While the ratio in Mrk 231 is $\sim 6 \times 10^{-5}$ (van der Werf et al. 2010), that in NGC 6240 is $\sim 7 \times 10^{-4}$, which is approximately an order of magnitude higher than the former value (Meijerink et al. 2013). The authors concluded that this large difference results from the difference in gas heating processes in the two galaxies. UV and X-ray photons effectively heat both gas and dust, and resulting in a far-IR spectrum that is continuum-dominated and, consequently, a small line-to-continuum ratio. The authors also

predicted the maximum line-to-continuum ratio in PDRs and XDRs as $\sim 10^{-4}$. Shocks, on the other hand, selectively heat gas by compression, maintaining the thermal decoupling of dust and attaining ratios higher than 10^{-4}. This leads to the conclusion that the dominant power sources for the CO gas clouds emitting rotational lines in Mrk 231 and NGC 6240 are UV to X-ray photons and shocks, respectively.

To make a similar analysis, we referred to Pearson et al. (2016), who observed the CO emission lines from $J = 5$–4 to $J = 13$–12 in 43 ULIRGs using the *Herschel Space Observatory*. Seven of their sample galaxies are included in our targets, namely, all of the *AKARI* targets and IRAS 00397−1312. We calculated the sub-total CO luminosity $L'_{\rm CO}$ spanning from $J = 5$–4 to $J = 13$–12 in the seven objects and then evaluated the line-to-continuum ratio from $L'_{\rm CO}/L_{\rm IR}$. We also derived the ratios in NGC 6240[2] and Mrk 231 for comparison and found the values of 4×10^{-4} and 6×10^{-5}, respectively. Among the seven galaxies in our sample, the lowest ratio was found in IRAS 08572+3915, in which the ratio is 3×10^{-5}, which is even smaller than that in Mrk 231. This object also shows a continuum dominated spectrum in the near- and mid-IR region. These facts strongly rule out the possibility of powerful shock heating within the galaxy. On the other hand, the highest ratio was found in IRAS 06035−7102, where the ratio is 2×10^{-4}, suggesting the possibility of shock heating, a conclusion supported by the facts that: a) the $N_{\rm CO}$ value found in this galaxy is relatively smaller than that in the other targets, and b): a widely used shock tracer H_2 vibrational emission around 2 μm was detected in this source (Dannerbauer et al. 2005). However, as the ratio $L'_{\rm CO}/L_{\rm IR}$ is lower by a factor of two than that in NGC 6240, shocks in IRAS 06035−7102 would not be as energetic as those in NGC 6240. In the remaining four galaxies, the ratio ranged within $(0.8\text{–}1.0)\times10^{-4}$, and there was no evidence of shock heating in these objects.

Given the above discussion, we conclude that the most reasonable heating mechanism of observed warm CO gas with large column densities is X-ray heating, which leads to the further conclusion that the observed CO gas is in the vicinity of the nucleus. Although the possibility that shock heating accounts for a substantial fraction of the total power cannot be ruled out in some objects, its contribution must be smaller than that of X-ray photons. In the following discussion, we presuppose that the primal heating source of the CO gas observed in absorption is X-ray photons from the central region of the AGN.

5.5.4 The Relations between the Column Density, Temperature, and IR Luminosity

Figure 5.7 plots $T_{\rm CO}$ versus $N_{\rm CO}$, showing that $T_{\rm CO}$ decreases with $N_{\rm CO}$. Although the confidence ranges of the best-fits show a strong degeneracy between the two parameters, these ranges are smaller than the scale of the overall decreasing tendency. This result can be interpreted as an attenuation in which the gas a large-column distant from the heating source is heated less than gas near the source in a small column if the heating powers in the respective targets are nearly

[2]Note that the line luminosities in NGC 6240 measured by Pearson et al. (2016) were substantially lower than the measurements by Meijerink et al. (2013). Pearson et al. (2016) claimed that the reason for this is unclear, as the two papers had used the same observation.

the same. Figure 5.8 shows that the dependence of $N_{\rm CO}$ and $T_{\rm CO}$ on the IR luminosity, $L_{\rm IR}$, is not clear. This supports the interpretation that the heating process in the CO gas observed in absorption is a local phenomenon occurring near the power source and is not tightly related to the global activities of the host galaxy.

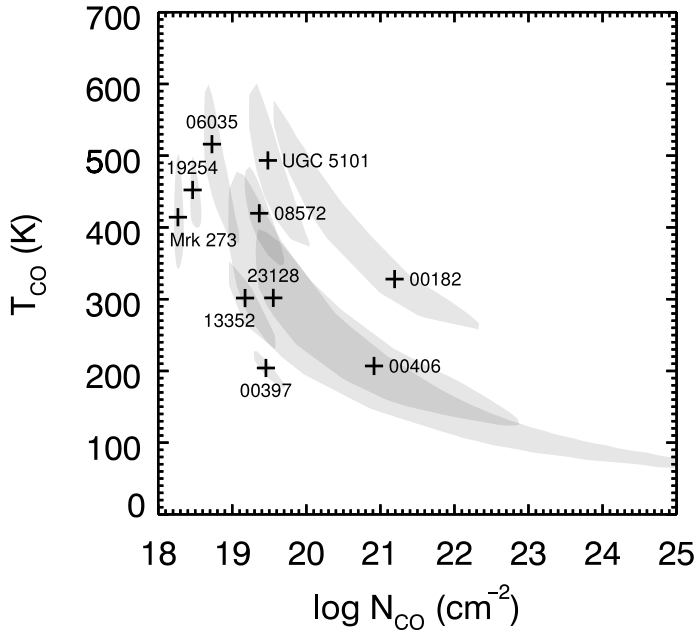

Figure 5.7: Plot of $T_{\rm CO}$ versus $N_{\rm CO}$. Black points indicate the best-fit values. Gray shaded areas are the projection of the three-dimensional 68% joint confidence regions along the $v_{\rm turb}$ axis. The unprojected 3D confidence regions are shown in Figure B.2.

5.5.5 Comparison with X-Ray Observations

To clarify the location of the region in which CO absorption originates, we compared the obtained CO column densities with neutral column densities estimated from other X-ray observations. Brightman & Nandra (2011b) performed a systematic X-ray spectral analysis for the *XMM-Newton* data (0.2–10 keV) of 126 nearby galaxies and investigated their AGN properties using a spectral model that assumes a spherical toroidal obscuring material. Four objects in their sample are common with our targets. Table 5.5 summarizes their line-of-sight hydrogen column densities determined by the X-ray spectral analysis.

A recent hydrodynamical gas model incorporating XDR chemistry (Wada et al. 2018) indicates that the CO abundance relative to molecular hydrogen has large scatter ranging from 10^{-5} to 10^{-3} in $N_{\rm CO} = 10^{18}$–10^{21} cm^{-2}. Although there is such a considerable uncertainty, we here adopt the abundance of CO/H $= 10^{-4}$, which is near the middle value, as the fiducial value to convert $N_{\rm CO}$ into $N_{\rm H}$. Figure 5.9 compares the two types of hydrogen column density. The hydrogen column density derived from the CO absorption, $N_{\rm H,4.67}$, is 2–30 times smaller than that inferred from the X-ray spectral analysis, $N_{\rm H,X}$. This comparison indicates that the two columns trace the amount of gas at different depths. The X-ray-derived column density $N_{\rm H,X}$

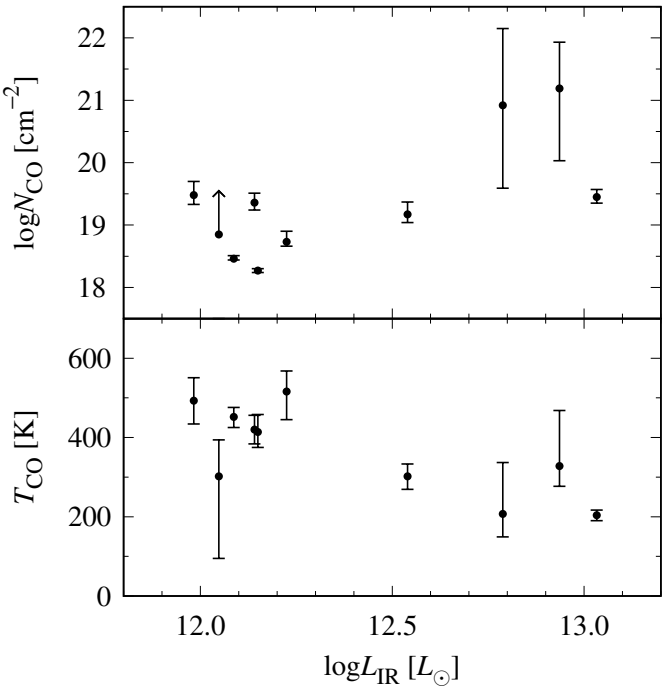

Figure 5.8: Dependence of $N_{\rm CO}$ (top) and $T_{\rm CO}$ (bottom) on $L_{\rm IR}$. The abscissa is the logarithm of $L_{\rm IR}$ in units of the solar luminosity $L_\odot$.

Table 5.5: Column density inferred from X-ray observations

Object	$N_{\rm H,X}$ (10^{22} cm^{-2})
(1)	(2)
UGC 5101	$49.6^{+25.4}_{-18.2}$
Mrk 273	$59.7^{+17.1}_{-12.8}$
IRAS 19254−7245	$38.1^{+39.2}_{-21.7}$
IRAS 23128−5919	> 150

NOTE—Column 1: object name. Column 2: hydrogen absorption column density, with errors quoted at 90% confidence level for one parameter of interest (Brightman & Nandra 2011b).

measures the gas in front of the central AGN nucleus using the X-ray radiation from it as the background. By contrast, $N_{\rm H,4.67}$ should measure the gas outside the X-ray emitting region, tracing a smaller amount of foreground gas. This consideration motivated by the assumption of CO/H $= 10^{-4}$ is consistent with the assumption that the near-IR background continuum source for CO absorption is a region in front of the nucleus being warmed by the radiation from the nucleus.

If the CO abundance is higher than CO/H $= 10^{-4}$, since $N_{\rm H,4.67}$ become smaller, the above picture still valid. On the other hand, if the abundance is 10^{-5}, $N_{\rm H,4.67}$ exceeds $N_{\rm H,X}$ in UGC 5101, although in Mrk 273 and IRAS 19254−7245 the former is still smaller than the latter. In this case, the above picture may be needed to be modified to account for the relation between the two column densities, at least for UGC 5101. However, $N_{\rm H,X}$ of the heavily obscured AGN UGC 5101 may be much larger than the value found by Brightman & Nandra (2011b). Oda et al. (2017), by fitting a torus model to a broadband 0.25–100 keV X-ray spectra, determined $N_{\rm H,X}$ to be 1.3×10^{24} cm^{-2}, which is 2.6 times larger than the value of Brightman & Nandra (2011b) and relaxes the excess of $N_{\rm H,4.67}$ from $N_{\rm H,X}$.

Although the above discussion comparing column densities derived from the CO absorption and X-ray observations strongly depends on the assumption of the CO abundance, we suggest that the most natural interpretation of the magnitude relation between $N_{\rm H,4.67}$ and $N_{\rm H,X}$ and of the presence of X-ray heated gas is that the CO absorption originates in molecular gas distribute outside the X-ray emitting region.

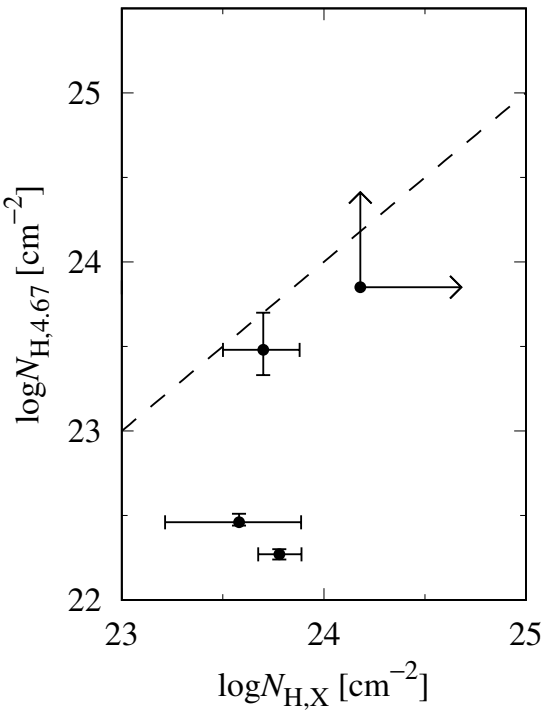

Figure 5.9: Comparison of the hydrogen column densities derived from an X-ray spectral analysis (abscissa; Table 5.5) and from CO absorption (ordinate). The dashed line denotes the identity.

5.5.6 Comparison with the 9.7 μm Silicate Absorption

Another major indicator of the degree of obscuration is the strength of the 9.7 μm silicate dust feature, as is seen in Figures 5.1 and 5.2. The optical depth of the feature $\tau_{9.7}$ in nearby AGNs have been measured in several studies (e.g., Dartois & Muñoz-Caro 2007; Imanishi et al. 2007a; Imanishi 2009). The depth $\tau_{9.7}$ can be converted into the hydrogen column density using two relations connected to visual extinction A_V: $A_V/\tau_{9.7} = 18.0$ mag (Whittet 2003), and $N_{\rm H}/A_V = 1.9 \times 10^{21}$ cm^{-2} mag^{-1} (Bohlin et al. 1978). Table 5.6 cites the values of $\tau_{9.7}$ from other papers and tabulates the derived column density, $N_{\rm H,9.7}$. Figure 5.10 compares the two types of hydrogen column density, $N_{\rm H,4.67}$ and $N_{\rm H,9.7}$. In contrast to the comparison with the X-ray observations, $N_{\rm H,4.67}$ is similar to or a bit larger than $N_{\rm H,9.7}$. We conclude that CO-absorbing gas and silicate dust roughly coexist in the same region.

Table 5.6: 9.7 μm silicate feature from literature

Object	$\tau_{9.7}$	$N_{\rm H,9.7}$ (10^{22} cm^{-2})
(1)	(2)	(3)
IRAS 06035−7102	2.9 (10%)[a]	9.9
IRAS 08572+3915	3.8 (5%)[b]	13
UGC 5101	1.9 (10%)[a]	6.5
Mrk 273	2.3 (10%)[a]	7.9
IRAS 19254−7245	1.5 (10%)[a]	5.1
IRAS 00182−7112	3.1 (10%)[a]	11
IRAS 00397−1312	2.7 (5%)[c]	9.2
IRAS 00406−3127	2.0 (10%)[a]	6.8

NOTE—Column 1: object name. Column 2: optical depth of the 9.7 μm silicate dust absorption with uncertainty in parenthesis. Column 3: hydrogen column density calculated from $\tau_{9.7}$ (see the text).
[a] Dartois & Muñoz-Caro (2007).
[b] Imanishi et al. (2007a).
[c] Imanishi (2009).

5.5.7 Distribution of the CO Gas

In our model, we assume that the covering factor of CO gas is unity. This assumption is not trivial but strongly supported by the observed deep absorption profiles. Such absorption indicates that the continuum source is almost entirely covered by the foreground gas. Because molecular clouds in star-forming regions distribute randomly, they cannot explain a large covering factor close to unity. Thus, we assume that the absorber is a molecular cloud just in front of the continuum source, which we now consider as the dust sublimation layer at the inner rim of the AGN obscuring material.

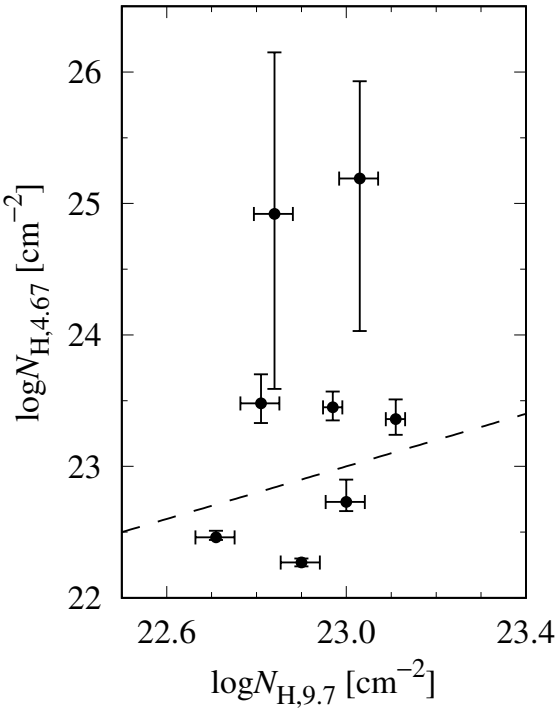

Figure 5.10: Comparison of hydrogen column densities derived from the 9.7 μm silicate dust absorption strength (abscissa; Table 5.6) and from the CO absorption (ordinate). The dashed line denotes the identity.

Figure 5.11 shows a schematic picture we propose to explain the relations of $N_{\rm H,4.67}$, $N_{\rm H,X}$, and $N_{\rm H,9.7}$, the observed large-column warm gas, and the required close-to-unity covering factor. X-ray, near-IR, and mid-IR emitting regions locate in this order from the center to outside, as the temperature decreases. In this geometry, because the absorption feature in each wavelength range traces the amount of gas in front of the corresponding background source, the magnitude relations of the column densities measured in the three ranges are naturally reproduced. Given that the CO gas is heated by X-ray radiation and that it almost entirely covers the continuum source, the origin of the CO absorption is likely to locate just in front of the inner rim of the AGN torus.

It is remarkable that a significant fraction of Sy2 galaxies do not show CO absorption. In the *AKARI* program AGNUL, IRAS 05189−2524, which is classified as Sy2 or hidden broad-line Sy1 (Véron-Cetty & Véron 2010), does not show any signature of CO absorption, as shown in Figure 5.12. Lutz et al. (2004) searched *ISO* spectra of nearby 19 type-1 and 12 type-2 AGNs for CO absorption, but none showed the signature of the absorption. One of their targets, the famous Sy2 galaxy NGC 1068, was re-observed by Geballe et al. (2009) using UKIRT, with CO absorption once again undetected. Here we speculate that the presence or absence of CO absorption originates from a complex innermost geometry in the putative AGN torus, e.g., a concave dust sublimation layer arising from an anisotropic radiation from the accretion disk (Kawaguchi & Mori 2010, 2011) or a turbulent structure near the nucleus arising from the interaction with other galaxies. This issue is also discussed in Section 6.6 based on the result of

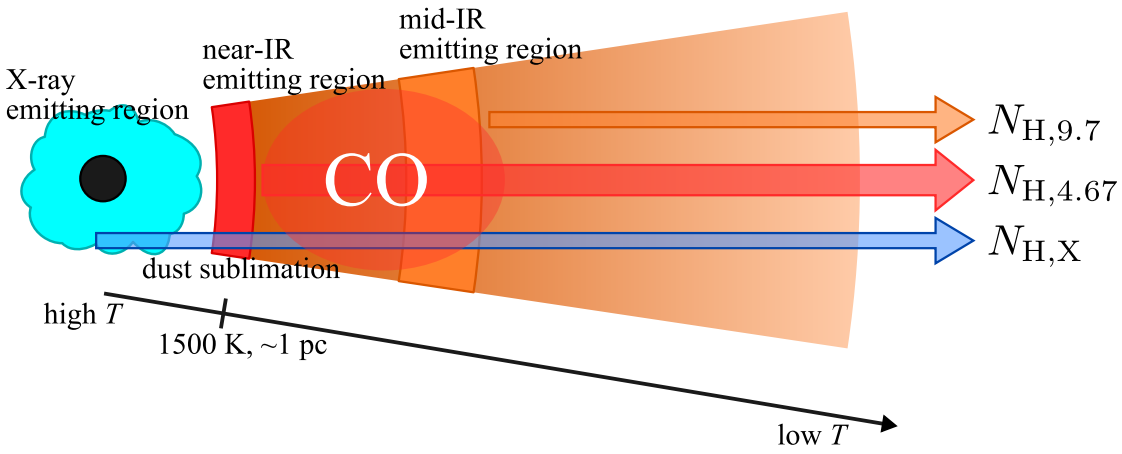

Figure 5.11: Schematic view of the location of the region where the CO absorption originates.

a systematic analysis.

5.6 Summary

In this chapter, we present a systematic spectral analysis of the CO ro-vibrational absorption band (4.67 μm) toward ten nearby obscured AGNs observed with the *AKARI* and *Spitzer* space telescopes. Using a gas model assuming LTE, slab geometry, and a single component gas, the CO column density and gas temperature were estimated for each target. The average CO column density of the sample was found to be $N_{\rm CO} \sim 10^{19.5}$ cm^{-2}, which corresponds to a hydrogen column density of $N_{\rm H} \sim 10^{23.5}$ cm^{-2} if we assume a standard abundance ratio [CO]/[H] $\sim 10^{-4}$. This large column density indicates that the AGNs are heavily obscured. On the other hand, the average temperature was found to be 360 K, which is much higher than the typical value in normal star-forming regions.

The observed warm gas of a large column density cannot be represented by UV heating or shock heating. The former can heat gas up to 10^3 K, but its maximum heating depth is only $N_{\rm CO} \sim 10^{16}$ cm^{-2}, which is two orders of magnitude smaller than the observed values. The latter can make gas warm ($\sim 10^2$ K) up to $N_{\rm CO} \sim 10^{18}$ cm^{-2}, a column density comparable to the smallest $N_{\rm CO}$ we observed. However, the low line-to-continuum ratios in the far-IR region of our sample galaxies indicate that, in addition to gas, dust is also heated up. This does not occur under shock heating, in which gas and dust are thermally decoupled. We conclude that the most convincing heating source is X-ray photons emitted from the nucleus. This mechanism can heat gas up to even $N_{\rm CO} \sim 10^{20}$ cm^{-2}, which is large enough to account for the observed values over 10^2 K. This conclusion suggests that the region probed by the CO absorption should be in the vicinity of the nucleus.

A comparison with an X-ray spectral analysis (Brightman & Nandra 2011b) shows that, if we adopt the CO abundance of CO/H $= 10^{-4}$ as the fiducial value, the hydrogen column density

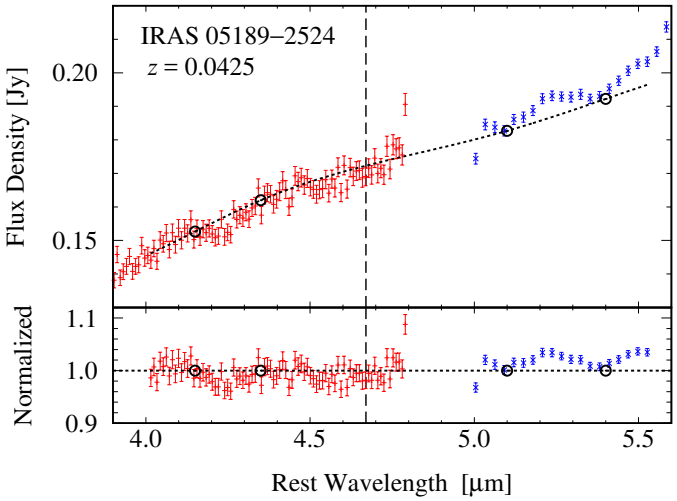

Figure 5.12: Top: 4.0–5.5 μm spectrum of the Sy2 galaxy IRAS 05189−2524. Red and blue points represent the *AKARI* and *Spitzer* data, observation ID 1100129.1 and AOR key 16909568, respectively. Data reduction was performed in the manner described in Section 5.2. The black dotted line denotes the continuum curve determined as explained in Section 5.3.1. The black dashed line indicates the expected wavelength of the CO band center. Bottom: continuum-normalized spectrum of the same galaxy.

converted from the CO column density is 2–30 times smaller than that inferred from the X-ray analysis. We suggest that the region probed by the near-IR CO absorption is located outside the X-ray emitting region. Moreover, the close-to-unity covering factor of the CO gas suggested by the observed deep absorption indicates that the gas is close to the continuum source, which we hypothesize to be the dust sublimation layer at the inner rim of the obscuring material around the AGN. In contrast to the comparison with the X-ray observations, the hydrogen column density derived from CO absorption is similar to or a bit larger than that calculated from the optical depth of the 9.7 μm silicate dust absorption. We conclude that CO-absorbing gas and silicate dust roughly coexist in the same region. These results can be explained in the picture where X-ray, near-IR, and mid-IR emitting regions locate in this order from the center, and the CO absorption originates just in front of the dust sublimation layer.

We reconfirmed a previously remarked-upon fact that not all Sy2 galaxies show CO absorption (Lutz et al. 2004; Geballe et al. 2009). The cryogenic phase *AKARI* AGNUL results for the Sy2 galaxy IRAS 05189−2524 do not show any signature of the feature. We speculate that the presence or absence of this absorption reflects the complex innermost geometry of the putative AGN torus, e.g., as a concave dust sublimation layer generated by anisotropic radiation from the accretion disk (Kawaguchi & Mori 2010, 2011) or a turbulent structure near the nucleus caused by interaction with other galaxies.

Chapter 6

The Near-Infrared CO Absorption in Nearby Infrared Galaxies

Motivated by the result of Chapter 5, we performed a systematic study of the CO absorption with a larger sample that includes less-luminous infrared galaxies. Nearby 47 infrared galaxies were selected from the *AKARI* post-cryogenic observations without any prior information on the presence or absence of the CO feature. Their band profiles were compared in different luminosity classes and optical classifications. Many of the sample galaxies, similar to the targets in the previous chapter, showed warm large-column gas of $N_{\rm CO} \gtrsim 10^{19}$ cm^{-2} and $T_{\rm CO} \sim$ several$\times 10^2$ K, which can be considered to be heated by X-rays. ULIRGs and LIRGs showed deeper absorption profiles than IRGs. We found that the fraction of galaxies with $N_{\rm CO} > 10^{19}$ cm^{-2} had a peak at a 14 μm monochromatic luminosity of 10^{10} $L_\odot$, being consistent with the obscured fraction measured in X-ray observations. Based on this result, the obscuring material observed in X-rays is being identified to be molecular gas. We also found that AGN-starburst composites had on average larger $N_{\rm CO}$ than Seyfert 2s. This result suggests that the obscuration by an AGN torus is also effective in composites and that the torus is geometrically thicker in composites than in typical Seyferts. This difference is qualitatively consistent with the connection that supernovae in the circum-nuclear disk inflate the scale height of the torus.

6.1 Introduction

In Chapter 5, we found that the CO absorption is effective as a probe to X-ray-heated warm gas in the vicinity of AGNs. However, the AGNs analyzed were limited to those of the ULIRG class ($L_{\rm IR} > 10^{12}$ $L_\odot$). As mentioned in Chapter 1, it is suggested that the torus geometry changes depending on the nuclear luminosity. The covering fraction of an AGN torus, measured as the fraction of type-2 AGNs in optical and IR surveys, decreases with increasing luminosity as predicted by the receding torus model (Simpson 2005; Toba et al. 2013, 2014). The obscured fraction observed in X-rays also decreases at high X-ray luminosity (Ueda et al. 2003; Lusso et al. 2013). Its behavior at low luminosity is, however, controversial because some groups argue

that it has a peak at a certain luminosity around $L_{\rm X} \sim 10^{43}$ erg s^{-1} (Brightman & Nandra 2011a; Burlon et al. 2011). For verification of the relation between the torus shape and the central luminosity by the CO absorption, it is necessary to investigate fainter AGNs embedded in LIRGs ($10^{11} < L_{\rm IR} < 10^{12}$ $L_\odot$) and IRGs ($L_{\rm IR} < 10^{11}$ $L_\odot$) additionally. Such low-luminosity galaxies are hardly observable with the *Spitzer*/IRS.

The ten targets of the previous chapter include Seyferts, LINERs, H II galaxies, and those composites. However, the number of each optical classification was not sufficient to discuss the difference between classifications in the CO column density and temperature. It is suggested that feedback from the surrounding environment such as star formation in circum-nuclear disks contributes to AGN activity and torus formation. Izumi et al. (2016) found that the mass accretion rate from a circum-nuclear disk (CND) estimated from the mass of dense gas agrees well with the sum of the accretion rate of the SMBH and the outflowing mass rate although there were only two Seyfert galaxies as the sample. The hydrodynamical simulation of Wada (2012) implies that to maintain a geometrically thick torus structure for millions of years the mass accretion rate into the center needs to be increased by some mechanisms, such as supernova explosions and stellar mass loss in the surrounding environment. If the behavior of the CO absorption were different between pure Seyferts and LINERs or AGN-starburst composites, it would help discussing the link between the torus geometry and the surrounding environment. For this purpose, it is necessary to increase the number of sample galaxies.

The dataset of the *AKARI* post-cryogenic observations is helpful to search for new targets. The number of near-IR spectroscopic observations is originally larger in Phase 3 than Phases 1 and 2. The mission program AGNUL, which we referred to in the previous chapter, observed a lot of LIRG and IRG during Phase 3. Because we have already corrected for the effect of the second-order light contamination for this phase in Chapter 4, we can utilize those observations as a sample of the systematic analysis of the CO absorption.

In this chapter, we investigate the difference in the column density and temperature obtained from the CO absorption between the luminosity classes and optical classifications. Section 6.2 shows sample selection, being followed by a description of observations and data reduction in Section 6.3. Section 6.4 explains the method of analysis. The results are presented in Section 6.5. We discuss the results in Section 6.6 and finally summarize this chapter in Section 6.7.

6.2 Sample Selection

We selected our sample from the galaxies observed as a part of the *AKARI* mission program AGNUL during the post-cryogenic phase. Some of the galaxies were discarded by the criteria explained below. The change in the number of accepted galaxies is summarized in Table 6.1. To avoid spectral confusion of different objects and ensure the spectral resolution adequate for the gas model fitting, we restricted observations to those conducted in the Np aperture with the grism. In this setup, 746 observations had been carried out in total. The number of observed galaxies is 240 because each galaxy had been observed several times. The redshift range within which the CO band is covered by the grism mode spectrum is $z < 0.07$, where 143 galaxies are

Table 6.1: Sample selection flow

Criterion	# of galaxies
AGNUL during Phase 3	240
$z < 0.07$	143
good IRC observation	134
with IRS spectrum	83
small jump at 14 μm	64
good *WISE* data	47

included. Nine of them were rejected because they were found not to have been properly observed due to miss pointing, contamination from neighbor objects, or too high or low brightness.

We need the *Spitzer*/IRS spectrum to determine the continuum over the CO absorption, as we do in Chapter 5. Among the 134 galaxies, 51 ones had not observed with IRS throughout 5.2–32 μm and thus were rejected. The IRS uses slits of different widths for divided wavelength ranges. In particular, $\lambda_{\rm obs} = 14$ μm is a point of connection between the Short-Low and Long-Low modes, whose slit widths are $\sim 4''$ and $\sim 10''$, respectively (Houck et al. 2004). Thus, depending on source extent, the spectrum does not necessarily connect smoothly at this point. In that case, the flux matching with the *AKARI*/IRC spectrum based on *WISE* as performed in Chapter 5 does not function properly. Many of the remaining 83 galaxies are nearer than the sample of Chapter 5. Therefore, this problem should be considered. We obtained the IRS spectra from the Cornell Atlas of Spitzer/IRS Sources (CASSIS; Lebouteiller et al. 2011, see Section 6.3) and then measured the jump at 14 μm as the ratio of the LL-mode average flux to the SL-mode one using 10 points at the edge of each mode. We excluded 19 galaxies that have the ratio higher than 1.5.

To perform the flux matching of the *AKARI* and *Spitzer* spectra as in Chapter 5, we required appropriate *WISE* photometric fluxes as the references. Cataloged $W1$–4 magnitudes were obtained from the AllWISE Source Catalog for each galaxy except for IRAS 15250+3609, for which the magnitudes in the WISE All-Sky Catalog were adopted because the former database does not identify this object. We set criteria that the magnitudes are measured with high signal-to-noise ratio (`ph_qual=AAAA`) and do not show time variability (`var_flg<5555`) and that no saturation occurs (`satnum=0000`). These criteria rejected 17 galaxies.

Eventually, 47 galaxies were selected as the sample of this study. Their names, coordinates, and redshifts are tabulated in Table 6.2. Mrk 273 and ESO 198-IG002 (=IRAS 23128−1919) are in common with the sample of Chapter 5. The infrared luminosity $L_{\rm IR}$ was calculated for each galaxy from the *N60*, *WIDE-S*, and *WIDE-L* bands of the *AKARI* FIS Bright Source Catalogue Ver.2 with the equation presented by Solarz et al. (2016). For some objects not resolved from neighboring galaxies in the FIS catalog, we distributed the FIS flux to the unresolved galaxies proportionally to their $W4$ fluxes. If the FIS fluxes are not available, we instead used *IRAS* four bands and the equation of Sanders & Mirabel (1996). The luminosity distance D_L was calculated upon the cosmology of $H_0 = 70$ km s^{-1} Mpc^{-1}, $\Omega_{\rm m} = 0.3$, and $\Omega_\Lambda = 0.7$. The derived luminosities are also listed in Table 6.2. Figure 6.1 is a scatter plot and histograms of z

and $L_{\rm IR}$. While all the targets studied in Chapter 5 are in the ULIRG class, the current sample additionally covers less-luminous galaxies: 19 IRGs, 24 LIRGs, and 4 ULIRGs.

We compiled optical classifications of the sample in literature, which are listed in Column (6) of Table 6.2, and then determined the class used in this study. If objects had been at least once classified as composite or classified both as H II and as another type, they were treated as composites. Otherwise, the most frequent classification was adopted. Although there is only one classification as an H II galaxy for IRAS 09022−3615, we overwrote it considering a small equivalent width of the 6.2 μm PAH emission EW$_{6.2}$=0.14 μm (Stierwalt et al. 2014). The 47 objects were finally classified as 2 Seyfert 1s, 13 Seyfert 2s, 3 LINERs, 24 composites, and 5 of no classification. Our sample has no galaxy purely classified as H II. This is partly due to the selection of the AGNUL sample biased to galaxies richer in absorption features. Thirty out of our sample are in common with the sample of the Great Observatories All-Sky LIRG Survey (GOALS; Armus et al. 2009).

Table 6.2: Basic data of the sample

Object	R.A. (J2000)	Dec. (J2000)	z	log $L_{\rm IR}$ ($L_\odot$)	optical class in literature	adopted
(1)	(2)	(3)	(4)	(5)	(6)	(7)
Mrk 334	$00^{\rm h}03^{\rm m}09\overset{\rm s}{.}62$	$+21°57'36\overset{''}{.}6$	0.021945	10.95	Sy1[6]	Sy1
NGC 23	$00^{\rm h}09^{\rm m}53\overset{\rm s}{.}41$	$+25°55'25\overset{''}{.}6$	0.015231	11.09	cp[8,9]	cp
MCG−02-01-051	$00^{\rm h}18^{\rm m}50\overset{\rm s}{.}88$	$-10°22'36\overset{''}{.}7$	0.027103	11.35[a]	H II[8,12] cp[2]	cp
NGC 232	$00^{\rm h}42^{\rm m}45\overset{\rm s}{.}82$	$-23°33'40\overset{''}{.}9$	0.022639	11.44	cp[8]	cp
I Zw 1	$00^{\rm h}53^{\rm m}34\overset{\rm s}{.}94$	$+12°41'36\overset{''}{.}2$	0.058900	11.51	Sy1[4,6]	Sy1
MCG−07-03-014	$01^{\rm h}18^{\rm m}08\overset{\rm s}{.}32$	$-44°27'42\overset{''}{.}2$	0.020928	11.05[b]	cp[8]	cp
CGCG 436-030	$01^{\rm h}20^{\rm m}02\overset{\rm s}{.}72$	$+14°21'42\overset{''}{.}9$	0.031229	11.69	H II[8] cp[2]	cp
NGC 612	$01^{\rm h}33^{\rm m}57\overset{\rm s}{.}74$	$-36°29'35\overset{''}{.}7$	0.029771	11.13	Sy2[6]	Sy2
ESO 353-G020	$01^{\rm h}34^{\rm m}51\overset{\rm s}{.}28$	$-36°08'14\overset{''}{.}0$	0.015921	11.13	?	—
ESO 297-G018	$01^{\rm h}38^{\rm m}37\overset{\rm s}{.}16$	$-40°00'41\overset{''}{.}1$	0.025227	10.43	Sy2[10]	Sy2
IRAS 02530+0211	$02^{\rm h}55^{\rm m}34\overset{\rm s}{.}43$	$+02°23'41\overset{''}{.}4$	0.027600	10.81	H II[12] cp[8]	cp
NGC 1614	$04^{\rm h}33^{\rm m}59\overset{\rm s}{.}85$	$-08°34'44\overset{''}{.}0$	0.015938	11.60	H II[6,12] cp[4,8]	cp
ESO 121-IG028	$06^{\rm h}23^{\rm m}45\overset{\rm s}{.}57$	$-60°58'44\overset{''}{.}4$	0.040521	$<$ 10.63[c]	Sy2[6,10]	Sy2
NGC 2623	$08^{\rm h}38^{\rm m}24\overset{\rm s}{.}08$	$+25°45'16\overset{''}{.}7$	0.018509	11.57	LI[1,11]	LI
Mrk 18	$09^{\rm h}01^{\rm m}58\overset{\rm s}{.}40$	$+60°09'06\overset{''}{.}2$	0.011088	10.11	H II[3] cp[1,2]	cp
IRAS 09022−3615	$09^{\rm h}04^{\rm m}12\overset{\rm s}{.}71$	$-36°27'01\overset{''}{.}0$	0.059641	12.30	H II[5]	cp[h]
ESO 434-G040	$09^{\rm h}47^{\rm m}40\overset{\rm s}{.}16$	$-30°56'55\overset{''}{.}4$	0.008486	9.62	Sy2[6,10]	Sy2
NGC 3081	$09^{\rm h}59^{\rm m}29\overset{\rm s}{.}54$	$-22°49'34\overset{''}{.}6$	0.007976	9.85	Sy2[6,7,10]	Sy2
NGC 3079	$10^{\rm h}01^{\rm m}57\overset{\rm s}{.}80$	$+55°40'47\overset{''}{.}2$	0.003723	10.61	Sy2[4,6]	Sy2
NGC 3268	$10^{\rm h}30^{\rm m}00\overset{\rm s}{.}66$	$-35°19'31\overset{''}{.}7$	0.009340	$<$ 9.46[d]	?	—
ESO 264-G057	$10^{\rm h}59^{\rm m}01\overset{\rm s}{.}79$	$-43°26'25\overset{''}{.}7$	0.017199	11.05	?	—
Arp 148	$11^{\rm h}03^{\rm m}53\overset{\rm s}{.}20$	$+40°50'57\overset{''}{.}0$	0.034524	11.64	cp[14]	cp
NGC 4102	$12^{\rm h}06^{\rm m}22\overset{\rm s}{.}99$	$+52°42'39\overset{''}{.}9$	0.002823	10.34	LI[6,7,10]	LI
NGC 4194	$12^{\rm h}14^{\rm m}09\overset{\rm s}{.}47$	$+54°31'36\overset{''}{.}6$	0.008342	10.86	Sy1[2] H II[1,6]	cp
M 106	$12^{\rm h}18^{\rm m}57\overset{\rm s}{.}50$	$+47°18'14\overset{''}{.}3$	0.001494	9.23	Sy2[6]	Sy2
NGC 4418	$12^{\rm h}26^{\rm m}54\overset{\rm s}{.}62$	$-00°52'39\overset{''}{.}4$	0.007268	10.97	Sy1[2] Sy2[6,14] cp[1]	cp
ESO 506-G027	$12^{\rm h}38^{\rm m}54\overset{\rm s}{.}59$	$-27°18'28\overset{''}{.}2$	0.025024	10.56[c]	Sy2[6,10]	Sy2
NGC 4818	$12^{\rm h}56^{\rm m}48\overset{\rm s}{.}90$	$-08°31'31\overset{''}{.}1$	0.003552	10.11	H II[12] cp[8]	cp
ESO 507-G070	$13^{\rm h}02^{\rm m}52\overset{\rm s}{.}35$	$-23°55'17\overset{''}{.}7$	0.021702	11.51	?	—
IC 860	$13^{\rm h}15^{\rm m}03\overset{\rm s}{.}53$	$+24°37'07\overset{''}{.}9$	0.011164	10.99	LI[1] H II[14]	cp
UGC 8335 W	$13^{\rm h}15^{\rm m}30\overset{\rm s}{.}59$	$+62°07'45\overset{''}{.}3$	0.030788	11.02[e]	cp[8]	cp
UGC 8335 E	$13^{\rm h}15^{\rm m}34\overset{\rm s}{.}98$	$+62°07'28\overset{''}{.}7$	0.031065	11.54[e]	cp[2,8]	cp

Table 6.2: (*Continued*)

Object	R.A. (J2000)	Dec. (J2000)	z	$\log L_{\rm IR}$ ($L_\odot$)	optical class in literature	adopted
(1)	(2)	(3)	(4)	(5)	(6)	(7)
MCG−03-34-064	$13^{\rm h}22^{\rm m}24\overset{\rm s}{.}46$	$-16°43'42\overset{''}{.}5$	0.016541	10.84	Sy1;[10] Sy2;[4,6] H II[8]	cp
NGC 5135	$13^{\rm h}25^{\rm m}44\overset{\rm s}{.}06$	$-29°50'01\overset{''}{.}2$	0.013693	11.32	Sy2[6,8,12]	Sy2
IC 4280	$13^{\rm h}32^{\rm m}53\overset{\rm s}{.}40$	$-24°12'25\overset{''}{.}7$	0.016308	11.04	?	—
Mrk 273	$13^{\rm h}44^{\rm m}42\overset{\rm s}{.}11$	$+55°53'12\overset{''}{.}7$	0.037780	12.13	Sy2[2,4,6,8,13,14]	Sy2
UGC 9618 N	$14^{\rm h}57^{\rm m}00\overset{\rm s}{.}83$	$+24°37'04\overset{''}{.}1$	0.033669	11.59[f]	H II;[2,16] cp[8]	cp
IRAS 15250+3609	$15^{\rm h}26^{\rm m}59\overset{\rm s}{.}40$	$+35°58'37\overset{''}{.}5$	0.055155	11.96	cp[1,2,8,14]	cp
Arp 220	$15^{\rm h}34^{\rm m}57\overset{\rm s}{.}25$	$+23°30'11\overset{''}{.}3$	0.018126	12.27	Sy1;[2] Sy2;[14] LI[1,8,11,13]	LI
NGC 6701	$18^{\rm h}43^{\rm m}12\overset{\rm s}{.}46$	$+60°39'12\overset{''}{.}0$	0.013226	11.06	cp[8,9]	cp
IC 5063	$20^{\rm h}52^{\rm m}02\overset{\rm s}{.}34$	$-57°04'07\overset{''}{.}6$	0.011348	10.45	Sy2[6,7,8,10,12]	Sy2
ESO 286-IG019	$20^{\rm h}58^{\rm m}26\overset{\rm s}{.}78$	$-42°39'00\overset{''}{.}2$	0.042996	12.00	H II;[5,6,8,12] cp[4]	cp
NGC 7130	$21^{\rm h}48^{\rm m}19\overset{\rm s}{.}52$	$-34°57'04\overset{''}{.}5$	0.016151	11.38[g]	Sy1;[6] Sy2[8]	Sy2
NGC 7213	$22^{\rm h}09^{\rm m}16\overset{\rm s}{.}31$	$-47°09'59\overset{''}{.}8$	0.005839	9.80	Sy1;[7,10] LI;[6] cp[4]	cp
ESO 148-IG002	$23^{\rm h}15^{\rm m}46\overset{\rm s}{.}75$	$-59°03'15\overset{''}{.}6$	0.044601	11.99	H II;[5,6,12] cp[4]	cp
IC 5298	$23^{\rm h}16^{\rm m}00\overset{\rm s}{.}70$	$+25°33'24\overset{''}{.}1$	0.027422	11.54	Sy2[6,8]	Sy2
Mrk 331	$23^{\rm h}51^{\rm m}26\overset{\rm s}{.}80$	$+20°35'09\overset{''}{.}9$	0.018483	11.47	H II;[8] cp[4]	cp

NOTE—Column 1: common object name used as an ID in this chapter. Columns 2 and 3: right ascension and declination (J2000). Column 4: redshift from the NASA/IPAC Extragalactic Database (NED). Column 5: logarithm of the infrared (8–1000 μm) luminosity in units of the solar luminosity derived from the *N60*, *WIDE-S*, and *WIDE-L* bands of the *AKARI* FIS Bright Source Catalogue Ver.2, otherwise noted. Column 6: optical spectral classification in literature. The abbreviations "Sy1", "Sy2", "LI", and "H II" indicate Seyfert 1 and 2 galaxies, LINERs, H II galaxies, respectively, and "cp" means composites of H II and AGNs or LINERs.

[a] MCG−02-01-051 is one of the galaxies consisting the early-stage merger Arp 256. The FIS catalog does not resolve MCG−02-01-051 and the other galaxy MCG−02-01-052.

[b] MCG−07-03-014 is the northern nucleus of the interacting pair ESO 244-IG012. The FIS catalog does not resolve MCG−07-03-014 and the southern nucleus MCG−07-03-013.

[c] Calculated from the fluxes in the *IRAS* Faint Source Catalog Version 2.0.

[d] Evaluated from the *IRAS* Faint Source Rejected Catalog.

[e] The FIS catalog does not resolve UGC 8335 W and E.

[f] The FIS catalog does not resolve UGC 9618 N and S.

[g] The FIS catalog does not resolve NGC 7130 and 6dFGS gJ214816.8-345632, which is far behind ($z = 0.12$) than NGC 7130.

[h] We overwrote the class of H II considering a small equivalent width of the 6.2 μm PAH emission $\mathrm{EW}_{6.2} = 0.14$ μm (Stierwalt et al. 2014).

[1] Toba et al. (2014).

[2] Toba et al. (2013).

[3] Stern & Laor (2013).

[4] Brightman & Nandra (2011a).

[5] Lee et al. (2011).

[6] Véron-Cetty & Véron (2010). Types Sy1.8, Sy1.9, Sy1n are here aggregated into Sy1, and types Sy1i, and Sy1h are aggregated into Sy2.

[7] Tueller et al. (2010). An intermediate type Sy1.5 is here aggregated into Sy1.

[8] Yuan et al. (2010).

[9] Alonso-Herrero et al. (2009).

[10] Tueller et al. (2008). Intermediate types Sy1.5 and Sy1.8 are here aggregated into Sy1.

[11] Lípari et al. (2004).

[12] Kewley et al. (2001).

[13] Veilleux et al. (1999).

[14] Baan et al. (1998).

6.3 Observations and Data Reduction

Table 6.3 summarizes the *AKARI*/IRC observations used for the following analysis. From each observation, a 2D spectral image was extracted with the toolkit. Bad pixels were filled with median values of their adjacent valid pixels, which is the same manner shown in Figure 4.2. In obtaining a 1D spectrum from the image, the spatial extraction width was determined from the FHWM of the source extent. The wavelength calibration curve and spectral response function

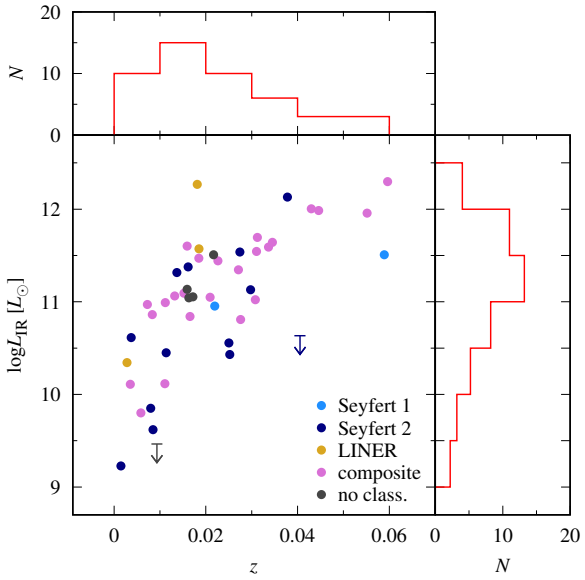

Figure 6.1: Distribution of z and $L_{\rm IR}$ of our sample. In the histogram of $L_{\rm IR}$, the counts of ESO 121-IG028 and NGC 3268 are equally distributed to bins below the respective upper limits. The classifications of the two upper limits are represented in the same colors as the other points.

revised in Chapter 4 were used. The contamination from the second-order light was subtracted. The wavelength calibration origin was adjusted by a few pixels based on the positions of the Brα and Brβ lines and the 3.3 μm PAH emission. For galaxies with multiple observations, we stacked the spectra from them to reduce noise.

The AOR keys of the used *Spitzer*/IRS observations are listed in Table 6.3. The calibrated IRS spectra were obtained from the CASSIS low-resolution atlas (Lebouteiller et al. 2011), the version LR7. The atlas provides two types of spectrum extracted by two methods: optimal extraction and tapered column extraction. For each object, we employed the spectrum that the atlas recommends based on the source extent. If multiple observations were available for an object, we used the spectrum whose jump at 14 μm measured as described in Section 6.2 was the smallest.

The IRC and IRS spectra of each galaxy were scaled to match the *WISE* fluxes in a similar manner of Section 5.2.3. Different from the previous way, we additionally used the $W2$ band to adjust the IRC spectrum. Because the $W1$ point could lie upon a prominent 3.3 μm PAH emission due to small redshift, scaling the IRC spectrum based only on the $W1$ flux could cause a large systematic error. The color correction factor for the $W2$ band, which overlaps the gap between the two spectra, was determined by the method described in Appendix C.1, but finally, it was found to be less critical than the factors for the $W1$ and $W3$ bands. The IRC spectrum was scaled to fit the color-corrected $W1$ and $W2$ fluxes, and the IRS one was as done with $W3$ and $W4$. The resultant connected spectra are shown in the left panels in Figure 6.2. Figure 6.3 is a scatter plot of the scaling factors. While the factor for the IRC spectra distributes around the unity, that for the IRS spectra spreads to higher values. This can be attributed to the flux missing in the IRS slit spectroscopy.

Table 6.3: Observation log of the *AKARI*/IRC and *Spitzer*/IRS

	AKARI		*Spitzer*	
Object	IDs	Dates	AOR Key	Date
Mrk 334	1120012.1, 2, 3	2008 Jul 1, Dec 31	10870016-1	2004 Dec 13
NGC 23	1122291.1	2010 Jan 4	20348672-1	2007 Feb 2
MCG−02-01-051	1120101.1, 2	2008 Jun 20, 2009 Jun 21	20313088-1	2006 Dec 17
NGC 232	1120102.1, 2	2008 Dec 20	20342016-1	2006 Dec 17
I Zw 1	1122142.1, 2, 3	2010 Jan 7	3761920-1	2004 Jan 7
MCG−07-03-014	1122223.1, 2, 3, 4	2009 Dec 16	20368384-1	2006 Nov 21
CGCG 436-030	1120013.1, 2; 1120105.2;[a] 1122123.1	2008 Jul 15, 2009 Jan 14, 2010 Jan 14	20356352-1	2007 Feb 1
NGC 612	1120076.1, 4, 5[b]	2008 Jun 24, 26	18945280-1	2007 Aug 1
ESO 353-G020	1122308.1, 2, 3, 4	2009 Dec 26	20366080-1	2006 Dec 17
ESO 297-G018	1120074.1, 2, 3, 4, 5	2008 Jun 23	18944768-1	2007 Aug 1
IRAS 02530+0211	1120025.1, 2, 3	2009 Aug 4	6652160-1	2005 Feb 10
NGC 1614	1120115.1[c]	2008 Aug 27	3757056-1	2004 Feb 6
ESO 121-IG028	1122044.1, 2, 3, 4, 5	2009 Oct 17, 18, 24	26484224-1	2008 May 28
NGC 2623	1120116.1, 2	2009 Apr 24, 25	9072896-1	2004 Apr 19
Mrk 18	1122043.1, 2, 3, 4, 5	2009 Oct 20	18944000-1	2007 May 1
IRAS 09022−3615	1122181.1, 2, 3	2009 Nov 25	12256000-1	2005 Jun 7
ESO 434-G040	1122050.1, 2, 3	2009 Dec 3, 5	26484992-1	2008 Jun 9
NGC 3081	1120082.1, 2, 3, 4, 5	2009 Jun 2	18509824-1	2007 Jun 11
NGC 3079	1120034.1, 2, 3	2009 Apr 30	3755520-1	2004 Apr 19
NGC 3268	1120024.1[d]	2008 Jun 17	17925376-1	2007 Feb 12
ESO 264-G057	1122277.1	2009 Dec 29	20347904-1	2007 Mar 11
Arp 148	1120122.1, 2	2008 Nov 21, 2009 May 19	15694592-2	2006 Dec 19
NGC 4102	1120232.1; 1122090.1	2009 May 25, Nov 27	18941952-1	2007 May 2
NGC 4194	1122091.1[e]	2009 Nov 26	3757824-1	2004 Jan 8
M 106	1120071.1, 2, 3	2008 Dec 2	18526208-1	2007 Jun 9
NGC 4418	1120010.1, 2, 3	2008 Jun 27	4935168-1	2005 Jul 7
ESO 506-G027	1120078.1, 2, 3; 1120079.1, 2	2009 Jan 10, 11, Jul 11	18941696-1	2007 Aug 5
NGC 4818	1120234.1, 2, 3	2009 Jan 6, Jul 8	9071104-1	2004 Jul 14
ESO 507-G070	1120128.1, 2; 1122218.1	2008 Jul 15, 2010 Jan 13	20326656-1	2007 Mar 10

Table 6.3: (*Continued*)

	AKARI		*Spitzer*	
Object	IDs	Dates	AOR Key	Date
IC 860	1120040.1, 2, 3	2008 Jun 28	6652416-1	2005 Feb 10
UGC 8335 W	1122132.1, 2, 3[f]	2009 Nov 26	20356864-1	2006 Dec 23
UGC 8335 E	1120129.1, 2	2009 May 23	20356864-2	2006 Dec 23
MCG−03-34-064	1120084.1, 2, 3, 4, 5; 1120247.1, 2	2008 Jul 17, 2009 Jul 18	20367616-1	2007 Mar 8
NGC 5135	1120132.1, 2	2008 Jul 23	18512384-1	2007 Jul 29
IC 4280	1122276.1, 2	2010 Jan 21	20350208-1	2007 Mar 10
Mrk 273	1122182.1, 2, 3, 4	2009 Dec 8, 9	4980224-1	2004 Apr 14
UGC 9618 N	1120136.1; 1122066.1, 2, 3	2008 Jul 24, 2010 Jan 22	20339456-1	2007 Mar 17
IRAS 15250+3609	1122003.1, 2, 3, 4	2010 Jan 23	4983040-1	2004 Mar 4
Arp 220	1120017.1, 2, 3; 1122005.1, 2, 3, 4	2008 Aug 5, 6, 2010 Feb 1, 2	32512768-1	2009 Apr 12
NGC 6701	1122292.1	2009 Nov 8	20341760-1	2006 Oct 24
IC 5063	1122041.1, 2, 3, 4, 5	2009 Oct 20, 21	18506752-1	2006 Oct 18
ESO 286-IG019	1120003.1, 2, 3; 1122176.1	2008 Oct 28, 2009 Apr 23, Oct 28	4990208-1	2004 May 14
NGC 7130	1120236.1, 2, 3; 1122232.1, 2, 3	2008 Nov 8, 9, 10, 2009 Nov 10	18507008-1	2006 Nov 17
NGC 7213	1120069.1, 2, 3	2008 Nov 8, 2009 May 5	4856320-1	2004 May 15
ESO 148-IG002	1122118.1, 2, 3, 4	2009 Nov 11	4991744-1	2004 May 11
IC 5298	1120146.2	2008 Jun 22	20356608-1	2006 Dec 20
Mrk 331	1120150.1, 2	2008 Dec 28	4344576-1	2005 Dec 12

[a] ID 1120105.1 was no used because the object had been acquired on the edge of the Np aperture, and thus the spectrum is severely damaged.

[b] IDs 1120076.2 and .3 were not used. The spectrum from the former observation is too noisy. The latter observation had failed to acquire the object in the Np aperture.

[c] ID 1120115.2 was not used because the object had been acquired on the edge of the Np aperture.

[d] IDs 1120024.2 and .3 were not used. The spectrum from the former observation is too noisy. The latter observation had failed to acquire the object in the Np aperture.

[e] ID 1122091.2 was not used because there was no source in the Nc aperture and we were not able to measure x- and y-shifts between spectroscopic sub-frames.

[f] ID 1122132.4 was not used because the object had been acquired on the edge of the Np aperture.

[g] The number after the hyphen is the pointing ID labeled in CASSIS.

6.4 Analysis

The CO band could be contaminated by the H I Pfβ line at 4.65 μm. We estimated its line flux from that of the Brα line with the predicted ratio of Pfβ/Brα=0.20 in the case B condition with $n_e \sim 10^2$–10^7 cm^{-3} and $T_e \sim$(3–30)$\times10^3$ K (Storey & Hummer 1995). The Brα flux was measured by fitting a Gaussian on a linear baseline with the FWHM fixed to 0.05 μm, which is the width found in the stacked spectrum of the sample galaxies. If the Brα line was detected with above the 3σ significance, we subtracted the Pfβ flux assuming a Gaussian line profile with the same FWHM. Similarly, the molecular hydrogen pure-rotational line H_2 0–0 S(9) at 4.69 μm could contaminate the CO absorption. We estimated its flux from those of higher-J lines, H_2 0–0 S(7) at 5.51 μm and S(3) at 9.66 μm. The lines between the two levels were not used because they overlap with other emission lines or bands. The flux of the two lines were measured as in that of the Brα line was. No correction for the dust extinction was performed. If the two lines were detected with the 3σ level, we derived the excitation temperature T_{ex} from the two lines assuming LTE and then subtracted the S(9) line flux predicted from the same T_{ex}. The Einstein A coefficients and the energy levels were taken from Turner et al. (1977) and Jennings et al. (1987), respectively. The estimated excitation temperatures are in the range of 900–1500 K, which is comparable with that of the hot components of the H_2 gas in ULIRGs found by Higdon et al. (2006). Table 6.4 summarizes the measurement and the estimates.

We set the continuum level over the CO band as a cubic spline curve interpolating pivots placed avoiding the Brα line at 4.05 μm, the CO_2 absorption at 4.26 μm, and the PAH emission at 5.3 μm. The right panels in Figure 6.2 show the adopted continuum curves and used pivots with the resultant optical depths at the position of the CO absorption. In the Sy2 galaxies NGC 3081 and MCG−03-34-064, a pivot was not put between the CO_2 and CO absorption band because the two galaxies show the [Mg VII] line at 4.5 μm. Figure 6.4 displays the individual continuum-normalized absorption spectra and their average. The average exhibit a double-peaked profile at 4.67 μm that can be identified as the P- and R-branches of the ro-vibrational transition of CO, in addition to the Brα line and the CO_2 absorption.

Before proceeding to the gas-model fitting, to approximately find the difference in the CO absorption by galaxies' characteristics, we stacked the spectra dividing the sample by the infrared luminosity and the optical classifications. The results for each luminosity range and each optical classification are shown in Figures 6.5 and 6.6, respectively. The former figure reveals that the CO absorption becomes deeper as the infrared luminosity L_{IR} becomes higher. The latter figure indicates that the absorption in Sy1s is weaker than that in Sy2s, which is consistent with the fundamental prediction in our observational strategy. On the other hand, the figure also shows that the absorption in AGN-starburst composites and LINERs are possibly stronger than in Sy2s. This difference may represent the contribution of nuclear starburst to the formation of a torus. These results are discussed in detail in Section 6.6. Figure 6.5 also shows that the CO_2 band is broader in IRGs than U/LIRGs. This may reflect the effect that the dominant component of the CO_2 absorption changes from nuclear gas to ice around young stellar objects as L_{IR} decreases.

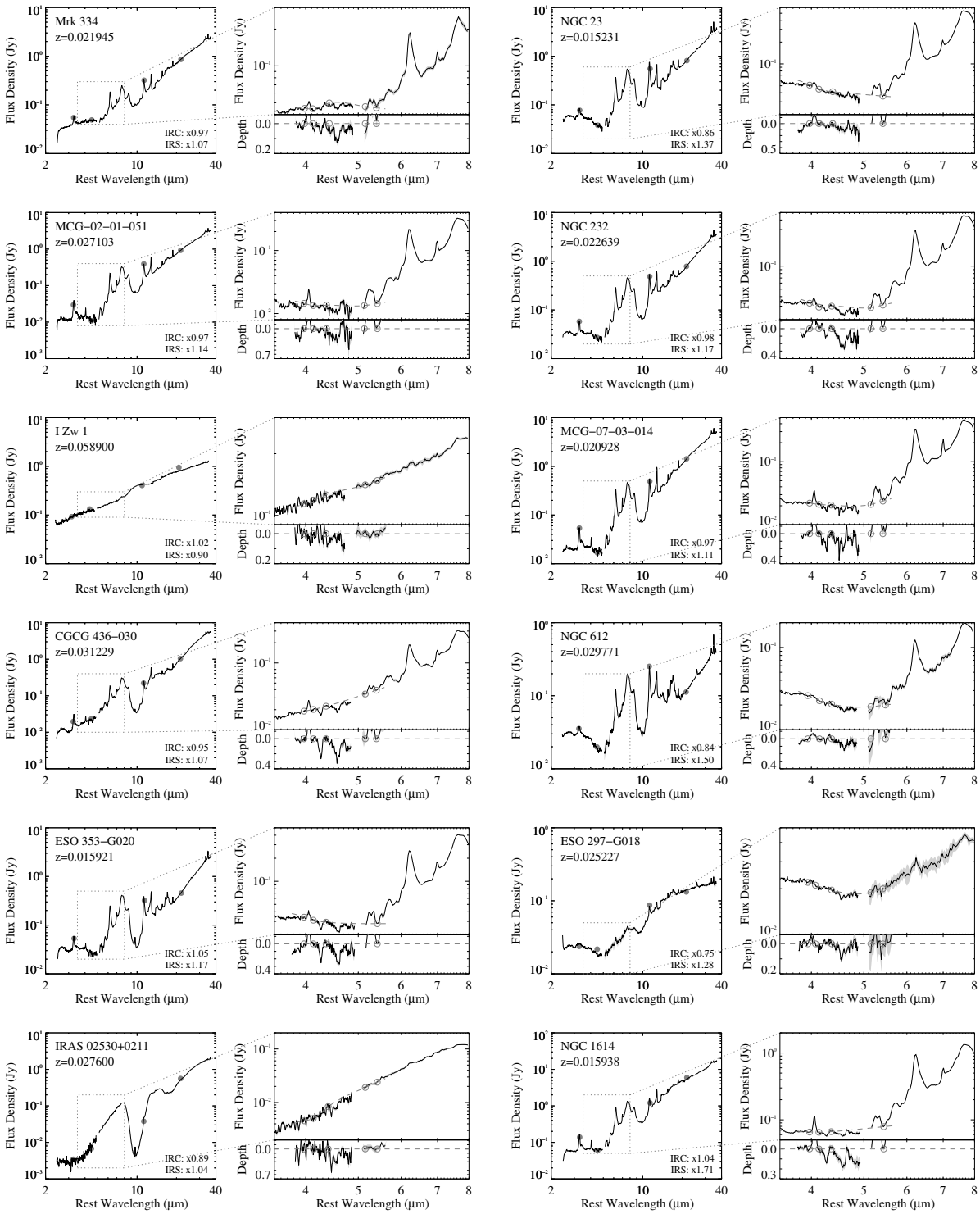

Figure 6.2: Combined spectrum and the adopted continuum of each target. In all panels, black solid lines show the *AKARI*/IRC and *Spitzer*/IRS spectra, and gray shades denote the uncertainties of them. The two spectra are scaled to match the *WISE* photometric flux densities, which are shown as gray filled points in the left panel. The scaling factors are noted in the right bottom corner. The right top panel is a zoom-in plot around the CO absorption. A dashed line is the adopted continuum: a cubic spline curve interpolating pivots shown as open circles. The right bottom panel displays the resultant optical depth.

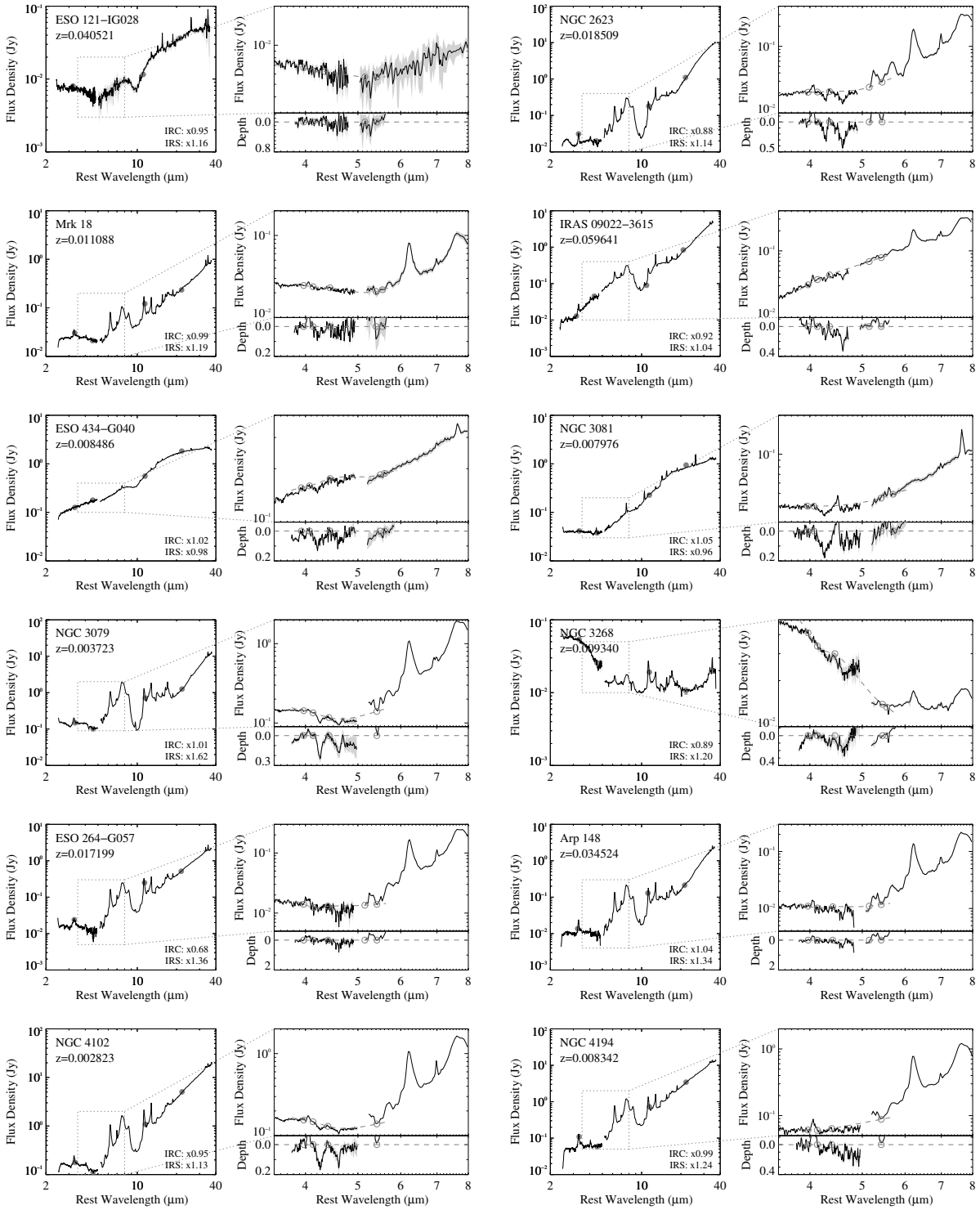

Figure 6.2: (*Continued*)

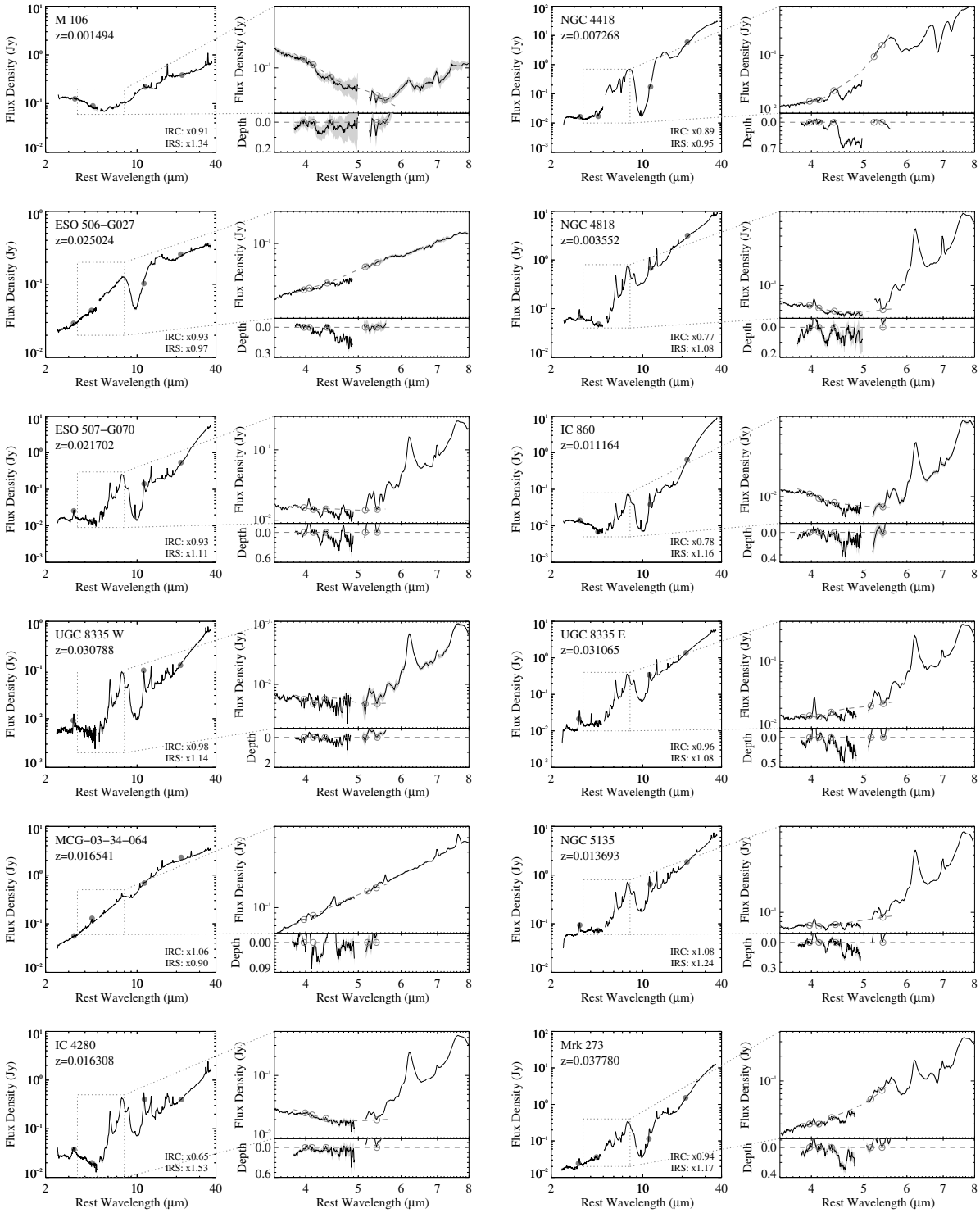

Figure 6.2: (*Continued*)

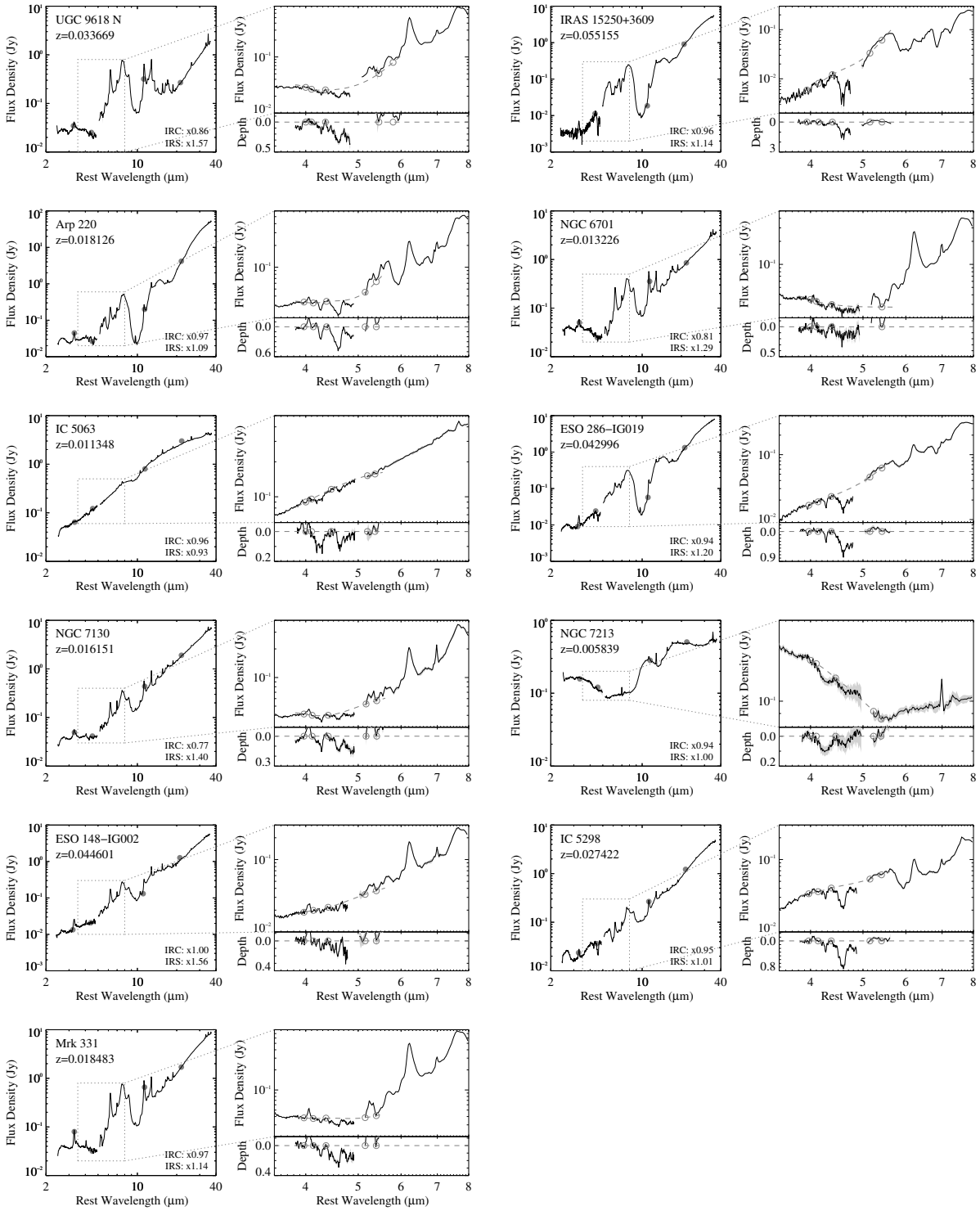

Figure 6.2: (*Continued*)

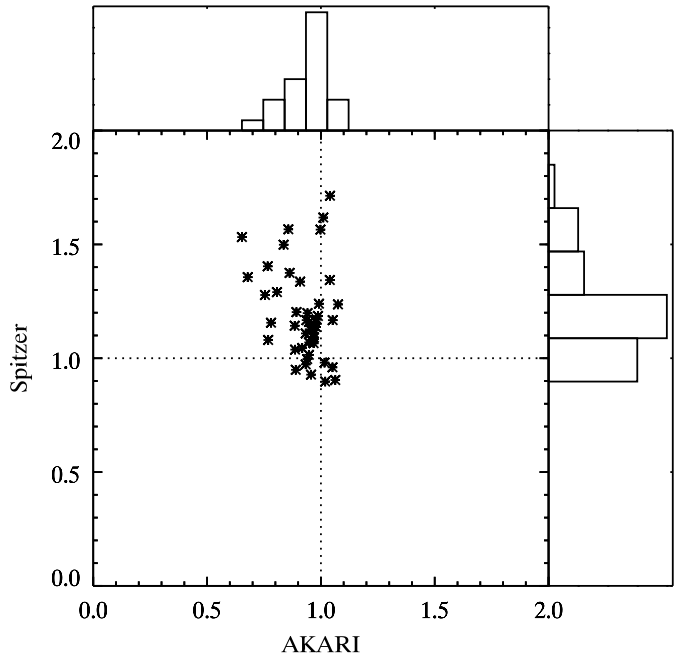

Figure 6.3: Scatter plot of the scaling factors for the *AKARI*/IRC and *Spitzer*/IRS spectra derived based on the WISE photometric fluxes.

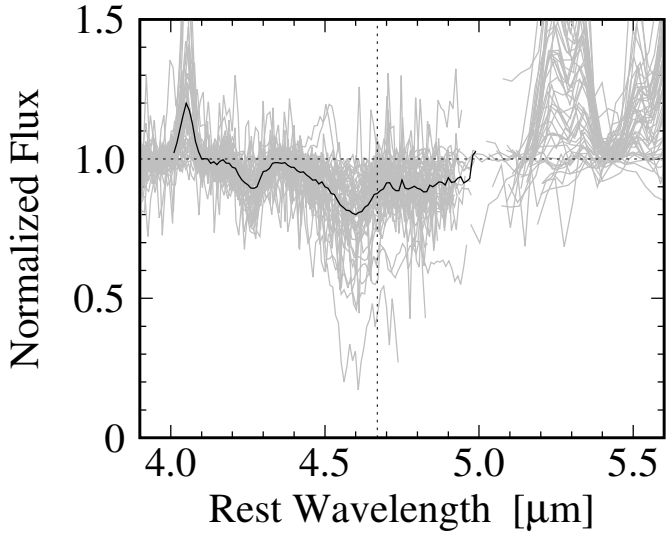

Figure 6.4: Line-subtracted CO absorption profiles (gray) and the average of the sample (black). Only the data from *AKARI* were used for the average. The vertical dotted line shows the predicted position of the band center.

Table 6.4: Measured and estimated line fluxes

Object	Measured			Estimated		
	Brα	H_2 0–0 S(3)	H_2 0–0 S(7)	Pfβ	T_{ex}	H_2 0–0 S(9)
Mrk 334	0.543±0.044	< 0.518	< 0.497	0.109±0.009		
NGC 23	0.717±0.096	0.305±0.062	0.849±0.042	0.143±0.019	932 ± 39	0.038±0.009
MCG−02-01-051	0.874±0.041	< 0.158	0.228±0.030	0.175±0.008		
NGC 232	0.564±0.045	< 0.198	0.415±0.026	0.113±0.009		
I Zw 1	< 0.290	< 0.739	< 0.650			
MCG−07-03-014	1.070±0.034	< 0.373	0.346±0.062	0.214±0.007		
CGCG 436-030	0.700±0.026	< 0.427	0.274±0.049	0.140±0.005		
NGC 612	< 0.147	< 0.254	< 0.170			
ESO 353-G020	0.646±0.039	0.342±0.050	0.616±0.026	0.129±0.008	1021 ± 34	0.056±0.010
ESO 297-G018	< 0.095	< 0.397	< 0.217			
IRAS 02530+0211	0.095±0.023	< 0.357	0.114±0.028	0.019±0.005		
NGC 1614	4.177±0.120	< 0.705	0.563±0.096	0.835±0.024		
ESO 121-IG028	< 0.035	< 0.195	< 0.095			
NGC 2623	0.537±0.036	< 0.585	< 0.451	0.107±0.007		
Mrk 18	0.264±0.026	< 0.363	< 0.299	0.053±0.005		
IRAS 09022−3615	0.790±0.040	< 0.607	0.489±0.082	0.158±0.008		
ESO 434-G040	0.688±0.125	< 1.189	< 0.625	0.138±0.025		
NGC 3081	0.232±0.043	< 0.662	< 0.492	0.046±0.009		
NGC 3079	< 1.578	3.141±0.171	1.896±0.085		1339 ± 27	1.056±0.075
NGC 3268	< 0.330	< 0.041	< 0.046			
ESO 264-G057	< 0.409	< 0.190	0.224±0.021			
Arp 148	0.356±0.030	< 0.221	0.197±0.046	0.071±0.006		
NGC 4102	2.325±0.164	0.411±0.121	1.127±0.090	0.465±0.033	935 ± 57	0.051±0.018
NGC 4194	2.091±0.118	< 0.305	0.664±0.114	0.418±0.024		
M 106	< 0.799	< 0.493	0.665±0.145			
NGC 4418	< 0.142	< 1.022	0.362±0.045			
ESO 506-G027	0.131±0.038	< 0.609	< 0.309	0.026±0.008		
NGC 4818	1.223±0.089	< 0.414	0.703±0.081	0.245±0.018		
ESO 507-G070	0.421±0.031	0.457±0.068	0.794±0.037	0.084±0.006	1029 ± 35	0.077±0.014
IC 860	< 0.066	0.149±0.042	0.251±0.020		1036 ± 67	0.026±0.009
UGC 8335 W	0.130±0.024	< 0.205	< 0.175	0.026±0.005		
UGC 8335 E	1.314±0.042	< 0.376	0.230±0.057	0.263±0.008		
MCG−03-34-064	0.868±0.052	< 0.398	< 0.186	0.174±0.010		
NGC 5135	1.221±0.087	0.319±0.104	0.936±0.087	0.244±0.017	923 ± 61	0.038±0.015
IC 4280	< 0.224	< 0.086	0.395±0.037			
Mrk 273	0.366±0.070	< 1.244	0.768±0.086	0.073±0.014		
UGC 9618 N	0.114±0.037	0.218±0.050	0.379±0.043	0.023±0.007	1028 ± 58	0.037±0.010
IRAS 15250+3609	0.149±0.023	< 0.689	< 0.168	0.030±0.005		
Arp 220	0.574±0.029	1.352±0.190	0.607±0.045	0.115±0.006	1463 ± 72	0.552±0.096
NGC 6701	0.565±0.079	0.208±0.043	0.659±0.035	0.113±0.016	909 ± 37	0.024±0.006
IC 5063	0.775±0.072	< 0.863	< 1.250	0.155±0.014		
ESO 286-IG019	0.099±0.026	< 0.769	0.377±0.065	0.020±0.005		
NGC 7130	0.532±0.040	< 0.739	0.598±0.131	0.106±0.008		
NGC 7213	< 1.086	< 0.572	< 0.679			
ESO 148-IG002	0.522±0.031	< 0.632	0.298±0.091	0.104±0.006		
IC 5298	0.366±0.063	< 0.499	0.219±0.072	0.073±0.013		
Mrk 331	1.229±0.051	< 0.347	0.480±0.062	0.246±0.010		

NOTE—The line fluxes are presented in units of 10^{-13} erg s^{-1} cm^{-2}, and the excitation temperature is presented in units of K.

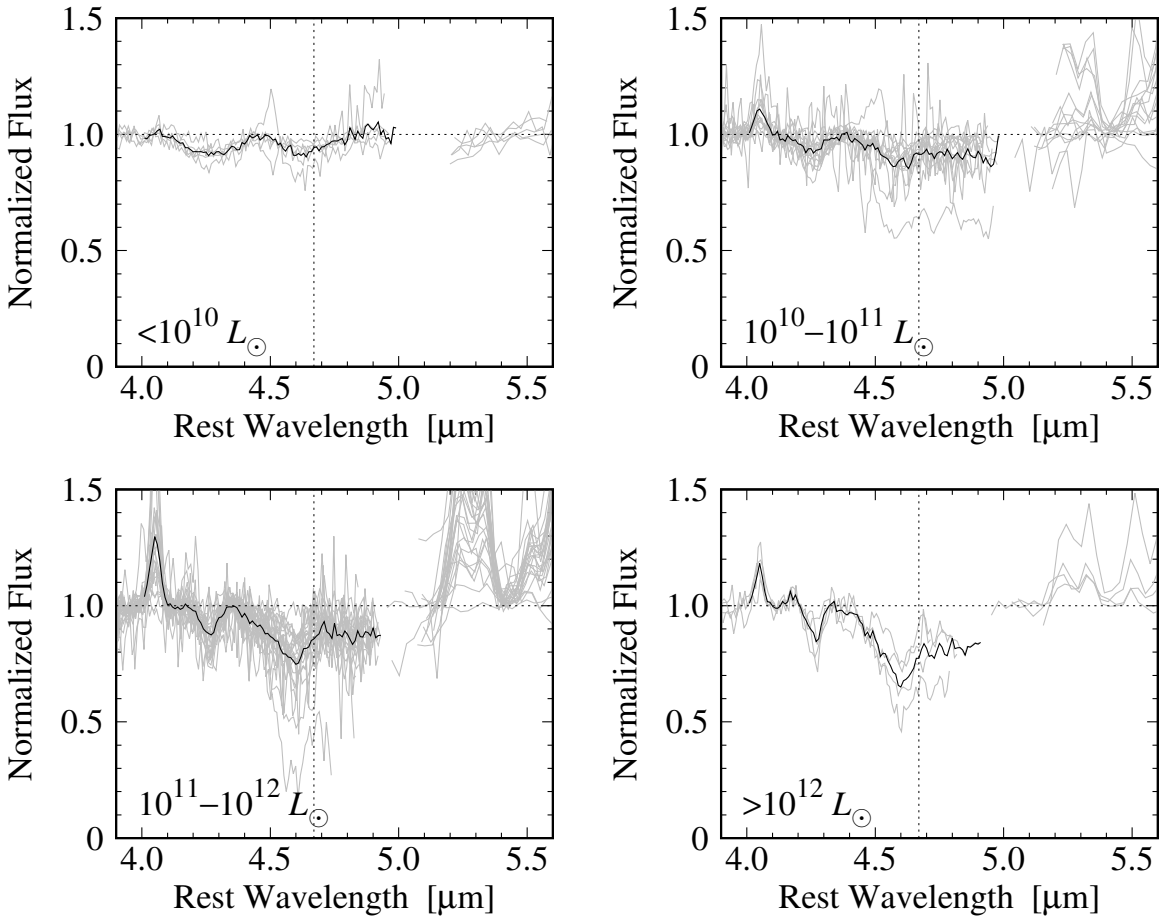

Figure 6.5: Observed CO absorption profiles divided by classes of the infrared luminosity. Gray lines represent individual spectra, and black lines show the average in the classes. Only the data from *AKARI* were used for the average.

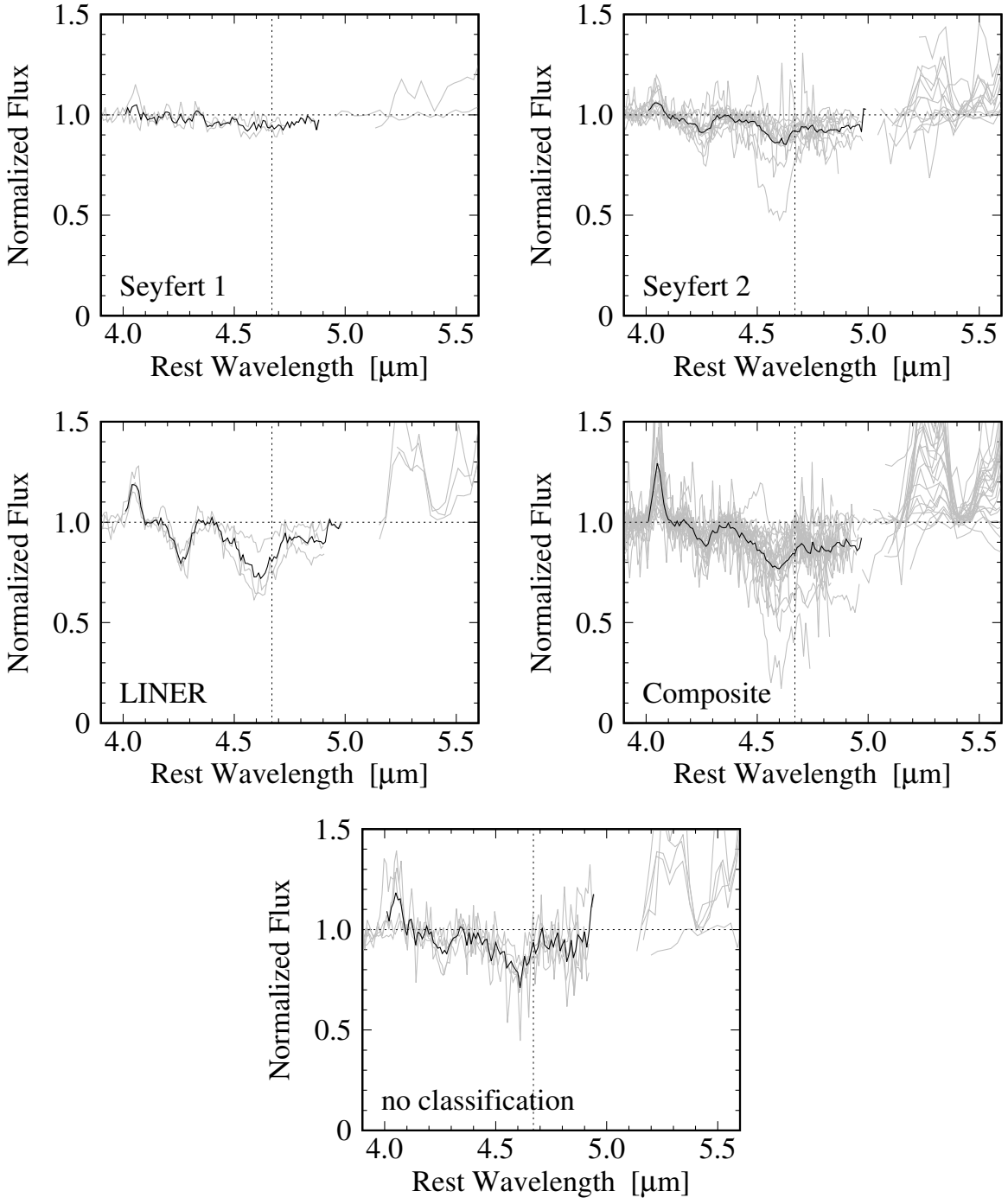

Figure 6.6: Same as Figure 6.5 but divided by the optical classes.

We fitted the observed absorption spectra with the same model with Chapter 5. The fitting range was determined as the interval from the wavelength of the pivot of the continuum between the CO_2 and CO bands to the end of the *AKARI*/IRS coverage ($\lambda_{\rm obs} = 5$ μm). For NGC 3081 and MCG−03-34-064, where we did not place that pivot, the beginning wavelength was set as the intersection of the continuum and the spectrum. Because of the lower signal-to-noise ratio of the *AKARI* spectra in the post cryogenic phase, it is difficult to constrain the degeneracy between the CO column density $N_{\rm CO}$ and the velocity width $v_{\rm turb}$ for the current sample. Hence we fixed $v_{\rm turb}$ to 63 km s^{-1}, which is the mean value obtained in the analysis for the cryogenic phase (see Table 5.4), and used the other two, the column density $N_{\rm CO}$ and the temperature $T_{\rm CO}$, as free parameters. For objects in which $N_{\rm CO}$ and $T_{\rm CO}$ cannot be constrained simultaneously with the 99% confidence level, we further fixed $T_{\rm CO}$ and found only the best-fit $N_{\rm CO}$. See Section 6.5 for the value of the fixed $T_{\rm CO}$.

6.5 Results

In 33 out of the 47 galaxies, both the column density $N_{\rm CO}$ and the temperature $T_{\rm CO}$ were successfully obtained with $v_{\rm turb}$ fixed. Figure 6.7 lists the best-fit gas model for each of them. The upper part of Table 6.5 summarizes the obtained parameters. A large fraction of the sample shows large column densities of $N_{\rm CO} > 10^{19}$ cm^{-2} with high temperatures of $T_{\rm CO} \sim$ several $\times\, 10^2$ K, similar to the results in Chapter 5. The average $T_{\rm CO}$ of these 33 objects and the targets of Chapter 5 is 623 K. In the remainder 14 galaxies, $T_{\rm CO}$ was fixed to this average. The result of the fitting with both $v_{\rm turb}$ and $T_{\rm CO}$ fixed are shown in Figure 6.8 and tabulated in the lower part of Table 6.5. For I Zw 1, whose spectrum considerably differs from the double-blanched profile, and for M 106 and NGC 7213, whose flux errors are large, only 99% upper limits were estimated.

Lutz et al. (2004) searched for the signature of the CO absorption in nearby 31 AGNs with *ISO* and found no significant detection in any of them. Their sample is summarized in Table C.2. Among the 31 AGNs, NGC 7213 and IC 5063 are common with our sample. In NGC 7213, we also did not find significant absorption. On the other hand, in IC 5063, we newly detected the CO feature previously not found, owing to the higher sensitivity of *AKARI* than that of *ISO*.

Table 6.5: Best-Fit parameters and goodness of fit

Object	$\log N_{\rm CO}$ (in cm^{-2})	$T_{\rm CO}$ (K)	χ^2/dof
Mrk 334	$19.54^{+0.33}_{-0.33}$	1418^{+19}_{-35}	71.6/47
MCG−02-01-051	$19.38^{+0.31}_{-0.27}$	1254^{+68}_{-98}	96.9/51
NGC 232	$18.76^{+0.11}_{-0.07}$	842^{+125}_{-101}	127.3/54
MCG−07-03-014	$19.52^{+0.23}_{-0.22}$	1340^{+30}_{-44}	200.6/55
CGCG 436-030	$18.59^{+0.03}_{-0.03}$	630^{+65}_{-55}	193.6/50
ESO 353-G020	$18.48^{+0.03}_{-0.03}$	456^{+66}_{-56}	212.8/57
IRAS 02530+0211	$19.33^{+0.18}_{-0.16}$	1193^{+57}_{-67}	135.6/47

Table 6.5: (*Continued*)

Object	$\log N_{\rm CO}$ (in cm^{-2})	$T_{\rm CO}$ (K)	χ^2/dof
NGC 1614	$19.32^{+0.20}_{-0.23}$	1283^{+44}_{-76}	85.5/58
NGC 2623	$18.75^{+0.04}_{-0.04}$	328^{+45}_{-39}	322.7/56
IRAS 09022−3615	$18.55^{+0.03}_{-0.03}$	269^{+29}_{-26}	347.9/38
ESO 434-G040	$17.86^{+0.12}_{-0.09}$	142^{+89}_{-56}	141.5/52
NGC 3081	$18.09^{+0.05}_{-0.05}$	376^{+141}_{-87}	54.4/42
NGC 3079	$18.35^{+0.07}_{-0.07}$	425^{+163}_{-123}	29.0/56
Arp 148	$18.88^{+0.09}_{-0.08}$	748^{+126}_{-112}	83.8/43
NGC 4102	$18.02^{+0.06}_{-0.06}$	275^{+147}_{-89}	70.3/59
NGC 4418	$19.58^{+0.02}_{-0.02}$	545^{+18}_{-18}	1429.3/56
ESO 506-G027	$18.38^{+0.03}_{-0.03}$	537^{+57}_{-50}	281.9/51
ESO 507-G070	$19.14^{+0.20}_{-0.17}$	1139^{+85}_{-109}	95.6/54
IC 860	$18.54^{+0.05}_{-0.05}$	564^{+125}_{-96}	105.5/54
UGC 8335 W	$20.12^{+0.35}_{-0.29}$	1259^{+46}_{-60}	112.5/52
UGC 8335 E	$19.13^{+0.14}_{-0.10}$	941^{+111}_{-109}	81.7/51
MCG−03-34-064	$17.51^{+0.09}_{-0.09}$	161^{+77}_{-53}	54.8/37
NGC 5135	$18.19^{+0.04}_{-0.04}$	345^{+67}_{-54}	140.4/51
Mrk 273	$18.75^{+0.08}_{-0.06}$	742^{+124}_{-103}	38.5/47
UGC 9618 N	$18.86^{+0.04}_{-0.03}$	602^{+89}_{-67}	240.0/50
IRAS 15250+3609	$21.23^{+0.17}_{-0.16}$	209^{+17}_{-15}	169.1/36
Arp 220	$18.97^{+0.02}_{-0.02}$	575^{+32}_{-29}	767.6/55
NGC 6701	$19.18^{+0.52}_{-0.60}$	1239^{+115}_{-489}	60.6/56
IC 5063	$18.04^{+0.04}_{-0.04}$	161^{+26}_{-23}	112.2/48
ESO 286-IG019	$19.51^{+0.04}_{-0.04}$	293^{+18}_{-16}	303.5/43
NGC 7130	$18.30^{+0.04}_{-0.04}$	562^{+101}_{-79}	241.2/53
IC 5298	$19.31^{+0.03}_{-0.03}$	537^{+43}_{-36}	670.1/51
Mrk 331	$19.49^{+0.12}_{-0.12}$	1258^{+28}_{-35}	128.3/56
NGC 23	$18.31^{+0.04}_{-0.05}$	623 (fixed)	50.7/55
I Zw 1	< 17.76	623 (fixed)	164.3/39
NGC 612	$18.17^{+0.04}_{-0.04}$	623 (fixed)	47.8/52
ESO 297-G018	$17.91^{+0.04}_{-0.04}$	623 (fixed)	98.7/53
ESO 121-IG028	$18.15^{+0.14}_{-0.18}$	623 (fixed)	63.2/47
Mrk 18	$17.79^{+0.06}_{-0.07}$	623 (fixed)	122.8/51
NGC 3268	$18.34^{+0.07}_{-0.08}$	623 (fixed)	51.2/51
ESO 264-G057	$18.74^{+0.08}_{-0.08}$	623 (fixed)	56.6/52
NGC 4194	$18.52^{+0.03}_{-0.03}$	623 (fixed)	197.0/58
M 106	< 18.11	623 (fixed)	3.1/55
NGC 4818	$18.16^{+0.05}_{-0.05}$	623 (fixed)	32.7/58
IC 4280	$18.18^{+0.08}_{-0.09}$	623 (fixed)	48.4/58
NGC 7213	< 18.02	623 (fixed)	11.4/53
ESO 148-IG002	$18.42^{+0.03}_{-0.03}$	623 (fixed)	118.6/40

NOTE—The upper and lower parts tabulate the results of the fitting with only $v_{\rm turb}$ fixed and with $v_{\rm turb}$ and $T_{\rm CO}$ fixed, respectively. All errors are quoted at the 68% joint confidence level for the respective number of free parameters ($\Delta\chi^2 = 2.28$ and 0.99 for the upper and lower parts, respectively).

6.6 Discussion

6.6.1 The N_{CO}–T_{CO} Relation

Figure 6.9 shows the scatter of N_{CO} and T_{CO} obtained in the first two-parameter fitting. Note that Figure 6.9 covers a wider parameter space than Figure 5.7 does in Chapter 5. The scatter in the current figure has two branches labeled as A and B in Figure 6.9. Branch A is the trend that extends from $N_{CO} \sim 10^{19}$ cm^{-2} and $T_{CO} \sim 600$ K to larger N_{CO} with decreasing T_{CO}. This trend corresponds to that seen in Figure 5.7. The other, Branch B, is nearly vertical in $N_{CO} = 10^{18}$–10^{19} cm^{-2}. However, this branch seems to be an artificial pattern that emerges because the absorption with N_{CO} smaller than this border is too shallow to constrain the gas model by the *AKARI* spectrum. Remind that this figure does not show the models that cannot be determined when both N_{CO} and T_{CO} are taken free.

Regardless of the distinction between the two branches, similar to the result of the previous chapter, most of the best-fit models have large CO column densities larger than 10^{18} cm^{-2} and high temperatures of $\sim 10^2$ K. Such large-column warm gas can be considered to be heated by X-ray photons, as discussed in Section 5.5.3.

It is notable that all the galaxies in Branch A, Arp 220, IC 5298, NGC 4418, ESO 286-IG019, and IRAS 15250+3609, and the targets in Chapter 5, show the 6.0 μm H_2O ice absorption and the 6.9 and 7.3 μm hydrogenated amorphous carbon absorptions (e.g., Spoon et al. 2001; Stierwalt et al. 2014, see also Figure 6.2). This indicates that the trend likely represents the relation in heavily obscured AGNs.

In Branch B, T_{CO} reaches over 1000 K with column densities of $N_{CO} \sim 10^{19}$ cm^{-2}. Such high temperatures, which have not been found in Chapter 5, are mainly seen in AGN-starburst composites. If the spatial extent of each source lowers the effective spectral resolution and broadens the band profile, the current fitting method would overestimate the gas temperature for that source. However, this interpretation is questionable because such broadening is not observed in the Brα line (see Figure 6.4). We suggest that the obscuration by an AGN torus is also effective in composites and speculate that the gas temperature higher in composite sources than in typical Sy2s.

6.6.2 Comparison with the 9.7 μm Silicate Absorption

Stierwalt et al. (2014) measured the optical depth of the 9.7 μm silicate dust absorption for the GOALS sample based on a multi-component spectral decomposition analysis. Twenty-seven galaxies of their sample are in common with our sample. As in Section 5.5.6, we compared the hydrogen column densities estimated from the CO absorption and from the optical depth of the silicate feature. The former ($N_{H,4.67}$) and the latter ($N_{H,9.7}$) were calculated as in the previous ways. The two column densities are plotted in Figure 6.10. This figure reproduces the previous magnitude relation that $N_{H,4.67}$ is similar to or a bit larger than $N_{H,9.7}$, supporting the picture that the warm CO gas and the silicate dust approximately coexist in the same region.

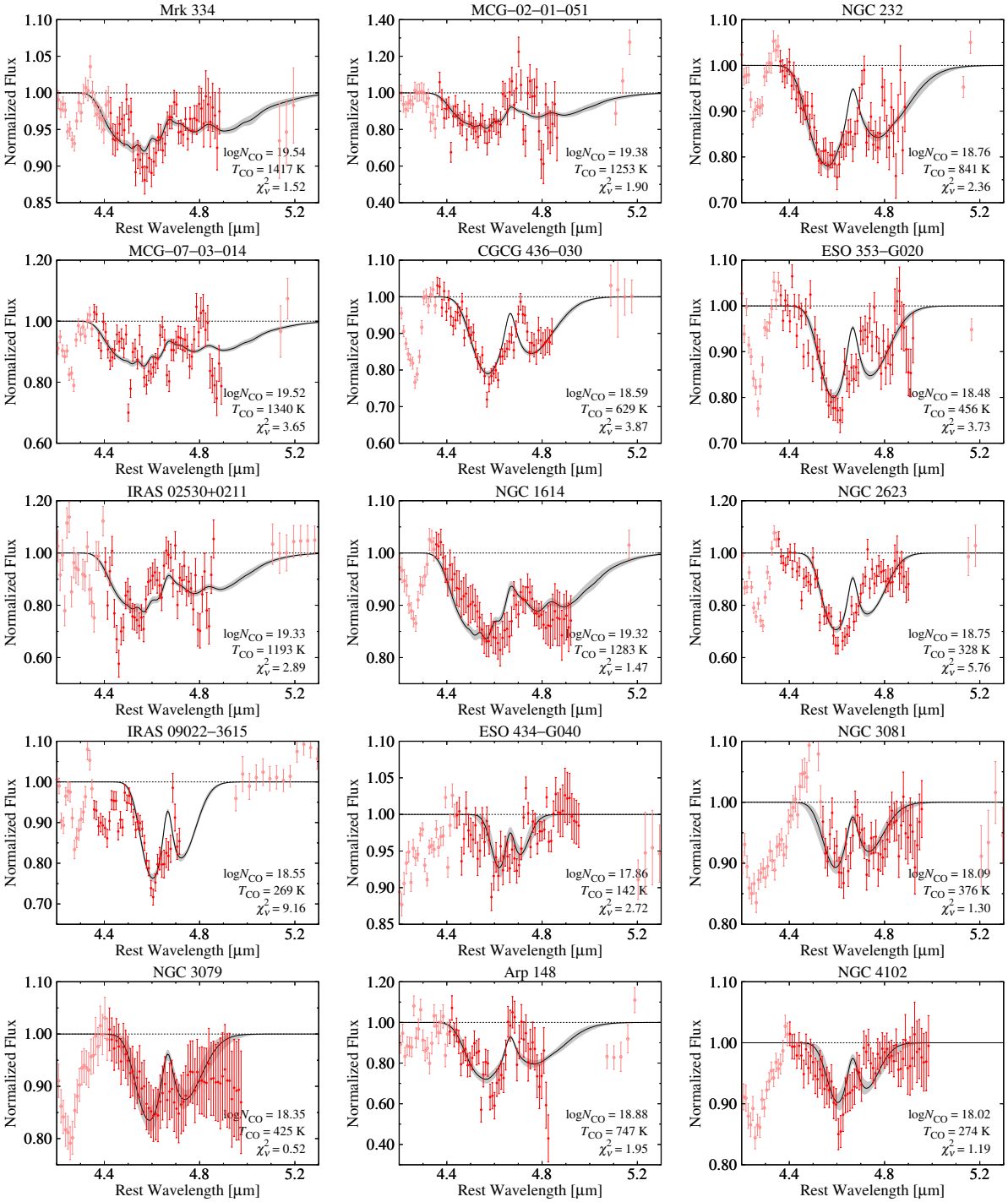

Figure 6.7: Each panel shows the result of the gas model fitting with $v_{\rm turb}$ fixed. Red closed and pink open circles show the data used and unused for the fitting, respectively. A black solid line denotes the best-fit model. A gray shaded area indicates the 68% confidence range. The best-fit parameters and the goodness-of-fit $\chi^2_\nu \equiv \chi^2/{\rm dof}$ are noted at the right bottom corner.

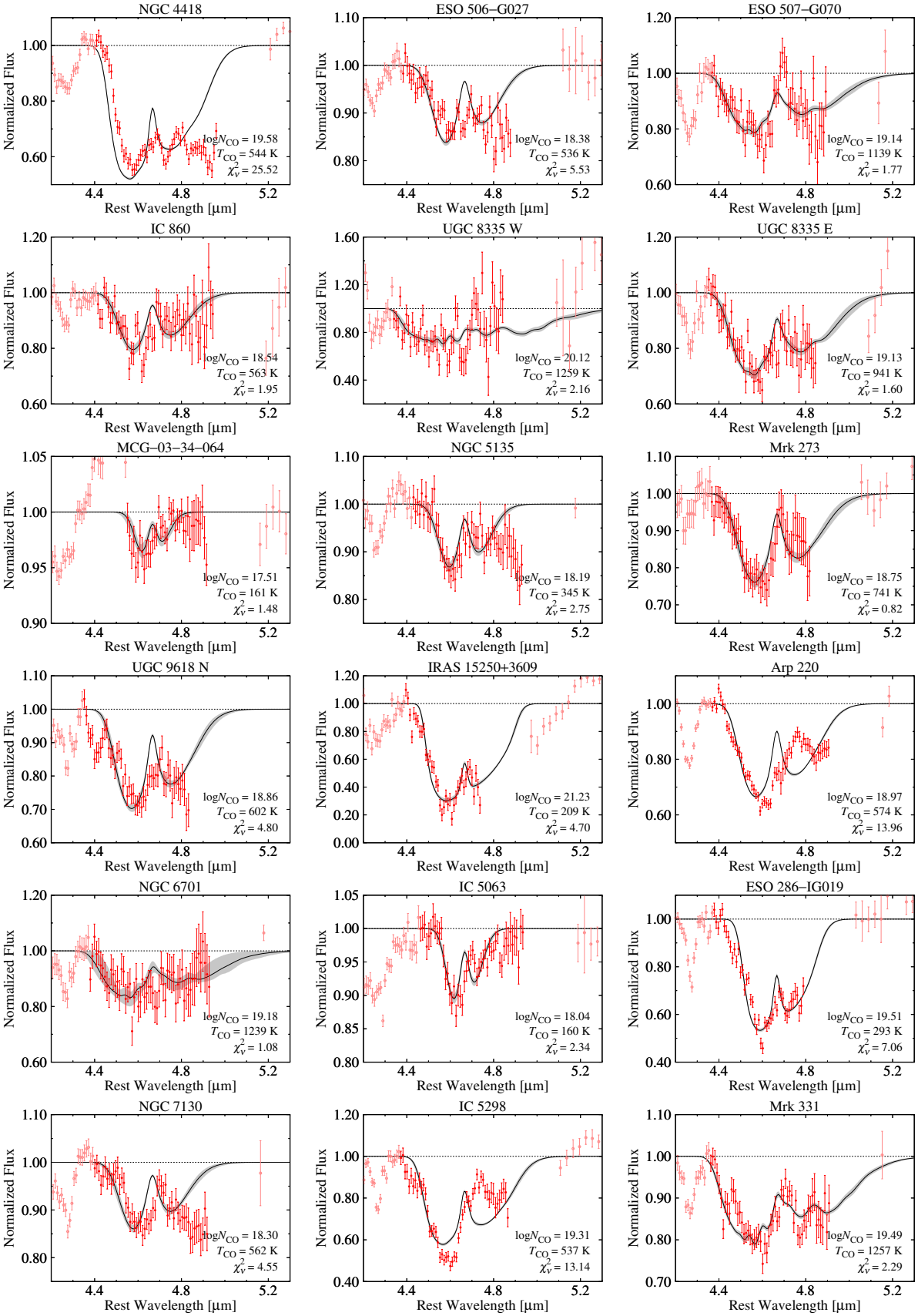

Figure 6.7: (*Continued*)

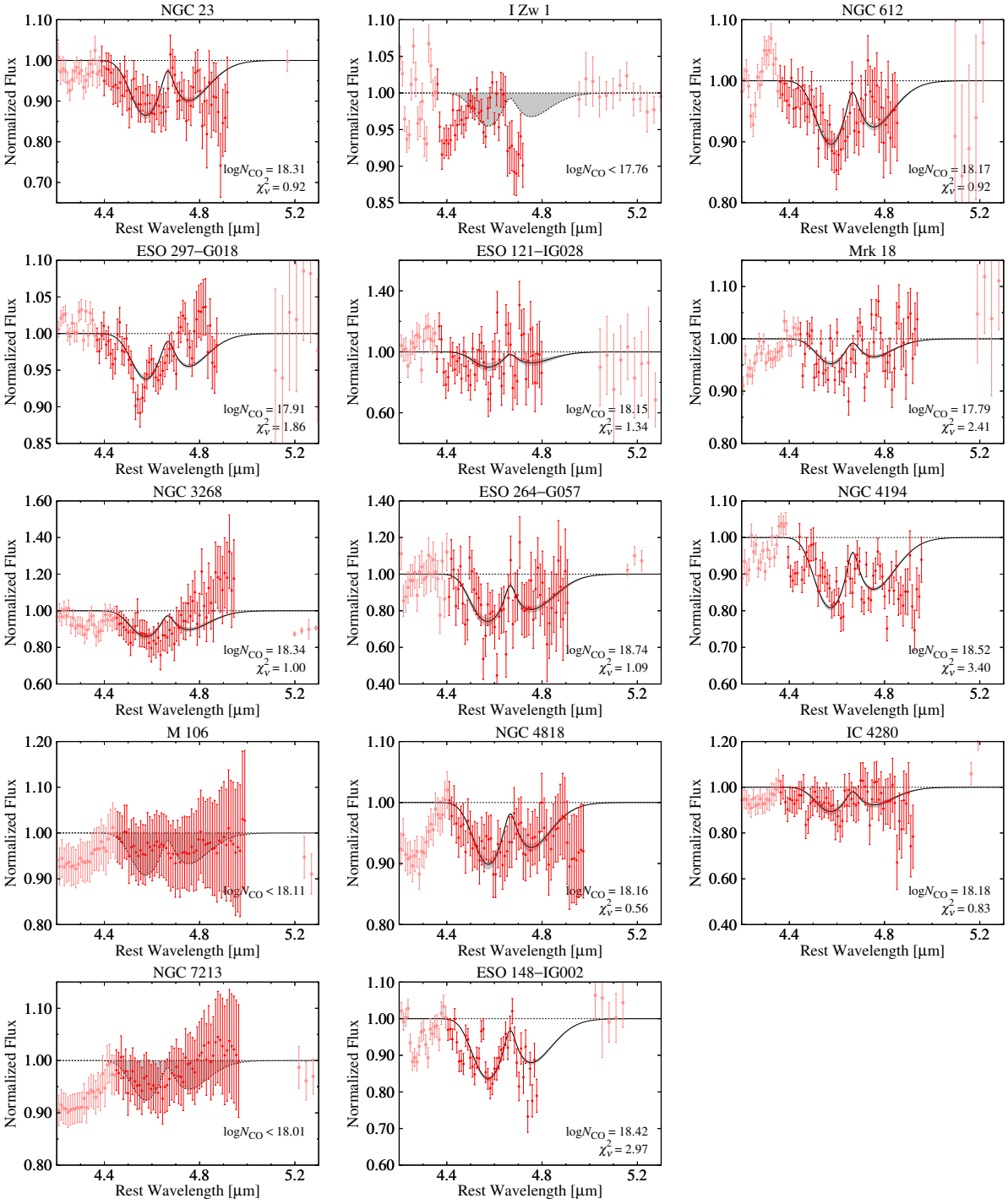

Figure 6.8: Each panel shows the result of the gas model fitting with both $v_{\rm turb}$ and $T_{\rm CO}$ fixed. Symbols are the same as Figure 6.7, but in I Zw 1, M 106, and NGC 7213, a dotted line indicates the 99% upper limit ($\Delta\chi^2 = 6.63$).

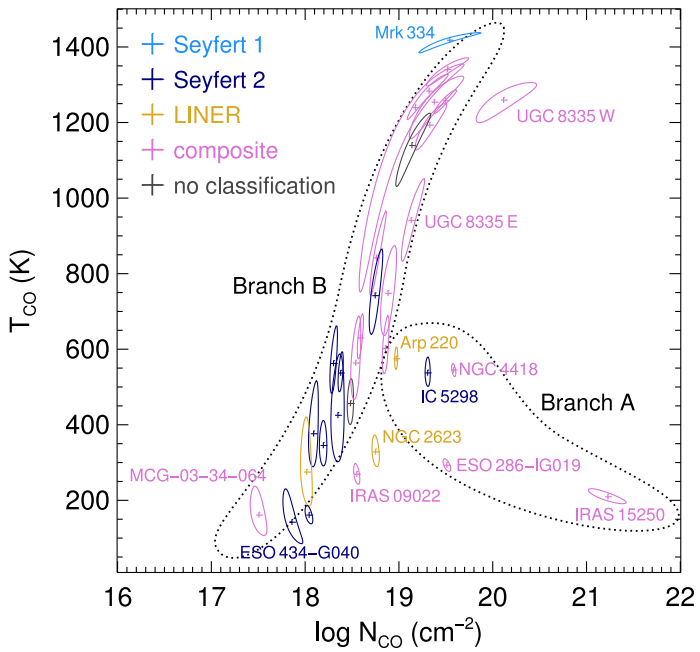

Figure 6.9: Scatter plot of $N_{\rm CO}$ and $T_{\rm CO}$ obtained in the model fitting with $v_{\rm turb}$ fixed. Cross symbols indicates the best-fits and closed curves show the 68% joint confidence range. Some outlying points are labeled with their object names. Dotted closed curves indicate the two branches A and B discussed in the text.

6.6.3 Luminosity Dependence

As seen in Figure 6.5, the CO absorption is deeper in U/LIRGs. Figure 6.11(a) plots the CO column density $N_{\rm CO}$ against the infrared luminosity $L_{\rm IR}$. While in low-luminosity galaxies of $L_{\rm IR} < 10^{10.7}\ L_\odot$ the column density $N_{\rm CO}$ did not exceed $10^{18.5}$ cm^{-2}, a large fraction of U/LIRGs showed high $N_{\rm CO} > 10^{19}$ cm^{-2}. This indicates that intense absorption by CO occurs in dusty environments. Combined with the discussion of the X-ray heating, this result supports the suggestion that the CO absorption probes the obscuring material in the vicinity of AGNs.

This luminosity dependence can explain why the 31 AGNs observed by Lutz et al. (2004) did not show any the CO feature. Table C.2 tabulates the IR luminosity of those AGNs and indicates that they are mainly IRGs. At such low luminosities, as 6.11(a) shows, a galaxy of large $N_{\rm CO}$ is rare. We thus consider that there was little chance to find the CO absorption, which resulted in the non-detection.

In X-ray surveys, the fraction of obscured objects, sometimes called as obscured fraction, has a peak around a hard X-ray luminosity of $L_{\rm X} \sim 10^{43}$ erg s^{-1} (Brightman & Nandra 2011b,a; Burlon et al. 2011). We tested whether the fraction of large $N_{\rm CO}$ has a similar luminosity dependence. Although X-ray analyses in literature are not available for all of our sample galaxies at present, it is known that X-ray luminosities correlate with mid-IR luminosities, where $L_{\rm X} \sim 10^{43}$ erg s^{-1} corresponds to the *IRAS* 12 μm luminosity of $10^{10}\ L_\odot$ (e.g., McKernan et al. 2009). We derived the rest 14 μm luminosity $L_{14\,\mu{\rm m}} \equiv \nu L_\nu(14\ \mu{\rm m})$ for each galaxy by measuring $F_\nu(14\ \mu{\rm m})$ from the spectrum in Figure 6.2. This wavelength is expected to avoid PAH emissions

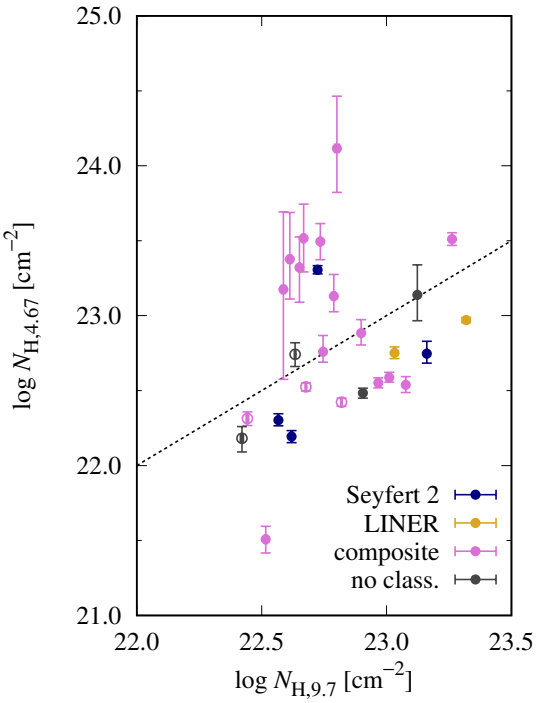

Figure 6.10: Comparison of the hydrogen column density converted from the CO column density (ordinate; $N_{\rm H,4.67}$) with that estimated from the optical depth of the 9.7 μm silicate dust absorption measured by Stierwalt et al. (2014) (abscissa; $N_{\rm H,9.7}$). Filled and open points represent the results from the fitting with only $v_{\rm turb}$ fixed and from that with both $v_{\rm turb}$ and $T_{\rm CO}$ fixed, respectively. Galaxies with $T_{\rm CO} > 1000$ K are emphasized in double circles. Error bars represent the 68% joint confidence range. A dotted line denotes the identity.

and silicate dust absorptions (Spoon et al. 2007). Figure 6.11(b) plots $N_{\rm CO}$ against $L_{14\,\mu{\rm m}}$ and shows that the scatter of $N_{\rm CO}$ has a peak around $L_{14\,\mu{\rm m}} \sim 10^{10}\ L_\odot$. Figure 6.12 is a histogram of $\log N_{\rm CO}$ plotted for two groups of $L_{14\,\mu{\rm m}} > 10^{9.5}\ L_\odot$ and $L_{14\,\mu{\rm m}} < 10^{9.5}\ L_\odot$. It clearly indicates that the more luminous group has a lager scatter of $N_{\rm CO}$ than the less luminous group. Therefore, based on the approximation that $L_{14\,\mu{\rm m}}$ is nearly equal to the IRAS 12 μm luminosity, the obscured fraction measured in the CO band is consistent with that measured in X-rays. This result supports the identification that obscuring material observed by X-rays is composed of molecular gas.

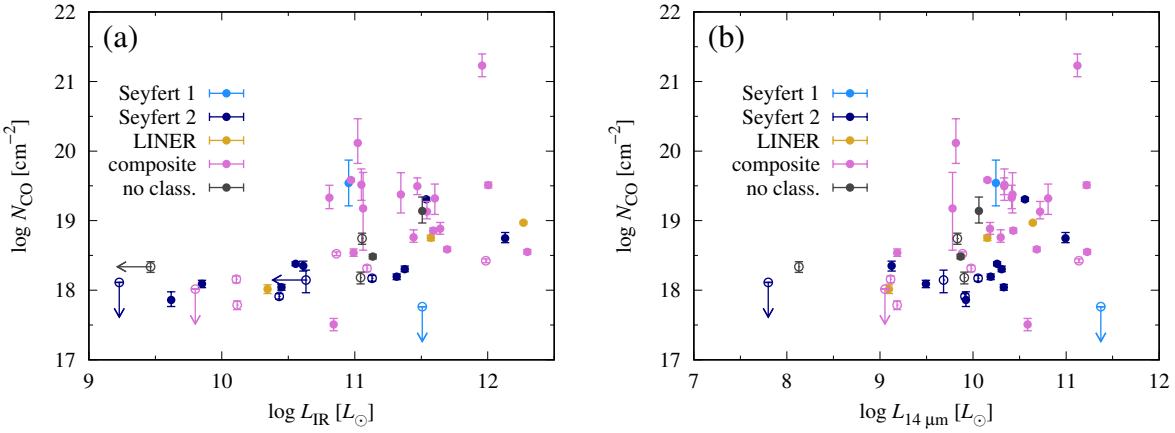

Figure 6.11: (a) Plot of $N_{\rm CO}$ against $L_{\rm IR}$. Filled and open points represent the results from the fitting with only $v_{\rm turb}$ fixed and from that with both $v_{\rm turb}$ and $T_{\rm CO}$ fixed, respectively. Error bars represent the 68% joint confidence range. (b) Same as (a) but for $L_{14\,\mu{\rm m}}$.

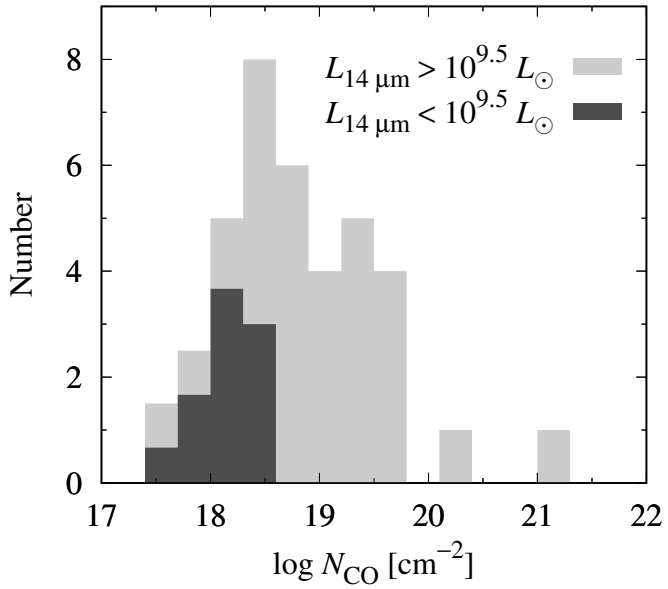

Figure 6.12: Histograms of $\log N_{\rm CO}$ for two groups of divided at $L_{14\,\mu{\rm m}} = 10^{9.5}\ L_\odot$.

6.6.4 Difference by Optical Classifications

The CO column density toward one of the two Sy1s, I Zw 1, was evaluated less than $N_{\rm CO} < 10^{17.8}$ cm^{-2}. This upper limit is significantly lower than the average $N_{\rm CO}$ in Sy2s ($10^{18.5}$ cm^{-2}), being consistent with our prediction that the CO absorption is observed when the AGN torus is edge-on. In contrast, the other one, Mrk 334, had a large $N_{\rm CO}$ of $10^{19.5}$ cm^{-2}. Although Mrk 334 was aggregated into Sy1s here, however, the original classification for it by Véron-Cetty & Véron (2010) is Seyfert 1.8. Thus its absorption could be attributed to a partial obscuration by a torus viewed moderately edge-on.

Figure 6.11 shows that AGN-starburst composites on average have larger Nco than pure Sy2s. Spoon et al. (2003) observed another composite galaxy NGC 4945 with *ISO* and detected the near-IR CO absorption, but the CO column density they obtained ($10^{18.3}$ cm^{-2}) is moderately small compared to our results, and the gas temperature they found (35 K) is far lower than our results. Hence we think the CO absorption in NGC 4945 is associated with the star formation in it, favoring the discussion by Spoon et al. (2003) that the gas phase CO is embedded in a star-forming molecular disk. Our result could be interpreted that the torus is geometrically thicker in composites than in typical Sy2s. A higher scale height of the torus would increase the probability that the line of sight intersects the obscuring material, which leads a large expected value of $N_{\rm CO}$.

The different scale heights between composites and Sy2s may be reflecting the influence of nuclear starburst in their CNDs. There have been many connections proposed between the AGN activity and nuclear starburst. For example, Izumi et al. (2016) measured the mass of dense molecular gas in the CNDs of ten Seyfert galaxies using the dense gas tracer HCN(1-0) line and found its positive correlation with the accretion rate of the central SMBHs. They claim that the star formation within the CNDs contributes to the fueling of the SMBHs. The hydrodynamical simulation model of the torus formation developed by Wada (2012) and his colleagues implies that a geometrically thick torus does not survive for millions of years or longer unless the mass accretion rate into the center is enhanced by some mechanisms, such as supernova explosions and stellar mass loss in the surrounding environment. We would be able to make more detailed discussion by observing the CO absorption in composites and Sy2s with a higher wavelength resolution and comparing the turbulent velocities within them from the width of each rotational line.

6.7 Summary

Motivated by the result of Chapter 5, we performed a systematic analysis of the CO absorption band with a larger sample than that of the previous chapter. Nearby 47 infrared galaxies were selected from the *AKARI* the post-cryogenic observations in the mission program AGNUL without any prior information on the presence or absence of the CO feature. The sample includes 4 ULIRGs, 24 LIRGs, and 19 IRGs, covering a lower luminosity range than the previous sample. Optical classifications of the galaxies were compiled from the literature, which resulted in 2 Seyfert 1s, 13 Seyfert 2s, 3 LINERs, 24 AGN-starburst composites, and 5 unclassified ones.

Observed data were reduced in a similar way to the previous chapter, but additionally, the subtraction of the line fluxes of H I Pfβ and H_2 0-0 S(9) was performed. The gas model was fitted at first with the velocity width fixed to the mean value of those obtained in the previous chapter. For the objects of unsuccessful fits, the model was fitted with the temperature also fixed. The CO absorption band was discovered in many of the sample galaxies. Especially, we newly detected the CO feature in IC 5063, where the absorption had not been found from observations with *ISO*. A large fraction of the sample showed CO column densities larger than 10^{19} cm^{-2} with high temperatures of several $\times$ 10^2 K, and such warm gas of a large column density can be considered to be heated by X-rays. The fraction of the galaxies with large column densities was higher in U/LIRGs than IRGs and had a peak at a 14 μm luminosity of $L_{14\,\mu\mathrm{m}} \sim 10^{10}\ L_{\odot}$, which corresponds to a hard X-ray luminosity of L_{X} 10^{43} erg s^{-1}. This tendency is consistent with the obscured fraction measured in X-rays. Based on this result, the obscuring material observed in X-rays is being identified as molecular gas. This luminosity dependence also could explain the rarity of the CO feature in the less-luminous AGNs that were observed with *ISO*. It was also found that composite sources had on average larger CO column densities than Sy2s. This result suggests that the obscuration by an AGN torus is also effective in composites and that the torus is geometrically thicker in composites than in typical Sy2s. This is qualitatively consistent with the advocated connection between the AGN activity and nuclear starburst that supernovae in circum-nuclear disks inflate the scale height of a torus.

Chapter 7

Conclusion

7.1 The Main Results of This Thesis

In this thesis, we have presented a series of studies conducted with the aim to investigate physical conditions and geometrical properties of AGN tori though the absorption spectroscopy of the near-IR CO fundamental ro-vibrational band centered at 4.67 μm. We here summarize the main results.

To improve the calibration of the *AKARI* near-IR grism spectroscopy at the wavelengths required for the current study, we revised the *AKARI* calibration by taking the effect of the contamination by the diffracted second-order light into account. The revision was started from the cryogenic phase of the satellite, during which the temperature of the instrument had been stably kept at cryogenic temperature (Chapter 3). The wavelength calibration was revised with the wavelength dependence of the refractive index of the disperser taken into consideration. As a result, it was revealed that the nonlinearity of the relation between wavelengths and pixel positions causes the contamination even if the order-sorting filter perfectly works. The spectral responses from the first- and second-order light were simultaneously derived by using a pair of standard objects that have contrasting colors. The decomposition of the mixing flux of the two orders was formulated as a matrix equation, and the contaminating component was quantitatively subtracted for the first time. These revisions enabled the analysis of the CO absorption band observed with *AKARI*, which is presented in Chapter 5.

We then revised the *AKARI* calibrations for the post-cryogenic phase of the satellite (Chapter 4). During this period, although the temperature was not stable and gradually increased, a large number of AGNs and IR galaxies of a wide luminosity range were observed. In addition to the treatment of the previous chapter, the effect of the temperature increase was also considered. The new wavelength calibration curve is consistent with that of the cryogenic phase and does not show any significant temperature dependence. The spectral response from the first-order light is lower than that of the cryogenic phase on average by 30% and decreases by 10% during the post-cryogenic phase without clear wavelength dependence. This response decline is consistent with that in imaging observations, indicating that the dominant cause of the decline is the worsening of the detector sensitivity. A correction factor for this temperature dependence was

obtained. The temperature dependence in the response from the second-order light is smaller than its uncertainty. These revisions pioneered the possibility of the study of the CO absorption in LIRGs and IRGs in Chapter 6.

In Chapter 5, we analyzed the CO absorption in nearby ten AGNs embedded in ULIRGs that had been known to show the CO feature using observations with the *AKARI*/IRC (during the cryogenic phase) and the *Spitzer*/IRS. The new calibration method established in Chapter 3 was utilized. The observed absorption spectra were fitted with a plane-parallel LTE gas model on the assumptions that the gas is single-component and that the background continuum source is the dust sublimation layer of 1500 K at the inner rim of an AGN torus. We found that the CO gas is warm (200–500 K) and has a large column density of $N_{\rm CO} > 10^{19}$ cm^{-2}, which corresponds to $N_{\rm H} > 10^{23}$ cm^{-2}. Such warm large-column gas is not attainable by either UV heating or shock heating, and the most convincing candidate is X-ray heating. If the CO abundance of CO/H $= 10^{-4}$ is adopted, the hydrogen column density converted from the CO one is smaller than that measured in X-ray spectral analyses. These results can be explained that the CO absorption band probes the immediate outside of the X-ray emitting region within the vicinity of the nuclei. The observed deep absorption profiles require almost unity covering factors and suggest that the probed region is close to the continuum source, i.e., the innermost part of the AGN tori.

In Chapter 6, motivated by the above result, we performed a systematic analysis of the CO absorption with a large sample including LIRGs and IRGs. Nearby 47 IR galaxies were selected from the *AKARI* post-cryogenic observations without any prior information on the presence or absence of the CO feature, and their band profiles were compared in different luminosity classes and optical classifications. This large sample, which contains LIRGs and IRGs and various optical classifications, was enabled for the first time by the above re-calibrations of *AKARI*. The CO absorption band was discovered in many of the sample galaxies. Especially, we newly detected the CO feature in IC 5063, where the absorption had not been found from observations with *ISO*. As well as the targets in the previous chapter, many of the sample galaxies show warm large-column gas of $N_{\rm CO} \gtrsim 10^{19}$ cm^{-2} and $T_{\rm CO} \sim$ several $\times\, 10^2$ K, which can be considered to be heated by X-rays. It was revealed that the CO absorption is stronger in ULIRGs and LIRGs than IRGs. We found that the fraction of the galaxies with column densities larger than $N_{\rm CO} = 10^{19}$ cm^{-2} had a peak at a 14 μm monochromatic luminosity of 10^{10} $L_\odot$. This tendency is consistent with the obscured fraction defined in X-ray surveys. Based on this result, the obscuring material observed in X-rays is being identified to be molecular gas. In addition, this luminosity dependence could explain the rarity of the presence of the CO feature in less-luminous AGNs observed with *ISO*. It was also found that the AGN-starburst composites had on average larger CO column densities than Seyfert 2s. This result can be interpreted that the obscuration by an AGN torus is also effective in composites and that the torus is geometrically thicker in composites than in typical Seyferts. This picture is qualitatively consistent with the theoretically and observationally advocated connection between the AGN activity and nuclear starburst that supernovae in circum-nuclear disks inflate the scale height of a torus.

The above studies indicate that warm molecular gas with a large column density exists in the

vicinity of AGNs and that such gas has properties common to the obscuring material observed in X-rays. These results suggest that the anisotropic structure around an AGN consists of molecular gas, agreeing with the AGN unified model.

7.2 Future Work

The above studies have demonstrated that the CO ro-vibrational absorption band is a promising tool to probe warm obscuring gas in the vicinity of AGNs, which cannot be resolved even by millimeter and submillimeter interferometers. Infrared astronomy is now about gaining a new powerful observatory, *James Webb Space Telescope* (*JWST*). *JWST* will, with its spectral resolution of 3,000, make it possible to separate different rotational levels. Observing the CO band with this telescope will provide a more detailed picture of AGN tori. Further, the *SPICA* telescope is being prepared. This space observatory is being planned to be equipped with wavelength resolving power as high as 10,000. This capability could enable, beyond the separation of each line, decomposition of the velocity profile of each line, and it has an impact to unravel the interaction between AGNs and the surrounding environment, such as molecular inflows and outflows, and the formation of AGN tori. The study of the CO band conducted in this thesis is a milestone for such developmental future works.

References

Aikawa, Y., Kamuro, D., Sakon, I., Itoh, Y., Terada, H., Noble, J. A., Pontoppidan, K. M., Fraser, H. J., Tamura, M., Kandori, R., Kawamura, A., and Ueno, M. 2012, "AKARI observations of ice absorption bands towards edge-on young stellar objects", *Astronomy and Astrophysics*, 538, A57

Allen, D. A., Norris, R. P., Meadows, V. S., and Roche, P. F. 1991, "A large sample of southern IRAS galaxies - Spectral classes and superclustering", *Monthly Notices of the Royal Astronomical Society*, 248, 528

Alonso-Herrero, A., García-Marín, M., Monreal-Ibero, A., Colina, L., Arribas, S., Alfonso-Garzón, J., and Labiano, A. 2009, "PMAS optical integral field spectroscopy of luminous infrared galaxies. I. The atlas", *Astronomy and Astrophysics*, 506, 1541

Alonso-Herrero, A., Ramos Almeida, C., Mason, R., Asensio Ramos, A., Roche, P. F., Levenson, N. A., Elitzur, M., Packham, C., Rodríguez Espinosa, J. M., Young, S., Díaz-Santos, T., and Pérez-García, A. M. 2011, "Torus and Active Galactic Nucleus Properties of Nearby Seyfert Galaxies: Results from Fitting Infrared Spectral Energy Distributions and Spectroscopy", *The Astrophysical Journal*, 736, 82

Antonucci, R. 1993, "Unified models for active galactic nuclei and quasars", *Annual Review of Astronomy and Astrophysics*, 31, 473

Antonucci, R. R. J. and Miller, J. S. 1985, "Spectropolarimetry and the nature of NGC 1068", *The Astrophysical Journal*, 297, 621

Armus, L., Heckman, T. M., and Miley, G. K. 1989, "Long-slit optical spectroscopy of powerful far-infrared galaxies - The nature of the nuclear energy source", *The Astrophysical Journal*, 347, 727

Armus, L., Mazzarella, J. M., Evans, A. S., Surace, J. A., Sanders, D. B., Iwasawa, K., Frayer, D. T., Howell, J. H., Chan, B., Petric, A., Vavilkin, T., Kim, D. C., Haan, S., Inami, H., Murphy, E. J., Appleton, P. N., Barnes, J. E., Bothun, G., Bridge, C. R., Charmandaris, V., Jensen, J. B., Kewley, L. J., Lord, S., Madore, B. F., Marshall, J. A., Melbourne, J. E., Rich,

J., Satyapal, S., Schulz, B., Spoon, H. W. W., Sturm, E., U, V., Veilleux, S., and Xu, K. 2009, "GOALS: The Great Observatories All-Sky LIRG Survey", *Publications of the Astronomical Society of the Pacific*, 121, 559

Baan, W. A., Salzer, J. J., and LeWinter, R. D. 1998, "Optical Classification of Megamaser Galaxies", *The Astrophysical Journal*, 509, 633

Baldwin, J. A., Phillips, M. M., and Terlevich, R. 1981, "Classification parameters for the emission-line spectra of extragalactic objects", *Publications of the Astronomical Society of the Pacific*, 93, 5

Barvainis, R. 1987, "Hot dust and the near-infrared bump in the continuum spectra of quasars and active galactic nuclei", *The Astrophysical Journal*, 320, 537

Black, J. H., van Dishoeck, E. F., Willner, S. P., and Woods, R. C. 1990, "Interstellar absorption lines toward NGC 2264 and AFGL 2591 - Abundances of H2, H3(+), and CO", *The Astrophysical Journal*, 358, 459

Bohlin, R. C., Savage, B. D., and Drake, J. F. 1978, "A survey of interstellar H I from L-alpha absorption measurements. II", *The Astrophysical Journal*, 224, 132

Boogert, A. C. A., Gerakines, P. A., and Whittet, D. C. B. 2015, "Observations of the icy universe.", *Annual Review of Astronomy and Astrophysics*, 53, 541

Braito, V., Reeves, J. N., Della Ceca, R., Ptak, A., Risaliti, G., and Yaqoob, T. 2009, "A Suzaku observation of the ULIRG IRAS19254-7245: discerning the AGN component", *Astronomy and Astrophysics*, 504, 53

Brightman, M. and Nandra, K. 2011a, "An XMM-Newton spectral survey of 12 μm selected galaxies - II. Implications for AGN selection and unification", *Monthly Notices of the Royal Astronomical Society*, 414, 3084

Brightman, M. and Nandra, K. 2011b, "An XMM-Newton spectral survey of 12 μm selected galaxies - I. X-ray data", *Monthly Notices of the Royal Astronomical Society*, 413, 1206

Burlon, D., Ajello, M., Greiner, J., Comastri, A., Merloni, A., and Gehrels, N. 2011, "Three-year Swift-BAT Survey of Active Galactic Nuclei: Reconciling Theory and Observations?", *The Astrophysical Journal*, 728, 58

Cami, J. 2002, "Molecular gas and dust around evolved stars", Ph.D. thesis, University of Amsterdam, http://dare.uva.nl/record/1/199084

Cohen, M. 2003, "Stellar Calibration in the Infrared: Extending the Legacy of KAO, ISO, and MSX to SIRTF and beyond", *The Calibration Legacy of the ISO Mission*, Volume 481 of *ESA Special Publication*, Page 135, http://adsabs.harvard.edu/abs/2003ESASP.481..135C

Cohen, M., Megeath, S. T., Hammersley, P. L., Martín-Luis, F., and Stauffer, J. 2003a, "Spectral Irradiance Calibration in the Infrared. XIII. "Supertemplates" and On-Orbit Calibrators for the SIRTF Infrared Array Camera", *The Astronomical Journal*, 125, 2645

Cohen, M., Walker, R. G., Carter, B., Hammersley, P., Kidger, M., and Noguchi, K. 1999, "Spectral Irradiance Calibration in the Infrared. X. A Self-Consistent Radiometric All-Sky Network of Absolutely Calibrated Stellar Spectra", *The Astronomical Journal*, 117, 1864

Cohen, M., Wheaton, W. A., and Megeath, S. T. 2003b, "Spectral Irradiance Calibration in the Infrared. XIV. The Absolute Calibration of 2MASS", *The Astronomical Journal*, 126, 1090

Cohen, M., Witteborn, F. C., Carbon, D. F., Davies, J. K., Wooden, D. H., and Bregman, J. D. 1996, "Spectral Irradiance Calibration in the Infrared.VII.New Composite Spectra, Comparison with Model Atmospheres, and Far-Infrared Extrapolations", *The Astronomical Journal*, 112, 2274

Conti, P. S. and Crowther, P. A. 2004, "MSX mid-infrared imaging of massive star birth environments - II. Giant HII regions", *Monthly Notices of the Royal Astronomical Society*, 355, 899

Crowther, P. A. and Conti, P. S. 2003, "MSX mid-infrared imaging of massive star birth environments - I. Ultracompact HII regions", *Monthly Notices of the Royal Astronomical Society*, 343, 143

Dannerbauer, H., Rigopoulou, D., Lutz, D., Genzel, R., Sturm, E., and Moorwood, A. F. M. 2005, "Follow-up near-infrared spectroscopy of ultraluminous infrared galaxies observed by ISO", *Astronomy and Astrophysics*, 441, 999

Dartois, E. and Muñoz-Caro, G. M. 2007, "Carbonaceous dust grains in luminous infrared galaxies. Spitzer/IRS reveals a-C:H as an abundant and ubiquitous ISM component", *Astronomy and Astrophysics*, 476, 1235

Dickman, R. L. 1978, "The ratio of carbon monoxide to molecular hydrogen in interstellar dark clouds", *The Astrophysical Journal Supplement Series*, 37, 407

Draine, B. T. 2003, "Interstellar Dust Grains", *Annual Review of Astronomy and Astrophysics*, 41, 241

Duc, P.-A., Mirabel, I. F., and Maza, J. 1997, "Southern ultraluminous infrared galaxies: an optical and infrared database", *Astronomy and Astrophysics Supplement Series*, 124, 533

Fabian, A. C. 2012, "Observational Evidence of Active Galactic Nuclei Feedback", *Annual Review of Astronomy and Astrophysics*, 50, 455

Fischer, J., Sturm, E., González-Alfonso, E., Graciá-Carpio, J., Hailey-Dunsheath, S., Poglitsch, A., Contursi, A., Lutz, D., Genzel, R., Sternberg, A., Verma, A., and Tacconi, L. 2010, "Herschel-PACS spectroscopic diagnostics of local ULIRGs: Conditions and kinematics in Markarian 231", *Astronomy and Astrophysics*, 518, L41

Frerking, M. A., Langer, W. D., and Wilson, R. W. 1982, "The relationship between carbon monoxide abundance and visual extinction in interstellar clouds", *The Astrophysical Journal*, 262, 590

Frey, B. J., Leviton, D. B., and Madison, T. J. 2006, "Temperature-dependent refractive index of silicon and germanium", *Society of Photo-Optical Instrumentation Engineers (SPIE) Conference Series*, Volume 6273 of *Society of Photo-Optical Instrumentation Engineers (SPIE) Conference Series*

García-Burillo, S., Combes, F., Ramos Almeida, C., Usero, A., Krips, M., Alonso-Herrero, A., Aalto, S., Casasola, V., Hunt, L. K., Martín, S., Viti, S., Colina, L., Costagliola, F., Eckart, A., Fuente, A., Henkel, C., Márquez, I., Neri, R., Schinnerer, E., Tacconi, L. J., and van der Werf, P. P. 2016, "ALMA Resolves the Torus of NGC 1068: Continuum and Molecular Line Emission", *The Astrophysical Journal Letters*, 823, L12

Geballe, T. R., Goto, M., Usuda, T., Oka, T., and McCall, B. J. 2006, "The Interstellar Medium of IRAS 08572+3915 NW: H^+_3 and Warm High-Velocity CO", *The Astrophysical Journal*, 644, 907

Geballe, T. R., Mason, R. E., Rodríguez-Ardila, A., and Axon, D. J. 2009, "The 3-5 μm Spectrum of NGC 1068 at High Angular Resolution: Distribution of Emission and Absorption Features Across the Nuclear Continuum Source", *The Astrophysical Journal*, 701, 1710

González-Alfonso, E., Fischer, J., Spoon, H. W. W., Stewart, K. P., Ashby, M. L. N., Veilleux, S., Smith, H. A., Sturm, E., Farrah, D., Falstad, N., Meléndez, M., Graciá-Carpio, J., Janssen, A. W., and Lebouteiller, V. 2017, "Molecular Outflows in Local ULIRGs: Energetics from Multitransition OH Analysis", *The Astrophysical Journal*, 836, 11

Goorvitch, D. 1994, "Infrared CO line for the X 1 Sigma(+) state", *The Astrophysical Journal Supplement Series*, 95, 535

Habing, H. J. 1969, "A comparison of radio and optical spectral lines of neutral interstellar gas", *Bulletin of the Astronomical Institutes of the Netherlands*, 20, 177

Heckman, T. M. 1980, "An optical and radio survey of the nuclei of bright galaxies - Activity in normal galactic nuclei", *Astronomy and Astrophysics*, 87, 152

Higdon, S. J. U., Armus, L., Higdon, J. L., Soifer, B. T., and Spoon, H. W. W. 2006, "A Spitzer Space Telescope Infrared Spectrograph Survey of Warm Molecular Hydrogen in Ultraluminous Infrared Galaxies", *The Astrophysical Journal*, 648, 323

Hollenbach, D. and McKee, C. F. 1989, "Molecule formation and infrared emission in fast interstellar shocks. III - Results for J shocks in molecular clouds", *The Astrophysical Journal*, 342, 306

Hollenbach, D. J. and Tielens, A. G. G. M. 1999, "Photodissociation regions in the interstellar medium of galaxies", *Reviews of Modern Physics*, 71, 173

Hönig, S. F. and Kishimoto, M. 2010, "The dusty heart of nearby active galaxies. II. From clumpy torus models to physical properties of dust around AGN", *Astronomy and Astrophysics*, 523, A27

Houck, J. R., Roellig, T. L., van Cleve, J., Forrest, W. J., Herter, T., Lawrence, C. R., Matthews, K., Reitsema, H. J., Soifer, B. T., Watson, D. M., Weedman, D., Huisjen, M., Troeltzsch, J., Barry, D. J., Bernard-Salas, J., Blacken, C. E., Brandl, B. R., Charmandaris, V., Devost, D., Gull, G. E., Hall, P., Henderson, C. P., Higdon, S. J. U., Pirger, B. E., Schoenwald, J., Sloan, G. C., Uchida, K. I., Appleton, P. N., Armus, L., Burgdorf, M. J., Fajardo-Acosta, S. B., Grillmair, C. J., Ingalls, J. G., Morris, P. W., and Teplitz, H. I. 2004, "The Infrared Spectrograph (IRS) on the Spitzer Space Telescope", *The Astrophysical Journal Supplement Series*, 154, 18

Ichikawa, K., Imanishi, M., Ueda, Y., Nakagawa, T., Shirahata, M., Kaneda, H., and Oyabu, S. 2014, "AKARI IRC 2.5-5 μm Spectroscopy of Infrared Galaxies over a Wide Luminosity Range", *The Astrophysical Journal*, 794, 139

Ichikawa, K., Packham, C., Ramos Almeida, C., Asensio Ramos, A., Alonso-Herrero, A., González-Martín, O., Lopez-Rodriguez, E., Ueda, Y., Díaz-Santos, T., Elitzur, M., Hönig, S. F., Imanishi, M., Levenson, N. A., Mason, R. E., Perlman, E. S., and Alsip, C. D. 2015, "The Differences in the Torus Geometry between Hidden and Non-hidden Broad Line Active Galactic Nuclei", *The Astrophysical Journal*, 803, 57

Imanishi, M. 2009, "Luminous Buried Active Galactic Nuclei as a Function of Galaxy Infrared Luminosity Revealed through Spitzer Low-resolution Infrared Spectroscopy", *The Astrophysical Journal*, 694, 751

Imanishi, M. and Dudley, C. C. 2000, "Energy Diagnoses of Nine Infrared Luminous Galaxies Based on 3-4 Micron Spectra", *The Astrophysical Journal*, 545, 701

Imanishi, M., Dudley, C. C., Maiolino, R., Maloney, P. R., Nakagawa, T., and Risaliti, G. 2007a, "A Spitzer IRS Low-Resolution Spectroscopic Search for Buried AGNs in Nearby Ultraluminous Infrared Galaxies: A Constraint on Geometry between Energy Sources and Dust", *The Astrophysical Journal Supplement Series*, 171, 72

Imanishi, M., Nakagawa, T., Ohyama, Y., Shirahata, M., Wada, T., Onaka, T., and Oi, N. 2008, "Systematic Infrared 2.5-5 μm Spectroscopy of Nearby Ultraluminous Infrared Galaxies with AKARI", *Publications of the Astronomical Society of Japan*, 60, 489

Imanishi, M., Nakagawa, T., Shirahata, M., Ohyama, Y., and Onaka, T. 2010, "AKARI IRC Infrared 2.5-5 μm Spectroscopy of a Large Sample of Luminous Infrared Galaxies", *The Astrophysical Journal*, 721, 1233

Imanishi, M., Nakanishi, K., and Izumi, T. 2016, "ALMA 0.1-0.2 arcsec Resolution Imaging of the NGC 1068 Nucleus: Compact Dense Molecular Gas Emission at the Putative AGN Location", *The Astrophysical Journal Letters*, 822, L10

Imanishi, M., Nakanishi, K., Tamura, Y., Oi, N., and Kohno, K. 2007b, "Millimeter Interferometric HCN(1-0) and HCO^+(1-0) Observations of Luminous Infrared Galaxies", *The Astronomical Journal*, 134, 2366

IRS Instrument Team and Science User Support Team. 2011, "IRS Instrument Handbook", 5th edition, IRS Instrument Team and Science User Support Team, http://irsa.ipac.caltech.edu/data/SPITZER/docs/irs/irsinstrumenthandbook/

Iwasawa, K., Sanders, D. B., Teng, S. H., U, V., Armus, L., Evans, A. S., Howell, J. H., Komossa, S., Mazzarella, J. M., Petric, A. O., Surace, J. A., Vavilkin, T., Veilleux, S., and Trentham, N. 2011, "C-GOALS: Chandra observations of a complete sample of luminous infrared galaxies from the IRAS Revised Bright Galaxy Survey", *Astronomy and Astrophysics*, 529, A106

Izumi, T., Kawakatu, N., and Kohno, K. 2016, "Do Circumnuclear Dense Gas Disks Drive Mass Accretion onto Supermassive Black Holes?", *The Astrophysical Journal*, 827, 81

Jarrett, T. H., Cohen, M., Masci, F., Wright, E., Stern, D., Benford, D., Blain, A., Carey, S., Cutri, R. M., Eisenhardt, P., Lonsdale, C., Mainzer, A., Marsh, K., Padgett, D., Petty, S., Ressler, M., Skrutskie, M., Stanford, S., Surace, J., Tsai, C. W., Wheelock, S., and Yan, D. L. 2011, "The Spitzer-WISE Survey of the Ecliptic Poles", *The Astrophysical Journal*, 735, 112

Jennings, D. E., Weber, A., and Brault, J. W. 1987, "FTS-Raman flame spectroscopy of high-J lines in H_2 and D_2", *Journal of Molecular Spectroscopy*, 126, 19

Kawada, M., Baba, H., Barthel, P. D., Clements, D., Cohen, M., Doi, Y., Figueredo, E., Fujiwara, M., Goto, T., Hasegawa, S., Hibi, Y., Hirao, T., Hiromoto, N., Jeong, W.-S., Kaneda, H., Kawai, T., Kawamura, A., Kester, D., Kii, T., Kobayashi, H., Kwon, S. M., Lee, H. M., Makiuti, S., Matsuo, H., Matsuura, S., Müller, T. G., Murakami, N., Nagata, H., Nakagawa, T., Narita, M., Noda, M., Oh, S. H., Okada, Y., Okuda, H., Oliver, S., Ootsubo, T., Pak, S., Park, Y.-S., Pearson, C. P., Rowan-Robinson, M., Saito, T., Salama, A., Sato, S., Savage, R. S., Serjeant, S., Shibai, H., Shirahata, M., Sohn, J., Suzuki, T., Takagi, T., Takahashi, H., Thomson, M., Usui, F., Verdugo, E., Watabe, T., White, G. J., Wang, L., Yamamura, I., Yamauchi, C., and Yasuda, A. 2007, "The Far-Infrared Surveyor (FIS) for AKARI", *Publications of the Astronomical Society of Japan*, 59, 389

Kawaguchi, T. and Mori, M. 2010, "Orientation Effects on the Inner Region of Dusty Torus of Active Galactic Nuclei", *The Astrophysical Journal Letters*, 724, L183

Kawaguchi, T. and Mori, M. 2011, "Near-infrared Reverberation by Dusty Clumpy Tori in Active Galactic Nuclei", *The Astrophysical Journal*, 737, 105

Kessler, M. F., Steinz, J. A., Anderegg, M. E., Clavel, J., Drechsel, G., Estaria, P., Faelker, J., Riedinger, J. R., Robson, A., Taylor, B. G., and Ximénez de Ferrán, S. 1996, "The Infrared Space Observatory (ISO) mission.", *Astronomy and Astrophysics*, 315, L27

Kewley, L. J., Heisler, C. A., Dopita, M. A., and Lumsden, S. 2001, "Optical Classification of Southern Warm Infrared Galaxies", *The Astrophysical Journal Supplement Series*, 132, 37

Khachikian, E. Y. and Weedman, D. W. 1974, "An atlas of Seyfert galaxies", *The Astrophysical Journal*, 192, 581

Kim, D., Im, M., Kim, J. H., Jun, H. D., Woo, J.-H., Lee, H. M., Lee, M. G., Nakagawa, T., Matsuhara, H., Wada, T., Oyabu, S., Takagi, T., Ohyama, Y., and Lee, S.-K. 2015, "The AKARI 2.5-5.0 μm Spectral Atlas of Type-1 Active Galactic Nuclei: Black Hole Mass Estimator, Line Ratio, and Hot Dust Temperature", *The Astrophysical Journal Supplement Series*, 216, 17

Kim, D.-C. and Sanders, D. B. 1998, "The IRAS 1 Jy Survey of Ultraluminous Infrared Galaxies. I. The Sample and Luminosity Function", *The Astrophysical Journal Supplement Series*, 119, 41

Kishimoto, M., Hönig, S. F., Beckert, T., and Weigelt, G. 2007, "The innermost region of AGN tori: implications from the HST/NICMOS type 1 point sources and near-IR reverberation", *Astronomy and Astrophysics*, 476, 713

Klaas, U., Acosta-Pulido, J. A., Ábrahám, P., Castañeda, H. O., Cornwall, L., Garzón, F., Hammersley, P., Heinrichsen, I., Kinkel, U., Lemke, D., Schubert, J., and Wells, M. 1997, "ISOPHOT-S: Capabilities and Calibration (Invited Paper)", *The first ISO workshop on Analytical Spectroscopy*, Volume 419 of *ESA Special Publication*, Page 113

Krolik, J. H. and Begelman, M. C. 1988, "Molecular tori in Seyfert galaxies - Feeding the monster and hiding it", *The Astrophysical Journal*, 329, 702

Lacy, J. H., Knacke, R., Geballe, T. R., and Tokunaga, A. T. 1994, "Detection of absorption by H2 in molecular clouds: A direct measurement of the H2:CO ratio", *The Astrophysical Journal Letters*, 428, L69

Lahuis, F., Spoon, H. W. W., Tielens, A. G. G. M., Doty, S. D., Armus, L., Charmandaris, V., Houck, J. R., Stäuber, P., and van Dishoeck, E. F. 2007, "Infrared Molecular Starburst Fingerprints in Deeply Obscured (Ultra)Luminous Infrared Galaxy Nuclei", *The Astrophysical Journal*, 659, 296

Lawrence, A. 1991, "The relative frequency of broad-lined and narrow-lined active galactic nuclei - Implications for unified schemes", *Monthly Notices of the Royal Astronomical Society*, 252, 586

Lebouteiller, V., Barry, D. J., Spoon, H. W. W., Bernard-Salas, J., Sloan, G. C., Houck, J. R., and Weedman, D. W. 2011, "CASSIS: The Cornell Atlas of Spitzer/Infrared Spectrograph Sources", *The Astrophysical Journal Supplement Series*, 196, 8

Lee, J. C., Hwang, H. S., Lee, M. G., Kim, M., and Kim, S. C. 2011, "Optical spectral classification of southern ultraluminous infrared galaxies", *Monthly Notices of the Royal Astronomical Society*, 414, 702

Lípari, S., Mediavilla, E., Díaz, R. J., García-Lorenzo, B., Acosta-Pulido, J., Agüero, M. P., and Terlevich, R. 2004, "Infrared mergers and infrared quasi-stellar objects with galactic winds - I. NGC 2623: nuclear outflow in a proto-elliptical candidate", *Monthly Notices of the Royal Astronomical Society*, 348, 369

Loenen, A. F., van der Werf, P. P., Güsten, R., Meijerink, R., Israel, F. P., Requena-Torres, M. A., García-Burillo, S., Harris, A. I., Klein, T., Kramer, C., Lord, S., Martín-Pintado, J., Röllig, M., Stutzki, J., Szczerba, R., Weiß, A., Philipp-May, S., Yorke, H., Caux, E., Delforge, B., Helmich, F., Lorenzani, A., Morris, P., Philips, T. G., Risacher, C., and Tielens, A. G. G. M. 2010, "Excitation of the molecular gas in the nuclear region of M 82", *Astronomy and Astrophysics*, 521, L2

Lu, Y., Wang, T.-G., Dong, X.-B., and Zhou, H.-Y. 2010, "Type 1 active galactic nucleus fraction in the SDSS/FIRST survey", *Monthly Notices of the Royal Astronomical Society*, 404, 1761

Lusso, E., Hennawi, J. F., Comastri, A., Zamorani, G., Richards, G. T., Vignali, C., Treister, E., Schawinski, K., Salvato, M., and Gilli, R. 2013, "The Obscured Fraction of Active Galactic Nuclei in the XMM-COSMOS Survey: A Spectral Energy Distribution Perspective", *The Astrophysical Journal*, 777, 86

Lutz, D., Sturm, E., Genzel, R., Moorwood, A. F. M., Alexander, T., Netzer, H., and Sternberg, A. 2000, "ISO-SWS Spectroscopy of NGC 1068", *The Astrophysical Journal*, 536, 697

Lutz, D., Sturm, E., Genzel, R., Spoon, H. W. W., and Stacey, G. J. 2004, "Gas near active galactic nuclei: A search for the 4.7 μm CO band", *Astronomy and Astrophysics*, 426, L5

Lutz, D., Feuchtgruber, H., Genzel, R., Kunze, D., Rigopoulou, D., Spoon, H. W. W., Wright, C. M., Egami, E., Katterloher, R., Sturm, E., Wieprecht, E., Sternberg, A., Moorwood, A. F. M., and de Graauw, T. 1996, "SWS observations of the Galactic center.", *Astronomy and Astrophysics*, 315, L269

Magorrian, J., Tremaine, S., Richstone, D., Bender, R., Bower, G., Dressler, A., Faber, S. M., Gebhardt, K., Green, R., Grillmair, C., Kormendy, J., and Lauer, T. 1998, "The Demography of Massive Dark Objects in Galaxy Centers", *The Astronomical Journal*, 115, 2285

Maia, M. A. G., Machado, R. S., and Willmer, C. N. A. 2003, "The Seyfert Population in the Local Universe", *The Astronomical Journal*, 126, 1750

Mainzer, A., Bauer, J., Grav, T., Masiero, J., Cutri, R. M., Dailey, J., Eisenhardt, P., McMillan, R. S., Wright, E., Walker, R., Jedicke, R., Spahr, T., Tholen, D., Alles, R., Beck, R., Brandenburg, H., Conrow, T., Evans, T., Fowler, J., Jarrett, T., Marsh, K., Masci, F., McCallon, H., Wheelock, S., Wittman, M., Wyatt, P., DeBaun, E., Elliott, G., Elsbury, D., Gautier, IV, T., Gomillion, S., Leisawitz, D., Maleszewski, C., Micheli, M., and Wilkins, A. 2011, "Preliminary Results from NEOWISE: An Enhancement to the Wide-field Infrared Survey Explorer for Solar System Science", *The Astrophysical Journal*, 731, 53

Marconi, A. and Hunt, L. K. 2003, "The Relation between Black Hole Mass, Bulge Mass, and Near-Infrared Luminosity", *The Astrophysical Journal Letters*, 589, L21

Mashian, N., Sturm, E., Sternberg, A., Janssen, A., Hailey-Dunsheath, S., Fischer, J., Contursi, A., González-Alfonso, E., Graciá-Carpio, J., Poglitsch, A., Veilleux, S., Davies, R., Genzel, R., Lutz, D., Tacconi, L., Verma, A., Weiß, A., Polisensky, E., and Nikola, T. 2015, "High-J CO Sleds in Nearby Infrared Bright Galaxies Observed By Herschel/PACS", *The Astrophysical Journal*, 802, 81

McKee, C. F., Chernoff, D. F., and Hollenbach, D. J. 1984, "Infrared spectroscopy of interstellar shocks", *Galactic and Extragalactic Infrared Spectroscopy* (Dordrecht: Springer), Volume 108 of *Astrophysics and Space Science Library*, Pages 103–131, https://link.springer.com/chapter/10.1007/978-94-009-7251-3_8

McKernan, B., Ford, K. E. S., Chang, N., and Reynolds, C. S. 2009, "Frying doughnuts: what can the reprocessing of X-rays to IR tell us about the AGN environment?", *Monthly Notices of the Royal Astronomical Society*, 394, 491

Meijerink, R. and Spaans, M. 2005, "Diagnostics of irradiated gas in galaxy nuclei. I. A far-ultraviolet and X-ray dominated region code", *Astronomy and Astrophysics*, 436, 397

Meijerink, R., Kristensen, L. E., Weiß, A., van der Werf, P. P., Walter, F., Spaans, M., Loenen, A. F., Fischer, J., Israel, F. P., Isaak, K., Papadopoulos, P. P., Aalto, S., Armus, L., Charmandaris, V., Dasyra, K. M., Diaz-Santos, T., Evans, A., Gao, Y., González-Alfonso, E., Güsten, R., Henkel, C., Kramer, C., Lord, S., Martín-Pintado, J., Naylor, D., Sanders, D. B., Smith, H., Spinoglio, L., Stacey, G., Veilleux, S., and Wiedner, M. C. 2013, "Evidence for CO Shock Excitation in NGC 6240 from Herschel SPIRE Spectroscopy", *The Astrophysical Journal Letters*, 762, L16

Mori, T. I., Onaka, T., Sakon, I., Ishihara, D., Shimonishi, T., Ohsawa, R., and Bell, A. C. 2014, "Observational Studies on the Near-infrared Unidentified Emission Bands in Galactic H II Regions", *The Astrophysical Journal*, 784, 53

Murakami, H., Baba, H., Barthel, P., Clements, D. L., Cohen, M., Doi, Y., Enya, K., Figueredo, E., Fujishiro, N., Fujiwara, H., Fujiwara, M., Garcia-Lario, P., Goto, T., Hasegawa, S., Hibi, Y., Hirao, T., Hiromoto, N., Hong, S. S., Imai, K., Ishigaki, M., Ishiguro, M., Ishihara, D., Ita, Y., Jeong, W.-S., Jeong, K. S., Kaneda, H., Kataza, H., Kawada, M., Kawai, T., Kawamura, A., Kessler, M. F., Kester, D., Kii, T., Kim, D. C., Kim, W., Kobayashi, H., Koo, B. C., Kwon, S. M., Lee, H. M., Lorente, R., Makiuti, S., Matsuhara, H., Matsumoto, T., Matsuo, H., Matsuura, S., Müller, T. G., Murakami, N., Nagata, H., Nakagawa, T., Naoi, T., Narita, M., Noda, M., Oh, S. H., Ohnishi, A., Ohyama, Y., Okada, Y., Okuda, H., Oliver, S., Onaka, T., Ootsubo, T., Oyabu, S., Pak, S., Park, Y.-S., Pearson, C. P., Rowan-Robinson, M., Saito, T., Sakon, I., Salama, A., Sato, S., Savage, R. S., Serjeant, S., Shibai, H., Shirahata, M., Sohn, J., Suzuki, T., Takagi, T., Takahashi, H., Tanabé, T., Takeuchi, T. T., Takita, S., Thomson, M., Uemizu, K., Ueno, M., Usui, F., Verdugo, E., Wada, T., Wang, L., Watabe,

T., Watarai, H., White, G. J., Yamamura, I., Yamauchi, C., and Yasuda, A. 2007, "The Infrared Astronomical Mission AKARI", *Publications of the Astronomical Society of Japan*, 59, 369

Nakagawa, T., Enya, K., Hirabayashi, M., Kaneda, H., Kii, T., Kimura, Y., Matsumoto, T., Murakami, H., Murakami, M., Narasaki, K., Narita, M., Ohnishi, A., Tsunematsu, S., and Yoshida, S. 2007, "Flight Performance of the AKARI Cryogenic System", *Publications of the Astronomical Society of Japan*, 59, 377

Nandra, K. and Iwasawa, K. 2007, "A Compton-thick active galactic nucleus powering the hyperluminous infrared galaxy IRAS 00182-7112", *Monthly Notices of the Royal Astronomical Society*, 382, L1

Nardini, E. and Risaliti, G. 2011, "Compton-thick active galactic nuclei inside local ultraluminous infrared galaxies", *Monthly Notices of the Royal Astronomical Society*, 415, 619

Nenkova, M., Sirocky, M. M., Ivezić, Ž., and Elitzur, M. 2008a, "AGN Dusty Tori. I. Handling of Clumpy Media", *The Astrophysical Journal*, 685, 147

Nenkova, M., Sirocky, M. M., Nikutta, R., Ivezić, Ž., and Elitzur, M. 2008b, "AGN Dusty Tori. II. Observational Implications of Clumpiness", *The Astrophysical Journal*, 685, 160

Netzer, H. 2015, "Revisiting the Unified Model of Active Galactic Nuclei", *Annual Review of Astronomy and Astrophysics*, 53, 365

Neufeld, D. A. and Dalgarno, A. 1989, "Fast molecular shocks. I - Reformation of molecules behind a dissociative shock", *The Astrophysical Journal*, 340, 869

Neugebauer, G., Habing, H. J., van Duinen, R., Aumann, H. H., Baud, B., Beichman, C. A., Beintema, D. A., Boggess, N., Clegg, P. E., de Jong, T., Emerson, J. P., Gautier, T. N., Gillett, F. C., Harris, S., Hauser, M. G., Houck, J. R., Jennings, R. E., Low, F. J., Marsden, P. L., Miley, G., Olnon, F. M., Pottasch, S. R., Raimond, E., Rowan-Robinson, M., Soifer, B. T., Walker, R. G., Wesselius, P. R., and Young, E. 1984, "The Infrared Astronomical Satellite (IRAS) mission", *The Astrophysical Journal Letters*, 278, L1

Oda, S., Tanimoto, A., Ueda, Y., Imanishi, M., Terashima, Y., and Ricci, C. 2017, "Shedding Light on the Compton-thick Active Galactic Nucleus in the Ultraluminous Infrared Galaxy UGC 5101 with Broadband X-Ray Spectroscopy", *The Astrophysical Journal*, 835, 179

Ohyama, Y., Onaka, T., Matsuhara, H., Wada, T., Kim, W., Fujishiro, N., Uemizu, K., Sakon, I., Cohen, M., Ishigaki, M., Ishihara, D., Ita, Y., Kataza, H., Matsumoto, T., Murakami, H., Oyabu, S., Tanabé, T., Takagi, T., Ueno, M., Usui, F., Watarai, H., Pearson, C. P., Takeyama, N., Yamamuro, T., and Ikeda, Y. 2007, "Near-Infrared and Mid-Infrared Spectroscopy with the Infrared Camera (IRC) for AKARI", *Publications of the Astronomical Society of Japan*, 59, 411

Onaka, T., Lorente, R., Ita, Y. Ohyama, Y., Tanabe, T., and Pearson, C. 2009, "AKARI IRC Data User Manual for Post-Helium (Phase 3) Mission", Version 1.1, http://www.ir.isas.jaxa.jp/AKARI/Observation/support/IRC/IDUM/IRC_IDUM_P3_1.1.pdf

Onaka, T., Matsuhara, H., Wada, T., Fujishiro, N., Fujiwara, H., Ishigaki, M., Ishihara, D., Ita, Y., Kataza, H., Kim, W., Matsumoto, T., Murakami, H., Ohyama, Y., Oyabu, S., Sakon, I., Tanabé, T., Takagi, T., Uemizu, K., Ueno, M., Usui, F., Watarai, H., Cohen, M., Enya, K., Ootsubo, T., Pearson, C. P., Takeyama, N., Yamamuro, T., and Ikeda, Y. 2007, "The Infrared Camera (IRC) for AKARI – Design and Imaging Performance", *Publications of the Astronomical Society of Japan*, 59, 401

Osterbrock, D. E. 1977, "Spectrophotometry of Seyfert 1 galaxies", *The Astrophysical Journal*, 215, 733

Osterbrock, D. E. 1981, "Seyfert galaxies with weak broad H alpha emission lines", *The Astrophysical Journal*, 249, 462

Pearson, C., Rigopoulou, D., Hurley, P., Farrah, D., Afonso, J., Bernard-Salas, J., Borys, C., Clements, D. L., Cormier, D., Efstathiou, A., Gonzalez-Alfonso, E., Lebouteiller, V., and Spoon, H. 2016, "HERUS: A CO Atlas from SPIRE Spectroscopy of Local ULIRGs", *The Astrophysical Journal Supplement Series*, 227, 9

Pier, E. A. and Krolik, J. H. 1992, "Infrared spectra of obscuring dust tori around active galactic nuclei. I - Calculational method and basic trends", *The Astrophysical Journal*, 401, 99

Ramos Almeida, C., Alonso-Herrero, A., Levenson, N. A., Asensio Ramos, A., Rodríguez Espinosa, J. M., González-Martín, O., Packham, C., and Martínez, M. 2014, "Investigating the sensitivity of observed spectral energy distributions to clumpy torus properties in Seyfert galaxies", *Monthly Notices of the Royal Astronomical Society*, 439, 3847

Ramos Almeida, C., Levenson, N. A., Alonso-Herrero, A., Asensio Ramos, A., Rodríguez Espinosa, J. M., Pérez García, A. M., Packham, C., Mason, R., Radomski, J. T., and Díaz-Santos, T. 2011, "Testing the Unification Model for Active Galactic Nuclei in the Infrared: Are the Obscuring Tori of Type 1 and 2 Seyferts Different?", *The Astrophysical Journal*, 731, 92

Reyes, R., Zakamska, N. L., Strauss, M. A., Green, J., Krolik, J. H., Shen, Y., Richards, G. T., Anderson, S. F., and Schneider, D. P. 2008, "Space Density of Optically Selected Type 2 Quasars", *The Astronomical Journal*, 136, 2373

Rieke, G. H., Blaylock, M., Decin, L., Engelbracht, C., Ogle, P., Avrett, E., Carpenter, J., Cutri, R. M., Armus, L., Gordon, K., Gray, R. O., Hinz, J., Su, K., and Willmer, C. N. A. 2008, "Absolute Physical Calibration in the Infrared", *The Astronomical Journal*, 135, 2245

Risaliti, G. and Elvis, M. 2004, "A Panchromatic View of AGN", *Supermassive Black Holes in the Distant Universe*, Volume 308 of *Astrophysics and Space Science Library*, Page 187

Sanders, D. B., Mazzarella, J. M., Kim, D.-C., Surace, J. A., and Soifer, B. T. 2003, "The IRAS Revised Bright Galaxy Sample", *The Astronomical Journal*, 126, 1607

Sanders, D. B. and Mirabel, I. F. 1996, "Luminous Infrared Galaxies", *Annual Review of Astronomy and Astrophysics*, 34, 749

Sargsyan, L., Weedman, D., Lebouteiller, V., Houck, J., Barry, D., Hovhannisyan, A., and Mickaelian, A. 2011, "Infrared Spectra and Spectral Energy Distributions for Dusty Starbursts and Active Galactic Nuclei", *The Astrophysical Journal*, 730, 19

Saunders, W., Sutherland, W. J., Maddox, S. J., Keeble, O., Oliver, S. J., Rowan-Robinson, M., McMahon, R. G., Efstathiou, G. P., Tadros, H., White, S. D. M., Frenk, C. S., Carramiñana, A., and Hawkins, M. R. S. 2000, "The PSCz catalogue", *Monthly Notices of the Royal Astronomical Society*, 317, 55

Schartmann, M., Burkert, A., Krause, M., Camenzind, M., Meisenheimer, K., and Davies, R. I. 2010, "Gas dynamics of the central few parsec region of NGC 1068 fuelled by the evolving nuclear star cluster", *Monthly Notices of the Royal Astronomical Society*, 403, 1801

Schartmann, M., Meisenheimer, K., Camenzind, M., Wolf, S., Tristram, K. R. W., and Henning, T. 2008, "Three-dimensional radiative transfer models of clumpy tori in Seyfert galaxies", *Astronomy and Astrophysics*, 482, 67

Schneider, S. E., Terzian, Y., Purgathofer, A., and Perinotto, M. 1983, "Radial velocities of planetary nebulae", *The Astrophysical Journal Supplement Series*, 52, 399

Scoville, N. Z., Evans, A. S., Thompson, R., Rieke, M., Hines, D. C., Low, F. J., Dinshaw, N., Surace, J. A., and Armus, L. 2000, "NICMOS Imaging of Infrared-Luminous Galaxies", *The Astronomical Journal*, 119, 991

SES data center. 2002, "ASTRO-F interim report" (Sagamihara: Japan Aerospace Exploration Agency Institute of Space and Astronautical Science), Volume 2, 1073, in Japanese

Shimonishi, T., Onaka, T., Kato, D., Sakon, I., Ita, Y., Kawamura, A., and Kaneda, H. 2013, "AKARI Infrared Camera Survey of the Large Magellanic Cloud. II. The Near-infrared Spectroscopic Catalog", *The Astronomical Journal*, 145, 32

Shirahata, M., Nakagawa, T., Usuda, T., Goto, M., Suto, H., and Geballe, T. R. 2013, "Infrared Spectroscopy of CO Ro-Vibrational Absorption Lines toward the Obscured AGN IRAS 08572+3915", *Publications of the Astronomical Society of Japan*, 65, 5

Simpson, C. 2005, "The luminosity dependence of the type 1 active galactic nucleus fraction", *Monthly Notices of the Royal Astronomical Society*, 360, 565

Skrutskie, M. F., Cutri, R. M., Stiening, R., Weinberg, M. D., Schneider, S., Carpenter, J. M., Beichman, C., Capps, R., Chester, T., Elias, J., Huchra, J., Liebert, J., Lonsdale, C., Monet, D. G., Price, S., Seitzer, P., Jarrett, T., Kirkpatrick, J. D., Gizis, J. E., Howard, E., Evans,

T., Fowler, J., Fullmer, L., Hurt, R., Light, R., Kopan, E. L., Marsh, K. A., McCallon, H. L., Tam, R., Van Dyk, S., and Wheelock, S. 2006, "The Two Micron All Sky Survey (2MASS)", *The Astronomical Journal*, 131, 1163

Smith, J. D. T., Draine, B. T., Dale, D. A., Moustakas, J., Kennicutt, Jr., R. C., Helou, G., Armus, L., Roussel, H., Sheth, K., Bendo, G. J., Buckalew, B. A., Calzetti, D., Engelbracht, C. W., Gordon, K. D., Hollenbach, D. J., Li, A., Malhotra, S., Murphy, E. J., and Walter, F. 2007, "The Mid-Infrared Spectrum of Star-forming Galaxies: Global Properties of Polycyclic Aromatic Hydrocarbon Emission", *The Astrophysical Journal*, 656, 770

Soifer, B. T., Neugebauer, G., Matthews, K., Egami, E., Becklin, E. E., Weinberger, A. J., Ressler, M., Werner, M. W., Evans, A. S., Scoville, N. Z., Surace, J. A., and Condon, J. J. 2000, "High Resolution Mid-Infrared Imaging of Ultraluminous Infrared Galaxies", *The Astronomical Journal*, 119, 509

Solarz, A., Takeuchi, T. T., and Pollo, A. 2016, "Total infrared luminosity estimation from local galaxies in AKARI all sky survey", *Astronomy and Astrophysics*, 592, A155

Spoon, H. W. W., Keane, J. V., Cami, J., Lahuis, F., Tielens, A. G. G. M., Armus, L., and Charmandaris, V. 2005, "Spitzer Observations of Deeply Obscured Galactic Nuclei", *Astrochemistry: Recent Successes and Current Challenges*, Volume 231 of *IAU Symposium*, Pages 281–290

Spoon, H. W. W., Keane, J. V., Tielens, A. G. G. M., Lutz, D., and Moorwood, A. F. M. 2001, "The obscured mid-infrared continuum of NGC 4418: A dust- and ice-enshrouded AGN", *Astronomy and Astrophysics*, 365, L353

Spoon, H. W. W., Marshall, J. A., Houck, J. R., Elitzur, M., Hao, L., Armus, L., Brandl, B. R., and Charmandaris, V. 2007, "Mid-Infrared Galaxy Classification Based on Silicate Obscuration and PAH Equivalent Width", *The Astrophysical Journal Letters*, 654, L49

Spoon, H. W. W., Moorwood, A. F. M., Pontoppidan, K. M., Cami, J., Kregel, M., Lutz, D., and Tielens, A. G. G. M. 2003, "Detection of strongly processed ice in the central starburst of NGC 4945", *Astronomy and Astrophysics*, 402, 499

Spoon, H. W. W., Armus, L., Cami, J., Tielens, A. G. G. M., Chiar, J. E., Peeters, E., Keane, J. V., Charmandaris, V., Appleton, P. N., Teplitz, H. I., and Burgdorf, M. J. 2004, "Fire and Ice: Spitzer Infrared Spectrograph (IRS) Mid-Infrared Spectroscopy of IRAS F00183-7111", *The Astrophysical Journal Supplement Series*, 154, 184

Spoon, H. W. W., Farrah, D., Lebouteiller, V., González-Alfonso, E., Bernard-Salas, J., Urrutia, T., Rigopoulou, D., Westmoquette, M. S., Smith, H. A., Afonso, J., Pearson, C., Cormier, D., Efstathiou, A., Borys, C., Verma, A., Etxaluze, M., and Clements, D. L. 2013, "Diagnostics of AGN-Driven Molecular Outflows in ULIRGs from Herschel-PACS Observations of OH at 119 μm", *The Astrophysical Journal*, 775, 127

Stern, J. and Laor, A. 2013, "Type 1 AGN at low z - III. The optical narrow-line ratios", *Monthly Notices of the Royal Astronomical Society*, 431, 836

Stierwalt, S., Armus, L., Charmandaris, V., Diaz-Santos, T., Marshall, J., Evans, A. S., Haan, S., Howell, J., Iwasawa, K., Kim, D. C., Murphy, E. J., Rich, J. A., Spoon, H. W. W., Inami, H., Petric, A. O., and U, V. 2014, "Mid-infrared Properties of Luminous Infrared Galaxies. II. Probing the Dust and Gas Physics of the GOALS Sample", *The Astrophysical Journal*, 790, 124

Storey, P. J. and Hummer, D. G. 1995, "Recombination line intensities for hydrogenic ions-IV. Total recombination coefficients and machine-readable tables for Z=1 to 8", *Monthly Notices of the Royal Astronomical Society*, 272, 41, link from ADS to On-line Data

Sturm, E., Lutz, D., Verma, A., Netzer, H., Sternberg, A., Moorwood, A. F. M., Oliva, E., and Genzel, R. 2002, "Mid-Infrared line diagnostics of active galaxies. A spectroscopic AGN survey with ISO-SWS", *Astronomy and Astrophysics*, 393, 821

Suganuma, M., Yoshii, Y., Kobayashi, Y., Minezaki, T., Enya, K., Tomita, H., Aoki, T., Koshida, S., and Peterson, B. A. 2006, "Reverberation Measurements of the Inner Radius of the Dust Torus in Nearby Seyfert 1 Galaxies", *The Astrophysical Journal*, 639, 46

Tanabé, T., Sakon, I., Cohen, M., Wada, T., Ita, Y., Ohyama, Y., Oyabu, S., Uemizu, K., Takagi, T., Ishihara, D., Kim, W., Ueno, M., Matsuhara, H., and Onaka, T. 2008, "Absolute Photometric Calibration of the Infrared Camera (IRC) aboard AKARI", *Publications of the Astronomical Society of Japan*, 60, 375

Tielens, A. G. G. M. and Hollenbach, D. 1985, "Photodissociation regions. I - Basic model. II - A model for the Orion photodissociation region", *The Astrophysical Journal*, 291, 722

Toba, Y., Oyabu, S., Matsuhara, H., Malkan, M. A., Ishihara, D., Wada, T., Ohyama, Y., Takita, S., and Yamauchi, C. 2013, "The 9 and 18 Micrometer Luminosity Functions of Various Types of Galaxies with AKARI: Implication for the Dust Torus Structure of AGN", *Publications of the Astronomical Society of Japan*, 65, 113

Toba, Y., Oyabu, S., Matsuhara, H., Malkan, M. A., Gandhi, P., Nakagawa, T., Isobe, N., Shirahata, M., Oi, N., Ohyama, Y., Takita, S., Yamauchi, C., and Yano, K. 2014, "Luminosity and Redshift Dependence of the Covering Factor of Active Galactic Nuclei viewed with WISE and Sloan Digital Sky Survey", *The Astrophysical Journal*, 788, 45

Tristram, K. R. W., Burtscher, L., Jaffe, W., Meisenheimer, K., Hönig, S. F., Kishimoto, M., Schartmann, M., and Weigelt, G. 2014, "The dusty torus in the Circinus galaxy: a dense disk and the torus funnel", *Astronomy and Astrophysics*, 563, A82

Tueller, J., Mushotzky, R. F., Barthelmy, S., Cannizzo, J. K., Gehrels, N., Markwardt, C. B., Skinner, G. K., and Winter, L. M. 2008, "Swift BAT Survey of AGNs", *The Astrophysical Journal*, 681, 113

Tueller, J., Baumgartner, W. H., Markwardt, C. B., Skinner, G. K., Mushotzky, R. F., Ajello, M., Barthelmy, S., Beardmore, A., Brandt, W. N., Burrows, D., Chincarini, G., Campana, S., Cummings, J., Cusumano, G., Evans, P., Fenimore, E., Gehrels, N., Godet, O., Grupe, D., Holland, S., Kennea, J., Krimm, H. A., Koss, M., Moretti, A., Mukai, K., Osborne, J. P., Okajima, T., Pagani, C., Page, K., Palmer, D., Parsons, A., Schneider, D. P., Sakamoto, T., Sambruna, R., Sato, G., Stamatikos, M., Stroh, M., Ukwata, T., and Winter, L. 2010, "The 22 Month Swift-BAT All-Sky Hard X-ray Survey", *The Astrophysical Journal Supplement Series*, 186, 378

Turner, J., Kirby-Docken, K., and Dalgarno, A. 1977, "The Quadrupole Vibration-Rotation Transition Probabilities of Molecular Hydrogen", *The Astrophysical Journal Supplement Series*, 35, 281

Ueda, Y., Akiyama, M., Ohta, K., and Miyaji, T. 2003, "Cosmological Evolution of the Hard X-Ray Active Galactic Nucleus Luminosity Function and the Origin of the Hard X-Ray Background", *The Astrophysical Journal*, 598, 886

Ueda, Y., Eguchi, S., Terashima, Y., Mushotzky, R., Tueller, J., Markwardt, C., Gehrels, N., Hashimoto, Y., and Potter, S. 2007, "Suzaku Observations of Active Galactic Nuclei Detected in the Swift BAT Survey: Discovery of a "New Type" of Buried Supermassive Black Holes", *The Astrophysical Journal Letters*, 664, L79

van der Werf, P. P., Isaak, K. G., Meijerink, R., Spaans, M., Rykala, A., Fulton, T., Loenen, A. F., Walter, F., Weiß, A., Armus, L., Fischer, J., Israel, F. P., Harris, A. I., Veilleux, S., Henkel, C., Savini, G., Lord, S., Smith, H. A., González-Alfonso, E., Naylor, D., Aalto, S., Charmandaris, V., Dasyra, K. M., Evans, A., Gao, Y., Greve, T. R., Güsten, R., Kramer, C., Martín-Pintado, J., Mazzarella, J., Papadopoulos, P. P., Sanders, D. B., Spinoglio, L., Stacey, G., Vlahakis, C., Wiedner, M. C., and Xilouris, E. M. 2010, "Black hole accretion and star formation as drivers of gas excitation and chemistry in Markarian 231", *Astronomy and Astrophysics*, 518, L42

Veilleux, S., Kim, D.-C., and Sanders, D. B. 1999, "Optical Spectroscopy of the IRAS 1 JY Sample of Ultraluminous Infrared Galaxies", *The Astrophysical Journal*, 522, 113

Veilleux, S., Kim, D.-C., Sanders, D. B., Mazzarella, J. M., and Soifer, B. T. 1995, "Optical Spectroscopy of Luminous Infrared Galaxies. II. Analysis of the Nuclear and Long-Slit Data", *The Astrophysical Journal Supplement Series*, 98, 171

Véron-Cetty, M.-P. and Véron, P. 2010, "A catalogue of quasars and active nuclei: 13th edition", *Astronomy and Astrophysics*, 518, A10

Wada, K. 2012, "Radiation-driven Fountain and Origin of Torus around Active Galactic Nuclei", *The Astrophysical Journal*, 758, 66

Wada, K., Fukushige, R., Izumi, T., and Tomisaka, K. 2018, "Circumnuclear Multi-phase Gas in the Circinus Galaxy. I. Non-LTE Calculations of CO Lines", *The Astrophysical Journal*, 852, 88

Wada, K. and Norman, C. A. 2002, "Obscuring Material around Seyfert Nuclei with Starbursts", *The Astrophysical Journal Letters*, 566, L21

Wada, K., Papadopoulos, P. P., and Spaans, M. 2009, "Molecular Gas Disk Structures Around Active Galactic Nuclei", *The Astrophysical Journal*, 702, 63

Watson, D. M., Genzel, R., Townes, C. H., and Storey, J. W. V. 1985, "Far-infrared emission lines of CO and OH in the Orion-KL molecular shock", *The Astrophysical Journal*, 298, 316

Werner, M. W., Roellig, T. L., Low, F. J., Rieke, G. H., Rieke, M., Hoffmann, W. F., Young, E., Houck, J. R., Brandl, B., Fazio, G. G., Hora, J. L., Gehrz, R. D., Helou, G., Soifer, B. T., Stauffer, J., Keene, J., Eisenhardt, P., Gallagher, D., Gautier, T. N., Irace, W., Lawrence, C. R., Simmons, L., Van Cleve, J. E., Jura, M., Wright, E. L., and Cruikshank, D. P. 2004, "The Spitzer Space Telescope Mission", *The Astrophysical Journal Supplement Series*, 154, 1

Whittet, D. C. B., editor. 2003, Dust in the galactic environment

Wright, E. L., Eisenhardt, P. R. M., Mainzer, A. K., Ressler, M. E., Cutri, R. M., Jarrett, T., Kirkpatrick, J. D., Padgett, D., McMillan, R. S., Skrutskie, M., Stanford, S. A., Cohen, M., Walker, R. G., Mather, J. C., Leisawitz, D., Gautier, III, T. N., McLean, I., Benford, D., Lonsdale, C. J., Blain, A., Mendez, B., Irace, W. R., Duval, V., Liu, F., Royer, D., Heinrichsen, I., Howard, J., Shannon, M., Kendall, M., Walsh, A. L., Larsen, M., Cardon, J. G., Schick, S., Schwalm, M., Abid, M., Fabinsky, B., Naes, L., and Tsai, C.-W. 2010, "The Wide-field Infrared Survey Explorer (WISE): Mission Description and Initial On-orbit Performance", *The Astronomical Journal*, 140, 1868

Yamada, R., Oyabu, S., Kaneda, H., Yamagishi, M., Ishihara, D., Kim, J. H., and Im, M. 2013, "A Relation of the PAH 3.3 μm Feature with Star-forming Activity for Galaxies with a Wide Range of Infrared Luminosity", *Publications of the Astronomical Society of Japan*, 65, 103

Yamagishi, M., Kaneda, H., Ishihara, D., Oyabu, S., Onaka, T., Shimonishi, T., and Suzuki, T. 2011, "AKARI Near-infrared Spectroscopic Observations of Interstellar Ices in the Edge-on Starburst Galaxy NGC 253", *The Astrophysical Journal Letters*, 731, L20

Yuan, T.-T., Kewley, L. J., and Sanders, D. B. 2010, "The Role of Starburst-Active Galactic Nucleus Composites in Luminous Infrared Galaxy Mergers: Insights from the New Optical Classification Scheme", *The Astrophysical Journal*, 709, 884

Appendix A

Appendix for Chapter 3

A.1 Inverse Matrix of the Response Matrix

We denote the response matrix defined by Equations (3.9), (3.10), and (3.11) as $\mathbf{R}$. $\mathbf{R}$ is a triangular matrix. Figure A.1 displays the nonzero elements of $\mathbf{R}$. The columns with nonzero off-diagonal elements shift rightward every two rows because the magnitude relation (3.6) holds.

By the sweep-out method or similar, the inverse matrix $\mathbf{D} \equiv \mathbf{R}^{-1}$ is obtained as follows:

$$\mathbf{D} = \begin{pmatrix} D_{1,1} & & & & \\ & D_{2,2} & & & \\ & & \ddots & & \\ D_{k,1} & D_{k,2} & & D_{k,k} & \\ \ddots & \ddots & & & \ddots \end{pmatrix} \tag{A.1}$$

$$D_{i,i} = \frac{1}{R_{i,i}} \tag{A.2}$$

$$D_{i,j} = -\frac{R_{i,j}}{R_{i,i}R_{j,j}} \tag{A.3}$$

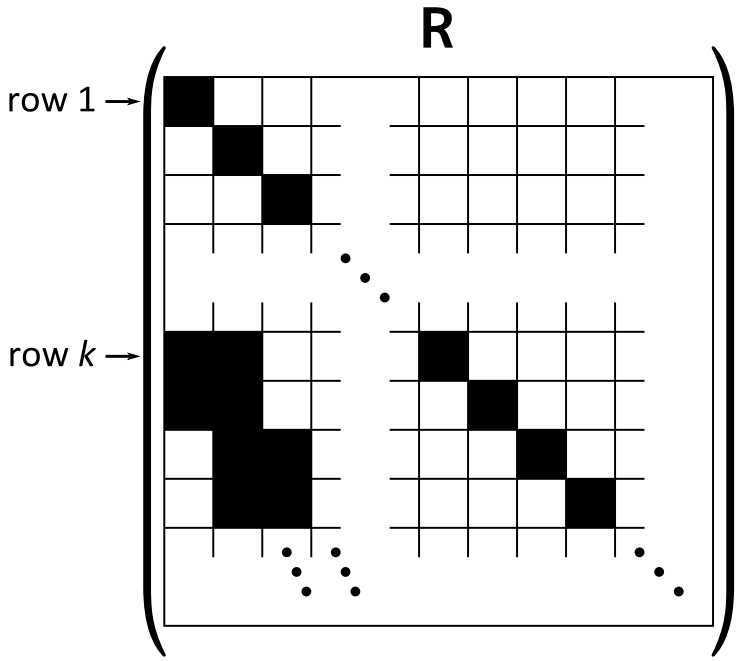

Figure A.1: Elements of the response matrix **R**. Black cells denote the nonzero elements. All other elements are zero.

Appendix B

Appendix for Chapter 5

B.1 Parameter Dependence of the Absorption Profile

Figure B.1 describes how our model depends on three parameters. If the column density, $N_{\rm CO}$, increases, the absorption profile becomes deeper because the optical depth is proportional to $N_{\rm CO}$. If the temperature, $T_{\rm CO}$, increases, the profile becomes wider because higher rotational levels are populated. If the velocity width, $v_{\rm turb}$, increases, the profile becomes deeper at the peaks of the P- and R-branches because the equivalent width is broadened only when the absorption is saturated. When the absorption is weak, we cannot determine $v_{\rm turb}$ from the model fitting unless we resolve rotational levels with a high spectral resolution. In this paper, however, we do not face this problem in most of the targets because they show sufficiently deep absorption profiles. We restrict the range of $v_{\rm turb}$ to less than 300 km s^{-1} because values higher than this upper limit do not substantially affect the profile as they involve two neighboring rotational lines to completely blend with each other.

B.2 $\Delta\chi^2$ Map

Figure B.2 shows a set of color maps of the $\Delta\chi^2$ value for all of the targets. The maps clearly show the degeneracy among the parameters. Large values of $N_{\rm CO}$ anti-correlates with $T_{\rm CO}$ and $v_{\rm turb}$. The $N_{\rm CO}$ versus $T_{\rm CO}$ anti-correlation can be interpreted as follows. At large $N_{\rm CO}$, the absorption is nearly saturated. Because the depths at the two peaks of the absorption profile do not change significantly with $N_{\rm CO}$, the depths at the band wings become more important in the determination of the solution. However, high values of $T_{\rm CO}$ instead of $N_{\rm CO}$ can also deepen the band wings, which results in the anti-correlation between $N_{\rm CO}$ and $T_{\rm CO}$. On the other hand, the $N_{\rm CO}$ versus $v_{\rm turb}$ anti-correlation originates because the two parameters similarly deepen the band profile when the absorption is saturated.

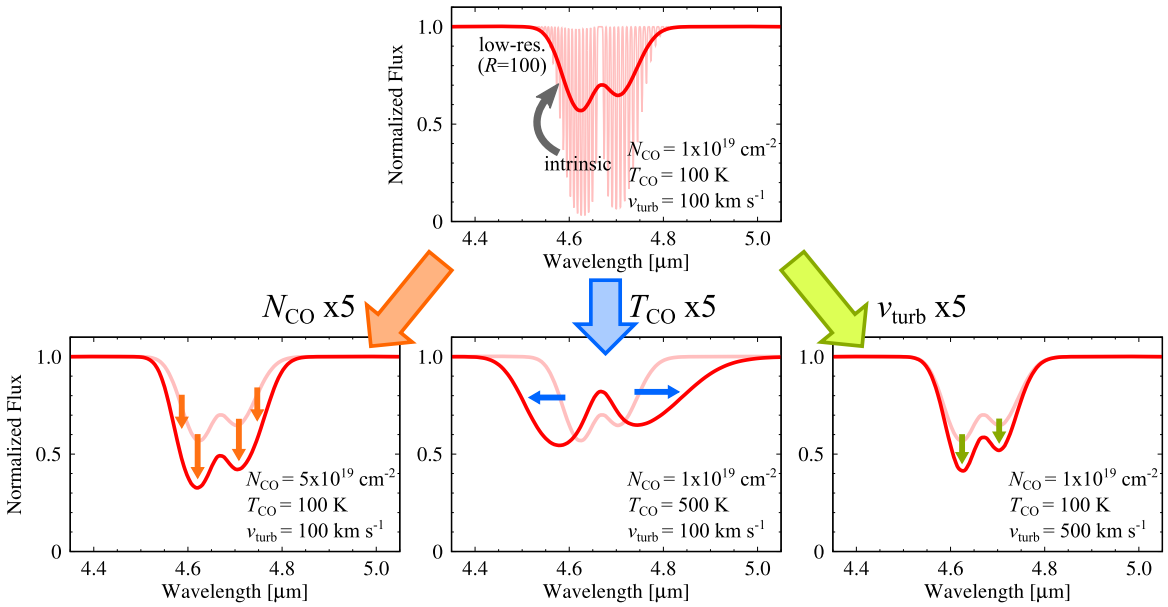

Figure B.1: Parameter dependence of the CO absorption model. The top panel compares the intrinsic model spectrum for the parameters noted at the right bottom corner with a blurred spectrum for a low spectral resolution ($R = 100$). The bottom panels show the changes in the absorption profile from the top panel when one parameter is multiplied by a factor of five.

B.3 Comparisons with Previous CO Analyses

B.3.1 IRAS 00182−7112

Our best-fit model for IRAS 00182−7112 (or IRAS F00183−7111) had a large column density and did not coincide with that of S04, who had performed a similar gas model fitting for a *Spitzer*/IRS spectrum based on an earlier IRS calibration. Our best-fitting parameters were, as tabulated in Table 3, $N_{CO} = 10^{21.2}$ cm^{-2}, $T_{CO} = 328$ K, and $v_{turb} = 28$ km s^{-1}, whereas those found by S04 were $10^{19.5}$ cm^{-2}, 720 K, and 50 km s^{-1}. Their solution largely differs from ours and locates near the edge of the 99% joint confidence region of our best-fit (See Figure B.2). However, in the analysis of S04, another solution with $N_{CO} = 10^{21.5}$ cm^{-2}, $T_{CO} = 400$ K, and $v_{turb} = 25$ km s^{-1}, which is similar to our result, was also found (H. Spoon & J. Cami, private communication). We therefore finally adopted our obtained large-column solution even though this solution has an uncertainty in the amount of gas hidden behind the $\tau = 1$ surface.

B.3.2 IRAS 08572+3915

IRAS 08572+3915 comprises two nuclei, with the one in the northwest (NW) being brighter than the one in southeast (SE) by 2.2 magnitudes at 2.2 μm (Scoville et al. 2000). The CO ro-vibrational absorption lines in IRAS 08572+3915 NW were first detected by Geballe et al. (2006) using UKIRT, and then observed with higher quality by S13 using Subaru. S13 obtained a high spectral resolution spectrum ($R \sim 5000$, $\Delta v \sim 60$ km s^{-1}) with individual absorption lines resolved and revealed a velocity profile comprising three distinct components centered at

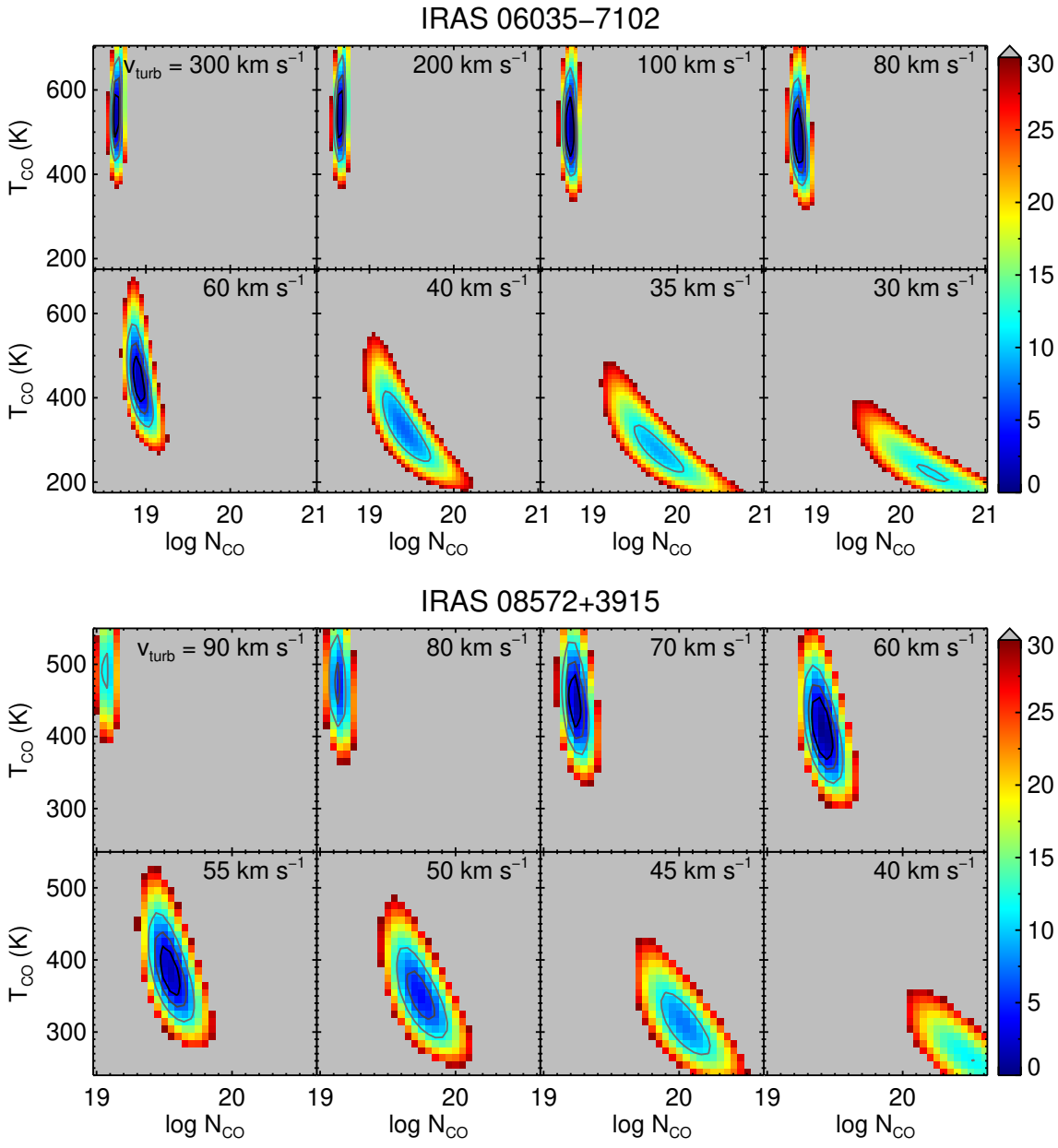

Figure B.2: Color maps of the $\Delta\chi^2$ values of the best-fit models shown in Figure 5.5 whose parameters are tabulated in Table 5.4. Each panel shows a slice of the three-dimensional parameter space at the turbulent velocity $v_{\rm turb}$ noted at the top right corner. From inside to outside, the closed solid curves denote the 68%, 90%, and 99% joint confidence levels, respectively.

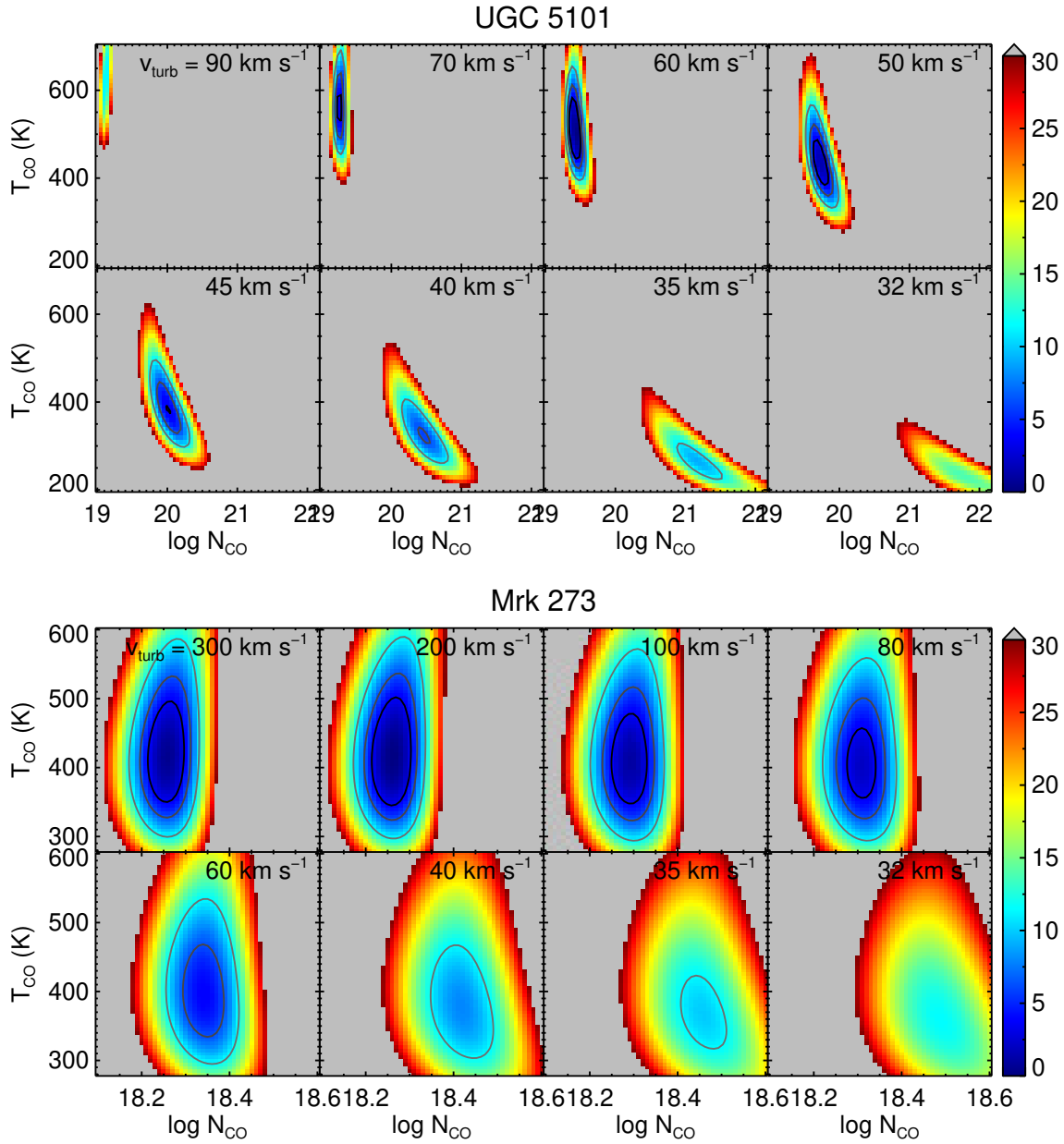

Figure B.2: (*Continued*)

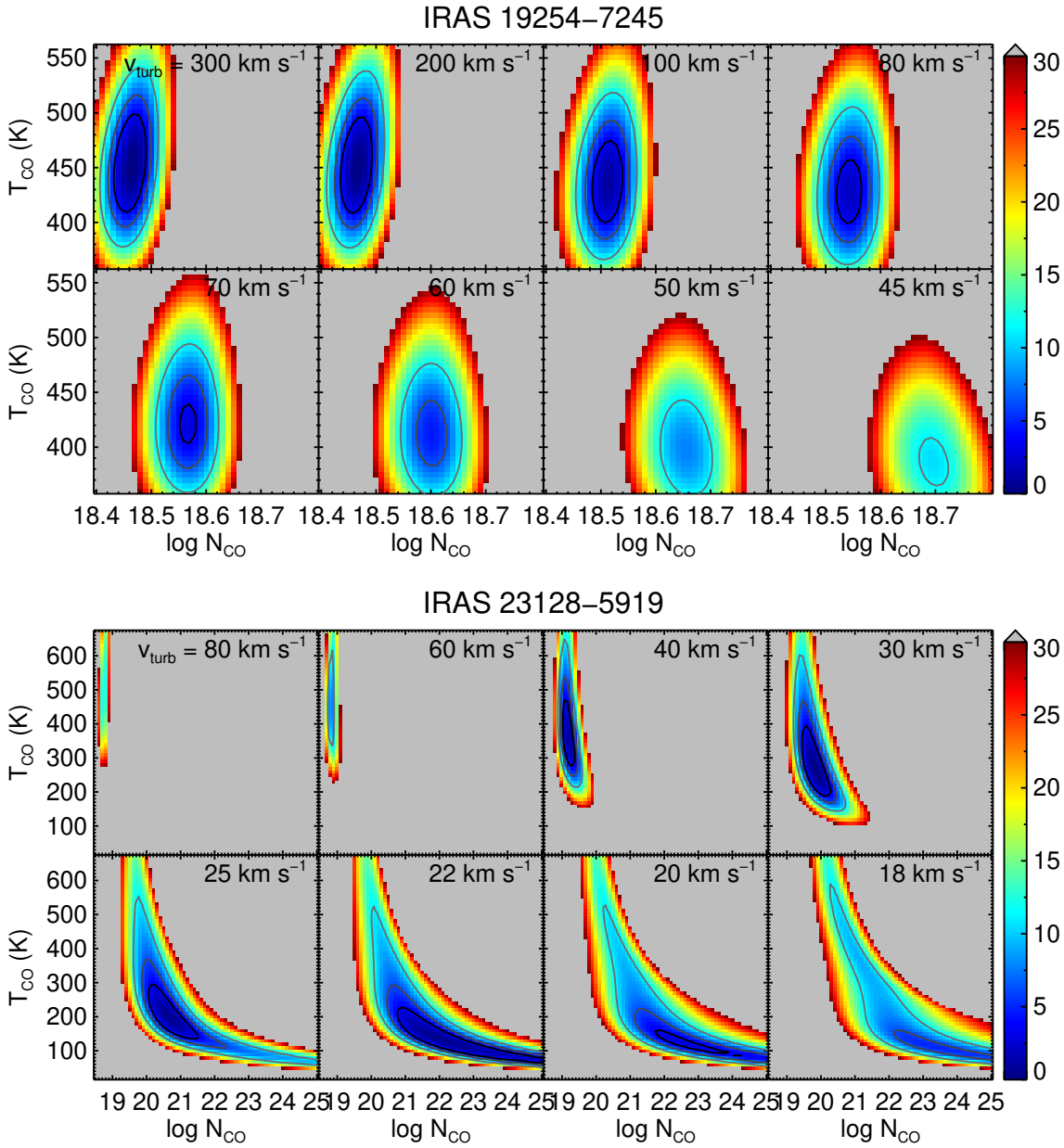

Figure B.2: (*Continued*)

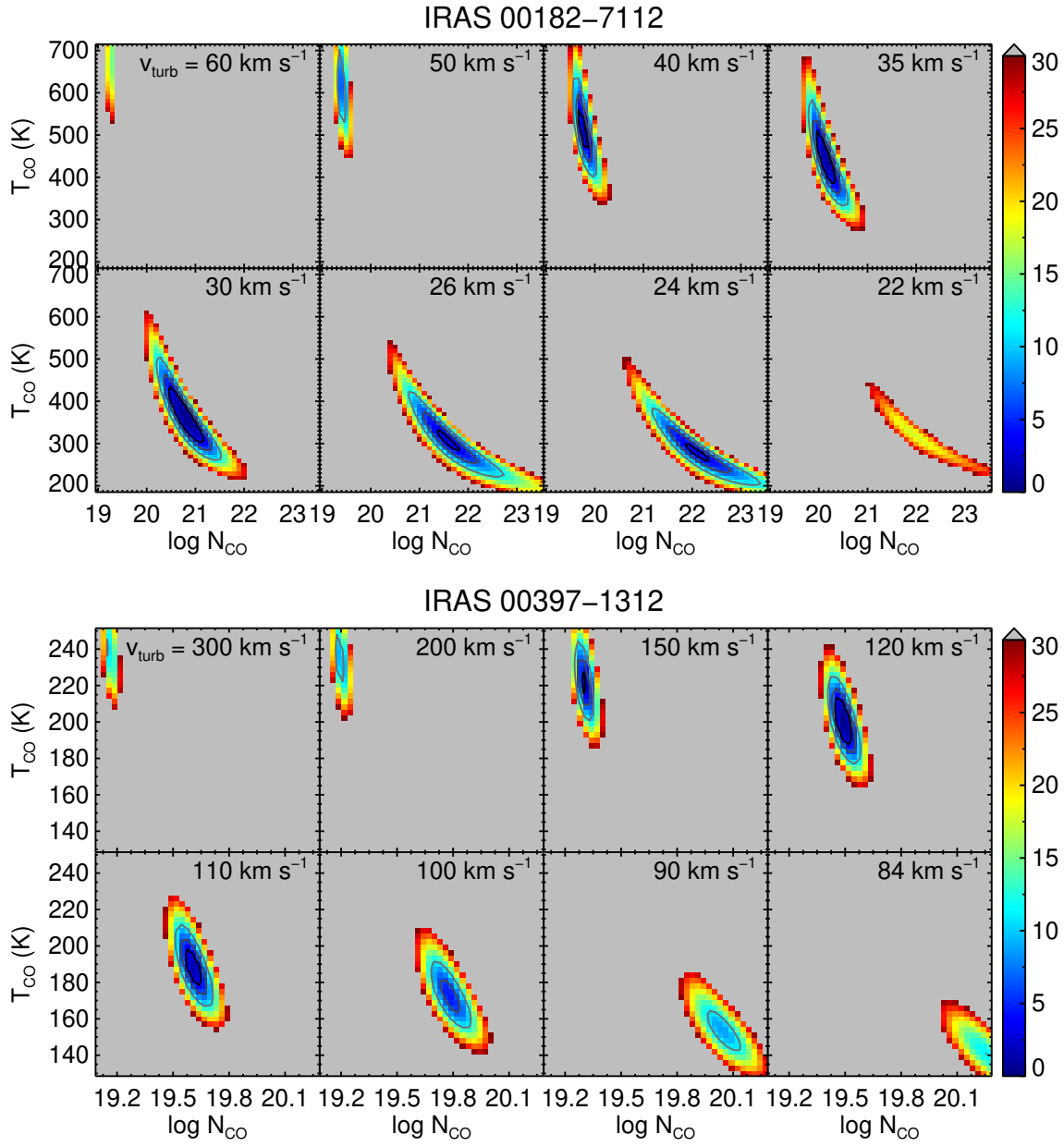

Figure B.2: (*Continued*)

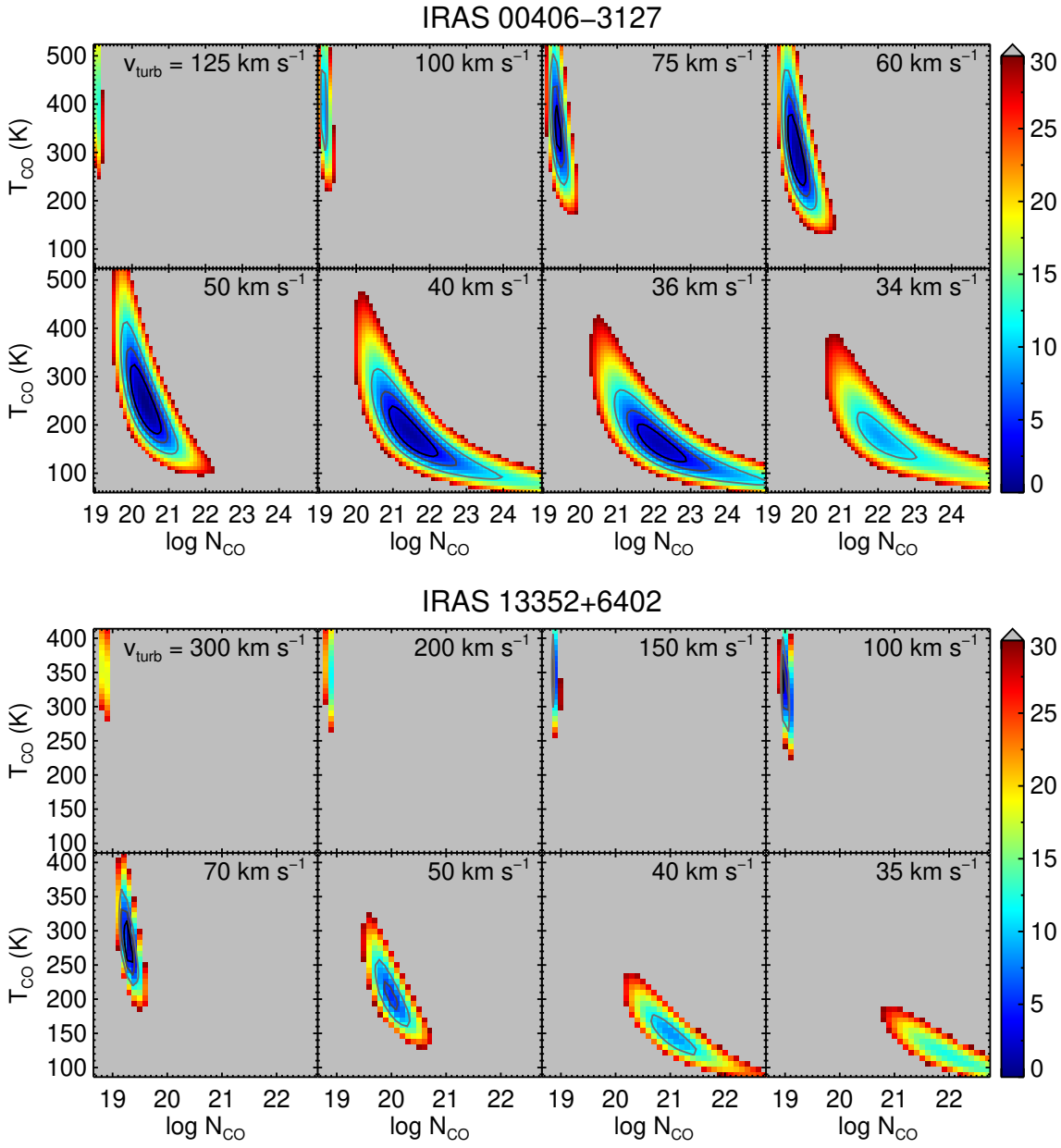

Figure B.2: (*Continued*)

0, −160, and +100 km s^{-1} relative to the systemic velocity of the galaxy. The authors analyzed the spectrum under the assumption of a three-component gas. Note that the numbers below are quoted from the full coverage case of S13, which is equivalent to our assumption, although the authors also discussed a partial coverage case. The first component was the blueshifted component, which had the largest CO column density of 2.7×10^{18} cm^{-2}, a warm temperature of 325 K, and a velocity width broader than 200 km s^{-1}. The second component was at the systemic velocity, with a column density of 5.7×10^{17} cm^{-2} and a temperature of 23 K. The third was the redshifted component, which was weaker than the other two components ($\sim 10^{17}$ cm^{-2}) and had the highest temperature ($\sim$ 700 K).

Although the *AKARI* observation used in this work did not spatially resolve the two nuclei, we assume that the contribution from the SE nucleus at around 4.67 μm is negligible as well as that at 2.2 μm, as SE is also much fainter in mid-IR wavelengths (Soifer et al. 2000). Our best-fitting column density, $N_{\rm CO} = 10^{19.4}$ cm^{-2}, and temperature, $T_{\rm CO} = 420$ K, were ~ 7 times larger and ~ 1.3 times higher, respectively, than those of the most prominent component of S13. Below, we discuss the source of this inconsistency.

The *AKARI* spectrum used in this study and the Subaru spectrum used in S13 have quite different wavelength coverages. The former covered only the *R*-branch, while the latter, which was limited by the atmospheric window, covered an almost opposite wavelength range corresponding to the *P*-branch. Thus, the discrepancy in the column densities found from the *R*- and *P*-branches can be attributed to the absorption profile becoming "asymmetric" and deviating from the current model prediction. Although it is possible that the effects mentioned in Section 5.5.1 can cause such an asymmetric absorption profile, these effects are weak to explain the difference.

We propose that the most plausible interpretation for the discrepancy is that S13 underestimated the continuum level in the calculation of the equivalent widths. As the Subaru spectrum used by S13 did not cover featureless wavelength regions, the authors determined the continuum level under the assumption that high-intensity peaks correspond to zero-absorption intensities. However, this determination is not trivial. The absorption depth in the Subaru spectrum coincides with that observed with *AKARI* if the actual continuum level is higher than that adopted by S13 by 30%. In this case, the equivalent width of each rotational line increases, and the excitation temperature of the dominant component obtained from the population diagram becomes 480 K. This change follows the trend in the discrepancy between our analyses and those of S13. To confirm this explanation, we require a seamless spectrum that continuously covers both the *P*- and *R*-branches. Such a spectrum can be acquired using the upcoming *James Webb Space Telescope*.

Appendix C

Appendix for Chapter 6

C.1 Color Correction of the *WISE* Data

Because some of the sample galaxies exhibit prominent PAH emissions and do not have monotonic spectral slopes within the *WISE* bands, the color-correction of the *WISE* magnitudes is essential, especially for $W1$ and $W3$, which could overlap the 3.3 μm and 11.2 μm PAH emissions, respectively. The color-correction factors for the $W1$, $W3$, and $W4$ bands, f_1, f_3, and f_4, respectively, were calculated in the same way of Section 5.2.3. However, because the $W2$ band overhangs both of the IRC and IRS spectra, the derivation of the factor for the band f_2 is not straightforward. We thus iteratively determined the factor. Initially, it was calculated from the relative spectral shape obtained by connecting the IRC and IRS spectra with no scaling. The IRS spectrum was scaled to fit the color-corrected $W3$ and $W4$ fluxes, and the IRC one was done based on the corrected $W1$ and the tentatively corrected $W2$. This initial scaling was used to update f_2. We repeated these processes three times to converge f_2. The final color-correction factors are summarized in Table C.1. The final f_2 becomes small when the CO absorption is deep, but its average among the sample points 1.03 with the standard deviation of 0.13. This distribution more concentrates on $f = 1$ than those of f_1 and $f3$ do because the latter two factors are significantly affected by the PAH emissions. Consequently, the color-correction of the $W2$ band is less critical than those of the $W1$ and $W3$ bands. The impact of the correction is the smallest in the $W4$ band, within which few emission or absorption features appear.

C.2 Galaxies observed with *ISO*

Lutz et al. (2004) searched for the signature of the CO absorption in nearby 31 AGNs observed with *ISO* and found no significant detection of the feature, even in type-2 AGNs. It is worth comparing their result with ours. Table C.2 lists the AGNs analyzed in Lutz et al. (2004) and indicates that those AGNs are mainly IRGs. This issue is discussed in Section 6.6.3. Among those AGNs, NGC 7213 and PKS 2048−57 = IC 5063 are common with our sample in Chapter 6. While in NGC 7213 we also did not detect significant absorption, in IC 5063, we could detect weak CO absorption owing to the sensitivity of *AKARI* (Section 6.5).

Table C.1: *WISE* color correction factors

Object	f_1	f_2	f_3	f_4
Mrk 334	0.725	0.949	0.624	0.998
NGC 23	0.750	1.021	0.517	1.018
MCG−02-01-051	0.504	1.180	0.505	1.007
NGC 232	0.604	1.034	0.477	1.013
I Zw 1	0.945	0.969	0.883	0.984
MCG−07-03-014	0.471	1.246	0.547	1.007
CGCG 436-030	0.712	0.969	0.900	1.014
NGC 612	0.824	1.030	0.370	1.021
ESO 353-G020	0.646	1.085	0.594	1.036
ESO 297-G018	0.934	0.988	0.750	0.988
IRAS 02530+0211	0.890	1.318	2.571	0.987
NGC 1614	0.481	1.056	0.867	0.984
ESO 121-IG028	0.896	0.987	1.122	1.014
NGC 2623	0.582	1.022	0.933	1.027
Mrk 18	0.832	1.029	0.730	0.996
IRAS 09022−3615	1.173	0.906	2.148	0.991
ESO 434-G040	0.973	0.959	1.040	0.989
NGC 3081	0.964	1.032	1.074	0.990
NGC 3079	0.912	1.139	0.942	1.061
NGC 3268	0.935	1.059	0.632	1.022
ESO 264-G057	0.702	0.994	0.545	1.016
Arp 148	0.789	0.935	0.634	1.037
NGC 4102	0.917	1.136	0.904	1.007
NGC 4194	0.580	1.091	0.903	1.000
M 106	0.947	1.008	0.844	1.002
NGC 4418	0.911	1.567	4.603	1.036
ESO 506-G027	0.963	0.968	1.161	0.989
NGC 4818	0.909	1.046	0.903	0.998
ESO 507-G070	0.623	1.046	0.753	1.035
IC 860	0.882	1.143	1.193	1.115
UGC 8335 W	0.722	0.997	0.455	1.016
UGC 8335 E	0.668	1.007	0.677	1.010
MCG−03-34-064	0.964	0.872	1.014	0.988
NGC 5135	0.709	0.994	0.712	1.007
IC 4280	0.753	1.008	0.503	1.026
Mrk 273	0.862	0.956	1.849	1.028
UGC 9618 N	0.810	0.962	0.492	1.055
IRAS 15250+3609	0.936	0.692	6.286	1.000
Arp 220	0.638	1.212	2.125	1.101
NGC 6701	0.749	1.106	0.627	1.016
IC 5063	0.989	0.963	1.009	1.002
ESO 286-IG019	1.044	0.824	3.892	0.994
NGC 7130	0.749	0.976	0.830	0.987
NGC 7213	0.975	0.992	0.776	0.995
ESO 148-IG002	1.017	0.981	1.742	0.971
IC 5298	0.839	0.979	0.791	1.013
Mrk 331	0.520	1.126	0.575	1.027
average	0.807	1.033	1.171	1.013
standard deviation	0.163	0.130	1.113	0.028

Table C.2: Sample of Lutz et al. (2004)

Object	Type	R.A. (J2000)	Dec. (J2000)	z	$\log L_{\rm IR}$ ($L_\odot$)
(1)	(2)	(3)	(4)	(5)	(6)
Mrk 335	Type 1	$00^{\rm h}06^{\rm m}19\overset{\rm s}{.}52$	$+20°12'10\overset{''}{.}5$	0.025785	10.7
Mrk 590	Type 1	$02^{\rm h}14^{\rm m}33\overset{\rm s}{.}56$	$-00°46'00\overset{''}{.}1$	0.026385	10.7
NGC 1097	Type 1	$02^{\rm h}46^{\rm m}19\overset{\rm s}{.}05$	$-30°16'29\overset{''}{.}6$	0.004240	10.7
NGC 1566	Type 1	$04^{\rm h}20^{\rm m}00\overset{\rm s}{.}42$	$-54°56'16\overset{''}{.}1$	0.005017	10.4
Ark 120	Type 1	$05^{\rm h}16^{\rm m}11\overset{\rm s}{.}42$	$-00°08'59\overset{''}{.}4$	0.032713	11.0
MCG 8−11−11	Type 1	$05^{\rm h}54^{\rm m}53\overset{\rm s}{.}61$	$+46°26'21\overset{''}{.}6$	0.020484	11.1
Mrk 6	Type 1	$06^{\rm h}52^{\rm m}12\overset{\rm s}{.}25$	$+74°25'37\overset{''}{.}5$	0.018813	10.6
Mrk 79	Type 1	$07^{\rm h}42^{\rm m}32\overset{\rm s}{.}80$	$+49°48'34\overset{''}{.}7$	0.022189	10.9
NGC 3227	Type 1	$10^{\rm h}23^{\rm m}30\overset{\rm s}{.}58$	$+19°51'54\overset{''}{.}2$	0.003859	9.9
NGC 3516	Type 1	$11^{\rm h}06^{\rm m}47\overset{\rm s}{.}49$	$+72°34'06\overset{''}{.}9$	0.008836	10.1
NGC 3783	Type 1	$11^{\rm h}39^{\rm m}01\overset{\rm s}{.}76$	$-37°44'19\overset{''}{.}2$	0.009730	10.6
NGC 4051	Type 1	$12^{\rm h}03^{\rm m}09\overset{\rm s}{.}61$	$+44°31'52\overset{''}{.}8$	0.002336	9.5
NGC 4151	Type 1	$12^{\rm h}10^{\rm m}32\overset{\rm s}{.}58$	$+39°24'20\overset{''}{.}6$	0.003319	9.9
Mrk 766	Type 1	$12^{\rm h}18^{\rm m}26\overset{\rm s}{.}51$	$+29°48'46\overset{''}{.}3$	0.012929	10.7
NGC 4593	Type 1	$12^{\rm h}39^{\rm m}39\overset{\rm s}{.}43$	$-05°20'39\overset{''}{.}3$	0.009000	10.3
IC 4329A	Type 1	$13^{\rm h}49^{\rm m}19\overset{\rm s}{.}27$	$-30°18'34\overset{''}{.}0$	0.016054	10.9
NGC 5548	Type 1	$14^{\rm h}17^{\rm m}59\overset{\rm s}{.}53$	$+25°08'12\overset{''}{.}4$	0.017175	10.6
NGC 7213	Type 1	$22^{\rm h}09^{\rm m}16\overset{\rm s}{.}31$	$-47°09'59\overset{''}{.}8$	0.005839	10.0
NGC 7469	Type 1	$23^{\rm h}03^{\rm m}15\overset{\rm s}{.}62$	$+08°52'26\overset{''}{.}4$	0.016317	11.6
NGC 1068	Type 2	$02^{\rm h}42^{\rm m}40\overset{\rm s}{.}71$	$-00°00'47\overset{''}{.}8$	0.003793	11.4
NGC 1365	Type 2	$03^{\rm h}33^{\rm m}36\overset{\rm s}{.}37$	$-36°08'25\overset{''}{.}4$	0.005457	11.1
NGC 1386	Type 2	$03^{\rm h}36^{\rm m}46\overset{\rm s}{.}18$	$-35°59'57\overset{''}{.}9$	0.002895	9.5
IRAS 04385−0828	Type 2	$04^{\rm h}40^{\rm m}54\overset{\rm s}{.}97$	$-08°22'22\overset{''}{.}2$	0.015100	10.7
NGC 4388	Type 2	$12^{\rm h}25^{\rm m}46\overset{\rm s}{.}75$	$+12°39'43\overset{''}{.}5$	0.008419	10.7
NGC 4507	Type 2	$12^{\rm h}35^{\rm m}36\overset{\rm s}{.}63$	$-39°54'33\overset{''}{.}3$	0.011801	10.6
Cen A	Type 2	$13^{\rm h}25^{\rm m}27\overset{\rm s}{.}62$	$-43°01'08\overset{''}{.}8$	0.001825	10.5
Circinus	Type 2	$14^{\rm h}13^{\rm m}09\overset{\rm s}{.}95$	$-65°20'21\overset{''}{.}2$	0.001448	10.7
NGC 5506	Type 2	$14^{\rm h}13^{\rm m}14\overset{\rm s}{.}89$	$-03°12'27\overset{''}{.}3$	0.006181	10.4
PKS 2048−57	Type 2	$20^{\rm h}52^{\rm m}02\overset{\rm s}{.}34$	$-57°04'07\overset{''}{.}6$	0.011348	10.8
NGC 7582	Type 2	$23^{\rm h}18^{\rm m}23\overset{\rm s}{.}50$	$-42°22'14\overset{''}{.}0$	0.005254	10.9
NGC 7674	Type 2	$23^{\rm h}27^{\rm m}56\overset{\rm s}{.}72$	$+08°46'44\overset{''}{.}5$	0.028924	11.6

NOTE—Column 1: object name (by courtesy of D. Lutz). Column 2: AGN type adopted in Lutz et al. (2004). Columns 3 and 4: right ascension and declination (J2000). Column 5: redshift from the NASA/IPAC Extragalactic Database (NED). Column 6: logarithm of the infrared (8–1000 μm) luminosity in units of the solar luminosity derived from the *IRAS* 4 bands.

Acknowledgments

A series of studies in this thesis would never have been achieved without the support of my surrounding people.

Prof. Takao Nakagawa, my supervisor, has always kindly supported me, even when he was truly busy at other works such as the SPICA project, etc., by regularly setting up time for discussion and by frequently advising me how to proceed studies. I have given him a lot of inconveniences so far, but he still patiently and kindly taught such a student. Whenever my research was in troubles, I was able to ask him for advice readily. Without his support, my graduate school life would not have worked. I courteously express my utmost appreciation for him.

I am sincerely grateful to Dr. Naoki Isobe and Dr. Hirano (Shirahata) Mai, who gave me detailed guidance ranging from how to proceed studies to how to write scientific documents. Their strict and insightful comments for my logic in discussions and for ambiguities of my writings were invaluable to learn an honest attitude toward science.

During the re-calibrations of the *AKARI* spectroscopy, Dr. Issei Yamamura, Dr. Takehiko Wada, Prof. Hideo Matsuhara, Prof. Takashi Onaka, Dr. Fumihiko Usui, Dr. Youichi Ohyama, Dr. Mitsuyoshi Yamagishi, Dr. Itsuki Sakon, Dr. Takashi Shimonishi, Dr. Takuji Yamashita gave me highly specialized knowledge about the satellite system and really helpful advice based on their extensive experience on data analysis. Without their cooperation, the recalibrations would not have succeeded. My research, which requires a new technique to fully utilize observed data, could not be accomplished unless I have studied at here Institute of Space and Astronautical Science (ISAS), the site of the birth of the satellite, and have communicated with researchers who had developed it. I deeply appreciate the above people and all the other members of the *AKARI* team.

In the analysis of the CO absorption band, I was kindly provided with information and received insightful comments and fruitful suggestions from Dr. Henrik Spoon and Dr. Jan Cami. Their help made the study more robust and valuable. I also obtained significant feedbacks from discussions with Dr. Masatoshi Imanishi, Prof. Keiichi Wada, Dr. Toshihiro Kawaguchi, Dr. Takuma Izumi, Dr. Kohei Ichikawa, Dr. Taiki Kawamuro, Dr. Yoshiyuki Inoue, Dr. Yoshiki Toba, Dr. Kazumi Murata, and Dr. Kei Sano. I would like to express my appreciation them and everyone who is interested in my research.

I would like to thank Dr. Jungmi Kwon, Ryosuke Doi, Hiroshi Maeshima, Shusuke Onishi, who gave me suggestions at the weekly meeting.

I am really grateful to my senpai and friends I met at ISAS, Dr. Koichi Nagase, Keita Yamamoto, Shuhei Koyama, Aoi Takahashi, Chihiro Uemura, Hiroshi Masuda, Satoshi Tonooka, Hiroaki Itsuji, Akihiro Iwasaki, Takayoshi Oba, Kenta Uehara, Satomi Nakahara, and Shota Kikuchi. They all always encouraged me.

I owe my gratitude to all the members of LIRA (Laboratory of Infrared Astronomy). They have really helped me in various respects. I show my special thanks to Kumiko Nishimatsu for her secretary assistance.

Finally, I would like to express my deepest appreciation to my family, for supporting and watching over me warmly.

Shunsuke Baba

This research is based on observations with *AKARI*, a JAXA project with the participation of ESA.

This work is based on observations made with the *Spitzer Space Telescope*, obtained from the NASA/IPAC Infrared Science Archive, both of which are operated by the Jet Propulsion Laboratory, California Institute of Technology under a contract with the National Aeronautics and Space Administration.

The Combined Atlas of Sources with *Spitzer* IRS Spectra (CASSIS) is a product of the IRS instrument team, supported by NASA and JPL.

This publication makes use of data products from the *Wide-field Infrared Survey Explorer*, which is a joint project of the University of California, Los Angeles, and the Jet Propulsion Laboratory/California Institute of Technology, and *NEOWISE*, which is a project of the Jet Propulsion Laboratory/California Institute of Technology. *WISE* and *NEOWISE* are funded by the National Aeronautics and Space Administration.

This publication makes use of data products from the Two Micron All Sky Survey, which is a joint project of the University of Massachusetts and the Infrared Processing and Analysis Center/California Institute of Technology, funded by the National Aeronautics and Space Administration and the National Science Foundation.

This research has made use of the NASA/IPAC Extragalactic Database (NED) which is operated by the Jet Propulsion Laboratory, California Institute of Technology, under contract with the National Aeronautics and Space Administration.